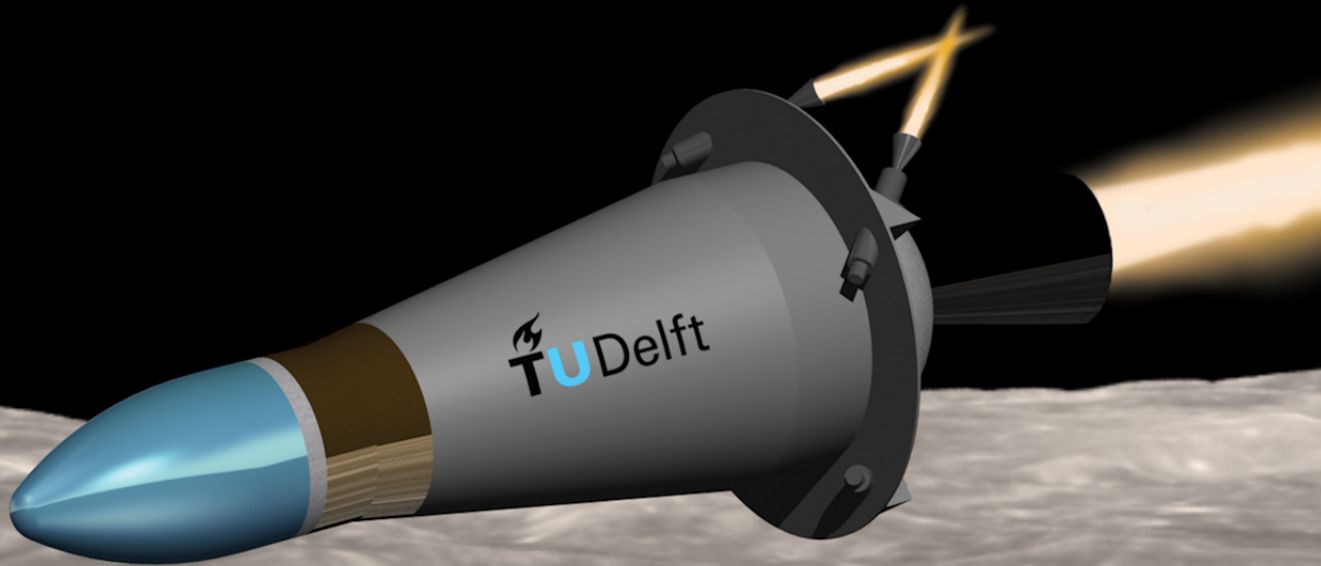


Design of the European Lunar Penetrator (ELUPE) Descent Module Controller

W.J. Bouma Master of Science Thesis



Design of the European Lunar Penetrator (ELUPE) Descent Module Controller

MASTER OF SCIENCE THESIS

For obtaining the degree of Master of Science in Aerospace Engineering
at Delft University of Technology

W.J. Bouma

To be defended publicly on:
August 29, 2019

Front cover background image courtesy:
[Lunar Reconnaissance Orbiter, NASA](#)

Faculty of Aerospace Engineering · Delft University of Technology



Copyright © Delft University of Technology
All rights reserved.

DELFT UNIVERSITY OF TECHNOLOGY
FACULTY OF AEROSPACE ENGINEERING
DEPARTMENT OF SPACE SYSTEMS ENGINEERING

The undersigned hereby certify that they have read and recommend to the Faculty of Aerospace Engineering for acceptance a thesis entitled DESIGN OF THE EUROPEAN LUNAR PENETRATOR (ELUPE) DESCENT MODULE CONTROLLER by W.J. BOUMA in partial fulfillment of the requirements for the degree of MASTER OF SCIENCE.

Dated: August 29, 2019

Head of department:

prof. dr. E.K.A. Gill

Supervisor:

dr. ir. R. Fonod

Co-supervisor:

dr. J. Guo

Reader:

ir. K.J. Cowan MBA

Preface

With this thesis, I conclude the master Space Flight at TU Delft’s faculty of Aerospace Engineering. The thesis was built on an earlier project, completed during my stay at ESA/ESTEC in the last half of 2017, and refined throughout 2018, while fulfilling the remainder of my course requirements. The actual thesis project ran from January to August 2019. In effect, the topic has been keeping me busy for two years – give or take.

*“It’s been uh... It’s been... interesting.
But I’m glad we have her done.”*

— Jack’s Mannequin, *MFEO*

Before moving on to the content, I would like to acknowledge a few people. First off, my daily supervisor, dr. ir. Robert Fonod; thank you for expressing your interest in supervising the project after having presented it to you back in November. Your involvement fuelled the project with some welcome new energy and fresh perspective. Thank you for our fruitful discussions and your invaluable feedback. Also, my co-supervisor, dr. Jian Guo; thank you for all the time you devoted to supervising the project right from the very start at ESTEC, when everything still had to take shape.

Outside the academic environment, I would like to thank my parents for endlessly supporting and encouraging me; without you, all of this would not have been possible. I would also like to thank my ‘parents-in-law’ for being sincerely invested in the progress of this project. I would like to thank my close friends; in particular Inger, for regularly checking in, and Syward, for proof-reading part of the content and having to endure my ongoing rambling about control algorithms and simulations. Finally, my gratitude and appreciation goes to my girlfriend, Floor, who has been there through thick and thin, low lows and high highs; thank you for bearing with me all this time – you are the greatest and sweetest.

*Wouter Bouma
Amsterdam, 2019*

Abstract

To obtain unambiguous ground truth of water-ice residing in permanently shaded regions of the Moon and to characterise the local regolith, ESA considers a mission involving an instrumented penetrator implanted there by high-speed impact. Released into lunar orbit, the European Lunar Penetrator (ELUPE) Descent Module will autonomously traverse a controlled trajectory to its designated target. The associated attitude control problem involves highly nonlinear large-angle slew manoeuvres and unstable minor-axis spin manoeuvres. To establish a benchmark, a controller based on classical control techniques was designed, verified and tested in a simulation. Legacy control algorithms were implemented and extended. A thruster management function was developed to translate the control commands into thruster actions. For the simulator, accurate models of the descent module and its environment were created.

A Monte Carlo simulation was run to determine the success rate of the ELUPE mission from a descent-and-landing perspective, and to assess the performance of the controller under off-nominal conditions. From the results, it was found that the success rate was 58.5% for a surface slope of 20° , and 74.2% for a slope of 10° or lower. Key factors affecting the success rate were identified to be the centre-of-mass offset and the solid rocket motor thrust misalignment angle. As further constraining these parameters would be unrealistic, it was recommended to modify the thrust curve of the solid rocket motor to improve the success rate.

Analysis of the attack angle and the nutation angle just prior to impact, revealed their success criteria were met in 98.7% and 99.8% of all cases, respectively. These successful results confirmed the attitude control problem could be satisfactorily solved by a ‘classical’ controller. However, despite its good global performance, the proposed controller was found to also exhibit some serious shortcomings. For this reason, it was recommended to explore the possibilities for a different controller.

To the best of the author’s knowledge, this thesis represented the first known attempt at designing a comprehensive controller for a fully actuated, thruster-controlled penetrator mission targeted for an airless body. In addition, it was the first known study to provide insight into the feasibility and success rate of such a mission from a descent-and-landing perspective.

Table of Contents

Preface	vi
Abstract	viii
List of Figures	xvii
List of Tables	xx
Nomenclature	xxi
1 Introduction	1
1-1 Background and Motivation	1
1-2 The ELUPE Mission	3
1-2-1 Mission Goals, Objectives and Outcomes	3
1-2-2 Spacecraft	4
1-2-3 Descent Scenario	5
1-3 Problem Statement	7
1-4 Literature Review	9
1-4-1 Planetary Penetrators	9
1-4-2 Control Techniques	10
1-5 Research Question	11
1-6 Contributions	12
1-7 Report Structure	12

2	Spacecraft Modelling	15
2-1	Preliminaries	15
2-2	Attitude and Orbit Control System	16
2-2-1	Reaction Control System	16
2-2-2	De-Orbit Motor	23
2-3	Inertial Parameters	24
2-4	Torque Capabilities	25
3	Spacecraft Motion and Disturbance Modelling	31
3-1	Reference Frames	31
3-2	State Representation	32
3-3	Attitude Kinematics	34
3-4	Attitude Dynamics	35
3-4-1	Equations of Motion	35
3-4-2	Disturbance Torques	38
4	Controller Design	45
4-1	Introduction	45
4-2	Large-Angle Slew Manoeuvres	46
4-2-1	Control Law	46
4-2-2	Gain Selection	47
4-2-3	Verification	50
4-3	Minor-Axis Spin Manoeuvres	54
4-3-1	Spin-Up and Spin-Down Manoeuvres	54
4-3-2	Denutation Manoeuvres	54
5	Mission Manager Logic	69
5-1	Control Phases and Control Modes	69
5-2	Target States and Control Setpoints	70
5-2-1	Target Spin Rates	72
5-2-2	Target Orientations	84
5-2-3	Overview of Target States	86

6	Simulation Study	87
6-1	Simulator Elements	87
6-1-1	Thruster Management Function	87
6-1-2	Navigation System	95
6-2	Simulator Architecture	97
6-3	Simulation Set-Up	99
6-3-1	Simulation Input	99
6-3-2	Integrator	99
6-3-3	Monte Carlo Simulations	103
6-3-4	Simulation Output	104
6-4	Simulation Results	105
6-4-1	Nominal Case	106
6-4-2	Off-Nominal Cases	114
7	Conclusions and Recommendations	127
A	Penetrator Descent Module	131
A-1	Penetrator	131
A-2	Penetrator Delivery System	133
A-3	Mass Budget	133
B	Mission Requirements	135
B-1	Penetration	135
B-2	Fly-Away Manoeuvre	138
C	Propellant Slugs	139
C-1	Solid Propellant Slug	139
C-2	Liquid Propellant Slug	150
D	State Variable Transformations	155
D-1	Euler Angles to Unit Quaternions	155
D-2	Unit Quaternions to Euler Angles	155
E	Frame Transformations	157

F Translational Equations of Motion	159
G Hardware Specifications	161
Bibliography	163

List of Figures

1-1	Spacecraft: CATIA render	4
1-2	Descent scenario: schematic of the descent trajectory	5
1-3	Descent scenario: schematic of the second phase of the descent	8
2-1	Preliminaries: schematic of spacecraft configuration	16
2-2	Reaction control system: schematic of thruster configuration	17
2-3	Reaction control system: performance diagram of thrusters	18
2-4	Reaction control system: schematic of propellant tank	20
2-5	Reaction control system: average output thrust capabilities of thrusters	22
2-6	De-orbit motor: performance diagrams	23
2-7	Inertial parameters: schematic of propellant slugs	25
2-8	Torque capabilities: schematic indicating force components and moment arms	27
3-1	Reference frames: definitions of reference frames considered	32
3-2	Viscous friction torque: example spin-axis transition manoeuvre	43
3-3	Viscous friction torque: reproduction of Figure 3-2	43
4-1	Large-angle slew manoeuvres: relative difference settling times	50
4-2	Large-angle slew manoeuvres: reevaluation of Figure 4-1	51
4-3	Large-angle slew manoeuvres: example time histories of quaternions	52
4-4	Large-angle slew manoeuvres: reproduction of Figure 4-3	52

4-5	Large-angle slew manoeuvres: example time histories of body rates and eigenangle	53
4-6	Large-angle slew manoeuvres: reproduction of Figure 4-5	53
4-7	Spin-up and spin-down manoeuvres: example results	55
4-8	Denutation manoeuvres: definition of angular momentum vector	56
4-9	Denutation manoeuvres: visualisation of thruster pulse timing strategy	57
4-10	Denutation manoeuvres: control logic	58
4-11	Denutation manoeuvres: example body rates and nutation angle	65
4-12	Denutation manoeuvres: reproduction of Figure 4-11	65
4-13	Denutation manoeuvres: example angular accelerations and control torque	66
4-14	Denutation manoeuvres: reproduction of Figure 4-13	66
4-15	Denutation manoeuvres: numerical and analytic results for torque-free ω_x and ω_y	67
4-16	Denutation manoeuvres: time histories of ω_y and θ_{nut} for different settling times	67
4-17	Denutation manoeuvres: results dual-axis controlled denutation process	68
5-1	Control phases and control modes: mission manager logic	71
5-2	De-orbit manoeuvre spin rate: schematic of thrust misalignments	73
5-3	De-orbit manoeuvre spin rate: time histories of the disturbance torques	75
5-4	De-orbit manoeuvre spin rate: transverse angular rate responses during DOM	76
5-5	De-orbit manoeuvre spin rate: results of the DOM for $4\pi \text{ rad s}^{-1}$ spin rate	77
5-6	De-orbit manoeuvre spin rate: success rates for the DOM	79
5-7	Penetrator release spin rate: nutation angle and landing distance versus spin rate	81
6-1	Thruster management function: firing duration correction procedure	89
6-2	Thruster management function: test results quaternions	92
6-3	Thruster management function: test results body rates and eigenangle-to-go	92
6-4	Thruster management function: test results torque commands	93
6-5	Thruster management function: test results actual torques	93
6-6	Thruster management function: test results Control Phase 4 manoeuvres	96
6-7	Thruster management function: test results Control Phase 7 manoeuvres	96
6-8	Thruster management function: improved results Control Phase 7 manoeuvres	97
6-9	Simulator architecture: architecture of the simulator	100
6-10	Simulation results: nominal descent trajectory PDM/PDS and penetrator	107

6-11	Simulation results: side views of Figure 6-10	108
6-12	Simulation results: nominal rotational state variables PDM/PDS	109
6-13	Simulation results: nominal torques and forces	110
6-14	Simulation results: nominal time histories inertial parameters	112
6-15	Simulation results: nominal rotational state variables penetrator and key angles . .	115
6-16	Simulation results: scatter plot penetrator landing sites	117
6-17	Simulation results: spin rate decrease	118
6-18	Simulation results: ineffective denutation algorithm	119
6-19	Simulation results: histograms penetrator landing parameters	121
6-20	Simulation results: histograms descent parameters	122
A-1	Penetrator: CATIA render	132
A-2	Penetrator: schematic representation	132
B-1	Penetration: definition of key angles	136
C-1	Solid propellant slug: schematic of a partial slug	140
C-2	Solid propellant slug: geometry spherical cap with respect to associated sphere . .	143
C-3	Solid propellant slug: mass versus CoM	149
C-4	Solid propellant slug: mass versus Mol	149
C-5	Liquid propellant slug: schematic of a partial slug	150
C-6	Liquid propellant slug: mass versus CoM	153
C-7	Liquid propellant slug: mass versus Mol	153

List of Tables

1-1	Descent scenario: sequence of events	6
2-1	Reaction control system: thruster positions	17
2-2	Reaction control system: feed pressure drop factors	19
2-3	Inertial parameters: inertia properties of spacecraft.	24
2-4	Hydrazine thrusters: expressions for thruster force components	26
2-5	Torque capabilities: parameter values for maximally loaded PDM	28
2-6	Torque capabilities: example thruster force and moment arm components	29
2-7	Torque capabilities: example torque capabilities and angular impulse bits	29
3-1	Gravity gradient torque: relevant characteristics of the Moon	39
3-2	Gravity gradient torque: worst-case impact	40
3-3	Solar radiation torque: surface properties of the spacecraft	41
3-4	Viscous friction torque: parameter values for verification	42
3-5	Viscous friction torque: parameter values for significance assessment	44
4-1	Large-angle slew manoeuvres: parameter values for testing	49
4-2	Large-angle slew manoeuvres: parameter values for verification	51
4-3	Denutation manoeuvres: parameter values for verification	63
4-4	Denutation manoeuvres: parameter values for testing	64
5-1	Control phases and control modes: mapping	72

5-2	De-orbit manoeuvre spin rate: three-sigma values thrust misalignments	74
5-3	Penetrator release spin rate: relative tip-off velocities	78
5-4	Penetrator release spin rate: parameter values for testing	83
5-5	Overview of target states: target state and maximum duration per control phase .	86
6-1	Thruster management function: comparison linear programming solvers	91
6-2	Thruster management function: parameter values for testing	94
6-3	Navigation system: eigenangle and angular rate uncertainties	97
6-4	Simulation input: model parameters	101
6-5	Simulation input: decision variables	102
6-6	Simulation input: model parameter and decision variable uncertainties	104
6-7	Simulation output: overview of output parameters	105
6-8	Simulation results: nominal descent parameters	111
6-9	Simulation results: success criteria penetrator landing	113
6-10	Simulation results: nominal penetrator landing parameters	114
6-11	Simulation results: penetrator landing success rate versus local slope	116
6-12	Simulation results: penetrator landing site statistical descriptors	120
6-13	Simulation results: landing parameter ranking	123
6-14	Simulation results: correlation coefficients descent and landing parameters	124
6-15	Simulation results: correlation coefficients descent and model parameters	125
A-1	Mass budget: mass budget of the PDM	134
C-1	Solid propellant slug: characteristics	146
C-2	Solid propellant slug: overview of MATLAB functions	148
C-3	Liquid propellant slug: characteristics	151
G-1	Hardware specifications: Aerojet's MR-111C hydrazine thruster	161
G-2	Hardware specifications: RAFAEL's PEPT-230 mono-propellant tank	161
G-3	Hardware specifications: Northrop Grumman's STAR 13B rocket motor	162

Nomenclature

Latin Symbols

a	Minimum value uniform distribution	-
A	Area	m^2
b	Maximum value uniform distribution	-
c	Speed of light	m s^{-1}
C	Direction Cosine Matrix	-
D	Derivative gain matrix	-
d	Derivative gain	-
d_e	Linear offset thrust application point	m
e	State error	-
e	Euler eigenaxis vector	-
E	Energy	J
E_n	$n \times n$ identity matrix	-
F	Force vector	N
G	Gravitational constant	$\text{N kg}^{-2} \text{m}^2$
g	Gravitational acceleration	m s^{-2}
h	Angular momentum vector	$\text{kg m}^2 \text{s}^{-1}$
h	Altitude	m
h	Height	m
h	Integration step-size	-
i	Impact angle	deg

i	Incidence angle	deg
\mathbf{I}	Inertia tensor	kg m ²
i	Thruster number	-
i	Unit imaginary number	-
I_{sp}	Specific impulse	s
J	Impulse	N s
\mathbf{K}	Proportional gain matrix	-
k	Number of open thrusters	-
k	Proportional gain	-
k	Runge-Kutta 4 integration stage	-
K_d	Derivative gain	-
K_i	Integral gain	-
K_p	Proportional gain	-
\mathbf{L}	Angular impulse vector	kg m ² s ⁻¹
m	Mass	kg
\dot{m}	Propellant mass flow	kg s ⁻¹
\mathbf{M}	Torque vector	N m
\mathbf{n}_{actual}	Normal to actual surface horizontal	-
N	Denutation control logic parameter	-
n	Amount of substance of gas	mol
n	Integration time-step	s
n	Number of thruster pulses	-
n	Order of the integration scheme	-
\mathbf{p}	Modified Rodrigues vector	-
p	Pressure	Pa
p	Probability value	-
\mathbf{q}	Unit quaternion	-
q	Reflection coefficient	-
$\dot{\mathbf{q}}$	Quaternion rates	-
\mathbf{R}	Displacement vector	m
\mathbf{r}	Position vector	m
R	Ideal gas constant	J K ⁻¹ mol ⁻¹
r	Radial distance/radius	m
$\ddot{\mathbf{r}}$	Acceleration vector	m s ⁻²
R	Mean equatorial radius	m
S	Solar constant	W m ⁻²

Δt	Firing duration vector	s
T	Period	s
T	Temperature	K
t	Time	s
T_s	Settling time	s
\mathbf{u}	Control torque vector	N m
\mathbf{u}	Euler angle vector	deg
u	Controller output	-
\mathbf{v}	Velocity vector	m s^{-1}
V	Volume	m^3
\mathbf{v}_e	Effective exhaust velocity	m s^{-1}
\mathbf{x}	State vector	-
x	Position in the x -direction	m
y	Position in the y -direction	m
\bar{z}	Centroid	m
\mathbf{Z}	Unit vector in the z -direction	-
z	Position in the z -direction	m

Greek Symbols

α	Angular distance from x_B -axis	deg
α	Attack angle	deg
α	Pressure drop factor	-
β	Angular distance from z_B -axis	deg
β	Force drop factor	-
δ	Descent angle	deg
δ_e	Thrust misalignment angle	deg
ϵ	Offset	-
η	Impulse efficiency	-
η	Nadir angle	deg
ϕ	Phase angle	deg
ϕ	Roll angle	deg
μ	Arithmetic mean	-
μ	Gravitational parameter	$\text{m}^3 \text{s}^{-2}$
μ	Gyroscopic coupling torque damping factor	-
μ	Viscous damping coefficient	-

ϕ	Thruster cant angle from x_G -axis	deg
ρ	Correlation coefficient	-
ρ	Density	kg m^{-3}
σ	Relative angular velocity vector	rad s^{-1}
$\dot{\sigma}$	Relative angular acceleration vector	rad s^{-2}
σ	Standard deviation	-
σ^2	Variance	-
σ_{local}	Local surface slope	deg
τ	Variable of integration	s
θ	Eigenangle	deg
θ	Pitch angle	deg
θ	Thruster cant angle from z_G -axis	deg
θ_{nut}	Nutation angle	deg
ω	Angular velocity vector	rad s^{-1}
$\dot{\omega}$	Angular acceleration vector	rad s^{-2}
ω_n	Natural frequency	rad s^{-1}
ω_{nut}	Nutation frequency	rad s^{-1}
ψ	Heading angle	deg
ψ	Yaw angle	deg
ζ	Damping ratio	-

Subscripts

s	Spin-axis
ave	Average
B	Body frame
cap	Hemispherical cap
ca	Centre-of-area
cm	Centre-of-mass
corr	Corrected
cyl	Cylinder
C	Coriolis
c	Commanded
denut	Denutation
dry	Without propellant
d	Delay

eff	Effective
ext	External
e	Error
e	Exhaust
fin	Final
fly	Fly-away
frus	Hemispherical frustum
F	Spacecraft-centred inertial frame
f	Feed
G	Geometric frame
g	Gravity
hemi	Hemisphere
hyd	Hydrazine
ini	Initial
liquid	Liquid propellant slug
max	Maximum
m	Moon
nav	Navigation
nom	Nominal
nut	Nutation
Pen	Penetrator
p	Pulse
rel	Relative
reorient	Reorientation
rot	Rotational
solid	Solid propellant slug
SR	Solar radiation
tank	Propellant tank
thres	Threshold
tip	Tip-off
togo	To-go
tot	Total
T	Thrust
ullage	Propellant tank ullage
wet	With propellant

Superscripts

B/F From F -frame to B -frame

Acronyms

AOCS	Attitude and Orbit Control System
CFRP	Carbon Fiber Reinforced Polymer
CoA	Centre of Area
CoG	Centre of Gravity
CoM	Centre of Mass
DCM	Direction Cosine Matrix
DOM	De-Orbit Manoeuvre
ELUPE	European Lunar Penetrator
EoM	Equations of Motion
ESA	European Space Agency
ESTEC	European Space Research and Technology Centre
FAM	Fly-Away Manoeuvre
GES	Goonhilly Earth Station
IMU	Inertial Measurement Unit
ISRU	In-Situ Resource Utilisation
JEOP	Jupiter Europa Orbiter Penetrator
JGOP	Jupiter Ganymede Orbiter Penetrator
L-DART	Lunar Direct Analysis of Resource Traps
LCROSS	Lunar Crater Observation and Sensing Satellite
LRO	Lunar Reconnaissance Orbiter
MoonLITE	Moon Lightweight Interior and Telecoms Experiment
MPC	Model Predictive Control
MRAC	Model Reference Adaptive Control
NASA	National Aeronautics and Space Administration
OBC	On-Board Computer
PCDU	Power Conditioning and Distribution Unit
PD	Proportional-Derivative
PDM	Penetrator Descent Module
PDS	Penetrator Delivery System
PID	Proportional-Integral-Derivative

PLM	Periapsis Lowering Manoeuvre
PSR	Permanently Shaded Region
RCS	Reaction Control System
RK4	Runge-Kutta 4
SMC	Sliding Mode Control
SPHERES	Synchronized Position Hold Engage and Reorient Experimental Satellite
SRM	Solid Rocket Motor
SSERVI	Solar System Exploration Research Virtual Institute
SSTL	Surrey Satellite Technology Ltd
TMF	Thruster Management Function
VSC	Variable Structure Control

Other Symbols

\mathcal{M}	Thruster torque response matrix
\mathcal{N}	Normal distribution
\mathcal{O}	Big O notation
\mathcal{U}	Uniform distribution

Chapter 1

Introduction

This Master of Science thesis is concerned with the design of the European Lunar Penetrator (ELUPE) descent module controller. First, some background information on the ELUPE mission is provided in Section 1-1, followed by an outline of the anticipated mission in Section 1-2. The problem central to this thesis, described in Section 1-3, along with the findings from the literature study presented in Section 1-4, lead to the formulation of the research question in Section 1-5. In Section 1-6, the contributions of this thesis to the open literature are summarised. Finally, Section 1-7 provides an outline of the structure of the report.

1-1 Background and Motivation

In 2009, NASA's Lunar Crater Observation and Sensing Satellite (LCROSS) mission spectacularly confirmed the presence of water molecules in a debris plume originating from the impact of the inert upper rocket stage of NASA's Lunar Reconnaissance Orbiter (LRO) mission into a permanently shaded region (PSR) near the lunar south pole. The visible part of the plume was measured to contain 155 ± 12 kg of water vapour and ice, from which it was deduced that the estimated total mass of excavated lunar material comprised $5.6 \pm 2.9\%$ H₂O (Colaprete et al., 2010). Earlier suggestions of 'lunar water' were made by Nozette et al. (1996) and Feldman et al. (1998, 2001), based on satellite data collected during NASA's Clementine and Lunar Prospector missions, respectively. More recently, additional analysis of the data generated by the M³ spectrometer aboard the Indian satellite Chandrayaan-1 was performed by Li et al. (2018), who claim to have found "direct and definitive evidence" of water ice sitting at the surface of a large amount of lunar PSRs. Yet, despite their significance, these discoveries were solely made through *remote* spectral analysis. In the light of ESA's future aspirations for a sustained humanly inhabited lunar base, *in-situ* measurements are needed to obtain unambiguous ground truth regarding the presence, abundance and distribution of water ice (and other icy volatiles) contained in the lunar regolith.

Midway through the 20th century, the first theories were postulated about water ice being present (Urey, 1952; Watson et al., 1961a) and stable (Watson et al., 1961b) in the heavily cratered polar regions of the Moon. Since the Moon’s rotation axis is tilted a mere 1.54° with respect to the ecliptic, the illumination conditions at the poles are predominantly subject to local topography. As a consequence, some areas in the polar regions – in particular crater floors – are shrouded in permanent darkness, making them exceptionally cold. Temperatures within such ‘cold traps’ generally do not rise above 110°K (Hayne et al., 2015) – a temperature at which the sublimation rate of H_2O is low enough to consider sublimation losses negligible over geological timescales (Vasavada et al., 1999). Hayne et al. (2015) concludes that it is in shaded areas where maximum temperatures stay below 110°K , that spectral evidence for water ice is found.

As another result of the Moon’s low rotational obliquity and rugged polar surfaces, there are also regions near the poles that endure near-continuous illumination. They are particularly found at topographic highs, such as crater rims and massif peaks (Speyerer & Robinson, 2013), and offer the potential for near-continuous generation of solar power during surface missions. Considering the relative proximity of these long duration sunlit regions to potential water ice-bearing PSRs, renders them particularly attractive for sustained human residence in *e.g.*, a ‘Moon Village’, which is an openly interpretable concept raised by ESA in the context of the agency’s own announced new era for space activities – ‘Space 4.0’ (Wörner, 2016). In this regard and in a more general context of *in-situ* resource utilisation (ISRU), recent studies (*e.g.*, Carpenter et al., 2016) mention the Cabeus and Shoemaker craters near the south pole and the Peary crater near the north pole as potentially interesting locations.

Apart from being shrouded in permanent shadow, very little is currently known about PSRs. Concluding from the findings of NASA’s Solar System Exploration Research Virtual Institute (SSERVI, 2015), speculations on the composition and characteristics of PSR regolith have primarily relied on remote measurements, or have otherwise been based on laboratory research performed on soil samples acquired from ‘small’ PSRs (*e.g.*, a permanent shadow cast by a large rock) during the Apollo surface missions. Direct *in-situ* prospecting is indisputably key to closing the knowledge gaps. That said, the absence of sunlight in the regions concerned, their typically sloped and rugged landscapes, and their extraordinary cold environments impose significant constraints on potential surface missions. Additionally, it is conjectured that the soil in PSRs is “extremely soft and unconsolidated” (Carpenter et al., 2016), which would make it difficult, if not impossible, to probe such regions using ‘conventional’ landers and rovers. Hence, it is evident that in order to address the outstanding questions about PSRs and their regolith constituents, alternative mission architectures must be considered.

To overcome the challenges mentioned, ESA is exploring the possibility of a surface mission entailing one or more instrumented penetrators implanted inside the PSR regolith by high-speed impact. The anticipated SSTL Lunar Pathfinder¹ (Saunders et al., 2016) is considered to deliver the mission to lunar orbit. As such, a study was conducted to assess the feasibility of a

¹The 2016 announced Lunar Pathfinder mission – led privately by commercial enterprises Surrey Satellite Technology Ltd (SSTL) and Goonhilly Earth Station Ltd (GES) – aims to deliver smaller missions to lunar orbit and facilitate communications for a “ticket price” of 1 million GBP per kilogram. In the frame of a confirmed new partnership scheme, ESA is currently investigating the possibility of utilising the Pathfinder mission to bring payloads to the Moon relevant for future human exploration.

penetrator mission as a payload option for the Lunar Pathfinder. The study was commissioned by the Lunar Exploration Office (HRE-IL) at ESTEC, and carried out there over the course of a six-month internship. The results of the study were condensed in Bouma (2017), presenting a mission concept for ELUPE – a single-penetrator mission proposed to be the sole passenger aboard a specially tailored Lunar Pathfinder.

Following separation from the Lunar Pathfinder in a polar and circular orbit of 200 km altitude, the ELUPE spacecraft will autonomously traverse a controlled trajectory to its designated target on the lunar surface. To this end, the spacecraft is equipped with a dedicated Attitude and Orbit Control System (AOCS). Several hardware configurations, resulting from trade-offs involving a variety of commercially available components, were proposed by Bouma (2017). The eventual configuration, briefly addressed in Section 1-2-2 and further elaborated in Chapter 2 and Appendix A, was selected based on its global performance in a first-order simulation. In order to gain deeper insight into the performance of the selected current-technology configuration, it must be investigated whether the AOCS is actually able to steer the instrumented penetrator in a such way that implantation may occur successfully. Notably, the success of implantation strongly depends on the orientation, or *attitude* of the penetrator with respect to the surface the moment just prior to impact, see *e.g.*, Lorenz (2011). To attain the desired orientation, an *attitude controller* must be implemented, generating appropriate control commands to be executed by the AOCS actuators. This Master of Science thesis will be dedicated to the design, verification and testing of a suitable attitude controller for the ELUPE spacecraft, so as to quantify the feasibility and success rate of the mission from a descent-and-landing perspective.

1-2 The ELUPE Mission

This section provides an introduction to the ELUPE mission concept. The content relies on Bouma (2017), and is complemented, improved and updated where necessary. Section 1-2-1 addresses the mission’s general goals, objectives and outcomes, followed by a brief introduction to the spacecraft in Section 1-2-2. The section concludes with an outline of the baseline descent scenario, provided in Section 1-2-3.

1-2-1 Mission Goals, Objectives and Outcomes

From a science perspective, the ELUPE mission is foreseen to conduct the first *in-situ* measurements of the lunar PSR regolith and to establish a connection between *in-situ* acquired data and existing (and future) remote data sets. In this respect, the focus is firstly on detection and identification of lunar volatiles, secondly on characterisation of the geotechnical properties of the regolith, thirdly on measuring the subsurface temperature environment, and fourthly on capturing the macro-scale geological context of the landing site. The results will assist in calibration of orbital data sets, and in addition provide crucial constraints for future prospecting missions and science models. In a broader context, the measurements, albeit taken from a single point, contribute to completion of the first step towards ISRU, that is

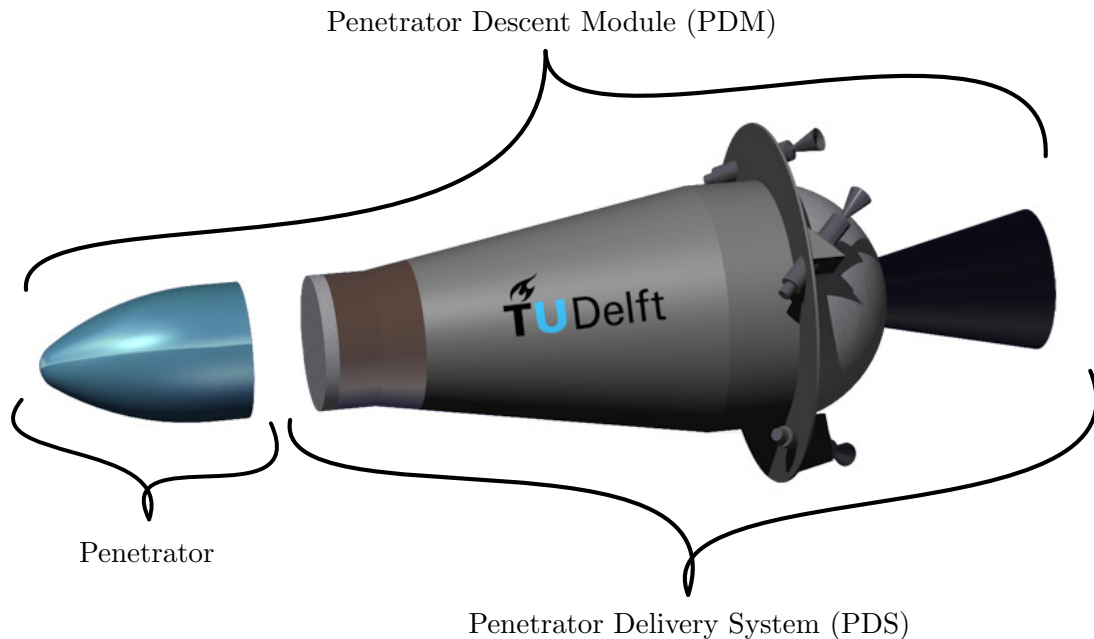


Figure 1-1: CATIA render of the ELUPE spacecraft: the PDM. Indicated are the two distinct systems that constitute the PDM, that is, the PDS and the Penetrator.

“find and characterise the resource deposits” (Carpenter et al., 2016), or even broader, towards enabling sustained human exploration of the Moon.

The objectives of the mission are to implant an instrumented penetrator inside the lunar PSR regolith, and to operate penetrator instrumentation and subsystems pre-, peri- and post-impact until all *in-situ* experiments have been concluded and the data acquired has been transmitted to the Lunar Pathfinder. If successful, the mission would demonstrate leading European hard landing technology on the Moon – or more generally: on an airless body – and as such could be a precursor to additional instrumented penetrator missions to the Moon (to establish regionally distributed point measurements) or to other airless destinations of interest, such as Enceladus, Europa and Ganymede.

1-2-2 Spacecraft

The ELUPE spacecraft, as currently proposed, is comprised of two distinct systems: an instrumented penetrator and a Penetrator Delivery System (PDS), which ensures a three-axis controlled descent trajectory from the Pathfinder to the lunar surface so as to deliver the instrumented penetrator to its designated landing site, under desired impact conditions. The ELUPE spacecraft, *i.e.*, the penetrator attached to the PDS, is referred to as the Penetrator Descent Module (PDM). The terminology is borrowed from Vijendran et al. (2010). A CATIA render of the PDM is depicted in Figure 1-1.

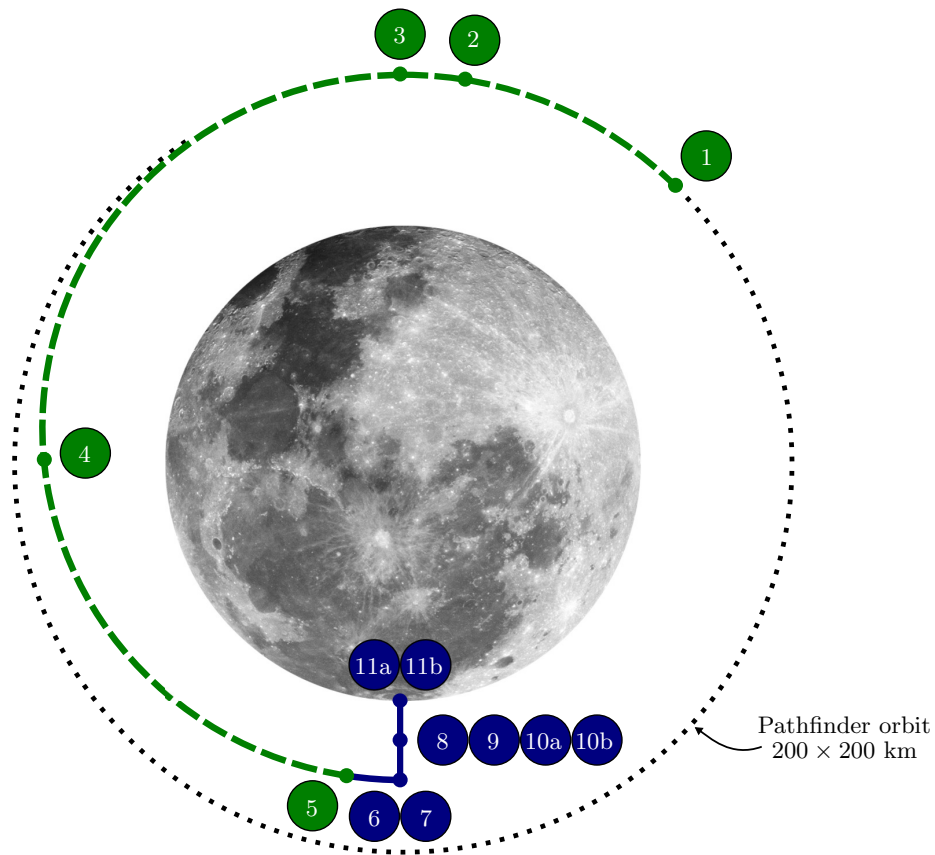


Figure 1-2: Schematic representation of the PDM's descent trajectory, which can be divided into two phases, further elaborated in the text. The first phase is represented by the dashed green line; the second by the solid blue line. The dotted line represents the orbit of the Pathfinder. The coloured dots indicate relevant epochs in the trajectory. Notably, the schematic is not to scale.

1-2-3 Descent Scenario

Figure 1-2 shows a schematic representation of the PDM's descent trajectory from separation from the Pathfinder through to impact. Also depicted is the orbit of the Pathfinder, which is polar and circular at an altitude of 200 km. Relevant epochs in the trajectory are indicated in Figure 1-2 and accompanied by a numbering system that corresponds to the sequence of events occurring during the descent phase, further detailed below and summarised in Table 1-1.

The baseline descent scenario of the PDM can be divided into two phases, which are outlined as follows. In the first phase, the PDM separates from the Pathfinder spacecraft in a polar and circular orbit of 200 km altitude by a relative linear tip-off velocity in the direction opposite to the Pathfinder velocity vector. After some period of passive drift, the PDM determines its orientation using the measurements of a star tracker and performs the required control actions in anticipation of the first orbital manoeuvre. When both spacecraft are safely separated, the PDM carries out a periapsis lowering manoeuvre (PLM) using its reaction control system

Table 1-1: Sequence of events occurring during the descent scenario of the PDM, from separation from the Pathfinder through to impact. Altitude and epoch values are indicative.

Event	Description	Altitude (km)	Epoch (s)
<i>First phase of the descent scenario</i>			
1	Separation from Pathfinder and drift	200	0
2	Attitude acquisition and control	200	900
3	Periapsis lowering manoeuvre	200	1000
4	Transfer and attitude maintenance	199	1060
5	Attitude acquisition and control	28	4470
<i>Second phase of the descent scenario</i>			
6	Spin-up and de-orbit manoeuvre	28	4570
7	Spin-down and reorientation	28	4586
8	Free-fall descent and spin-up	25	4636
9	Penetrator separation from PDS and drift	22	4656
10a	Penetrator passive free-fall descent	22	4656
10b	PDS spin-down, reorientation and fly-away	19	4676
11a	Penetrator impact	0	4758
11b	PDS impact	0	4758

(RCS), in order to bring the periapsis of its orbit down to 28 km altitude – the altitude from which an object in free-fall towards the Moon would reach a velocity² of 300 m s^{-1} just prior to impacting the surface.

Next, the PDM coasts towards the periapsis while maintaining an attitude such that the communications link with the Pathfinder spacecraft remains intact and the star tracker’s field-of-view is unobstructed. During the transfer, the PDM accelerates due to increased dominance of the Moon’s gravitational pull and consequently overtakes the Pathfinder spacecraft. The resulting lead is eventually key to ensure a continuous line-of-sight between the Pathfinder and the PDM throughout the latter’s descent to the lunar surface, as it compensates for the Pathfinder catching up to the PDM during the de-orbit phase. Before the PDM reaches its orbital periapsis, it carries out an attitude acquisition and control sequence to align its symmetry axis with the velocity vector, such that the nozzle of the solid rocket motor (SRM) is pointing in the forward direction. This event marks the end of the first phase.

In the second phase of the descent scenario, the PDM spins up for gyroscopic stability in anticipation of the de-orbit manoeuvre (DOM). Shortly after, the SRM ignites to fully cancel the PDM’s orbital velocity of approximately 1705 m s^{-1} . Following termination of the DOM,

²This impact velocity was chosen based on the few full-scale impact tests that were performed during previous penetrator studies; impacts occurred at velocities around 300 m s^{-1} in sand and ice targets (Smith et al., 2010; Vijendran et al., 2014). As some of the technologies that survived the tests are envisaged for the ELUPE mission, it is prudent to adhere to the conditions under which they were tested. It is noted that lower impact velocities, down to a minimum value required to ensure sufficient penetration, are inherently safer, however also impose unwanted additional constraints on the mission.

the PDM spins down and slews vertically so that its symmetry axis is directed towards the surface. During its free-fall descent phase, the PDM spins up again, in order to provide the penetrator with a final stabilising spin upon separation from the PDS. Next, the penetrator separates from the spinning PDS, followed by a short period of drift. Finally, the PDS spins down and performs a fly-away manoeuvre (FAM), so as to avoid crashing onto the implanted penetrator, contaminating the landing site and as such compromising the measurements. The penetrator continues its spin-stabilised descent until it impacts the surface at about 300 m s^{-1} . A schematic of the events occurring during the second phase of the descent scenario is depicted in Figure 1-3.

1-3 Problem Statement

As was stated in Section 1-1, this thesis will be concerned with the design, verification and testing of a suitable attitude controller (henceforth just *controller*) for the PDM. The candidate controller will be tested in a simulation of the second phase of the descent scenario (see Section 1-2-3). This phase is of particular interest from a control perspective, as the following challenging rotational manoeuvres are involved:

- **Large-angle slew manoeuvres.** The reorientation manoeuvres entail 90 degrees slews, and may therefore be referred to as large-angle slew manoeuvres. Controlling such manoeuvres generally poses a difficult problem, as their dynamics are highly non-linear (Markley & Crassidis, 2014).
- **Minor-axis spin manoeuvres.** The spin manoeuvres are performed about the axis of minimum moment of inertia – the minor axis. This renders the PDM a so-called *prolate spinner* following a spin-up. It is commonplace (*e.g.*, Wie, 2008) that prolate spinners are unstable in the presence of internal energy dissipation (due to *e.g.*, the motion of liquid propellants). Under such circumstances, the spin-axis becomes subject to a nutation, which, if left uncontrolled, will gradually amplify until the spacecraft attains a minimum-energy state and spins about its axis of maximum moment of inertia – the major axis. This type of spinning motion is also referred to as *flat spin*. In this thesis, a minor-axis spin manoeuvre involves a spin-up about the minor axis, an actively controlled subsequent spin and finally a spin-down.

In addition to the challenges these manoeuvres pose, the controller must also account for varying system parameters. Over the course of the descent, control actions carried out by the RCS require propellant be consumed, which brings about changes in the PDM's inertial parameters and torque capabilities. The latter not only due to a moving centre-of-mass, but also because the RCS operates in a *blow-down mode* (see Section 2-2-1).

Concluding, the attitude control problem concerned involves highly nonlinear large-angle slew manoeuvres and unstable minor-axis spin manoeuvres, which must be performed by a spacecraft whose inertial parameters and torque capabilities vary while in the act. A suitable controller is thus defined as one that is able to satisfactorily address these manoeuvres, while at the same time accounting for varying system parameters.

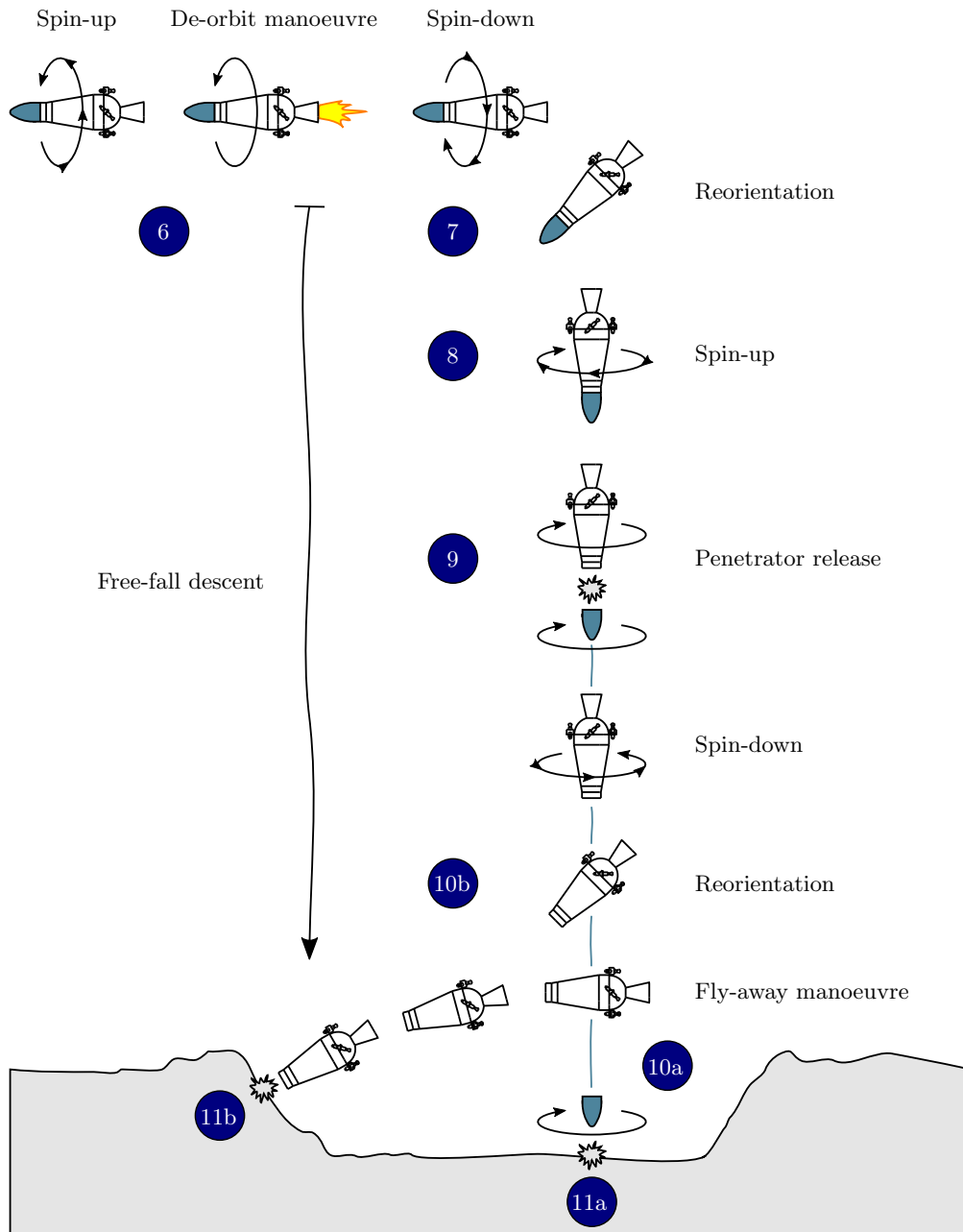


Figure 1-3: Schematic representation of the second phase of the PDM's descent scenario. Refer to Table 1-1 for clarification on the numbered dots. The schematic is not to scale.

1-4 Literature Review

A literature review was conducted to attain an overview of the state-of-the-art with regard to planetary penetrators and control techniques. The literature review is set out in two parts. The first part (Section 1-4-1) touches briefly upon the history of planetary penetrators and covers a survey of previous missions that resemble ELUPE, focusing on their control solutions. The second part (Section 1-4-2) presents a review of the literature on control techniques for large-angle slew manoeuvres and minor-axis spin manoeuvres – two challenging rotational manoeuvres that are both part of the PDM’s attitude control problem (see Section 1-3).

1-4-1 Planetary Penetrators

Planetary penetrators are a peculiar case in the spaceflight arena. Although having received persistent attention over the last four to five decades, seemingly benefiting from compelling heritage in the defence sector, they never succeeded in a mission (Lorenz, 2011). Since the beginning of the space era, there have been many planetary penetrator proposals, fewer comprehensive studies and only two actual missions: Russian Mars-96 (Surkov & Kremnev, 1998) and NASA’s Deep Space 2 (Smrekar et al., 1999), which were both targeted for Mars. Mars-96 failed at the fourth stage of its launch and consequently burnt up into Earth’s atmosphere. The two penetrators of Deep Space 2 succeeded to reach the surface of Mars, however for reasons only speculated on, no signal was received from either afterwards. Similar to early Mars proposals (Lumpkin, 1974; Manning, 1977), the penetrators were designed to take advantage of the Martian atmosphere to achieve acceptable impact conditions. Since the Moon has a negligible atmosphere, aerodynamic control techniques are not relevant for the ELUPE mission, hence further details will be omitted.

More representative penetrator concepts bear resemblance to ELUPE’s concept in two aspects: 1) they have an airless destination, and 2) they are released into orbit around the target body. Most of the previous concepts sharing these aspects were anticipated for the Moon, and would have been part of the missions LUNAR-A (Morita et al., 1992), Luna-Glob (Surkov et al., 1999), Polar Night (Mosher & Lucey, 2006), and the Moon Lightweight Interior and Telecoms Experiment (MoonLITE) (Gao et al., 2008), as well as its direct derivatives; LunarEX (Smith et al., 2009); LunarNet (Smith et al., 2012); and the single-penetrator mission Lunar Direct Analysis of Resource Traps (L-DART) (Barber et al., 2017). Two other representative concepts, namely the Jupiter Ganymede Orbiter Penetrator (JGOP) (Vijendran et al., 2010) and the Jupiter Europa Orbiter Penetrator (JEOP) (Barraclough et al., 2015), were envisaged to penetrate airless Jovian moons Ganymede and Europa, respectively.

By and large the most mature penetrator concept of those mentioned was part of the Japanese LUNAR-A mission. The mission came close to a launch, but was eventually cancelled in 2007 after a development period of 15 years characterised by many hurdles and delays (Shiraishi et al., 2008). The AOCS of the LUNAR-A penetrator was modestly set up using only a sun sensor and a single cold gas thruster for attitude determination and control, and a dedicated SRM to cancel the orbital velocity (Nakajima et al., 1996). The module would be given a stabilising spin upon release from its carrier at its de-orbit altitude, where it would execute a de-orbit

manoeuvre followed by a *rhumb line* slew manoeuvre in order to precess the spin-axis towards the vertical (Morita et al., 1992). Such reorientation of a spinning penetrator has recently been topic of study, as similar slew strategies were foreseen for MoonLITE and LunarEX. Raus et al. (2012) performed a comparative analysis of a series of open-loop manoeuvring techniques for prolate spinners controlled by a single thruster. Si et al. (2018) extended this work by incorporating attitude and spin-rate feedback into the control loops of two of these techniques, greatly improving their robustness. As far as the open literature goes, it seems that these have been the only closed-loop control algorithms that were developed in the context of one of the aforementioned penetrator concepts.

It is safe to assume that no controller development took place for Luna-Glob and Polar Night, as neither of those concepts progressed beyond their proposal phase (Lorenz, 2011). The instrumented penetrators anticipated for MoonLITE (and its derivatives), JGOP and JEOP were in fact further advanced, and prototypes of these penetrators were tested during a series of impact trials (Smith et al., 2012; Vijendran et al., 2014). However, as the focus of these studies was predominantly on maturing the penetrator system and to a lesser extent on the delivery module, no effort went into the development of their respective controllers³. As such, it appears that no comprehensive controller has ever been developed for a fully actuated, thruster-controlled penetrator mission targeted for an airless body. The design of such a controller and its testing in a simulation would provide better insight into the feasibility and success rate of such a mission from a descent-and-landing perspective. This is particularly relevant since ESA is considering a penetrator mission as a payload option for SSTL's Lunar Pathfinder.

1-4-2 Control Techniques

In the following, a brief review is presented of the various control techniques that have been considered in the literature to address large-angle slew manoeuvres and minor-axis spin manoeuvres. It should be noted that the specifics of the techniques mentioned below are not provided here. Techniques relevant in the context of this thesis will be covered in later chapters. For an elaboration of the other control techniques mentioned, the reader is referred to the works cited.

- **Control techniques for large-angle slew manoeuvres** were a vivid topic of study in 1980s and 1990s. This period spawned some important solutions to this highly nonlinear control problem. In particular, proportional-derivative (PD) quaternion-error feedback laws were invented (Wie & Barba, 1985; Wie et al., 1989; Wen & Kreutz-Delgado, 1991; Joshi et al., 1995), as were robust control schemes based on Sliding Mode Control (SMC), or more generally Variable Structure Control (VSC) techniques (Vadali, 1986; Lo & Chen, 1995; Dwyer & Sira-Ramirez, 1988). Other well-known control techniques, such as Model Reference Adaptive Control (MRAC) (Van Den Bosch et al., 1986; Singh, 1987) and nonlinear H_∞ (Kang, 1995; Dalsmo & Egeland, 1997; Yang & Kung, 2000), have

³Perkinson, M.-C., personal communication, 2017

also been considered in the literature to address the problem of large-angle reorientation, albeit to a seemingly lesser extent than SMC/VSC techniques.

- **Control techniques for minor-axis spin manoeuvres**, achieving spin-axis stabilisation or equivalently, Active Nutation Control (ANC) (Devey et al., 1977), were first investigated in the 1960s in the context of spin-stabilised satellites and upper rocket stages, and were analogue in nature (Grasshoff, 1968). More recent controllers were based on linear proportional-integral-derivative (PID) techniques (Tsiotras & Longuski, 1994; Zhang et al., 2008; Gui & Vukovich, 2015) or nonlinear techniques such as *non-linear dynamic inversion* (Elias & Vega-Navarez, 2008) and *Lyapunov feedback control* (Lawrence & Holden, 2007), and were developed for *e.g.*, unbalanced ballistic missiles and (small) spacecraft, controlled by either thrusters or reaction wheels or a combination of both, under fully actuated or underactuated conditions.

Surveying the large body of literature that has been established on control techniques, it can reasonably be concluded that their evolution has mainly been driven by the need for improved methods to determine appropriate controller gains for increasingly complex systems. Advances in applied mathematics and computer technology have enabled the design of stable controllers for systems that are represented by time-varying, nonlinear or even unknown dynamics. For most practical aerospace applications though, the use of classical PID control is still the norm (Markley & Crassidis, 2014) – simply because this technique often suffices and there is extensive heritage in its use. It would hence be of practical relevance to design a classical controller for the PDM. In addition, given that in-depth studies on control solutions for penetrator missions such as ELUPE appear to be lacking (Section 1-4-1), the design and testing of a controller based on classical control techniques would establish a benchmark for future work. In this respect, it is therefore decided to implement the PD quaternion-error feedback controller as developed by Wie et al. (1989) to generate control commands for the large-angle slew manoeuvres, and the ANC logic as described by Devey et al. (1977) to stabilise the spin-axis during minor-axis spin manoeuvres. Notably, the control techniques will be tailored to the needs of the PDM and will be refined where necessary.

1-5 Research Question

In line with the foregoing, the following twofold research question can be formulated:

Is it possible to satisfactorily solve the attitude control problem of a current-technology penetrator mission targeted for an airless body through the use of classical control techniques, and if so, what are, from a descent-and-landing perspective, the key factors affecting the success rate of such a mission?

To answer this question, a classical controller will be designed, verified and tested in a simulation of the second phase of the PDM's descent scenario. The controller will be provided with realistic state feedback and its output will be fed to a *thruster management function*, which

will generate the appropriate thruster commands. The simulator will comprise a model of the PDM, which will be subject to uncertainty. The results of a sensitivity analysis will provide insight into the performance of the controller, as well as the success rate of the mission from a descent-and-landing perspective.

1-6 Contributions

To the best of the author's knowledge, this thesis makes the following contributions to the open literature:

- A classical controller and a thruster management function were developed for a fully actuated, thruster-controlled penetrator mission targeted for an airless body. In addition, a simulator was developed to test their performance under nominal and off-nominal conditions. This has provided insight into the success rate of such a mission from a descent-and-landing perspective, and has set a benchmark.
- The work of [Wie et al. \(1989\)](#) was extended by the development of a method to empirically derive a corrective factor to be applied to the standard expression for approximating the natural frequency – which is used by [Wie et al. \(1989\)](#) to calculate the gain matrices – based on a chosen settling time, see Section [4-2-2](#). As such, it is possible to satisfactorily address the nonlinear effects caused by the term $\sin(\theta/2)$.
- The work of [Devey et al. \(1977\)](#) was extended by the development of a strategy to determine the optimal thruster pulse width based on a chosen settling time and the torque capabilities of the spacecraft perpendicular to the spin-axis, see Section [4-3-2-2](#).
- A procedure was developed to correct the solution to the general *jet selection problem* for the anticipated pressure drop that occurs when multiple thrusters operating in blow-down mode are simultaneously active, see Section [6-1-1](#).
- Based on findings of Stack Exchange-users 'zeta' and 'probably_someone', analytic equations for the mass moments of inertia of a (hemi)spherical cap, in terms of its mass, height and spherical radius, were derived and verified, see Appendix [C-1](#). These equations were not found in the literature.
- Analytic equations for the centroid and the mass moments of inertia of a hemispherical frustum, in terms of its mass, height and spherical radius, were derived and verified, see Appendix [C-1](#). These equations were not found in the literature.

1-7 Report Structure

The report is organised as follows. First, accurate models for the spacecraft and its environment will be created. In Chapter [2](#), this is done for the spacecraft, which will be represented in the simulator by its inertial parameters and torque capabilities. In Chapter [3](#), the spacecraft's

dynamics and environment are modelled, by setting up the rotational equations of motion and investigating the significance of the disturbance torques. In addition, the chapter covers the reference frames considered, as well as the state representation. Chapter 4 is concerned with the design of the controller. The control algorithms for the large-angle slew manoeuvres and the minor-axis spin manoeuvres are described in detail, and refined where necessary. Chapter 5 defines the mission manager logic, as well as the target states it transmits to the controller. In Chapter 6, the remaining simulator elements, *i.e.*, the thruster management function and the navigation system are discussed, which is followed by an elaboration of the architecture of the simulator. Then, the simulation set-up is described in detail, after which the simulation results are presented, at the end of the chapter. Finally, in Chapter 7, the most important conclusions drawn from the thesis are summarised, the limitations to which the thesis was subject are discussed, and recommendations for future work are made.

Chapter 2

Spacecraft Modelling

Crucial to an accurate simulation is an accurate model of the spacecraft. Starting with some preliminaries regarding the configuration of the spacecraft in Section 2-1, a detailed description of the AOCS model is provided in Section 2-2. In the simulator, the spacecraft is represented by its inertial parameters, which are discussed in Section 2-3, and its torque capabilities, lastly covered in Section 2-4

2-1 Preliminaries

As was stated in Sections 1-2-2 and 1-2-3, the PDM consists of the PDS and the instrumented penetrator, which separate just prior to impact. In Figure 2-1, the PDM is schematically depicted. The PDS incorporates the AOCS, which includes an SRM to perform the DOM and a mono-propellant, or more specifically, a *hydrazine* RCS for all other manoeuvres. The PDS also contains an avionics bay which accommodates the electronic equipment, including the AOCS sensors (see Appendix A-2). The instrumented penetrator is connected to the PDS via a release mechanism. Since the release mechanism is not yet specified, assumptions will be made in regard to the *tip-off velocities* imparted to the penetrator upon release from the PDS, see Section 5-2-1-2.

Physical positions on the spacecraft are measured from the centre of the geometric frame (G -frame, see Section 3-1), a *right-handed Cartesian* reference frame whose origin is located at the centre of the release mechanism between the PDS and the penetrator (see Figure 2-1). The z_G -axis is aligned with the symmetry axis and points towards the nose of the penetrator, see Figure 2-1. The x_G - and y_G -axes are defined in Figure 2-2.

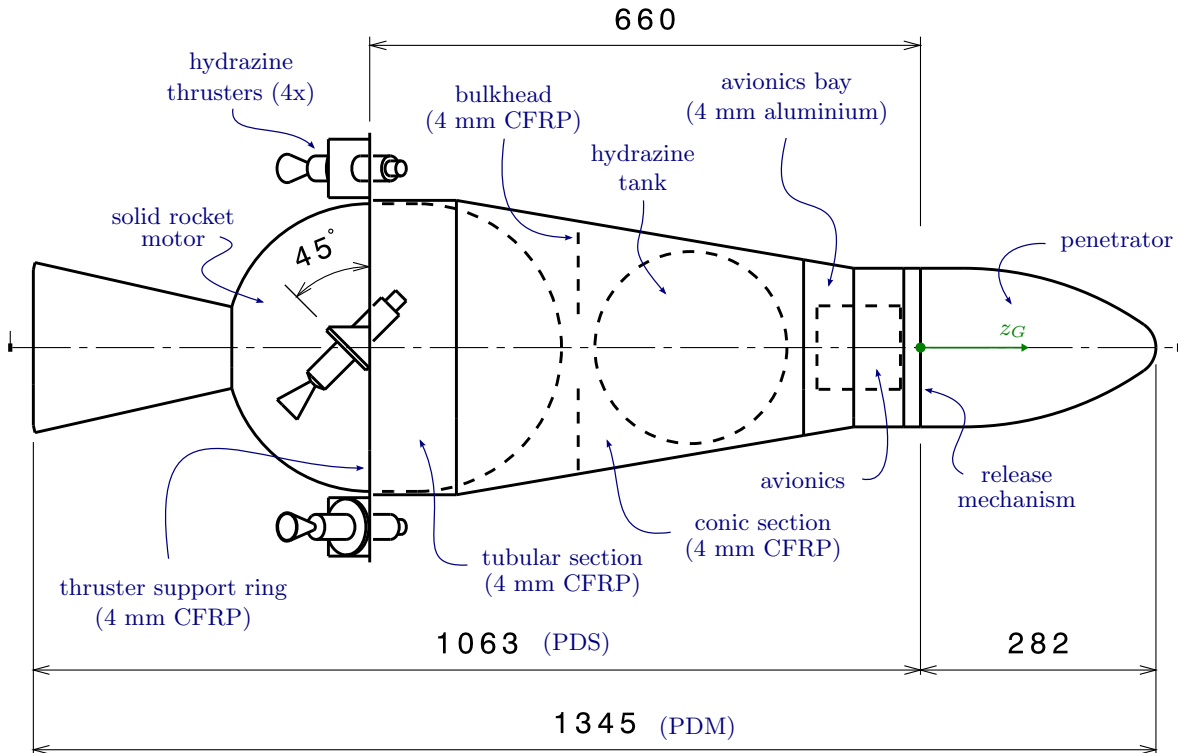


Figure 2-1: Schematic representation of the PDM configuration. The origin and z -axis of the G -frame are depicted. The dimensions shown are in millimetres. The acronym CFRP stands for Carbon Fiber Reinforced Polymer.

2-2 Attitude and Orbit Control System

This section is dedicated to modelling the actuating elements of the AOCS. In Sections 2-2-1 and 2-2-2, detailed descriptions of the RCS and the de-orbit motor are provided, respectively. The AOCS elements are modelled using actual specifications and performance diagrams.

2-2-1 Reaction Control System

The hydrazine RCS includes four thrusters that are used for attitude and orbit control. The thrusters are mounted on the thruster support ring and symmetrically canted *off-axis* to enable three-axis control; see Figure 2-2 for a schematic representation of this configuration. The thruster positions on the spacecraft are provided in Table 2-1.

The off-the-shelf thruster model selected for the RCS is Aerojet's MR-111C hydrazine thruster. The MR-111C is capable of delivering thrust forces between 1.3 and 5.3 N, depending on the momentary propellant *feed pressure*. In Table G-1, further relevant specifications of this thruster model are provided. The MR-111C performance diagram is depicted in Figure 2-3. The diagram was generated using the empirical relations derived by Swink et al. (1999), which

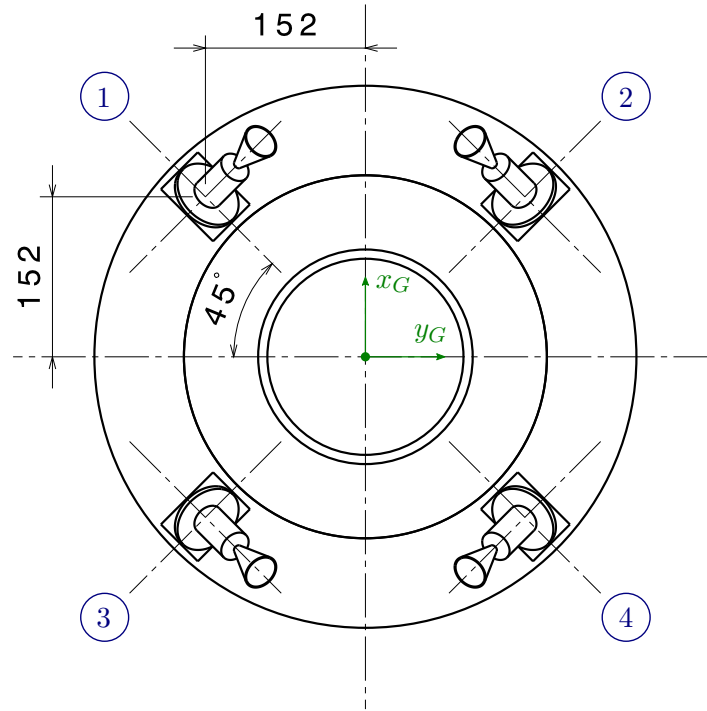


Figure 2-2: Schematic representation of the thruster configuration. The x - and y -axes of the G -frame are depicted, as well as the thruster numbering. The dimensions shown are in millimetres.

Table 2-1: Thruster positions with respect to the G -frame.

Thruster	x (mm)	y (mm)	z (mm)
1	152	-152	-660
2	152	152	-660
3	-152	-152	-660
4	-152	152	-660

were converted to SI units:

$$F_{\text{thruster}} = \frac{16.3166 \cdot p_f}{p_f + 58.1864} \quad (2.1)$$

$$I_{\text{sp, thruster}} = \frac{232.786 \cdot p_f}{p_f + 0.437491} \quad (2.2)$$

where F_{thruster} is the thruster force in Newtons, $I_{\text{sp, thruster}}$ is the thruster specific impulse in seconds and p_f is the feed pressure in bars. F_{thruster} and $I_{\text{sp, thruster}}$ are related through the following expression:

$$F_{\text{thruster}} = g_0 \cdot I_{\text{sp, thruster}} \cdot \dot{m}_{\text{thruster}} = v_{\text{e, thruster}} \cdot \dot{m}_{\text{thruster}} \quad (2.3)$$

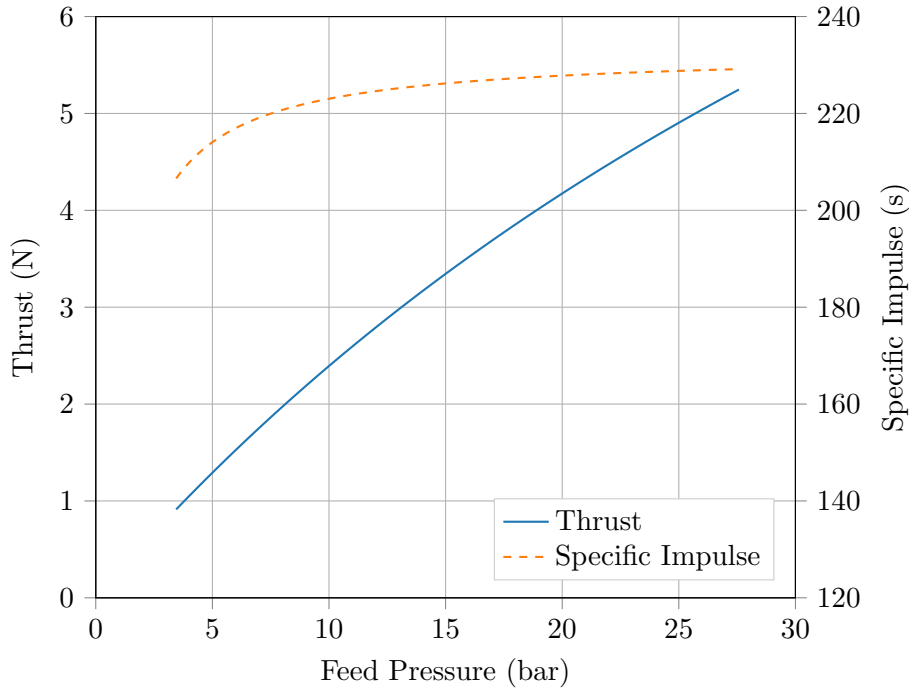


Figure 2-3: Performance diagram of Aerojet's MR-111C hydrazine thruster (Swink et al., 1999), converted to SI units.

where $g_0 = 9.80665 \text{ m s}^{-2}$ (e.g., Wertz, 2005) is the nominal gravitational acceleration near the surface of the Earth, $\dot{m}_{\text{thruster}}$ is the rate at which mass is expelled from the thruster and $v_{e, \text{thruster}}$ is the effective exhaust velocity. Substituting Equations (2.1) and (2.2) in Equation (2.3) and rearranging yields:

$$\dot{m}_{\text{thruster}} = \frac{0.00714747 \cdot p_f + 0.00312695}{p_f + 58.1864} \quad (2.4)$$

which calculates the mass flow as a function of feed pressure for the MR-111C. Via supplying pipes, the four thrusters are fed from a propellant tank, which is filled with hydrazine and an inert pressurant gas. The RCS operates in a so-called *blow-down mode*, meaning that the pressure in the pre-pressurised tank drops as propellant is expelled. In the context of this thesis, it is reasonable to assume that the pressure in the tank is equal to the feed pressure, provided that only one thruster is firing. When multiple thrusters are simultaneously active, there will be a slight pressure drop in the supplying pipes. The extent of this decrease in feed pressure depends on the number of thrusters operational at the same time. Blanc-Paques (2005) performed a thruster calibration exercise for the Synchronized Position Hold Engage and Reorient Experimental Satellite (SPHERES) spacecraft and determined the feed pressure drop factor α_k as a function of the number of open thrusters k . The relevant results of this exercise are presented in Table 2-2. For the purpose of introducing a feed pressure drop as a consequence of multiple thrusters firing, the results in Table 2-2 are directly incorporated in

Table 2-2: Feed pressure drop factor per number of open thrusters for SPHERES.

Number of open thrusters, k	Pressure drop factor, α_k
1	1.00
2	0.96
3	0.90
4	0.83

the simulation model for the RCS. The actual feed pressure drop factors should be obtained through dedicated experimentation, which is out of the scope of this thesis. Equations (2.1), (2.2) and (2.4) are modified to include the feed pressure drop factor, as follows:

$$(F_{\text{thruster}})_k = \frac{16.3166 \cdot (\alpha_k p_f)}{(\alpha_k p_f) + 58.1864} \quad (2.5)$$

$$(I_{\text{sp, thruster}})_k = \frac{232.786 \cdot (\alpha_k p_f)}{(\alpha_k p_f) + 0.437491} \quad (2.6)$$

$$(\dot{m}_{\text{thruster}})_k = \frac{0.00714747 \cdot (\alpha_k p_f) + 0.00312695}{(\alpha_k p_f) + 58.1864} \quad (2.7)$$

The off-the-shelf propellant tank selected for the RCS is RAFAEL's PEPT-230 tank, whose specifications are listed in Table G-2. The nominal empty volume of this tank is 6 litres and its operating pressure ranges between 5.5 and 24 bars. Notably, the liquid propellant is separated from the pressurant gas by a *rubber diaphragm*, see Figure 2-4. This has several advantages; for one, it helps to smoothly expel the propellant from the tank in a micro-gravity environment. Another advantage is that a diaphragm restrains the so-called *free surface* of the liquid, thereby preventing to a great extent any forms of *lateral* and *vertical* liquid sloshing in the propellant tank. Since, in addition, the liquid propellant slug inside the PDM represents only a small fraction of the overall spacecraft mass (4% in a worst-case scenario – *i.e.*, the PDM without solid propellant, see also Table A-1), of which only a small top layer would be affected for a short period of time, it is reasonable to assume that the impact of these types of liquid motion on the dynamics of the spacecraft can be neglected, thereby preventing a great deal of unnecessary complexity from being added to the model. *Swirling* – that is, rotational liquid motion – on the other hand, is typically not prevented by a diaphragm. The significance of the disturbance torque that is exerted on the spacecraft by this type of liquid motion will be investigated in Section 3-4-2-3.

In order to determine how the tank should initially be pressurised given a certain initial amount of hydrazine, it is required to define how the RCS should perform in terms of output thrust per thruster. Given the current RCS configuration, the upper pressure limit is prescribed by the tank and the lower pressure limit by the thrusters, respectively 24 bars (see Table G-2) and 6 bars (see Table G-1, with a margin of 0.5 bar). Using Equation (2.1),

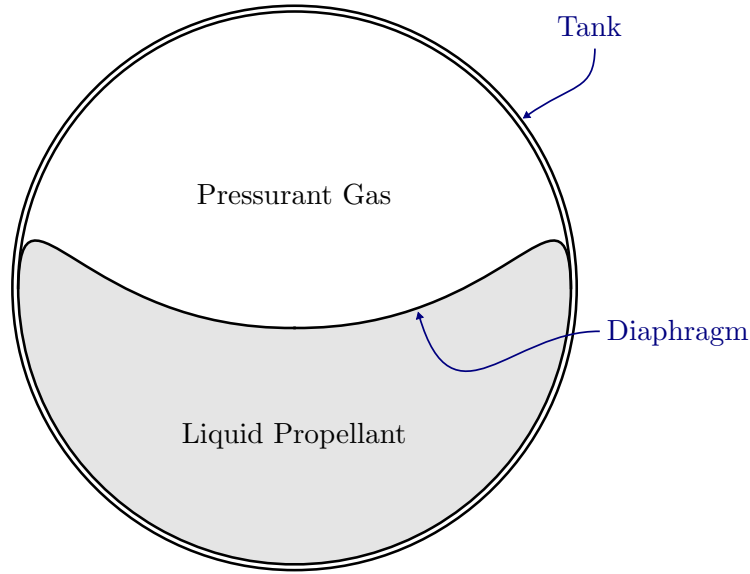


Figure 2-4: Schematic representation of a spherical propellant tank with a diaphragm.

the thrust values corresponding to these pressure limits are 4.8 N and 1.5 N, respectively. Since the RCS operates in a blow-down setting, and thus pressure and output thrust are not constant, it is convenient to define the performance of the RCS in terms of average output thrust. As can be observed from Figure 2-3, the relation between pressure and output thrust is represented by a nearly straight line. It may therefore be assumed that the average output thrust per thruster is well approximated by:

$$F_{ave} = \frac{F_{ini} + F_{fin}}{2} \quad (2.8)$$

where F_{ini} and F_{fin} are the initial and final output thrust, respectively. In order to find the initial pressure as a function of the tank volume, initial amount of hydrazine and average output thrust, the *ideal gas law* (Émile Clapeyron, 1799-1864) is used:

$$pV = nRT \quad (2.9)$$

where p is gas pressure, V is gas volume, T is temperature, n is the amount of substance and R is the ideal gas constant. In this thesis, it is assumed that the process of expelling propellant from the tank is *isothermal*, thus T is constant. This implies that:

$$pV = \text{constant} \quad (2.10)$$

and thus:

$$p_{ini} V_{ini} = p_{fin} V_{fin} \quad (2.11)$$

where p_{ini} and p_{fin} are the initial and final pressure, respectively, V_{ini} is the initial volume of the pressurant gas, generally referred to as the *initial ullage* of the tank, so: $V_{ini} = V_{ullage, ini}$, and

V_{fin} is the final volume of the pressurant gas, equal to the total tank volume, so: $V_{\text{fin}} = V_{\text{tank}}$. It furthermore holds that:

$$V_{\text{tank}} = V_{\text{hyd, ini}} + V_{\text{ullage, ini}} \quad (2.12)$$

where $V_{\text{hyd, ini}}$ is the initial volume of the hydrazine propellant. Solving Equation (2.1) for feed pressure p_f yields:

$$p_f = \frac{58.1864 \cdot F_{\text{thruuster}}}{16.3166 - F_{\text{thruuster}}} \quad (2.13)$$

The equation for the initial output thrust can be derived by first substituting Equation (2.13) into Equation (2.11), such that:

$$\frac{58.1864 \cdot F_{\text{ini}}}{16.3166 - F_{\text{ini}}} V_{\text{ini}} = \frac{58.1864 \cdot F_{\text{fin}}}{16.3166 - F_{\text{fin}}} V_{\text{fin}} \quad (2.14)$$

Then, using the information provided above, along with Equations (2.8) and (2.12), Equation (2.14) can be written as:

$$\frac{58.1864 \cdot F_{\text{ini}}}{16.3166 - F_{\text{ini}}} (V_{\text{tank}} - V_{\text{hyd, ini}}) = \frac{58.1864 \cdot (2 F_{\text{ave}} - F_{\text{ini}})}{16.3166 - (2 F_{\text{ave}} - F_{\text{ini}})} V_{\text{tank}} \quad (2.15)$$

Solving Equation (2.15) for F_{ini} using MATLAB's Symbolic Math Toolbox finally gives:

$$F_{\text{ini}} = F_{\text{ave}} - \frac{\sqrt{V_{\text{hyd, ini}}^2 (F_{\text{ave}} - 8.1583)^2 - 266.231 \cdot V_{\text{hyd, ini}} V_{\text{tank}} + 266.231 \cdot V_{\text{tank}}^2}}{V_{\text{hyd, ini}}} + \frac{16.3166 \cdot V_{\text{tank}}}{V_{\text{hyd, ini}}} - 8.1583 \quad (2.16)$$

To obtain the initial pressure p_{ini} , Equation (2.16) can be filled out in Equation (2.13). Equation (2.16) holds for a blow-down RCS, incorporating Aerojet's MR-111C hydrazine thruster connected to some propellant tank, under the assumptions that tank pressure is equal to thruster feed pressure, the relation between feed pressure and output thrust is linear, the pressurant behaves like an ideal gas, and the tank is isothermally depleted. When such a system includes RAFAEL's PEPT-230 tank, which implies that $V_{\text{tank}} = 6$ litres, selecting a feasible average output thrust value to define the desired performance of the RCS can be done using the diagram depicted in Figure 2-5, where the average output thrust capabilities of the system, as a function of the initial hydrazine mass required for the mission, are grey-shaded. In generating this diagram, it was assumed that the density of hydrazine $\rho_{\text{hyd}} = 1008 \text{ kg m}^{-3}$ (Ley et al., 2009).

From Figure 2-5, it can be deduced that the PDM's RCS is able to handle a maximum initial hydrazine mass of 4.5 kg, for which only one pressure setting is possible, leading to an average output thrust of 3.15 N. Since this particular average output thrust value can be achieved for the entire range of initial hydrazine mass values (0 - 4.5 kg), it is decided that, in the context

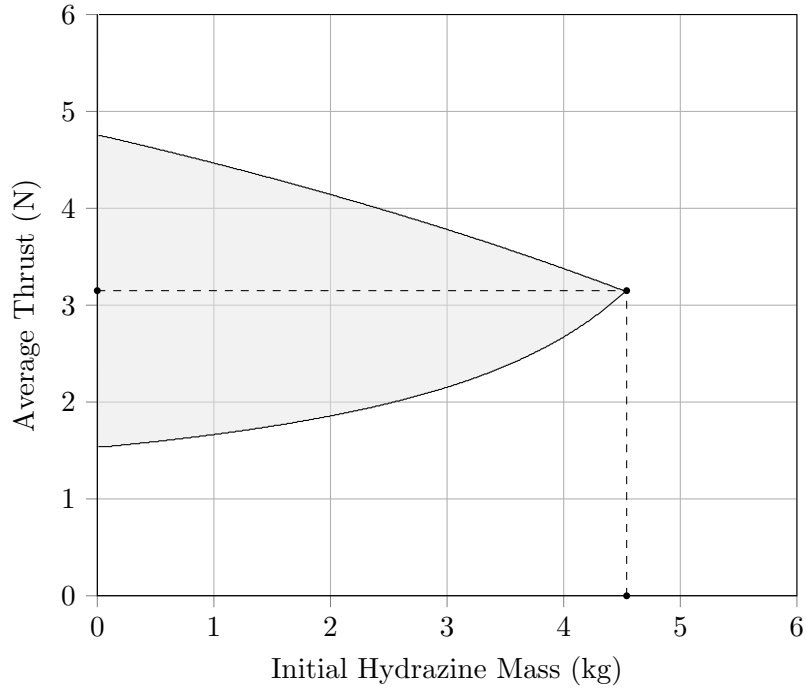


Figure 2-5: Average output thrust capabilities (grey-shaded area) of Aerojet's MR-111C hydrazine thruster when connected to RAFAEL's PEPT-230 tank, as a function of initial hydrazine mass contained in the tank. Tank volume is 6 l, pressure limits are set at 24 and 6 bar. Maximum hydrazine capacity for this setting is 4.5 kg. A maximally loaded tank can only be pressurised such that an average thrust of 3.15 N is produced.

of this thesis, the desired average output thrust produced by the RCS will be 3.15 N, which allows for a variable initial hydrazine mass without having to consider the feasibility of the performance setting.

Given $F_{ave} = 3.15$ N, $V_{tank} = 6$ l and a certain initial hydrazine mass, Equations (2.13) and (2.16) can be used to calculate the initial pressure. Then using Equations (2.10) and (2.12), the following equation can be derived for calculating the momentary pressure as a function of the initial pressure, tank volume, initial hydrazine mass $m_{hyd, ini}$ and momentary hydrazine mass m_{hyd} :

$$p = p_{ini} \left(\frac{V_{tank} - V_{hyd, ini}}{V_{tank} - V_{hyd}} \right) \quad (2.17)$$

with:

$$V_{hyd} = \frac{m_{hyd}}{\rho_{hyd}} \quad (2.18)$$

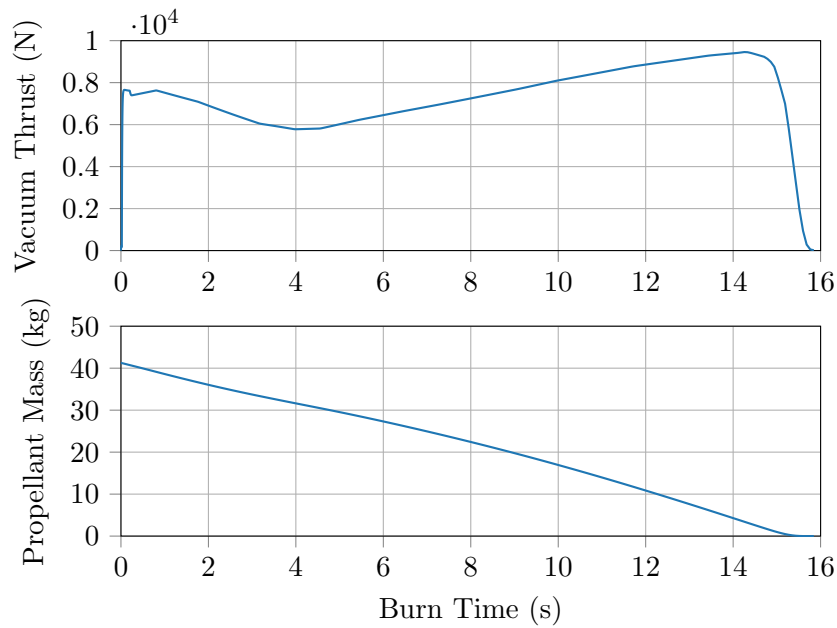


Figure 2-6: Performance diagrams of Northrop Grumman's STAR 13B motor. Top: vacuum thrust produced by the motor as a function of burn time. Bottom: propellant mass as a function of burn time. Data provided by M. Lara (Northrop Grumman), personal communication, 2018.

2-2-2 De-Orbit Motor

For the large braking impulse that must be imparted to the PDM during the DOM, Northrop Grumman's off-the-shelf STAR 13B solid rocket motor is selected. Capable of burning 41.2 kg of solid propellant in 14.8 s, STAR 13B produces an average thrust of 7598 N. Additional relevant specifications of the SRM are listed in Table G-3. The full burn history of STAR 13B is depicted in Figure 2-6. The two plots in this figure are generated using actual test data provided by Northrop Grumman.

Considering the large amount of thrust the SRM will exert on the PDM, any inevitable misalignment of the thrust vector could lead to significant parasitic torques. In order to ensure that the PDM remains stable under such circumstances, it is spun up about its symmetry axis before the SRM is ignited. The spin rate required to guarantee sufficient gyroscopic stability during the DOM will be investigated in Section 5-2-1-1. Notably, the STAR 13B SRM has been qualified for spin rates up to 120 rpm.

The amount of solid propellant needed for the DOM is currently estimated to be less than 41.2 kg, implicating that the SRM must be *off-loaded*. For STAR 13B, propellant off-loading is allowed up to 20% without additional qualification testing (see Table G-3). The off-load will be designed to match a point in time of the nominal burn profile, meaning that the starting point on the thrust curve will be shifted from the left.

Table 2-3: Inertia properties of the penetrator, dry PDS and dry PDM.

System	Mass (kg)	CoM* (m)			MoI (kg m ²)		
		x_G	y_G	z_G	I_{xx}	I_{yy}	I_{zz}
Penetrator	17.6	0	0	0.119	0.149	0.149	0.082
PDS (dry)	28.1	0	0	-0.441	2.553	2.553	0.526
PDM (dry)	45.7	0	0	-0.225	6.102	6.102	0.608

*The CoM is measured relative to the G -frame, see Figures 2-1 and 2-2 and Section 3-1

2-3 Inertial Parameters

The inertial parameters relevant to the design of the controller are the total mass, the location of the centre of mass (CoM), the mass moments of inertia (MoI) and the products of inertia (PoI) of the PDM, PDS and penetrator at each moment in time during the course of the descent. The MoI and PoI constitute the so-called *inertia tensor*, defined as:

$$\mathbf{I} = \begin{bmatrix} I_{xx} & -I_{xy} & -I_{xz} \\ -I_{xy} & I_{yy} & -I_{yz} \\ -I_{xz} & -I_{yz} & I_{zz} \end{bmatrix} \quad (2.19)$$

where the diagonal elements, I_{xx} , I_{yy} and I_{zz} , represent the MoI – also referred to as the *principal MoI*, as they are referenced to the *principal axes* of the body concerned – and the nondiagonal elements, I_{xy} , I_{xz} and I_{yz} , represent the PoI, which can be regarded as a measure of unbalance of the body. Due to the symmetry of the PDM, PDS and penetrator about the z_G -axis, the CoMs of these mass systems may be assumed to be nominally located on the z_G -axis. As a consequence, in the nominal case, the systems are balanced and the PoI are zero. In Table 2-3, the inertia properties of the penetrator, dry PDS and dry PDM are presented.

In order to obtain the inertia properties for the wet PDM, the momentary inertia properties of the solid and liquid propellant slugs must be combined with the inertia properties of the dry PDM. In this regard, the total mass is calculated by a straightforward summation of masses:

$$m_{\text{PDM, wet}} = m_{\text{Pen}} + m_{\text{PDS, dry}} + m_{\text{solid}} + m_{\text{hyd}} \quad (2.20)$$

The CoM of the wet PDM is calculated by:

$$(\mathbf{r}_{cm})_{\text{PDM, wet}} = \frac{(m\mathbf{r}_{cm})_{\text{Pen}} + (m\mathbf{r}_{cm})_{\text{PDS, dry}} + (m\mathbf{r}_{cm})_{\text{solid}} + (m\mathbf{r}_{cm})_{\text{hyd}}}{m_{\text{PDM, wet}}} \quad (2.21)$$

where m is the mass of the associated body and \mathbf{r}_{cm} is the position vector of the CoM of the associated body, relative to the G -frame. The inertia tensor of the wet PDM is calculated by:

$$\mathbf{I}_{\text{PDM, wet}} = (\mathbf{I}_{\text{Pen}})_{\text{PDM, wet}} + (\mathbf{I}_{\text{PDS, dry}})_{\text{PDM, wet}} + (\mathbf{I}_{\text{solid}})_{\text{PDM, wet}} + (\mathbf{I}_{\text{hyd}})_{\text{PDM, wet}} \quad (2.22)$$

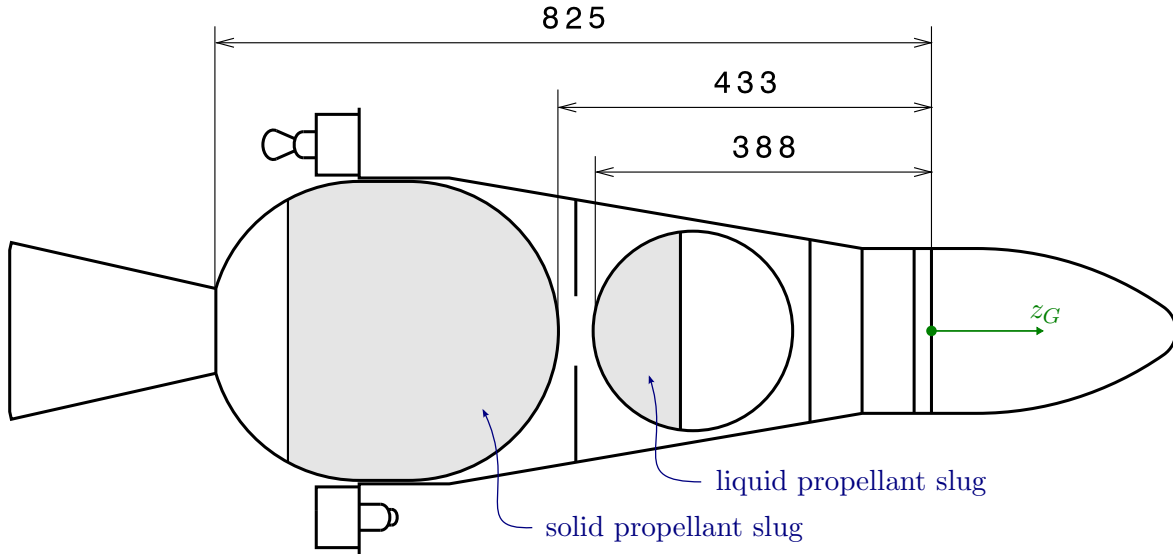


Figure 2-7: Schematic cross-section of a wet PDM, showing the shape and position of both propellant slugs inside the PDM at an arbitrary epoch. The z -axis of the G -frame is also depicted. The dimensions shown are in millimetres.

where the elements on the right-hand side are the inertia tensors of, respectively, the penetrator, the dry PDS, the solid propellant slug and the liquid propellant slug, expressed with respect to a coordinate system located at the CoM of the wet PDM. In order to first obtain $\mathbf{I}_{\text{solid}}$ and \mathbf{I}_{hyd} , assumptions are made with respect to the shapes of both propellant slugs, see Figure 2-7 for their two-dimensional representation.

In Appendix C, it is comprehensively described how the CoMs and inertia tensors of the propellant slugs are calculated based on their momentary mass. It is assumed that the propellant slugs have a symmetry axis which is nominally aligned with the symmetry axis of the dry PDM. Using the *parallel axis theorem*, given by Equation (C.3), it is then possible to express the inertia tensors of the slugs with respect to the aforementioned coordinate system located at the CoM of the wet PDM.

2-4 Torque Capabilities

The ability of the spacecraft to control its attitude can be quantified in terms of torque capabilities about a set of reference axes originating in the CoM the spacecraft. These reference axes are chosen to be parallel to the axes of the G -frame, implying that in the nominal case, they coincide with the principal axes of the spacecraft (see Section 2-3). Since the spacecraft is thruster-controlled, the torque that each thruster produces is calculated by:

$$\mathbf{M}_{\text{thruster}} = (\mathbf{r}_{\text{thruster}} - \mathbf{r}_{cm}) \times \mathbf{F}_{\text{thruster}} \quad (2.23)$$

where $\mathbf{r}_{\text{thruster}}$ is the position vector of the associated thruster (see Table 2-1) and \mathbf{r}_{cm} is the

Table 2-4: Expressions to calculate the thruster force x - and y -components with respect to the nominal principal axes. The thruster geometry and numbering is shown in Figure 2-8

Thruster	F_x (N)	F_y (N)
1	$F'_{\text{thruster}} \cos(180^\circ + \phi_{\text{thruster}})$	$F'_{\text{thruster}} \sin(180^\circ + \phi_{\text{thruster}})$
2	$F'_{\text{thruster}} \cos(180^\circ - \phi_{\text{thruster}})$	$F'_{\text{thruster}} \sin(180^\circ - \phi_{\text{thruster}})$
3	$F'_{\text{thruster}} \cos(360^\circ - \phi_{\text{thruster}})$	$F'_{\text{thruster}} \sin(360^\circ - \phi_{\text{thruster}})$
4	$F'_{\text{thruster}} \cos(\phi_{\text{thruster}})$	$F'_{\text{thruster}} \sin(\phi_{\text{thruster}})$

position vector of the CoM of the spacecraft, both expressed with respect to the G -frame, see Figure 2-8. $\mathbf{F}_{\text{thruster}}$ is the thruster force vector expressed relative to the G -frame:

$$\mathbf{F}_{\text{thruster}} = \begin{bmatrix} F_x \\ F_y \\ F_z \end{bmatrix}_{\text{thruster}} \quad (2.24)$$

The z -component of the thruster force vector is calculated by:

$$F_z = F_{\text{thruster}} \cos(\theta_{\text{thruster}}) \quad (2.25)$$

where F_{thruster} is obtained using Equation (2.1) and θ_{thruster} is the thruster cant angle from the z_G -axis, see Figure 2-8. In order to calculate the x - and y -components of the thruster force vector, the following auxiliary parameter is defined:

$$F'_{\text{thruster}} = F_{\text{thruster}} \sin(\theta_{\text{thruster}}) \quad (2.26)$$

Additionally defined is ϕ_{thruster} , which represents the thruster cant angle from the x_G -axis, see Figure 2-8. Since the thrusters are symmetrically canted, the x - and y -components of the thruster force vector are calculated differently for each individual thruster, see Table 2-4.

It is clear from Equation (2.23) that the torque generated by each thruster depends on a continuously degrading thruster force vector (as the RCS operates in blow-down mode, see Section 2-2-1) and a varying CoM position vector (as propellant is consumed). As such, the torque capabilities of the spacecraft persistently vary. To give an impression of the order of magnitude of the spacecraft's torque capabilities, they are calculated for the case of a maximally loaded PDM. The values for the parameters required for this calculation are provided in Table 2-5.

Using the parameter values from Table 2-5, Equations (2.13) and (2.16) are first evaluated to determine the initial pressure inside the propellant tank. Next, Equation (2.17) is evaluated to find the current pressure, which is filled out in Equation (2.1) to obtain the current thruster force (assuming tank pressure is equal to thruster feed pressure). Then, using the expressions listed in Table 2-4 and Equation (2.25), the thruster force components are calculated, constituting the thruster force vectors associated with each thruster. Finally, the CoM of the wet

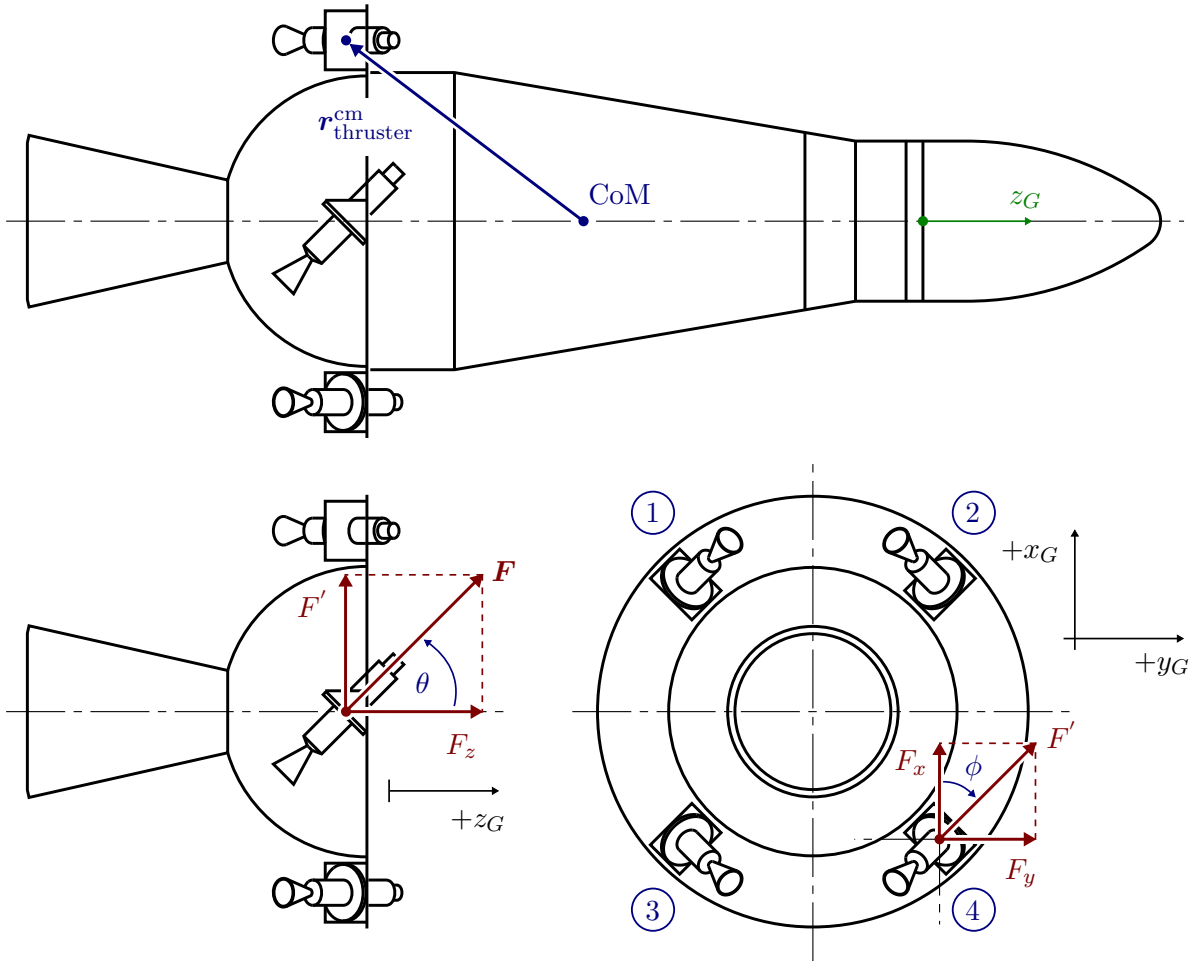


Figure 2-8: Schematic indicating the thruster numbering, cant angles, force components and thruster moment arm. The location of the CoM in the figure is arbitrary.

PDM is obtained through Equation (2.21), which is then component-wise subtracted from each of the thruster position vectors given in Table 2-1 to find the moment arm components for each thruster. Table 2-6 presents the results of the above computations, *i.e.*, the thruster force components and moment arm components per thruster, for a maximally loaded PDM.

In order to provide a complete overview of the torque capabilities of a maximally loaded PDM, the torques generated by each thruster combination must be calculated. To this end, first the thruster force components per thruster are computed for each k , denoting the number of thrusters active at once. This is done by repeating the procedure as described above, albeit using Equation (2.5), which is a modification of Equation (2.1), to account for the feed pressure drop that occurs when multiple thrusters are fired simultaneously (see Section 2-2-1). Next, using the obtained results and the moment arms presented in Table 2-6, Equation (2.23) is evaluated, providing the torque vectors per thruster for each k . The torques generated by each thruster combination are then calculated by summing the torque vectors associated with

Table 2-5: Parameter values for calculating the torque capabilities of a maximally loaded PDM.

Parameter	Value	Unit
$m_{\text{PDM, dry}}$	45.7	kg
$(z_{cm})_{\text{PDM, dry}}$	-0.225	m
$(I_{xx})_{\text{PDM, dry}}$	6.102	kg m ²
$(I_{yy})_{\text{PDM, dry}}$	6.102	kg m ²
$(I_{zz})_{\text{PDM, dry}}$	0.608	kg m ²
m_{solid}	41.2	kg
m_{hyd}	4.5	kg
$m_{\text{hyd, ini}}$	4.5	kg
F_{ave}	3.15	N
V_{tank}	0.006	m ³
p_{max}	24	bar
p_{min}	6	bar
θ_{thruster}	45	deg
ϕ_{thruster}	45	deg

the thrusters concerned, considering that four *on/off*-thrusters allow for $2^4 = 16$ thruster combinations.

Finally, the associated minimum angular impulse bits $\Delta \mathbf{L} = [\Delta L_x, \Delta L_y, \Delta L_z]^T$ are computed by multiplying the torques by the *minimum pulse width*, which is 0.020 seconds for Aerojet's MR-111C thruster, see Table G-1. The results of these computations, *i.e.*, the torque capabilities and minimum angular impulse bits per combination of thrusters, for a maximally loaded PDM, are presented in Table 2-7. It should be noted that solely the results of 15 thruster combinations are listed, as for the 16th combination no thrusters are firing.

Table 2-6: Example thruster force components (N) and moment arm components (m) per thruster, for a maximally loaded PDM.

Thruster	F_x	F_y	F_z	$(r_x)_{\text{thruster}}^{\text{cm}}$	$(r_y)_{\text{thruster}}^{\text{cm}}$	$(r_z)_{\text{thruster}}^{\text{cm}}$
1	-2.374	-2.374	3.358	0.152	-0.152	-0.248
2	-2.374	2.374	3.358	0.152	0.152	-0.248
3	2.374	-2.374	3.358	-0.152	-0.152	-0.248
4	2.374	2.374	3.358	-0.152	0.152	-0.248

Table 2-7: Example torque capabilities (N m) and minimum angular impulse bits ($\text{kg m}^2 \text{s}^{-1}$) per combination of thrusters, for a maximally loaded PDM. In the table, 'T1' stands for 'Thruster 1', 'T2' for 'Thruster 2', etc.

Comb.	T1	T2	T3	T4	M_x	M_y	M_z	ΔL_x	ΔL_y	ΔL_z
1	1	0	0	0	-1.100	0.079	-0.722	-0.022	0.002	-0.014
2	0	1	0	0	1.100	0.079	0.722	0.022	0.002	0.014
3	0	0	1	0	-1.100	-0.079	0.722	-0.022	-0.002	0.014
4	0	0	0	1	1.100	-0.079	-0.722	0.022	-0.002	-0.014
5	1	1	0	0	0	0.154	0	0	0.003	0
6	1	0	1	0	-2.137	0	0	-0.043	0	0
7 ^a	1	0	0	1	0	0	-1.402	0	0	-0.028
8 ^a	0	1	1	0	0	0	1.402	0	0	0.028
9	0	1	0	1	2.137	0	0	0.043	0	0
10	0	0	1	1	0	-0.154	0	0	-0.003	0
11	1	1	1	0	-1.020	0.074	0.669	-0.020	0.001	0.013
12	1	1	0	1	1.020	0.074	-0.669	0.020	0.001	-0.013
13	1	0	1	1	-1.020	-0.074	-0.669	-0.020	-0.001	-0.013
14	0	1	1	1	1.020	-0.074	0.669	0.020	-0.001	0.013
15 ^b	1	1	1	1	0	0	0	0	0	0

^aThis thruster combination also imparts a velocity change along the z_B -axis.

^bThis thruster combination can be used to achieve pure translational motion along the z_B -axis.

Spacecraft Motion and Disturbance Modelling

In a simulation, *real world* systems and processes are represented by mathematical models. Traditionally, they comprise a set of governing differential equations that must be integrated to propagate the state of the system. In order to make mathematical models computationally manageable, they are simplified by imposing reasonable assumptions. This always comes at the cost of accuracy, and hence the extent of simplification should be the result of careful consideration. This chapter investigates the mathematical representations and models available to describe the state of the spacecraft, its dynamics and its environment.

In Section 3-1, relevant reference frames are defined. This is followed by a discussion on the benefits and drawbacks of the various rotational state parameterisations in Section 3-2. In Section 3-3, relations for the attitude kinematics are provided. Finally, in Section 3-4, the rotational equations of motion of the spacecraft are set up, and a thorough assessment of the significance of the disturbance torques acting on the spacecraft is presented.

3-1 Reference Frames

The current and target states of a spacecraft are always expressed with respect to some frame of reference. In this section, three frames of reference – also called *coordinate systems* – are defined. For one's reference, they are also depicted in Figure 3-1. The reference frames considered in this thesis are *right-handed Cartesian* (René Descartes, 1596-1650).

- **Geometric Frame;** denoted by index G . The origin of the G -frame is located at the centre of the release mechanism between the PDS and the penetrator. The z_G -axis is aligned with the symmetry axis and points towards the nose of the penetrator; the

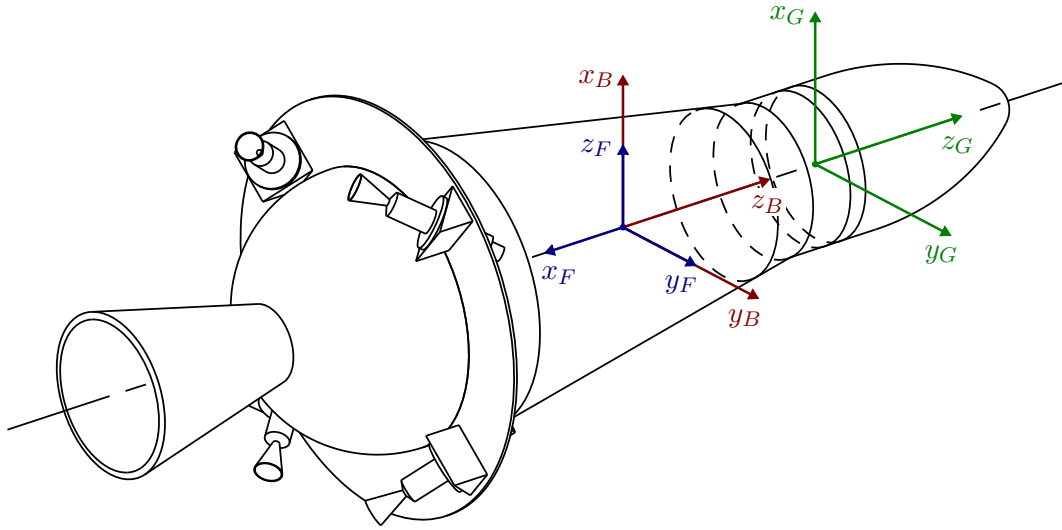


Figure 3-1: Definitions of the geometric frame (G), the body frame (B) and the spacecraft-centred inertial frame (F) at $t = 0$. Note that the x_F -axis points in the direction of the orbital velocity. The x_B -axis coincides with the z_F -axis at $t = 0$. The location of the CoM in the figure is arbitrary.

x_G -axis is in the symmetry plane and points upward (see Figure 2-2 for the definition of ‘upward’); the y_G -axis completes the right-handed system.

- **Body Frame;** denoted by index B . The origin of the B -frame is located at the momentary CoM of the spacecraft. The axes of the B -frame coincide with the nominal *principal axes of inertia* (see Section 2-3) of the spacecraft, and are hence parallel to the G -frame.
- **Spacecraft-Centred Inertial Frame;** denoted by index F . The origin of the F -frame is located at the momentary CoM of the spacecraft. The axes of the F -frame coincide with those of the Local Vertical-Local Horizontal (LVLH) frame (*e.g.*, Curtis, 2014) at the start of the DOM. The z_F -axis points radially outward from the centre of the Moon; the x_F -axis is aligned with the local horizontal; the y_F -axis completes the right-handed system. It is noted that, since the distance traversed by the PDM during the second phase of the descent scenario is only small relative to the distance of the PDM from the centre of the Moon, the rotation of the LVLH frame about its y -axis is considered negligible. Hence, it is reasonable to assume that the F -frame is non-rotating, *i.e.*, inertial, throughout the simulation.

3-2 State Representation

The rotational state of the spacecraft is given by its current orientation and rotation rate. The orientation – also called the *attitude* – of the spacecraft (the B -frame) with respect to

an inertial frame of reference (the F -frame) can be parameterised in different ways. Below, three attitude parameterisations most common in aerospace applications are described, and their advantages and disadvantages are discussed. The section closes with a decision on how the attitude and rotation rate of the PDM will be represented in its rotational state vector.

- **Euler Angles.** Named after Leonhard Euler (1707-1783), the Euler angles are physically intuitive parameters to describe the attitude of a rigid body with respect to an inertial reference frame. They are defined by $\{\phi, \theta, \psi\}$, where ϕ is the roll angle, θ the pitch angle and ψ the yaw angle, resulting from rotations about the x_B -, y_B - and z_B -axes, respectively. The rotation sequence is important here, as it uniquely defines the orientation. Most commonly in the field of aerospace engineering, a *yaw-pitch-roll* ($\phi \leftarrow \theta \leftarrow \psi$) sequence is used (Diebel, 2006). Associated with this sequence are singularities that occur when θ equals an uneven multiple of 90° . Under such circumstances, the second rotation in the sequence will cause the first and third rotation axes to align. Consequently, one degree-of-freedom is lost and a unique solution cannot be obtained. This undesired phenomenon is also referred to as *gimbal lock* (e.g., Diebel, 2006).
- **Quaternions.** Introduced by William Rowan Hamilton (1805-1865), the unit quaternion (henceforth just *quaternion*) is a mathematical construct to parameterise the attitude of a rigid body with respect to an inertial reference frame. Its components are known as *quaternions* or *Euler symmetric parameters* (Shuster, 1993), and are defined by $\{q_1, q_2, q_3, q_4\}$, where

$$\mathbf{q} \equiv \begin{bmatrix} \mathbf{q}_{1:3} \\ q_4 \end{bmatrix} \quad (3.1)$$

with

$$\mathbf{q}_{1:3} \equiv \begin{bmatrix} q_1 \\ q_2 \\ q_3 \end{bmatrix} = \mathbf{e} \sin\left(\frac{\theta}{2}\right) \quad (3.2a)$$

$$q_4 = \cos\left(\frac{\theta}{2}\right) \quad (3.2b)$$

In Equations (3.1), (3.2a) and (3.2b), $\mathbf{q}_{1:3}$ is the vector part and q_4 is the scalar part of the quaternion; \mathbf{e} is the 3×1 *Euler eigenaxis* vector, and θ is the rotation angle about the Euler eigenaxis (e.g., Wie, 2008), also referred to as the *eigenangle*. The quaternion uses four components to represent a three-dimensional attitude – the redundant fourth component ensures a nonsingular representation. Not only do quaternions not suffer from singularities, they are also computationally more efficient than Euler angles (Wie, 2008) and more accurate when integrating rotation rates over time (Diebel, 2006). That said, the fact that quaternions are mathematical constructs makes it difficult to physically interpret them. Also, for a unit quaternion to be a valid rotation, the Euclidean norm must be equal to one, such that:

$$\|\mathbf{q}\| = \sqrt{q_1^2 + q_2^2 + q_3^2 + q_4^2} = 1 \quad (3.3)$$

Equation (3.3) is referred to as the quaternion *unity-norm constraint*.

- **Modified Rodrigues Parameters.** First described by Wiener (1962), the modified Rodrigues parameters are another commonly used means of expressing the attitude of a rigid body with respect to an inertial reference frame. They are defined by $\{p_1, p_2, p_3\}$, where, in terms of quaternions,

$$\mathbf{p} = \frac{\mathbf{q}_{1:3}}{1 + q_4} = \mathbf{e} \tan\left(\frac{\theta}{4}\right) \quad (3.4)$$

As the modified Rodrigues vector \mathbf{p} uses three components to encode a three-dimensional attitude, it is nonredundant. It hence avoids the unity-norm constraint imposed on the unit quaternion. The modified Rodrigues parameters are as mathematically elegant as quaternions and enjoy the same advantages over Euler angles. However, they are only able to describe rotations up to 360° , which becomes problematic when describing the attitude of a spinning spacecraft (Shuster, 1993).

It is clear from the foregoing that modified Rodrigues parameters are preferable over Euler angles and quaternions when encoding rotations up to 360° , as they are not affected by singularities up to that point and not constrained by a unity-norm. The PDM however will be spinning during parts of the descent scenario, implicating that rotations larger than 360° occur. It is therefore decided to parameterise the attitude of the PDM by quaternions. To overcome the limitation that quaternions lack direct physical meaning, Euler angles are used for the definition of the initial and target rotational states (see Chapter 5). Converting between Euler angles and quaternions, and *vice versa*, is discussed in Appendix D.

Finally, the rotation rates – also called the *angular velocities* – are defined by $\{\omega_x, \omega_y, \omega_z\}$; where $\boldsymbol{\omega} = [\omega_x, \omega_y, \omega_z]^T$ is the angular velocity vector of the spacecraft with respect to the inertial reference frame, expressed in components along the x_B -, y_B - and z_B -axes. The rotational state vector of the PDM is hence parameterised by:

$$\mathbf{x} = \begin{bmatrix} \mathbf{q} \\ \boldsymbol{\omega} \end{bmatrix} \quad (3.5)$$

3-3 Attitude Kinematics

The attitude kinematics describe the rotational motion of the spacecraft without considering the torques that initiated the motion. Since quaternions are used to parameterise the attitude of the spacecraft, it is convenient to directly relate the time derivatives of the quaternion components $\dot{\mathbf{q}}$ to the angular velocity vector. Wie (2008) provides these relations:

$$\dot{\mathbf{q}} = \begin{bmatrix} \dot{q}_1 \\ \dot{q}_2 \\ \dot{q}_3 \\ \dot{q}_4 \end{bmatrix} = \frac{1}{2} \begin{bmatrix} 0 & \omega_3 & -\omega_2 & \omega_1 \\ -\omega_3 & 0 & \omega_1 & \omega_2 \\ \omega_2 & -\omega_1 & 0 & \omega_3 \\ -\omega_1 & -\omega_2 & -\omega_3 & 0 \end{bmatrix} \begin{bmatrix} q_1 \\ q_2 \\ q_3 \\ q_4 \end{bmatrix} \quad (3.6)$$

In compact form, Equation (3.6) can be rewritten as:

$$\dot{\mathbf{q}}_{1:3} = \frac{1}{2} (q_4 \boldsymbol{\omega} - \boldsymbol{\omega} \times \mathbf{q}_{1:3}) \quad (3.7a)$$

$$\dot{q}_4 = -\frac{1}{2} \boldsymbol{\omega} \cdot \mathbf{q}_{1:3} \quad (3.7b)$$

3-4 Attitude Dynamics

The attitude dynamics of the spacecraft are described by a set of differential equations, known as the *rotational equations of motion*. In Section 3-4-1, these equations are set up. Then, in Section 3-4-2, the disturbance torques acting on the spacecraft are assessed for their significance in the context of the descent scenario.

3-4-1 Equations of Motion

By applying the three Laws of Motion¹ of Isaac Newton (1642-1727), the rotational equations of motion (EoM) of an arbitrary *non-rigid mass-varying* body can be derived as (Cornelisse et al., 1979; Mooij, 1994):

$$\begin{aligned} \mathbf{M}_{\text{cm}} = & \overbrace{\int_m \tilde{\mathbf{r}}_{dm} \times \left(\frac{d\boldsymbol{\omega}}{dt} \times \tilde{\mathbf{r}}_{dm} \right) dm}^{\text{apparent moment due to angular acceleration}} + \overbrace{\int_m \tilde{\mathbf{r}}_{dm} \times [\boldsymbol{\omega} \times (\boldsymbol{\omega} \times \tilde{\mathbf{r}}_{dm})] dm}^{\text{apparent moment due to angular velocity}} \\ & + \underbrace{2 \int_m \tilde{\mathbf{r}}_{dm} \times \left(\boldsymbol{\omega} \times \frac{\delta \tilde{\mathbf{r}}_{dm}}{\delta t} \right) dm}_{\text{Coriolis moment due to variable mass}} + \underbrace{\int_m \tilde{\mathbf{r}}_{dm} \times \frac{\delta^2 \tilde{\mathbf{r}}_{dm}}{\delta t^2} dm}_{\text{relative moment due to variable mass}} \quad (3.8) \end{aligned}$$

where \mathbf{M}_{cm} is the total (disturbing) moment about the CoM of the body, dm is the mass of a mass element within the body and $\tilde{\mathbf{r}}_{dm}$ is the position vector of the mass element with respect to the CoM of the body. The first two terms on the right-hand side of Equation (3.8) emerge as a result of the angular acceleration and angular velocity of dm with respect to the inertial reference frame, respectively, and are also referred to as the *tangential* and *centripetal* apparent moments. The last two terms are due to the velocity and acceleration of dm with respect to the body frame (hence the symbol δ is used to denote the derivatives), as seen from the inertial reference frame. Respectively, they are also referred to as the *Coriolis* and *relative*

¹**First Law:** “Every particle continues in its state of uniform motion in a straight line (or rest), unless compelled to change that state by forces acting upon it.” – **Second Law:** “The time rate of change of linear momentum of a particle is proportional to the force acting upon that particle and is collinear with and in the direction of that force.” – **Third Law:** “The mutual forces of two particle acting upon each other are equal in magnitude and opposite in direction.” (Cornelisse et al., 1979)

apparent moments. It should be noted that these latter two terms only arise when the body has a variable mass distribution. In case of a *rigid body*², the position vectors of the mass elements with respect to the CoM of the body do not change over time, and the terms are zero. Defining \mathbf{M}_C , the apparent Coriolis moment, and \mathbf{M}_{rel} , the apparent relative moment:

$$\mathbf{M}_C = -2 \int_m \tilde{\mathbf{r}}_{dm} \times \left(\boldsymbol{\omega} \times \frac{\delta \tilde{\mathbf{r}}_{dm}}{\delta t} \right) dm \quad (3.9)$$

$$\mathbf{M}_{\text{rel}} = - \int_m \tilde{\mathbf{r}}_{dm} \times \frac{\delta^2 \tilde{\mathbf{r}}_{dm}}{\delta t^2} dm \quad (3.10)$$

then Equation (3.8) can be written as:

$$\begin{aligned} \tilde{\mathbf{M}}_{\text{cm}} = \mathbf{M}_{\text{cm}} + \mathbf{M}_C + \mathbf{M}_{\text{rel}} = \int_m \tilde{\mathbf{r}}_{dm} \times \left(\frac{d\boldsymbol{\omega}}{dt} \times \tilde{\mathbf{r}}_{dm} \right) dm \\ + \int_m \tilde{\mathbf{r}}_{dm} \times [\boldsymbol{\omega} \times (\boldsymbol{\omega} \times \tilde{\mathbf{r}}_{dm})] dm \end{aligned} \quad (3.11)$$

Cornelisse et al. (1979) show that the terms on the right-hand side of Equation (3.11) represent the rotational EoM of an arbitrary *rigid body*, and state that through the *Principle of Solidification* (Cornelisse et al., 1979, p. 41), Equation (3.8) at time t can be written as Equation (3.11), if m is equal to the mass of the body at time t and two apparent moments, being \mathbf{M}_C and \mathbf{M}_{rel} , are added to the true total (disturbing) moment \mathbf{M}_{cm} . In order to simplify Equations (3.9) and (3.10), Cornelisse et al. (1979) make the following assumptions:

- Assumption 1.** The body is non-elastic, but not rigid. Its mass distribution changes when propellant is consumed and the resulting combustion gasses are expelled.
- Assumption 2.** The flowfield of expelled combustion gasses is axisymmetric.
- Assumption 3.** The total mass of moving combustion gasses within the body is small as compared to the mass of the body, making their contribution to the angular momentum of the body negligible.
- Assumption 4.** The velocity of the CoM of the body with respect to the body is very small as compared to the exhaust velocity.

Applying these assumptions, Equations (3.9) and (3.10) simplify to, respectively,

$$\mathbf{M}_C = -\frac{\delta \mathbf{I}}{\delta t} \boldsymbol{\omega} - \overbrace{\dot{m} \mathbf{r}_e \times (\boldsymbol{\omega} \times \mathbf{r}_e)}^{\text{exhaust jet damping moment}} \quad (3.12)$$

²A rigid body is defined as a bounded mass system within which the distribution of mass does not change.

$$\mathbf{M}_{\text{rel}} = \overbrace{-\dot{m}\mathbf{r}_e \times \mathbf{v}_e}^{\text{moment due to impulse thrust}} \quad (3.13)$$

where \dot{m} is the exhaust mass flow, \mathbf{r}_e is the position vector of the centre of the exhaust mass flow relative to the CoM of the body and \mathbf{v}_e is the effective exhaust velocity vector. The first term on the right-hand side of Equation (3.12) – in some literature referred to as the *inertia-dot* term (e.g. Van Der Ha & Janssens, 2005) – represents a loss of angular momentum occurring as a direct result of propellant consumption. For *spinning* spacecraft, dynamic models that include the inertia-dot term predict significant changes in the spin rate. However, no such changes have been observed during actual single-nozzle SRM firings (Wertz, 1978). A physical explanation for this is given by G. K. Tandon in Wertz (1978), who reasons that the angular momentum flux is wholly conserved in the combustion gases, which are expelled from the nozzle before noticeably interacting with the spacecraft. Hence, the inertia-dot term may be dropped from Equation (3.12), such that

$$\mathbf{M}_C = -\overbrace{\dot{m}\mathbf{r}_e \times (\boldsymbol{\omega} \times \mathbf{r}_e)}^{\text{exhaust jet damping moment}} \quad (3.14)$$

Equation (3.14) represents the *exhaust jet damping moment*, which emerges as a result of a “wagging of the jet stream” (Armstrong, 1965), i.e., angular velocities perpendicular to \mathbf{r}_e . The term owes its name to its damping effect on these velocities. As for Equations (3.13) and (3.14), it is clear that they only apply for a single firing thruster. When multiple thrusters fire simultaneously, it is easily figured that Equations (3.13) and (3.14) expand as:

$$\mathbf{M}_C = -\sum_{i=1}^k \dot{m}_i(\mathbf{r}_e)_i \times [\boldsymbol{\omega} \times (\mathbf{r}_e)_i] \quad (3.15)$$

$$\mathbf{M}_{\text{rel}} = -\sum_{i=1}^k \dot{m}_i(\mathbf{r}_e)_i \times (\mathbf{v}_e)_i \quad (3.16)$$

where k is the number of thrusters firing simultaneously. For the case of the PDM, the assumptions underlying Equations (3.13) to (3.16) also apply. It should hereby be noted that the liquid propellant slug inside the propellant tank is assumed to be a rigid body surrounded by a viscous layer that is only coupled to the PDM by means of viscous friction. In Section 3-4-2-3, the significance of the disturbance torque that is caused by viscous friction will be investigated. The exhaust mass flow \dot{m}_i in Equation (3.15) is calculated as a function of the feed pressure p_f and the feed pressure drop factor α_k , see Equation (2.7).

Examining Equation (3.16), it is clear that the apparent relative moment \mathbf{M}_{rel} represents the total torque produced by thrust forces. Therefore, the term will henceforth be denoted

by \mathbf{M}_T . Using Equations (2.3), (2.5) and (2.23) in combination with Equation (3.16), the following expression for \mathbf{M}_T can be derived:

$$\mathbf{M}_{\text{rel}} \equiv \mathbf{M}_T = \sum_{i=1}^k (\mathbf{r}_e)_i \times (\mathbf{F}_i)_n \quad (3.17)$$

As was shown before, the rotational dynamics of a rigid body are described by Equation (3.11). However, they can also be described by *Euler's equations of motion* (e.g., Mooij, 1994):

$$\tilde{\mathbf{M}}_{\text{cm}} = \mathbf{I}\dot{\boldsymbol{\omega}} + \boldsymbol{\omega} \times \mathbf{I}\boldsymbol{\omega} \quad (3.18)$$

where $\dot{\boldsymbol{\omega}} = [\dot{\omega}_x, \dot{\omega}_y, \dot{\omega}_z]^T$ is the angular acceleration vector of the body with respect to the inertial reference frame, expressed in components along the axes of the B -frame, and \mathbf{I} is the inertia tensor of the body, referenced to the body frame (see Section 2-3). Solving for the angular acceleration vector $\dot{\boldsymbol{\omega}}$, Equation (3.18) can be rearranged such that the following differential equations arise:

$$\dot{\boldsymbol{\omega}} = \mathbf{I}^{-1} \left(\tilde{\mathbf{M}}_{\text{cm}} - \boldsymbol{\omega} \times \mathbf{I}\boldsymbol{\omega} \right) \quad (3.19)$$

where

$$\tilde{\mathbf{M}}_{\text{cm}} = \mathbf{M}_{\text{cm}} + \mathbf{M}_C + \mathbf{M}_T \quad (3.20)$$

and \mathbf{M}_{cm} represents the sum of the individual disturbing moments – also referred to as *disturbance torques*, see Section 3-4-2.

3-4-2 Disturbance Torques

Disturbance torques emerge as a result of disturbance forces not acting through the CoM of the body. In space, typical *external* disturbance torques exerted on a spacecraft are the *gravity gradient torque*, the *solar radiation torque*, the *aerodynamic torque* and the *magnetic disturbance torque* (e.g., Ley et al., 2009). Since the PDM is in orbit around the Moon, which has a negligible atmosphere and a very weak magnetic field (Lissauer & De Pater, 2013), the impact of the latter two disturbance torques may be ignored. The significance of the gravity gradient torque and solar radiation torque during the second phase of the PDM's descent scenario (see Section 1-2-3) will be investigated in Sections 3-4-2-1 and 3-4-2-2, respectively. Lastly, in Section 3-4-2-3, the significance of an *internal* disturbance torque induced by viscous friction between the liquid propellant slug and the PDM will be assessed.

3-4-2-1 Gravity Gradient Torque

Gravity gradient torques arise when gravitational forces do not act through the CoM of the body. Forces of gravitational origin always act through the centre of gravity (CoG) of the body. The CoG coincides with the CoM if the body is spherically symmetric and uniform, which is not the case for the PDM. This implicates that the PDM would indeed be affected by gravity gradient torques, if the CoM is not aligned with the CoG along the line of action of gravity. As [Cornelisse et al. \(1979\)](#) point out, gravity gradient torques are very small relative to the torques produced by thrust forces. If nevertheless taken into account, the only gravity gradient torque of interest would be the one generated by the gravitational force of the central body, which for the case of the PDM is the Moon. The equation for the gravity gradient torque in vector form is given by ([Meyer, 1999](#)):

$$\mathbf{M}_g = 3 \frac{\mu}{r^5} [\mathbf{r}_B \times (\mathbf{I} \mathbf{r}_B)] \quad (3.21)$$

for which spherical gravity is assumed. In Equation (3.21), μ is the gravitational parameter of the central body, r is the distance between the CoM of the body and the CoM of the central body and \mathbf{r}_B is the position vector of the CoM of the body with respect to the CoM of the central body, expressed in the B -frame. The gravitational parameter μ is calculated by multiplying the gravitational constant $G = 6.674 \times 10^{-11} \text{ m}^3 \text{ kg}^{-1} \text{ s}^{-2}$ ([Lissauer & De Pater, 2013](#)) by the mass of the central body. In Table 3-1, some physical properties of the Moon, including its gravitational parameter, are listed.

Table 3-1: Relevant characteristics of the Moon.

Characteristic	Value	Comment
R_m	$1.738 \times 10^6 \text{ m}$	Equatorial radius ^a
m_m	$7.349 \times 10^{22} \text{ kg}$	Mass ^a
μ_m	$4.905 \times 10^{12} \text{ m}^3 \text{ s}^{-2}$	Calculated

^aSource: [Lissauer and De Pater \(2013\)](#).

In order to assess the significance of the gravity gradient torque during the second phase of the PDM's descent scenario, its worst-case magnitude is estimated for the separate cases of the penetrator, dry PDS and dry PDM. To this end, each system is taken to be as close to the Moon as possible, under the least favourable angle. As such, \mathbf{r}_B is taken to be the equatorial radius of the Moon, R_m , in vector form, expressed in the B -frame, which is canted 45° with respect to the z -axis of the F -frame. Transforming a vector expressed in the F -frame to the B -frame is explained in Appendix E. The associated inertia tensors can be found in Table 2-3. The resulting worst-case estimates for the gravity gradient torques are presented in Table 3-2.

As is seen in Table 3-2, the worst-case gravity gradient torque exerted on the controlled spacecraft during the second phase of the descent scenario is on the order of 10^{-6} . Considering that the spacecraft's weakest torque capabilities are five orders of magnitude larger (see Table 2-7), and that any irregularity in thruster performance (also called *thruster roughness*), which is

Table 3-2: Worst-case gravity gradient torque estimates.

System	M_g (N m)
Penetrator	9.418×10^{-8}
PDS (dry)	2.837×10^{-6}
PDM (dry)	7.697×10^{-6}

typically as high as 2-3% of the nominal performance (Sidi, 1997), will introduce errors on the order of 10^{-3} , it is reasonably concluded that the impact of the gravity gradient torque is too insignificant, hence it will not be included in the dynamics model.

3-4-2-2 Solar Radiation Torque

The Sun puts out radiation that exerts a force on a body in space. This so-called force due to solar radiation pressure applies to the centre of area (CoA) of the body. When the CoM and CoA are not aligned along the line of action of the solar radiation force, a torque is produced. The magnitude of the solar radiation torque is calculated by (Wertz, 2005):

$$M_{SR} = \frac{S}{c} A (1 + q) r_{ca} \cos i \quad (3.22)$$

where $S = 1367 \text{ W m}^{-2}$ (Wertz, 2005) is the solar constant at one astronomical unit from the Sun (approximately the distance between the Moon and the Sun), $c = 2.998 \times 10^8 \text{ m s}^{-1}$ (Wertz, 2005) is the speed of light, A is the surface area of the body, q is the reflection coefficient, r_{ca} is the distance between the CoM and CoA of the body and i is the angle of incidence of the Sun. In order to assess the significance of the solar radiation torque during the second phase of the PDM's descent scenario, its worst-case magnitude is estimated for the dry PDM. To this end, it is assumed that the PDM is oriented in such a way that it is maximally exposed to the Sun and that any incident radiation is reflected maximally. As such, $q = 1$ and $i = 0^\circ$. Table 3-3 provides the maximum surface area of the PDM as well as the distance of the CoA of the PDM from the CoM of the dry PDM. Filling out Equation (3.22) yields:

$$M_{SR} = 5.618 \times 10^{-7} \text{ N m}$$

which in fact is an order of magnitude smaller than the worst-case gravity gradient torque exerted on the dry PDM. Since it was decided to exclude the latter from the model because of lacking significance, so will be the solar radiation torque.

3-4-2-3 Viscous Friction Torque

The dynamic behaviour of the liquid propellant slug that is contained inside the propellant tank is directly influenced by the motion of the spacecraft. In turn, a moving liquid also affects the dynamics of the spacecraft. Hence, the dynamics of the liquid propellant slug and the

Table 3-3: Surface properties of the PDM.

Characteristic	Value	Unit	Comment
$A_{\text{PDM, max}}$	0.305	m ²	Maximum surface area PDM ^a
$z_{\text{PDM, cm}}$	-0.225	m	Location CoM in G -frame ^a
$z_{\text{PDM, ca}}$	-0.427	m	Location CoA in G -frame ^a
$r_{\text{PDM, ca}}$	0.202	m	Calculated

^aDerived from CATIA.

spacecraft are *coupled*. The lateral and vertical movement of a liquid in a container is referred to as *sloshing*, which, strictly speaking, can only occur when the liquid has a so-called *free surface* (e.g., Dodge, 2000; Ibrahim, 2005). As was explained in Section 2-2-1, the free surface of the liquid propellant slug inside the tank is restrained by a diaphragm, which is assumed to dampen any forms of lateral and vertical sloshing to such a degree that their impact on the dynamics of the spacecraft may be neglected. As the tank does not incorporate any devices that prevent the liquid from rotating, rotational liquid motion, also referred to as *swirling*, can in fact occur, and therefore its impact on the dynamics of the spacecraft will be assessed.

The motion of a liquid inside a spinning body is very complicated (Ibrahim, 2005), as are the mathematics behind it. It is considered beyond the scope of this thesis to provide a full analysis of the swirling dynamics. For the purpose of investigating the effect of internal energy dissipation caused by rotational liquid motion, the liquid propellant slug is modelled as a rigid body surrounded by a viscous layer, coupled to the spacecraft only by means of viscous friction. Rahn and Barba (1991) provide the full set of the equations of motion for such a coupled system – comprised of a rigid spacecraft and a rigid *spherical* propellant slug, which is enclosed by a viscous boundary layer and centred on the CoM of the spacecraft – as follows:

$$\dot{\omega} = (\mathbf{I} - \mathbf{I}_{\text{liquid}})^{-1} (\mathbf{M} + \mu\boldsymbol{\sigma} - \boldsymbol{\omega} \times \mathbf{I}\boldsymbol{\omega}) \quad (3.23a)$$

$$\dot{\boldsymbol{\sigma}} = -\dot{\boldsymbol{\omega}} - \mathbf{I}_{\text{liquid}}^{-1} (\mu\boldsymbol{\sigma}) - \boldsymbol{\omega} \times \boldsymbol{\sigma} \quad (3.23b)$$

where \mathbf{I} is the inertia tensor of the spacecraft *including* the propellant slug, $\mathbf{I}_{\text{liquid}}$ is the inertia tensor of the spherical propellant slug, $\boldsymbol{\sigma}$ is the angular velocity of the slug relative to the spacecraft and μ is the viscous damping coefficient. Before the impact of swirling on the dynamics of the PDM is tested, it is first verified whether Equations (3.23a) and (3.23b) have been correctly implemented. To this end, the results of a spin-axis transition manoeuvre as presented by Rahn and Barba (1991), see Figure 3-2, are reproduced. Using the parameter values from Table 3-4 and the following equation for the total angular momentum:

$$h_{\text{tot}}^2 = (I_{xx}\omega_x + I_{\text{liquid}}\sigma_x)^2 + (I_{yy}\omega_y + I_{\text{liquid}}\sigma_y)^2 + (I_{zz}\omega_z + I_{\text{liquid}}\sigma_z)^2, \quad (3.24)$$

Table 3-4: Parameter values used by [Rahn and Barba \(1991\)](#) to simulate a spin-axis transition manoeuvre. Note that since the liquid propellant slug is spherical, I_{liquid} is a singular value.

Parameter	Value	Unit
I_{xx}	2000	kg m ²
I_{yy}	1500	kg m ²
I_{zz}	1000	kg m ²
I_{liquid}	18	kg m ²
μ	30	N m s
ω_x	0.1224	rad s ⁻¹
ω_y	0	rad s ⁻¹
ω_z	2.99	rad s ⁻¹
M_x, M_y, M_z	0	N m
$\sigma_x, \sigma_y, \sigma_z$	0	rad s ⁻¹

Figure 3-3 is generated, which, when compared to its original, shows very good agreement. The implementation of Equations (3.23a) and (3.23b) can hence be considered successful.

In order to validly apply Equations (3.23a) and (3.23b) to assess the impact of rotational liquid motion on the dynamics of the PDM, some questionable assumptions must be made. Namely, that the liquid propellant slug is a sphere, which is tightly enclosed by the propellant tank and is centred on the CoM of the PDM, at all times. This is of course far from true, and hence the outcome of simulating the PDM's rotational dynamics using this model should be regarded as a conservative estimate of the effects of swirling.

In selecting the appropriate test values, it is assumed that a spinning PDM has just completed the DOM. As such, the PDM is nearly dry, except for 1.0 kg of liquid propellant remaining. At this particular moment during the descent, the liquid propellant slug has maximum potential to affect the dynamics of the PDM. The inertia of the hydrazine sphere can be calculated using (*e.g.*, [Hibbeler, 2010](#)):

$$I_{\text{sphere}} = \frac{2}{5} m r^2 \quad (3.25)$$

where the radius r of the sphere can be obtained through:

$$r = \left(\frac{3m}{4\pi\rho} \right)^{\frac{1}{3}} \quad (3.26)$$

Filling out $m = 1.0$ kg and $\rho = 1008$ kg m⁻³, the density of hydrazine, then gives $I_{\text{sphere}} = 0.0015$ kg m². Furthermore, the spin rate is assumed to be 4π rad s⁻¹ and the transverse angular rate to be 0.5 rad s⁻¹, which is equal to the worst-case disturbance encountered during the DOM, see Figure 5-5. Finally, the viscous damping coefficient μ must be determined. Unfortunately, [Rahn and Barba \(1991\)](#) do not disclose how this is done. However, it is plausible to assume that its value is proportional to area of the sphere times the radius, since

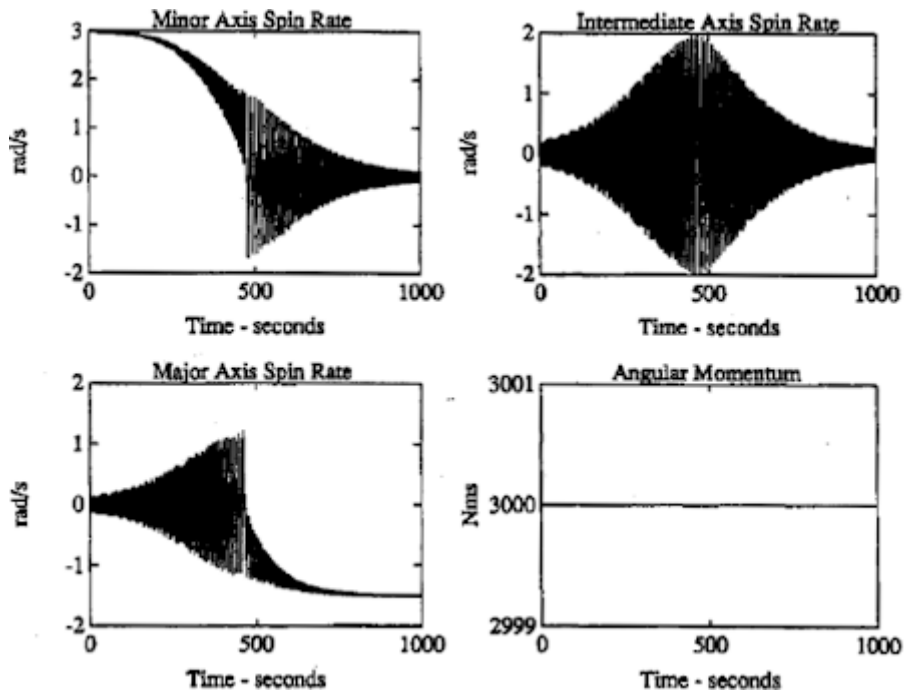


Figure 3-2: Results of a spin-axis transition manoeuvre as presented in Rahn and Barba (1991).

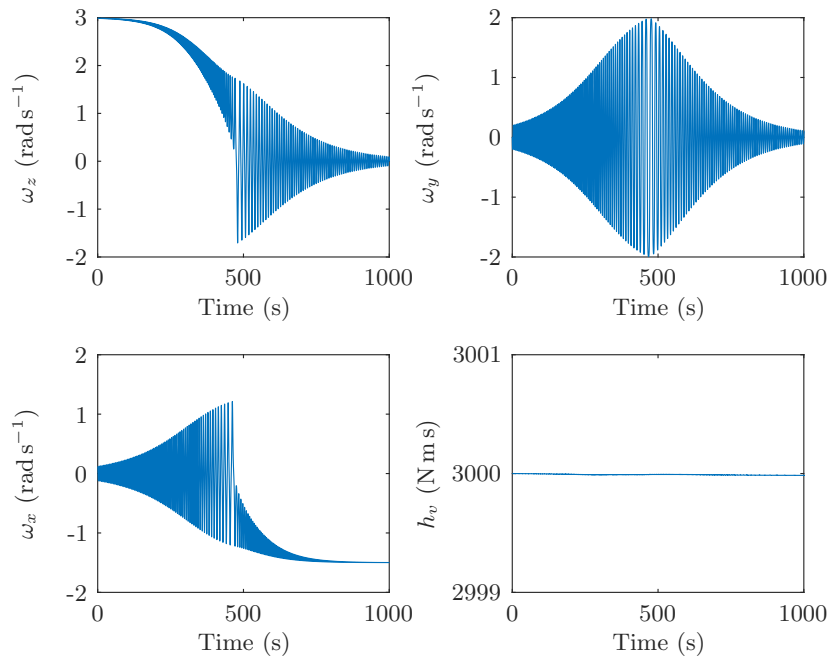


Figure 3-3: Reproduction of Figure 3-2, verifying the correct implementation of Equation (3.23).

Table 3-5: Parameter values used to investigate the impact of viscous friction.

Parameter	Value	Unit
I_{xx}	6.102	kg m ²
I_{yy}	6.102	kg m ²
I_{zz}	0.608	kg m ²
I_{liquid}	0.0015	kg m ²
μ	0.108	N m s
ω_x	0.5	rad s ⁻¹
ω_y	0	rad s ⁻¹
ω_z	12.566	rad s ⁻¹
M_x, M_y, M_z	0	N m
$\sigma_x, \sigma_y, \sigma_z$	0	rad s ⁻¹

the amount of viscous friction, *i.e.*, damping, is proportional to the area, and the torque that is induced by such friction is proportional to the radius, *i.e.*, the moment arm. To find the ratio characterising $\mu \propto (A_{\text{sphere}} \cdot r)$, the area and radius of the liquid sphere considered in [Rahn and Barba \(1991\)](#) must be obtained. Since the liquid is not specified, it is assumed to be hydrazine. The area of a sphere can be calculated using:

$$A_{\text{sphere}} = 4 \pi r^2 \quad (3.27)$$

Combining Equations (3.25) to (3.27) and rearranging yields:

$$r = \left(\frac{15 I_{\text{sphere}}}{8 \pi \rho} \right)^{\frac{1}{5}} \quad (3.28)$$

and

$$A_{\text{sphere}} = 4 \pi \left(\frac{15 I_{\text{sphere}}}{8 \pi \rho} \right)^{\frac{2}{5}} \quad (3.29)$$

Filling out $I_{\text{sphere}} = 18 \text{ kg m}^2$ and $\rho = 1008 \text{ kg m}^{-3}$, gives $r = 0.403 \text{ m}$ and $A_{\text{sphere}} = 2.043 \text{ m}^2$; the supposed radius and area of the liquid sphere considered in [Rahn and Barba \(1991\)](#). Using these values and $\mu = 30 \text{ N m s}$, the aforementioned ratio is calculated to be 36.4. Then multiplying this ratio by the product of the area and radius of the PDM's hydrazine sphere gives $\mu = 0.108 \text{ N m s}$. The parameter values are listed in Table 3-5. Now simulating the dynamics of an uncontrolled PDM using these parameters and Equations (3.23a) and (3.23b) indicates that it takes about 2 hours before the spin rate is reduced by 1 rad s⁻¹. For the short period considered after the DOM, this reduction is negligible. Hence, it is concluded that the viscous friction torque, because of its apparent insignificance, will not be included in the dynamics model.

Controller Design

This chapter is concerned with the design of the controller of the PDM, which will be based on classical control techniques. First, a brief introduction to classical control is provided in Section 4-1. Then, the control law implemented for the large-angle slew manoeuvres is discussed in Section 4-2. Finally, Section 4-3 describes the control logic for the minor-axis spin manoeuvres.

4-1 Introduction

Classical control, typically synonymous with PID control, is arguably the most applied control strategy across many different industries requiring feedback controllers (*e.g.*, Kozák, 2014), including aerospace. For a standard PID controller, the following control law applies:

$$u(t) = K_p e(t) + K_i \int_0^t e(\tau) d\tau + K_d \frac{de(t)}{dt} \quad (4.1)$$

where u represents the output of the controller, e is the difference between the current state and the target state, t is present time and τ is the variable of integration, taking on values between 0 and t . The parameters K_p , K_i and K_d are the proportional, integral and derivative controller gains, respectively. Their values are usually heuristically selected in a process referred to as *gain tuning*, such that the controller attains its desired performance. For each degree-of-freedom in the dynamic model, a separate control law of the form given by Equation (4.1) can be defined. The controller consequently generates an output vector of a size equal to the number of control laws involved. Based on the design goals, the individual control terms – P, I and D – can also be used selectively to form P, PI or PD controllers. PID still provides the base structure for many of today’s advanced control algorithms, which in turn often rely on more sophisticated methods to tune the controller gains.

4-2 Large-Angle Slew Manoeuvres

For the large-angle slew manoeuvres, the well-known quaternion-error feedback controller developed by [Wie et al. \(1989\)](#) is implemented. The governing control law is essentially equivalent to a classical PD control law, and is further discussed in Section 4-2-1. Through a *Lyapunov stability* analysis, [Wie et al. \(1989\)](#) demonstrated the global stability of the controller in the presence of minor inertia uncertainty and small initial body rates. In addition, they showed that in the ideal case of known inertia and zero initial body rates, the resulting large-angle slew manoeuvre represents a so-called *eigenaxis rotation*. A rotation about the Euler eigenaxis (see Section 3-2 for the mathematical definition) guarantees the shortest path between two orientations, and can thus be considered ‘optimal’. In order for the controller to deliver the desired performance, appropriate gains must be selected. The gain selection process is discussed in Section 4-2-2. Finally, in Section 4-2-3, the successful implementation of the controller is verified.

4-2-1 Control Law

The quaternion-error feedback control law as proposed by [Wie et al. \(1989\)](#) consists of two linear feedback terms related to the error quaternion and the body-rate error, and one nonlinear feedback term related to the body rate, which is in place to cancel the gyroscopic coupling term appearing in Euler’s equations of rotational motion, see Equation (3.19). The control law is defined by:

$$\mathbf{u} = \mu (\boldsymbol{\omega} \times \mathbf{I}\boldsymbol{\omega}) - \mathbf{D} \boldsymbol{\omega}_e - \text{sgn}(q_{4,0}) \mathbf{K} \mathbf{q}_e \quad (4.2)$$

where \mathbf{u} is the control torque vector; \mathbf{D} and \mathbf{K} are 3×3 constant gain matrices, further discussed in Section 4-2-2; μ is gyroscopic coupling torque damping factor, which takes a value between 0 and 1 and essentially represents a measure of uncertainty about the inertia tensor; $\boldsymbol{\omega}_e$ is the body-rate error, which is in fact equal to the body rate $\boldsymbol{\omega}$, as the target body rate is always zero; $q_{4,0}$ is the initial value of the scalar element of the quaternion; sgn is the *sign function*; and $\mathbf{q}_e = [q_{1,e}, q_{2,e}, q_{3,e}]^T$ is the vector part of the error quaternion, whose elements are calculated by:

$$\begin{bmatrix} q_{1,e} \\ q_{2,e} \\ q_{3,e} \\ q_{4,e} \end{bmatrix} = \begin{bmatrix} q_{4,c} & q_{3,c} & -q_{2,c} & -q_{1,c} \\ -q_{3,c} & q_{4,c} & q_{1,c} & -q_{2,c} \\ q_{2,c} & -q_{1,c} & q_{4,c} & -q_{3,c} \\ q_{1,c} & q_{2,c} & q_{3,c} & q_{4,c} \end{bmatrix} \begin{bmatrix} q_1 \\ q_2 \\ q_3 \\ q_4 \end{bmatrix} \quad (4.3)$$

where $[q_{1,c}, q_{2,c}, q_{3,c}, q_{4,c}]^T$ is the commanded quaternion defining the target orientation and $[q_1, q_2, q_3, q_4]^T$ is the current quaternion defining the current orientation. It should be noted that for slow rotational manoeuvres, *i.e.*, $\boldsymbol{\omega} \approx \mathbf{0}$, the gyroscopic coupling torque is very small, which allows for discarding the nonlinear feedback term.

4-2-2 Gain Selection

In order to achieve a large-angle rest-to-rest rotation about the eigenaxis, [Wie et al. \(1989\)](#) find that the gain matrices \mathbf{D} and \mathbf{K} in Equation (4.2) should satisfy:

$$\mathbf{D} = d\mathbf{I} \quad (4.4)$$

$$\mathbf{K} = k\mathbf{I} \quad (4.5)$$

where d and k are positive scalars. In order to determine d and k , Equation (4.2) is filled out in Equation (3.19), assuming that $\tilde{\mathbf{M}}_{\text{cm}} = \mathbf{u}$, $\mu = 1$ and $q_{4,0}$ is positive. This yields:

$$\dot{\boldsymbol{\omega}} + d\boldsymbol{\omega} + k\mathbf{q}_e = 0 \quad (4.6)$$

Using Equation (3.2a) and the fact that for an eigenaxis rotation holds that $\boldsymbol{\omega} = \mathbf{e}\dot{\theta}$, Equation (4.6) becomes:

$$\left(\ddot{\theta} + d\dot{\theta} + k \sin \frac{\theta}{2} \right) \mathbf{e} = 0 \quad (4.7)$$

where θ is also referred to as the *eigenangle*. Since $\mathbf{e} \neq 0$:

$$\ddot{\theta} + d\dot{\theta} + k \sin \frac{\theta}{2} = 0 \quad (4.8)$$

For small eigenangles,

$$\sin \frac{\theta}{2} \approx \frac{\theta}{2} \quad (4.9)$$

is an acceptable approximation. Using Equation (4.9), Equation (4.8) takes the form of a specific linear second-order differential equation, referred to as the *damped harmonic oscillator equation*:

$$\ddot{\theta} + d\dot{\theta} + \frac{k}{2}\theta = 0 \quad (4.10)$$

As such:

$$d = 2\zeta\omega_n \quad (4.11)$$

$$k = 2\omega_n^2 \quad (4.12)$$

Concluding from Equations (4.11) and (4.12), the damping ratio ζ and the natural frequency ω_n are the key parameters to be properly selected to define d and k , and ultimately gain matrices \mathbf{D} and \mathbf{K} . In spacecraft attitude control, the damping ratio ζ is indicative of how fast the controller is able to achieve the target state. A lower damping ratio is associated with a faster response, however, in case of *underdamping* ($\zeta < 1$), also with a greater overshoot, meaning that the spacecraft goes beyond the target state and additional control effort is needed in order to establish an equilibrium. When $\zeta = 1$, the response is *critically damped* and the target state is achieved fastest without overshoot. Generally in spacecraft attitude control, some overshoot is acceptable if in return a much faster control law is obtained. A commonly chosen damping ratio in this regard is one that leads to a zero peak frequency ω_p in the frequency domain (Nise, 2011, p. 581):

$$\omega_p = \omega_n \sqrt{1 - 2\zeta^2} = 0 \quad (4.13)$$

Solving Equation (4.13) for ζ then yields:

$$\zeta = \frac{1}{2}\sqrt{2} \quad (4.14)$$

or $\zeta = 0.707$ (Pisacane, 2005, p. 296), which implies that the response is slightly underdamped. For an underdamped second-order response, it is possible to relate the natural frequency ω_n directly to the more intuitive settling time T_s , through the following well-known approximation (e.g., Nise, 2011):

$$\omega_n = \frac{4}{\zeta T_s} \quad (4.15)$$

for which a settling band of $\pm 2\%$ of the steady-state value assumed. It should however be stressed that Equation (4.15) only holds true for linear systems. Due to the nonlinear effects caused by the term $\sin(\theta/2)$, the quaternion-error feedback controller as proposed by Wie et al. (1989) may only be considered linear for small eigenangles. As can be seen from Figure 4-1, where the relative difference between the chosen settling time and the actual settling time δT_s for q_1 , q_2 and q_3 is plotted against the eigenangle-to-go θ_{togo} , the relation in Equation (4.15) breaks down for larger eigenangles. Figure 4-1 was generated by integrating Equations (3.7) and (4.10) over a time span of 150 seconds, using Equations (4.3), (4.11) and (4.12) and the parameter values provided in Table 4-1, for each θ_{togo} , ranging from 1° to 180° . The actual settling time for each response was obtained using the function `lsiminfo` provided in MATLAB's Control System Toolbox, which by default defines the settling time as the time it takes to reach and stay within a settling band of $\pm 2\%$ of the *peak* value, centred on the the steady-state value. This makes it possible to calculate the settling time when the steady-state value is zero, which was in fact the case during the simulations; see $q_{1,c}$, $q_{2,c}$ and $q_{3,c}$ in Table 4-1. The relative difference between the chosen settling time and the actual settling time was calculated by:

$$\delta T_s = \frac{T_{s,\text{actual}}}{T_s} - 1 \quad (4.16)$$

Table 4-1: Parameter values used to generate Figures 4-1 and 4-2.

Parameter	Value	Unit
I_{xx}	6.102	kg m ²
I_{yy}	6.102	kg m ²
I_{zz}	0.608	kg m ²
$\omega_x, \omega_y, \omega_z$	0	rad s ⁻¹
ζ	0.707	-
μ	1	-
e_1, e_2, e_3	0.577	-
$q_{1,c}, q_{2,c}, q_{3,c}$	0	-
$q_{4,c}$	1	-

Observing Figure 4-1, it is clear that the magnitude of δT_s is independent of the chosen settling time. Additional testing confirmed that changing the inertia values or the direction of the eigenaxis does not affect the magnitude of δT_s either. However, δT_s does depend on the eigenangle-to-go and the damping ratio, which implies that the corrective factor that must be applied to Equation (4.15) to effectively address the nonlinearities introduced by $\sin(\theta/2)$ is a function of the eigenangle-to-go and the damping ratio. For the purpose of deriving an appropriate corrective factor specifically for the quaternion-error feedback controller considered in this thesis, for which the damping ratio is given by Equation (4.14), the average of the five plots in Figure 4-1 was calculated and a two-term power series model was fitted to the average data with a nonlinear least squares method. This was done using the function `fit` provided in MATLAB's Curve Fitting Toolbox. The resulting fit is described by:

$$(\delta T_s)_{\zeta=0.707} = 0.0124 \theta_{\text{togo}}^{2.2220} + 0.0551 \quad (4.17)$$

for which $R^2 = 0.99986$ and θ_{togo} is expressed in radians. Equation (4.17) is plotted in Figure 4-1 as a solid curve. It is not entirely clear what causes the baseline 5.5% offset between the chosen settling time and the actual settling time, however it could be due to MATLAB's definition of the settling time, which does not correspond to the definition of the settling time underlying the relation in Equation (4.15). Additional testing revealed that there is a positive relation between the offset and the damping ratio, which breaks down when $\zeta > 0.775$. Regardless of the cause, the offset is accounted for in Equation (4.17), which, when applied as a corrective factor after filling out Equation (4.14) in Equation (4.15), yields the following relation between the natural frequency and the settling time and eigenangle-to-go:

$$\omega_n = \frac{4\sqrt{2}}{T_s} \left(1 + (\delta T_s)_{\zeta=0.707} \right) = \frac{4\sqrt{2}}{T_s} (0.0124 \theta_{\text{togo}}^{2.2220} + 1.0551) \quad (4.18)$$

which holds for a damping ratio of 0.707. Repeating the simulations, using Equation (4.18) to calculate the natural frequency, generates Figure 4-2, from which it can be seen that δT_s is reduced to nearly zero. A sinusoidal-like offset remains, implying that some trigonometric

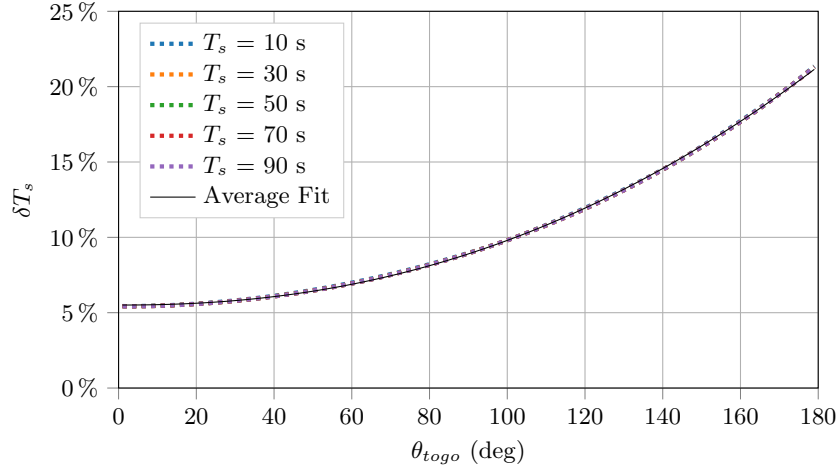


Figure 4-1: Relative difference between the chosen settling time and the actual settling time for q_1 , q_2 and q_3 , plotted against the eigenangle-to-go for a range of different chosen settling times. The damping ratio used is 0.707 and ω_n is calculated with Equation (4.15). The solid curve fits the average of the plots, with $R^2 = 0.99986$.

term must be added to Equation (4.17) in order to fully eliminate δT_s . However, in the context of this thesis, the remaining offset is small enough to consider the correction that is established with Equation (4.17) as sufficient. Finding the actual corrective factor as a function of both θ_{togo} and ζ would however make an interesting topic for future research. Concluding, the gain matrices for the quaternion-error feedback controller are calculated by Equations (4.4) and (4.5), where d and k are respectively calculated by Equations (4.11) and (4.12), and ζ and ω_n are respectively defined by Equation (4.14) and calculated by Equation (4.18).

4-2-3 Verification

In order to verify the correct implementation of Equation (4.2), the control design example as presented in Wie et al. (1989) is reperformed. In the example, an asymmetric rigid spacecraft is considered, characterised by the following inertia tensor:

$$\mathbf{I} = \begin{bmatrix} 1200 & 100 & -200 \\ 100 & 2200 & 300 \\ -200 & 300 & 3100 \end{bmatrix} \text{ kg m}^2 \quad (4.19)$$

Additionally required parameter values are provided in Table 4-2. The response is assumed to be critically damped, hence $\zeta = 1$. Using Equations (4.11) and (4.12), d and k are respectively calculated to be equal to 0.316 and 0.05. Gain matrix \mathbf{D} is defined as:

$$\mathbf{D} = d \cdot \text{diag}(1200, 2200, 3100)$$

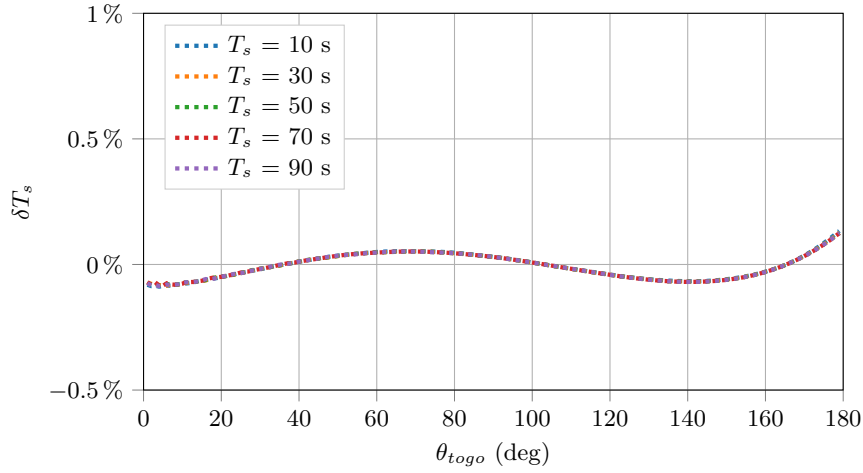


Figure 4-2: Reevaluation of Figure 4-1, where ω_n is calculated with Equation (4.18).

Gain matrix \mathbf{K} is defined in four different ways:

Case 1: $\mathbf{K} = \text{diag}(201, 110, 78)$

Case 2: $\mathbf{K} = \text{diag}(110, 110, 110)$

Case 3: $\mathbf{K} = \text{diag}(72, 110, 204)$

Case 4: $\mathbf{K} = \text{diag}(60, 110, 155)$

Refer to [Wie et al. \(1989\)](#) for details on how these gain matrices were determined. Using Equation (4.3) and the parameter values provided, Equations (3.7) and (3.19) were integrated over a time span of 100 seconds. This process was repeated for each of the aforementioned cases. For reference, the simulation results as presented by [Wie et al. \(1989\)](#) are depicted in Figures 4-3 and 4-5. Reproductions of these figures are presented in Figures 4-4 and 4-6, respectively. Comparing the reproductions to their respective originals, it can be concluded that they match very well. This confirms the successful implementation of Equation (4.2).

Table 4-2: Parameter values used by [Wie et al. \(1989\)](#) to test the performance of their quaternion-error feedback controller in a simulation.

Parameter	Value	Unit
q_1, q_2, q_3	0.57	-
q_4	0.159	-
$\omega_x, \omega_y, \omega_z$	0.01	rad s ⁻¹
ζ	1	-
ω_n	0.158	rad s ⁻¹
μ	0.9	-
$q_{1,c}, q_{2,c}, q_{3,c}$	0	-
$q_{4,c}$	1	-

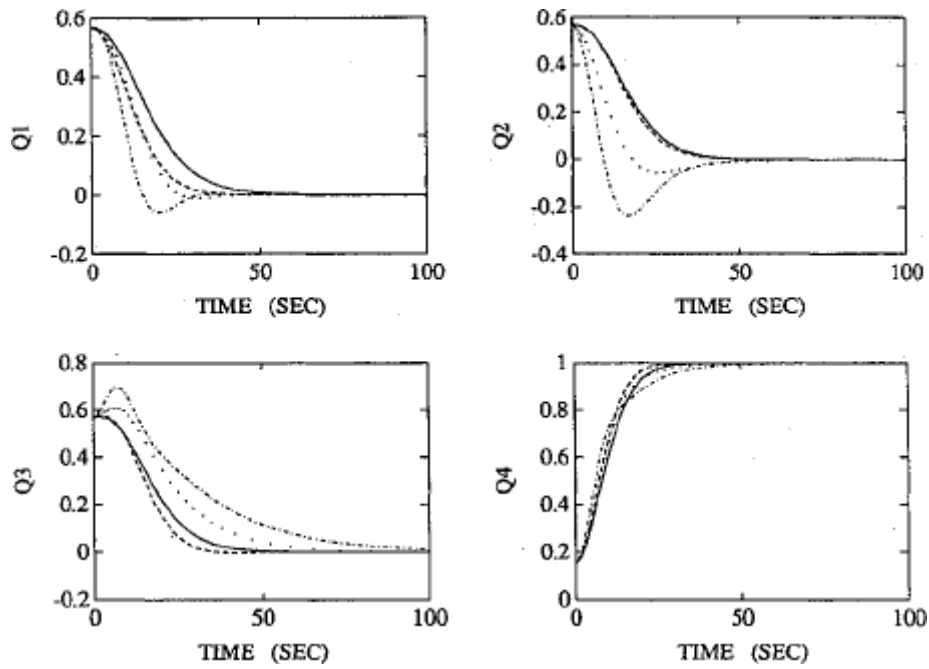


Figure 4-3: Time histories of quaternions as presented in [Wie et al. \(1989\)](#).

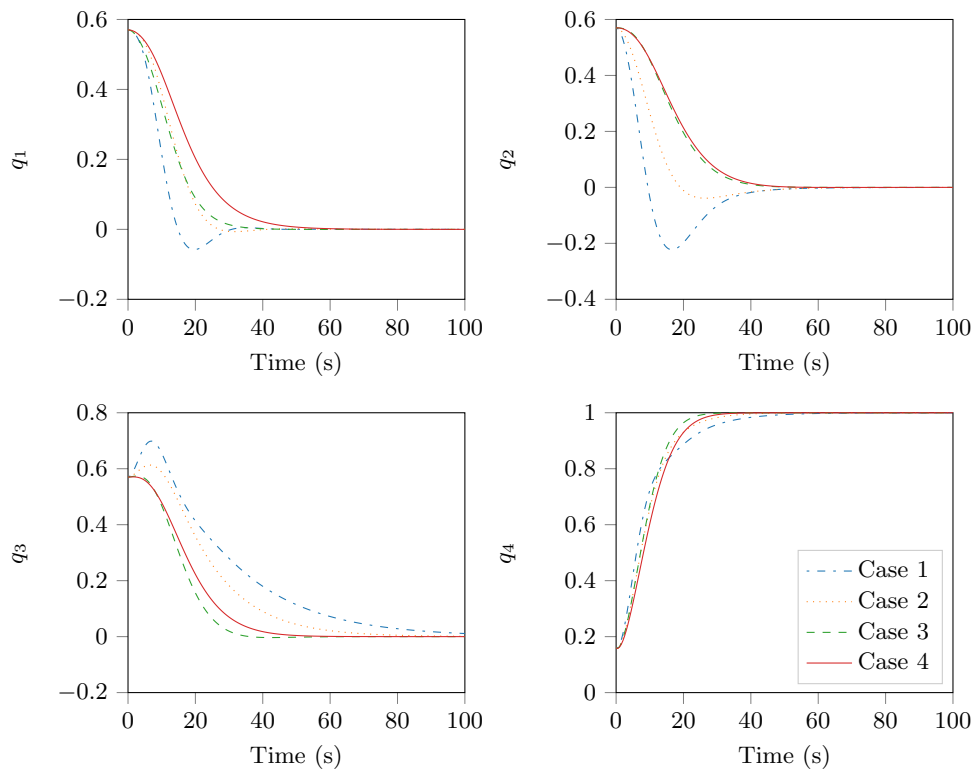


Figure 4-4: Reproduction of [Figure 4-3](#), verifying the correct implementation of [Equation \(4.2\)](#).

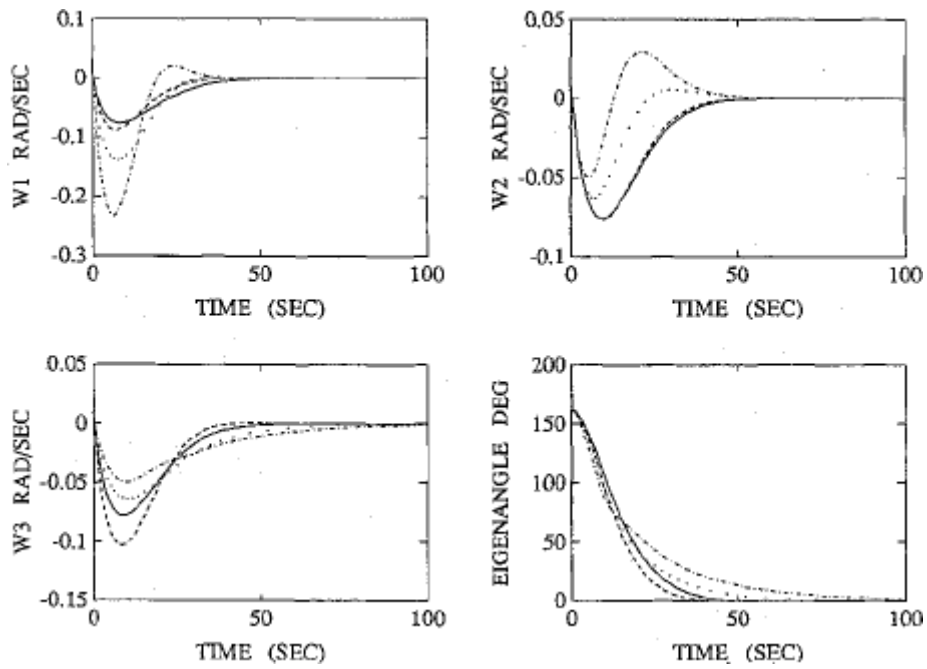


Figure 4-5: Time histories of body rates and eigenangle-to-go as presented in Wie et al. (1989).

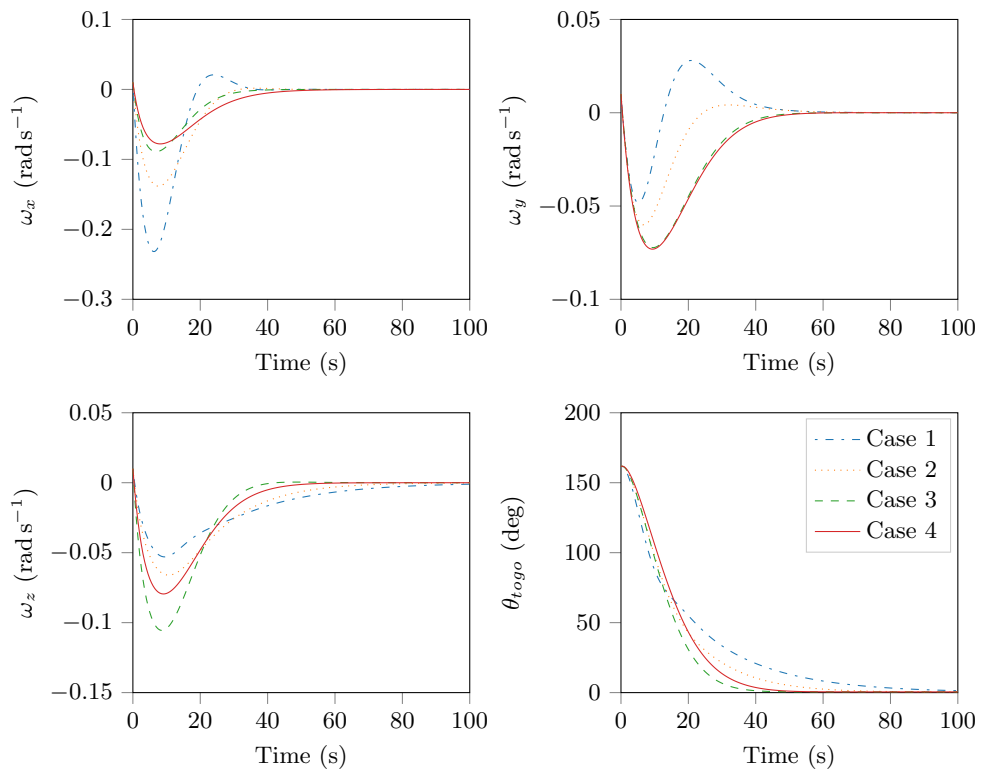


Figure 4-6: Reproduction of Figure 4-5, verifying the correct implementation of Equation (4.2).

4-3 Minor-Axis Spin Manoeuvres

As was explained in Section 1-3, a minor-axis spin manoeuvre involves the consecutive execution of three different rotational manoeuvres: first, a *spin-up manoeuvre* about the minor axis of the spacecraft; second, a *denutation manoeuvre* to remove any nutational angular motion affecting the spin-axis; third and last, a *spin-down manoeuvre*. In the following, the specifics and implementation of the control schemes governing the spin-up and spin-down manoeuvres, and the denutation manoeuvres are covered, respectively in Sections 4-3-1 and 4-3-2.

4-3-1 Spin-Up and Spin-Down Manoeuvres

The control logic for spin-up or spin-down manoeuvres is very simple. Given that the actuators used are *on/off* thrusters, for a spin-up, it is only a matter of activating the thrusters that produce a positive torque about the z_B -axis until the target spin rate is achieved. Conversely, for a spin-down, those thrusters that produce a negative torque about the z_B -axis are activated until the angular velocity enters a so-called *deadband*, which is bounded by a positive and a negative threshold value and centred on the zero line. This deadband is in place to prevent the *chatter* effect, which is explained in Section 4-3-2-1.

Figure 4-7 shows the results of an example spin-up manoeuvre before the DOM, which takes 15.61 seconds to complete, and an example spin-down manoeuvre after the DOM, which is performed in 8.62 seconds. Since the PDM burns about 40 kilograms of solid propellant during the DOM, the MoI about the spin-axis decreases significantly and consequently, the spin-down manoeuvre only needs half the time to complete. In order to verify the numerical results, analytic results are obtained through Equation (5.20), which is first evaluated using $I_s = 1.105 \text{ kg m}^2$ and $M_z = 0.892 \text{ N m}$, giving 15.56 seconds, and then with $I_s = 0.611 \text{ kg m}^2$ and $M_z = 0.892 \text{ N m}$, which yields 8.61 seconds. Comparing the analytic results to the numerical results, it is noted that the latter are slightly larger. This can be explained by the fact that the simulator accounts for varying inertial parameters and torque capabilities during the spin manoeuvres, and Equation (5.20) does not. As such, the correct implementation of the control logic can be confidently confirmed.

4-3-2 Denutation Manoeuvres

Following a spin-up, the spin-axis will inevitably exhibit some degree of *nutaton*, which is explained as a slow rotation – relative to the spin rate – of the spin-axis about the angular momentum vector. Nutation is caused by disturbances transverse to the spin-axis, such as torques emanating from *e.g.*, sloshing propellants or the tip-off between two separating spacecraft. In spaceflight, deliberately induced nutation is generally referred to as *precession* (Wertz, 2005). The angle between the spin-axis and the angular momentum vector is called the nutation angle θ_{nut} , see Figure 4-8, and is calculated by (Wie, 2008):

$$\tan(\theta_{\text{nut}}) = \frac{h_t}{h_z} = \frac{\sqrt{h_x^2 + h_y^2}}{h_z} = \frac{\sqrt{I_{xx}^2 \omega_x^2 + I_{yy}^2 \omega_y^2}}{I_{zz} \omega_z} \quad (4.20)$$

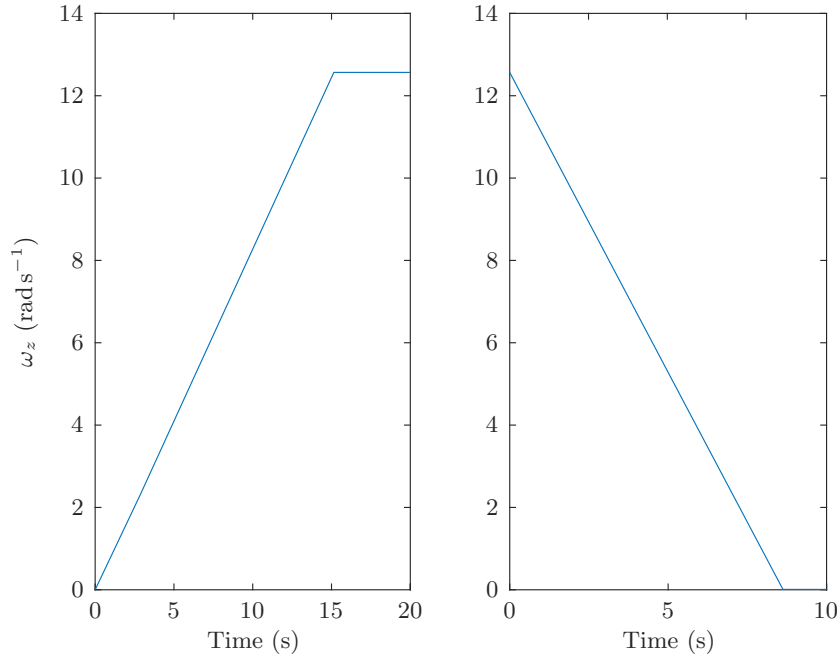


Figure 4-7: Results of an example spin-up manoeuvre before the DOM (left), for which the target spin rate is assumed to be 4π rad s⁻¹, and an example spin-down manoeuvre after the DOM (right).

where:

$$\mathbf{h} = [h_x, h_y, h_z]^T$$

is the angular momentum vector expressed in the B -frame, and:

$$\mathbf{h}_t = [h_x, h_y]^T$$

is the *transverse* angular momentum vector, implying that h_z is directed along the spin-axis, see Figure 4-8. In order to reduce the nutation angle, the transverse angular momentum must be counteracted by a control torque, which is most effectively applied when both vectors are aligned and opposite to each other. As such, an adequate control logic for denutation ensures the actuators are active precisely at that time. When the actuators used are *on/off* thrusters, the control logic should arrange for the finite pulse width to be *centred* on the instant of opposite alignment of the aforementioned vectors. In Section 4-3-2-1, a control logic that achieves just that is described. Then in Section 4-3-2-2, a strategy to determine the optimal width of a thruster pulse is developed. Lastly, in Section 4-3-2-3, the successful implementation of the control logic and the pulse width determination strategy is verified.

4-3-2-1 Control Logic

For the denutation manoeuvres, the control logic as developed by Devey et al. (1977) is implemented and extended. In order to schedule the thruster pulses, the control logic utilises

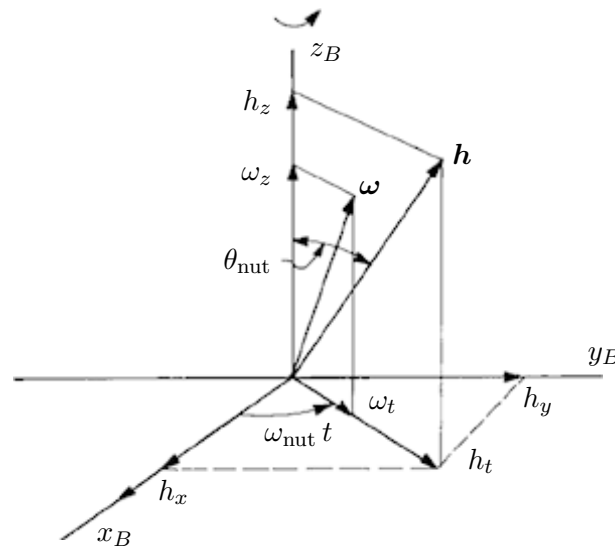


Figure 4-8: The angular momentum vector \mathbf{h} in B -frame coordinates. The original image is credited to [Hrastar \(1974\)](#).

the response of the sensors that are in place to measure the components of the *transverse angular rate vector*, which – notably – are collinear with the components of the transverse angular momentum vector. This implies that thruster pulses must be applied around the peak of the sensor signal, *i.e.*, the peak of the transverse angular rate component as measured by the sensor. In Figure 4-9, this timing strategy is visualised.

The control logic works by virtue of two detectors: one to detect when the signal exceeds a certain threshold and one to detect a subsequent zero crossing. Following the zero crossing, a timer is activated to fire the thruster(s) of concern exactly at that point in time such that the pulse is centred on the peak of signal. This process is repeated until the signal settles below said threshold. For a visualisation of this process, review Figure 4-9. The control logic is depicted in Figure 4-10.

Ideally, the denutation manoeuvre reduces the transverse angular rate, *i.e.*, the nutation angle to down to zero. However, setting such an objective for the controller would be impractical, as the minimum impulse bit that is delivered by a thruster (or a configuration of thrusters) is finite. This means that at one point during the denutation process, the shortest thruster pulse would impart a change in transverse angular rate more than twice as large as the excess rate to be reduced to zero, consequently generating a greater excess rate in the opposite direction. In response, the controller would try to compensate for the overshoot by commanding a counter pulse, causing the signal to again cross the zero line, again requiring compensation. This undesired phenomenon would continue indefinitely if not interrupted and is referred to as *chatter*, which in the case of a thruster-controlled spacecraft can lead to a great waste of propellant. To prevent the chatter effect, a so-called *deadband* is defined, which is bounded by the positive and negative threshold value and thus centred on the zero line. When the signal remains within this deadband, no control action is taken. In order to determine the minimum threshold value for the transverse angular rate, first the minimum allowable threshold value

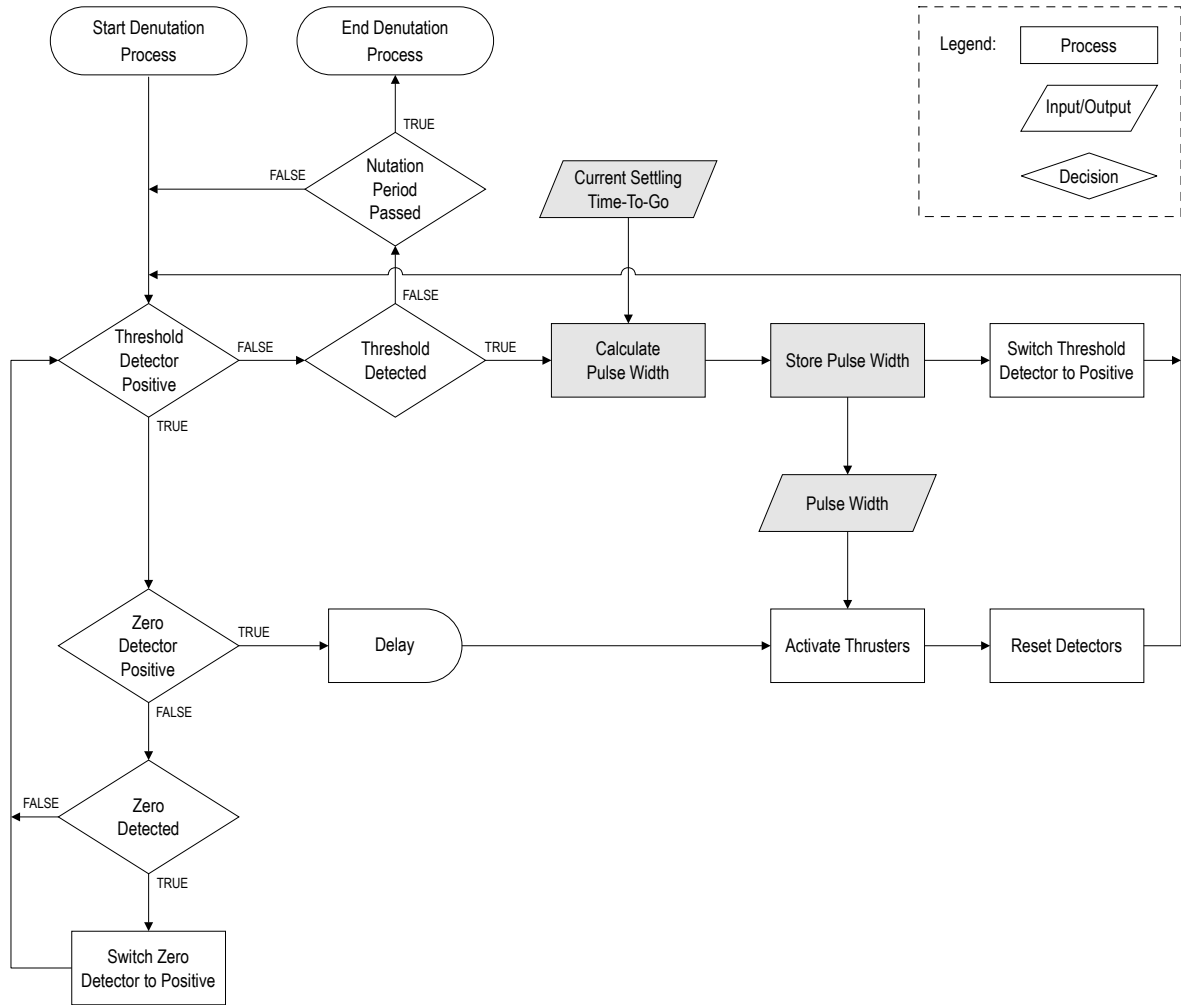


Figure 4-10: Control logic for the denutation manoeuvres. The colourless elements constitute the original logic as developed by [Devey et al. \(1977\)](#). The grey-shaded elements represent an extension to this logic.

For the x -component, the parameters associated with the y -axis in Equation (4.25) should be modified accordingly. Equation (4.25) provides the first of three key parameters to be tuned for the control logic, given the spin rate and the physical characteristics and transverse torque capabilities of the spacecraft. The second key parameter is the delay time t_d following a zero crossing, calculated by ([Devey et al., 1977](#)):

$$t_d = \frac{N}{4} T_{\text{nut}} - \frac{1}{2} \Delta t_p \quad (4.26)$$

where $N = 1$ for two thruster pulses, and $N = 3$ for only one thruster pulse per nutation

period, T_{nut} , which is calculated by:

$$T_{\text{nut}} = \frac{2\pi}{\omega_{\text{nut}}} \quad (4.27)$$

The pulse width Δt_p represents the third key parameter to be tuned. Two different strategies to determine the pulse width were encountered in the literature. The first strategy, described by Devey et al. (1977), entails selecting the pulse width heuristically and keeping it constant throughout the control process. A second, more commonly employed strategy does not entail selecting or calculating a pulse width, but rather activating the thruster(s) immediately after the signal crosses the threshold and maintaining the pulse until the signal re-enters the deadband, see *e.g.*, Grasshoff (1968); Hrastar (1974); Webster (1985); Sidi (1997). This second strategy thus ensures the nutational angular motion is damped fastest. However, when a certain amount of time is allocated to the control process, and the goal is not necessarily to reduce the nutation angle as fast as possible, it is not an optimal strategy in terms of propellant usage. It is hence concluded that, although both strategies have proven to work satisfactorily for the purpose intended, they lack the necessary refinement. For this reason, a new pulse width determination strategy is developed in Section 4-3-2-2.

4-3-2-2 Pulse Width Determination

Thruster pulses fired to denutate the spin-axis are most effective, *i.e.*, efficient, when delivered closest to the peak of a transverse angular rate component. As such, the optimal pulse width is as small as possible. Naturally, applying only minimum width pulses would be most efficient, however would also result in an – for most cases – undesirably long acquisition time. To limit the duration of a denutation manoeuvre, a new parameter, the *settling time-to-go* is introduced: $T_{s, \text{togo}}$. The total number of thruster pulses, n , that can be fired within the time period spanned by $T_{s, \text{togo}}$ depends on the length of the nutation period, T_{nut} , and the desired number of thruster pulses applied during one nutation period, as follows:

$$n = \left\lfloor \left(\frac{5}{2} - \frac{1}{2} N \right) \left(\frac{T_{s, \text{togo}}}{T_{\text{nut}}} \right) \right\rfloor \quad (4.28)$$

where $\lfloor \dots \rfloor$ denotes the *floor function*, which effectively ensures all thruster pulses are fired before $T_{s, \text{togo}}$ runs out. In the following, it is without loss of generality assumed that the transverse axis of concern is the y_B -axis. As such, the total transverse angular rate to be reduced $\Delta\omega_{y, \text{togo}}$ is defined as the difference between the peak value $\omega_{y, \text{peak}}$ and the threshold value $\omega_{y, \text{threshold}}$:

$$\Delta\omega_{y, \text{togo}} = \omega_{y, \text{peak}} - \omega_{y, \text{threshold}} \quad (4.29)$$

The peak, or maximum value of the transverse angular rate of concern can be calculated using the components of the current angular velocity vector and the MoI of the spacecraft. To this end, the momentary rotational motion of the spacecraft is assumed to be *torque-free*. For a

rigid body in torque-free rotational motion it holds that the angular momentum as well as the rotational kinetic energy are constant (*e.g.*, Wie, 2008). As such:

$$h^2 = (I_{xx} \omega_x)^2 + (I_{yy} \omega_y)^2 + (I_{zz} \omega_z)^2 = \text{constant} \quad (4.30)$$

$$2E_{\text{rot}} = I_{xx} \omega_x^2 + I_{yy} \omega_y^2 + I_{zz} \omega_z^2 = \text{constant} \quad (4.31)$$

Equations (4.30) and (4.31) can also be written as, respectively (Wie, 2008):

$$\frac{\omega_x^2}{(h I_{xx}^{-1})^2} + \frac{\omega_y^2}{(h I_{yy}^{-1})^2} + \frac{\omega_z^2}{(h I_{zz}^{-1})^2} = 1 \quad (4.32)$$

$$\frac{\omega_x^2}{(2E_{\text{rot}} I_{xx}^{-1})} + \frac{\omega_y^2}{(2E_{\text{rot}} I_{yy}^{-1})} + \frac{\omega_z^2}{(2E_{\text{rot}} I_{zz}^{-1})} = 1 \quad (4.33)$$

Equations (4.32) and (4.33) have the same structure as the equation to describe an *ellipsoid*, which implies geometrically that the angular velocity vector must lie on the intersection between the surfaces of the *angular momentum ellipsoid* and the *kinetic energy ellipsoid*. This intersecting curve is also referred to as a *polhode*. Using Equations (4.32) and (4.33), Wie (2008) derives the *polhode equation*:

$$I_{xx} (I_{xx} - J^*) \omega_x^2 + I_{yy} (I_{yy} - J^*) \omega_y^2 + I_{zz} (I_{zz} - J^*) \omega_z^2 = 0 \quad (4.34)$$

where J^* is an auxiliary constant parameter, defined combining Equations (4.30) and (4.31):

$$J^* \equiv \frac{h^2}{2E_{\text{rot}}} = \frac{(I_{xx} \omega_x)^2 + (I_{yy} \omega_y)^2 + (I_{zz} \omega_z)^2}{I_{xx} \omega_x^2 + I_{yy} \omega_y^2 + I_{zz} \omega_z^2} \quad (4.35)$$

Now assuming that $\omega_x = 0$, Equation (4.34) can be rearranged to solve for the peak of the transverse angular rate about the y_B -axis, as follows:

$$\omega_{y, \text{peak}} = \omega_z \sqrt{\frac{I_{zz} (J^* - I_{zz})}{I_{yy} (I_{yy} - J^*)}} \quad (4.36)$$

Note that in order to calculate the peak of the transverse angular rate about the x_B -axis, I_{yy} in Equation (4.36) should be replaced by I_{xx} . The threshold value for the transverse angular rate of concern, representing the second term on the right-hand side of Equation (4.29), can be obtained through Equation (4.25), given a threshold value for the nutation angle. Then using the results of Equations (4.28) and (4.29), it is possible to calculate the change in transverse angular rate each thruster pulse must bring about:

$$\Delta\omega_y = \frac{\Delta\omega_{y, \text{togo}}}{n} \quad (4.37)$$

The change in transverse angular rate is related to the thruster pulse width through the following expression (Devey et al., 1977):

$$\Delta\omega_y = \frac{2 M_y}{I_{yy} \omega_{\text{nut}}} \sin\left(\frac{\omega_{\text{nut}} \Delta t_{p,y}}{2}\right) \quad (4.38)$$

Now equating Equation (4.37) to Equation (4.38), and solving for $\Delta t_{p,y}$, yields:

$$\Delta t_{p,y} = \frac{2}{\omega_{\text{nut}}} \sin^{-1}\left(\frac{I_{yy} \omega_{\text{nut}}}{2 M_y} \frac{\Delta\omega_{y,\text{togo}}}{n}\right) \quad (4.39)$$

for which it holds that:

$$\Delta t_{p,\min} \leq \Delta t_{p,y} \leq \Delta t_{p,\max} \quad (4.40)$$

where $\Delta t_{p,\max}$ is the time interval between two threshold crossings, see Figure 4-9. The practical implications of the saturation constraint defined in Equation (4.40) entail that for a calculated pulse width smaller than the minimum pulse width, no control actions are taken, and for a calculated pulse width larger than the maximum pulse width, the thrusters will be fired for the duration of the maximum pulse width.

In the foregoing, control solely about one of the transverse axes (that is: the y_B -axis) was considered. When the spacecraft has torque capabilities about both transverse axes, using them in tandem can enhance either the accuracy or the efficiency of the denutation manoeuvre, depending on how the transverse torque capabilities relate to each other. In this respect, two cases are distinguished:

- **Case 1: $M_x > M_y$ or $M_y > M_x$.** When the torque capabilities about one transverse axis are greater than about the other, two different minimum deadbands can be defined. The minimum deadband for the angular rate about the transverse axis associated with the smallest torque capabilities is narrower, as the minimum angular impulse bit is smaller. This implies that better accuracy can be achieved, *i.e.*, the nutation angle can reach closer to zero. However, it is only efficient to apply the smaller torques when the peak of the signal is located within the other minimum deadband, that is, the one defined for the angular rate about the transverse axis associated with the largest torque capabilities (assuming the thrusters are of the same type). Outside this latter deadband, the larger torques will first be applied to reduce the transverse angular rate. In the special case of the PDM, where the same number of thrusters (that is: two) is used to generate both the smaller and the larger torques, it is, in addition, only efficient to use minimum width pulses when using the smaller torques to further decrease the peak of the transverse angular rate from the outer to the inner threshold. To enable the use of only minimum width pulses, the time period that is spanned by the initial settling time-to-go is split into two sub-periods, of which the latter is of sufficient length to accommodate the number of minimum width pulses needed to fulfil the objective. The first sub-period is then reserved for any pulses needed to first attenuate the transverse

angular rate towards the outer threshold, using the larger torques. As such, both torque capabilities are leveraged consecutively. In case the larger torques are indeed needed, the length of the first sub-period must be at least as long as one nutation period. If this in turn leads to a second sub-period of insufficient length to enable the use of only minimum width pulses, the widths of the pulses fired during this period will be slightly enlarged, so that the objective may still be met.

- **Case 2:** $M_x \approx M_y$. When the torque capabilities about the transverse axes are equal or approximately equal (that is: the relative difference between them is no larger than a certain predefined value), both can be applied in an alternating fashion. As such, the maximum amount of thruster pulses that can be fired during one nutation period is doubled to four. This implies that for a given settling time-to-go, the widths of the thruster pulses can be reduced, consequently improving the efficiency of the denutation manoeuvre.

Considering the PDM has torque capabilities about both transverse axes (see Section 2-4), and their relation to one another can be classified as a Case 1 relation, the general pulse width determination strategy as described above is implemented in conjunction with the dual-axis control strategy as described for Case 1 relations, and incorporated as an extension to the original control logic, see Figure 4-10. The algorithm will recalculate n and $\Delta\omega_{y, \text{togo}}$ or $\Delta\omega_{x, \text{togo}}$ using the current state, moments of inertia and settling time-to-go, at each threshold crossing for $N = 1$, or each *second* threshold crossing for $N = 3$. Then, based on these newly acquired parameters and the momentary torque capabilities, $\Delta t_{p, y}$ or $\Delta t_{p, x}$ will be calculated. As such, the control logic is fully adaptive. If after $T_{s, \text{togo}} = 0$, the amount of time allocated to the denutation manoeuvre has not fully elapsed (for instance because the initial settling time-to-go was not set equal to the allocated amount of time), the mission manager (see Figure 5-1) will redefine the settling time-to-go to be equal to the remaining time, so that any transverse disturbances that might arise during this period will still be counteracted.

4-3-2-3 Verification

The correct implementation of the original, fixed-pulse-width control logic is verified in an exercise to reproduce the simulation results as presented by Devey et al. (1977), see Figures 4-11 and 4-13. To this end, new simulations are carried out using the exact same initial parameter values as used by Devey et al. (1977), see Table 4-3. The results of these simulations are depicted in Figures 4-12 and 4-14. Comparing these figures to their respective originals, it can be seen that they are fully identical, except for the plots representing the transverse angular rate and acceleration about the y_B -axis. In the original figures, these plots run in the exact opposite direction as compared to those in the reproductions. However, when plotting the analytic results for ω_x and ω_y , obtained through evaluation of the following equations describing the torque-free motion of a spinning body (Devey et al., 1977):

$$\omega_x(t) = \omega_{x,0} \cos(\omega_{\text{nut}} t) \quad (4.41)$$

Table 4-3: Parameter values used by Devey et al. (1977) to test the performance of their nutation control logic in a simulation.

Parameter	Value	Unit
I_{xx}	205	kg m ²
I_{yy}	195	kg m ²
I_{zz}	185	kg m ²
ω_x	0.1	rad s ⁻¹
ω_y	0	rad s ⁻¹
ω_z	6.283	rad s ⁻¹
M_y	15	N m
Δt	0.140	s
$\theta_{\text{nut, thres}}$	0.2	deg
N	3	-

$$\omega_y(t) = -\omega_{x,0} \sqrt{\left(\frac{\omega_{\text{nut},y}}{\omega_{\text{nut},x}}\right)} \sin(\omega_{\text{nut}} t) \quad (4.42)$$

where $\omega_{x,0}$ is the angular rate about the x_B -axis at zero time, it can be observed that the analytic results actually agree with the numerical results acquired for the torque-free part of the simulations, see Figure 4-15. As such, it appears that the respective plots in the original figures were erroneously printed, leading to the conclusion that the original control logic was indeed correctly implemented.

The general pulse width determination strategy as developed in Section 4-3-2-2 is verified through numerical simulation, using the initial parameter values provided in Table 4-3, except for – of course – Δt . For a range of different initial settling times-to-go, the responses for ω_y and θ_{nut} were numerically obtained and plotted in Figure 4-16. As can be seen from the top plot, the responses for ω_y settle neatly within the deadband bounded by ± 0.02 rad s⁻¹ thresholds (corresponding to $\theta_{\text{nut, thres}} = 0.2$ deg), only slightly before the time periods spanned by their respective initial settling times-to-go have elapsed. This ‘premature’ settling is directly attributed to the fact that the calculated total number of thruster pulses is floored in Equation (4.28), and is intended.

Verification of the dual-axis control strategy as described for Case 1 relations between transverse torque capabilities is also done through numerical simulation, albeit using the initial parameter values provided in Table 4-4. The MoI and transverse torque capabilities listed in Table 4-4 are associated with a maximally loaded PDM, see also Section 2-4. The spin rate is equal to 4π rad s⁻¹ and the initial transverse angular rate about the x_B -axis is assumed to be 0.1 rad s⁻¹. Furthermore, the minimum allowable pulse width is 20 milliseconds and the initial settling time-to-go is chosen to be 10 seconds. Finally, the desired number of thruster pulses applied during one nutation period is 2, hence $N = 1$. Plots of the simulation results are depicted in Figure 4-17, from which a number of observations can be made. Firstly, it can be seen that the response for ω_x settles after about 6 seconds within a deadband bounded

Table 4-4: Parameter values for testing the dual-axis control strategy as described for Case 1 relations between transverse torque capabilities, see Section 4-3-2-2.

Parameter	Value	Unit
I_{xx}	6.102	kg m ²
I_{yy}	6.102	kg m ²
I_{zz}	0.608	kg m ²
ω_x	0.1	rad s ⁻¹
ω_y	0	rad s ⁻¹
ω_z	12.566	rad s ⁻¹
M_x	2.137	N m
M_y	0.154	N m
$\Delta t_{p, \min}$	0.02	s
$T_{s, \text{togo}}$	10	s
N	1	-

by $\pm 0.007 \text{ rad s}^{-1}$ thresholds. Secondly, in a similar fashion, the ω_y response settles within a deadband bounded by $\pm 5 \times 10^{-4} \text{ rad s}^{-1}$ thresholds in slightly less than 10 seconds – the chosen initial settling time-to-go. Both thresholds were calculated using Equation (4.25). Thirdly, the response for θ_{nut} is seen not to oscillate, as opposed to what is seen in *e.g.*, Figures 4-11, 4-12 and 4-16. This is due to the symmetry of the PDM around the z_B -axis, which renders I_{xx} equal to I_{yy} . Any inequality between the transverse MoI will lead to an oscillating nutation angle. Fourthly, and last, the bottom plot shows that the first pulse is delivered only after about 2.5 seconds, despite it being preceded by multiple threshold crossings. The reason for this is that, apparently, only 13 minimum width pulses are needed about x_B -axis – the transverse axis associated with the largest torque capabilities – to reduce the peak of ω_x to below its threshold. To execute this series of thruster pulses, about 3.5 seconds suffice, which is 2.5 seconds shy of the total of 6 seconds allotted to the first sub-period, see Section 4-3-2-2. Consequently, during the first 2.5 seconds of the denutation manoeuvre, the pulse widths calculated are smaller than the minimum allowable pulse width. Therefore, the controller initially refrains from taking action, which, as a matter of fact, nicely illustrates the effect of the saturation constraint defined in Equation (4.40).

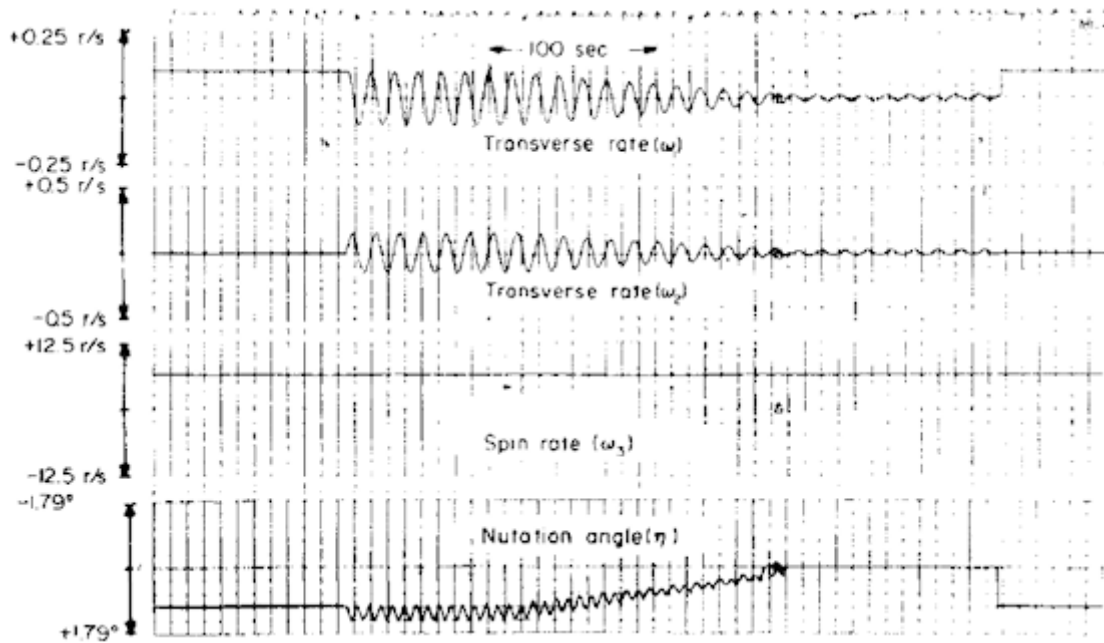


Figure 4-11: Time histories of the body rates and the nutation angle as presented in [Devey et al. \(1977\)](#). The original image is of poor quality.

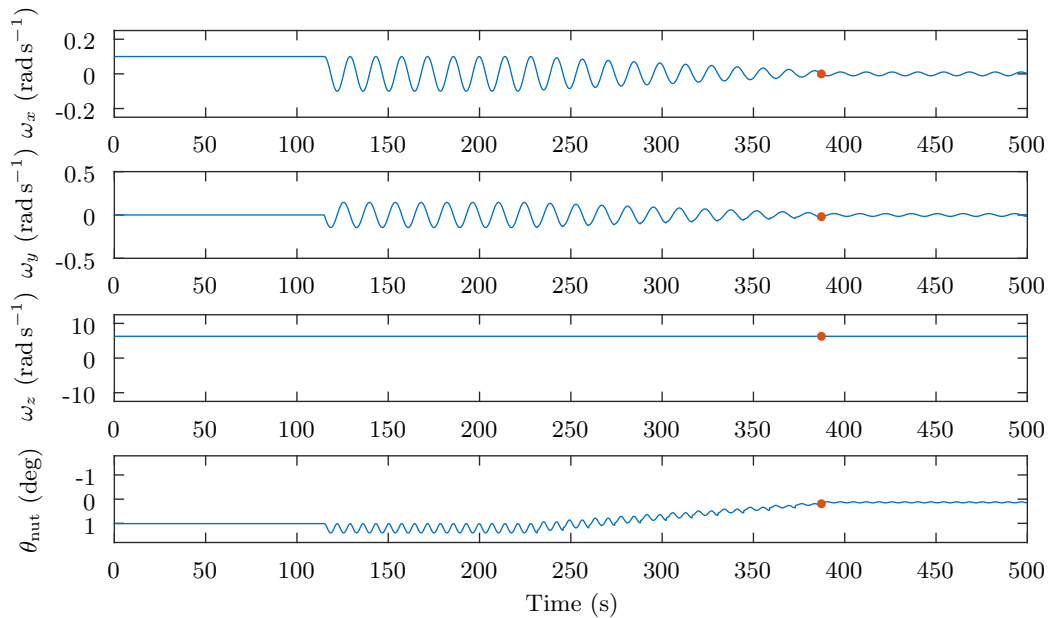


Figure 4-12: Reproduction of [Figure 4-11](#), verifying the correct implementation of the original control logic. The thick dot indicates when ω_y settles below the threshold value.

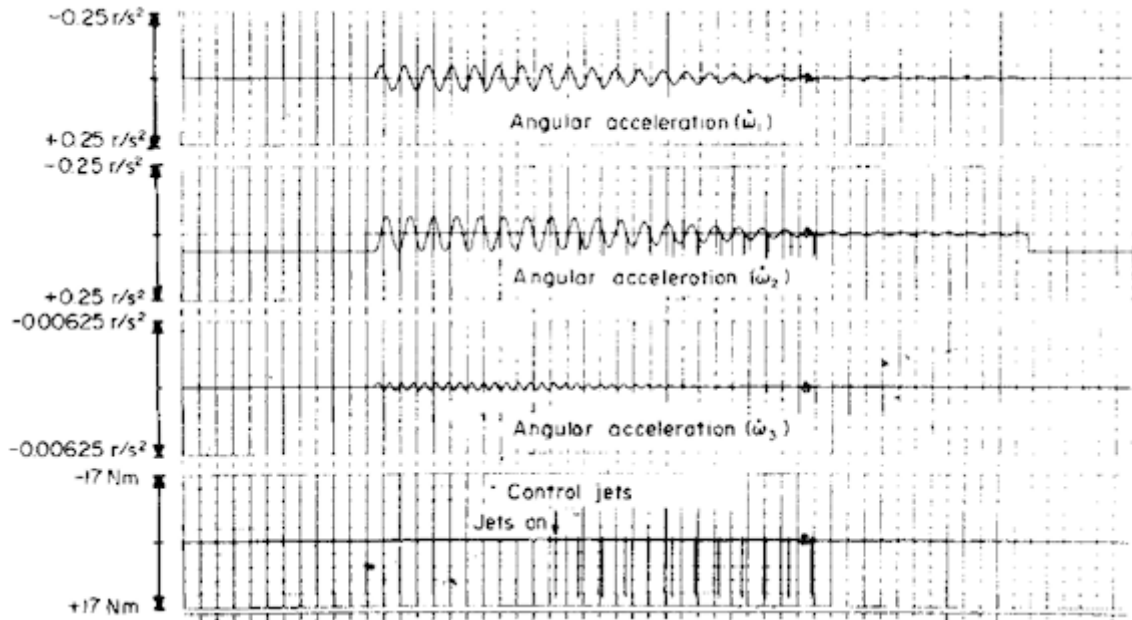


Figure 4-13: Time histories of the angular accelerations and the control torque about the y_B -axis as presented in [Devey et al. \(1977\)](#). The original image is of poor quality.

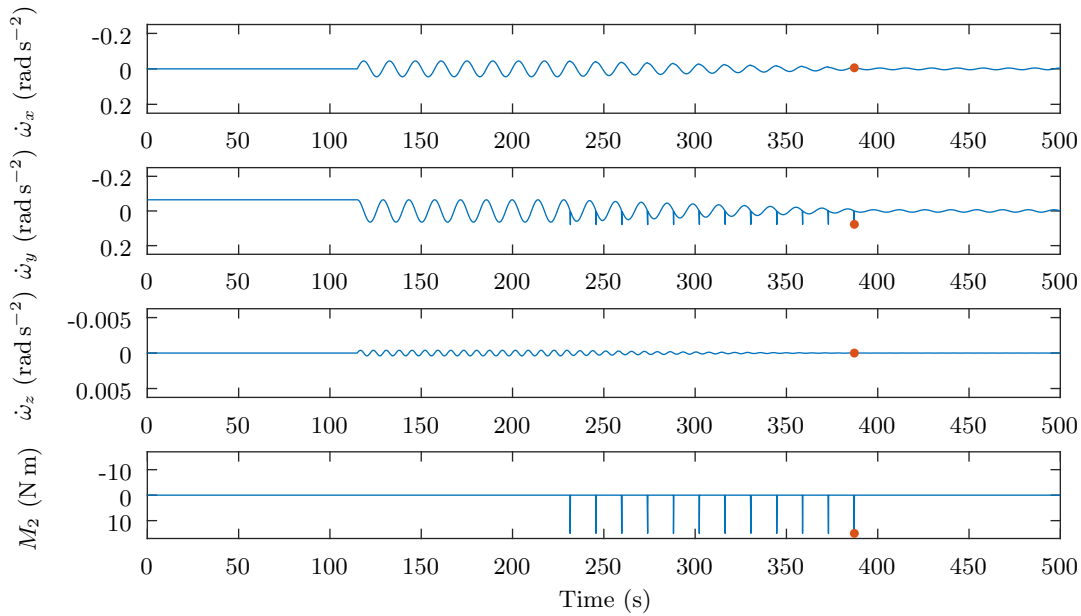


Figure 4-14: Reproduction of [Figure 4-13](#), verifying the correct implementation of the original control logic. The thick dot indicates when ω_y settles below the threshold value.

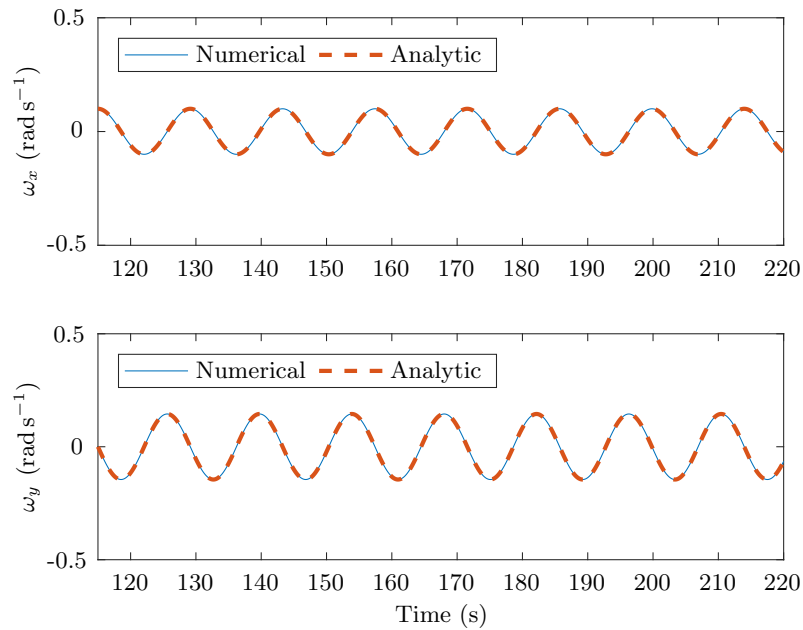


Figure 4-15: Numerical and analytic results for ω_x and ω_y during the torque-free part of the simulations.

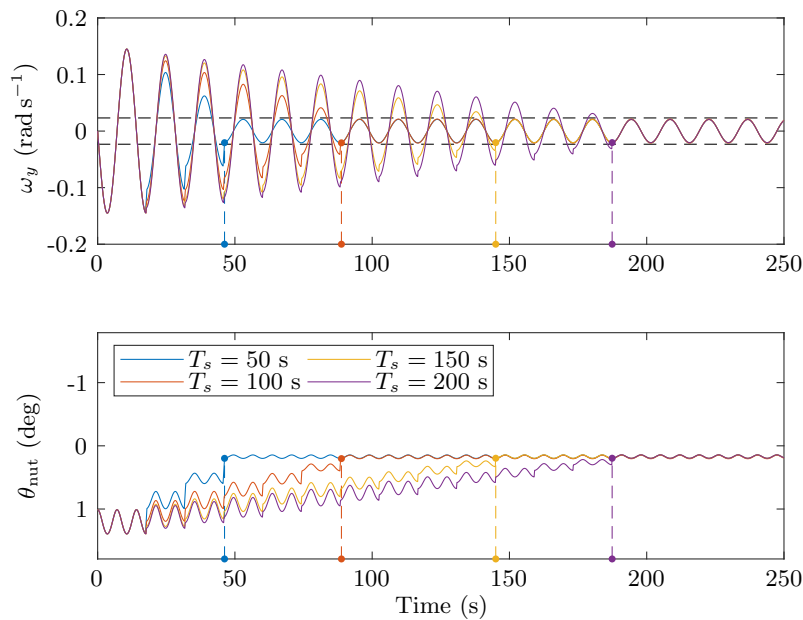


Figure 4-16: Time histories of ω_y and θ_{nut} for a range of different initial settling times-to-go. The actual settling times indicated. The dashed lines in the top plot designate the deadband.

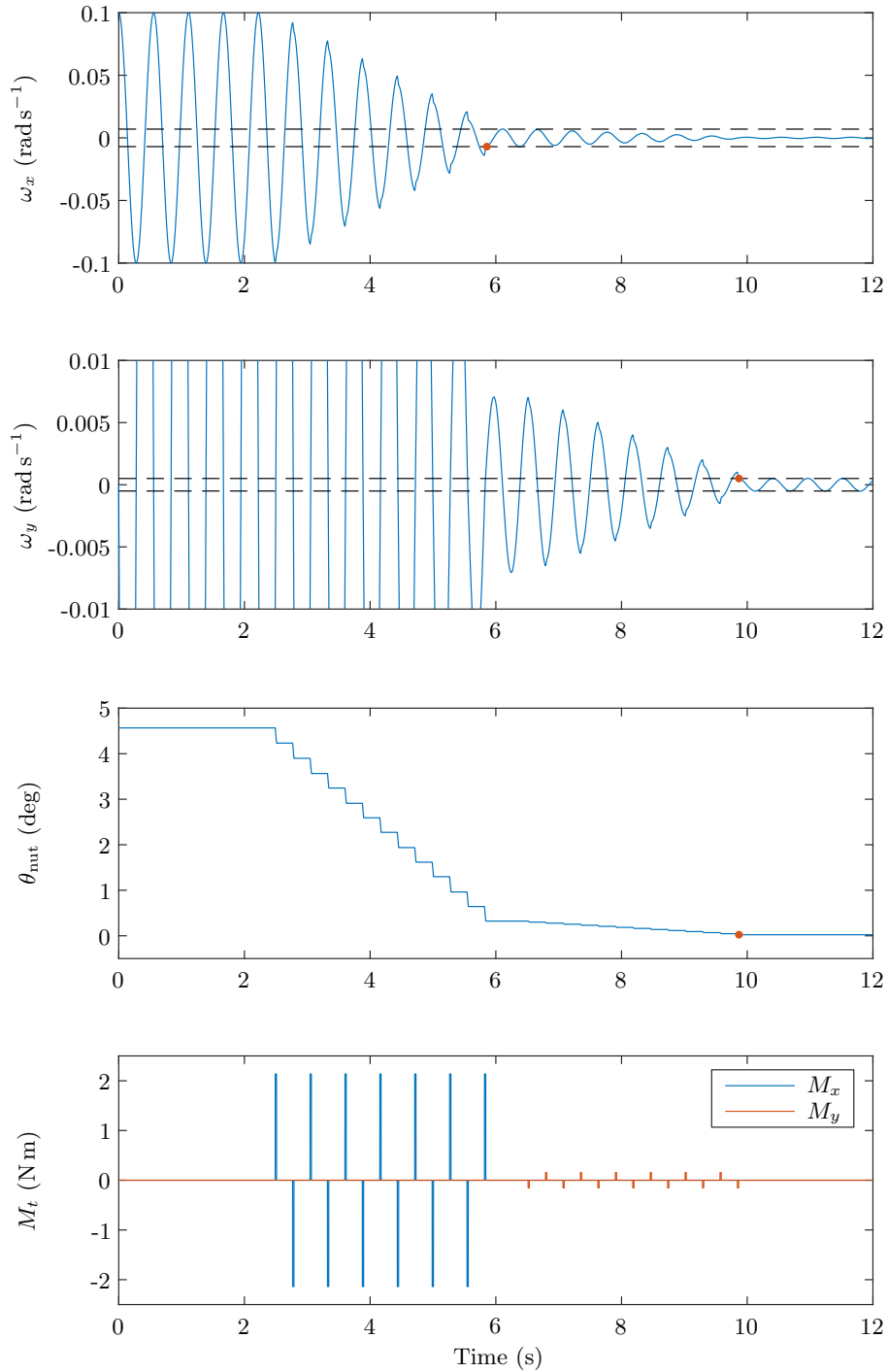


Figure 4-17: Example time histories of ω_x , ω_y , θ_{nut} and the transverse control torque M_t , associated with the dual-axis controlled denutation process of a spinning, maximally loaded PDM.

Mission Manager Logic

The overarching logic deciding which target state is fed to the controller and which control mode is active is called the *mission manager*. The underlying decision-making process operates on the basis of time-tagged *control phases*, which, along with the various control modes, are defined in Section 5-1. Then, in Section 5-2, target states are formulated for each control phase.

5-1 Control Phases and Control Modes

The second phase of the descent scenario as delineated in Section 1-2-3, tabulated in Table 1-1 and illustrated in Figure 1-3 can be broken down into sub-phases related to the activity of the controller. As such, these sub-phases are referred to as *control phases*. The following eight consecutive control phases can be identified:

1. **Initialisation phase.** The controller is initialised and fed with the initial state and the target state. In case of any deviations, the controller will command the actuations required to attain the target state. Note that this phase is actually artificial, as in reality, it will be preceded by the first phase of the descent scenario, for which the controller will already have been initialised. This control phase is defined here only for the purpose of initiating the control process.
2. **Pre-de-orbit manoeuvre spin-up phase.** The controller receives the current state and target spin rate to initiate a spin-up about the symmetry axis, in anticipation of the de-orbit manoeuvre. After the spin-up, the controller will actively suppress any nutation affecting the spin-axis, until the timer triggers the next phase.
3. **De-orbit manoeuvre phase.** The SRM is ignited and the PDM will lose its orbital velocity entirely. As the PDM is spin-stabilised during the de-orbit manoeuvre, which will occur in an *open loop* manner, the controller is idle.

4. **Post-de-orbit manoeuvre spin-down and reorientation phase.** Following the de-orbit manoeuvre, the PDM will free-fall vertically towards the surface. The controller will generate commands to denutate and spin-down the PDM, after which it will redirect the PDM to align the symmetry axis with the local vertical.
5. **Pre-penetrator release spin-up phase.** Similar to Control Phase 2, the controller initiates a spin-up, albeit in anticipation of the release of the penetrator. Likewise, following the spin-up, the controller will actively suppress any nutation affecting the spin-axis, until the timer triggers the next phase.
6. **Penetrator release phase.** The release mechanism is activated, pushing the penetrator away from the PDS. The release is followed by a predefined period of drift. During this phase, the controller is idle.
7. **Pre-fly-away manoeuvre spin-down and reorientation phase.** Similar to Control Phase 4, the controller will sequentially denutate, spin-down and slew the PDM to align the symmetry axis with the local horizontal.
8. **Fly-away manoeuvre phase.** All four thrusters will be activated in an open loop manner to perform a final translational manoeuvre. The thrusters will remain active until the propellant tank is depleted. No attitude control is required.

From the control phase definitions provided above and from Section 1-3, the following four modes of operation, or *control modes*, can be identified for the PDM:

1. **Reorientation mode.**
2. **Spin-up mode.**
3. **Denutation mode.**
4. **Spin-down mode.**

Table 5-1 summarises the nominal controller activity anticipated for each control phase. The full control process executed during the second phase of the descent scenario of the PDM is visualised in Figure 5-1, providing the control phase and mode switch logic, *i.e.*, the mission manager logic.

5-2 Target States and Control Setpoints

The target states transmitted to the controller during Control Phases 1, 2, 4, 5 and 7 (see Figure 5-1) are each comprised of seven target values, or *setpoints* – one for each variable in the rotational state vector, see Equation (3.5). In Section 5-2-1, the target spin rates for Control Phases 2 and 5 are determined. In Section 5-2-2, the target orientations for Control Phases 1, 4 and 7 are parameterised. Finally, in Section 5-2-3, an overview of the defined target states is provided.

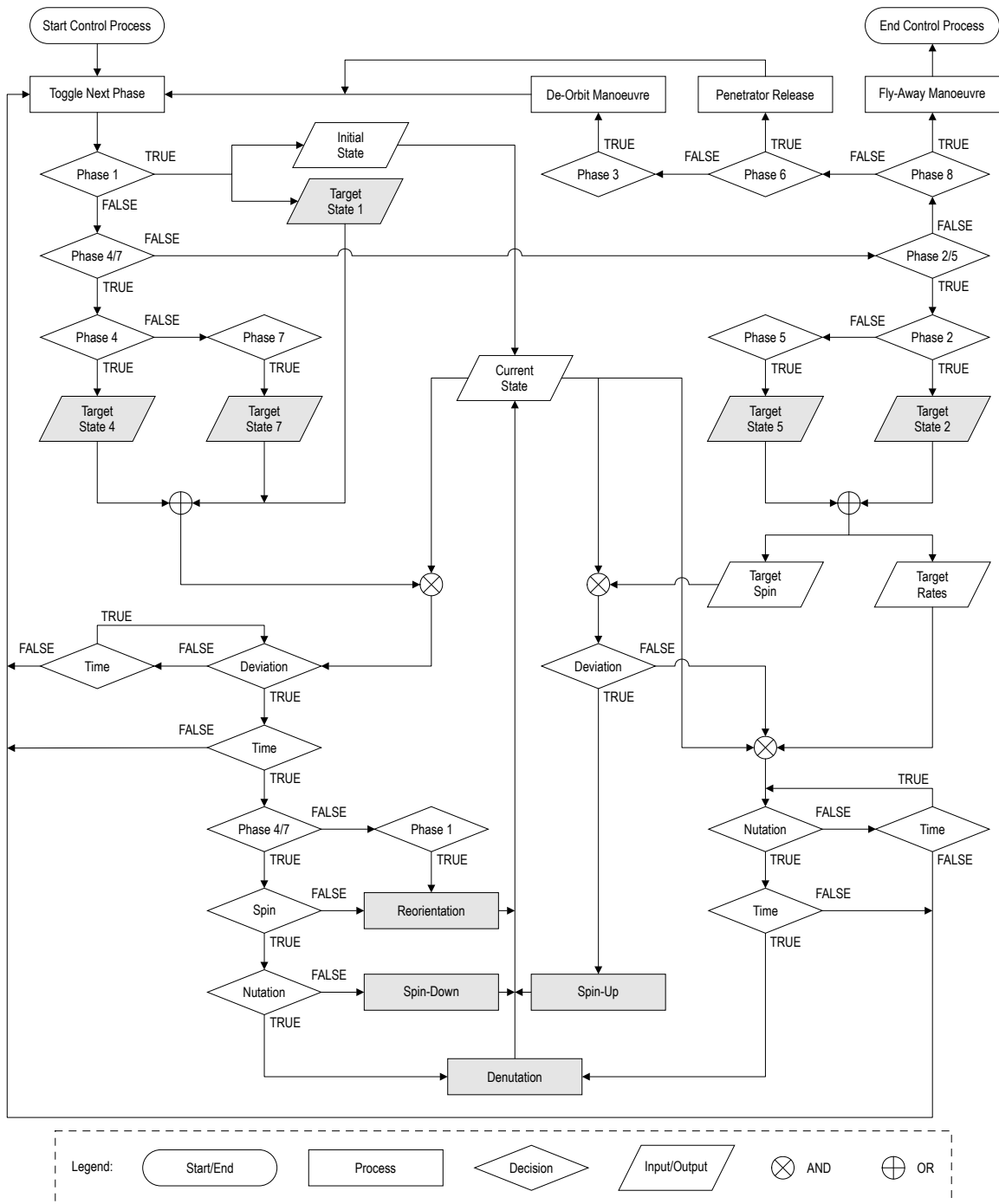


Figure 5-1: Mission manager logic for the second phase of the descent scenario of the PDM. The grey-shaded parallelograms designate the target states for the different control phases. The grey-shaded rectangles designate the control modes.

Table 5-1: Control modes mapped to the various control phases.

Control Phase	Control Modes
1	Reorientation
2	Spin-up, Denutation
3	<i>No attitude control</i>
4	Denutation, Spin-down and Reorientation
5	Spin-up, Denutation
6	<i>No attitude control</i>
7	Denutation, Spin-down and Reorientation
8	<i>No attitude control</i>

5-2-1 Target Spin Rates

The target spin rates fed to the controller during Control Phases 2 and 5 must ensure sufficient gyroscopic stability during subsequent Control Phases 3 and 6, respectively. The spin rates appropriate in this respect are determined in Sections 5-2-1-1 and 5-2-1-2, for the DOM and the passive free-fall descent of the penetrator, respectively.

5-2-1-1 De-Orbit Manoeuvre Spin Rate

Considering the large amount of thrust that is produced by the SRM during the DOM (see Figure 2-6), even the slightest misalignment of the thrust vector will lead to disastrous disturbance torques. As the RCS is not sized to compensate for such torques, the PDM will spin up prior to firing the SRM so that it is gyroscopically stable during the SRM burn. In order to guarantee sufficient stability, the ideal DOM spin rate will be determined based on worst-case expected misalignments.

The individual offsets that constitute the net misalignment of the thrust vector are of both linear and angular nature. Figure 5-2 shows a misaligned thrust vector and its geometric relation to the SRM nozzle throat. The linear offset of the thrust application point from the nominal symmetry axis is denoted by d_e and its associated phase angle by ϕ_{d_e} . The angular offset between the thrust vector and the nominal symmetry axis is denoted by δ_e and its associated phase angle by ϕ_{δ_e} . These misalignments can be attributed to imperfections within the SRM, which Knauber (1996) extensively describes and categorises. The individual misalignments with respect to the SRM are aggregated into the *effective misalignment angle*, which is the effective angular offset between the thrust vector acting at the nominal centre of mass flow (see Section 3-4-1) and the nominal symmetry axis. Refer to *e.g.*, Armstrong (1965); Knauber (1996) for a mathematical definition of the effective misalignment angle.

Other sources of misalignment include 1) the lack of concentricity and parallelism of the SRM with respect to the nominal symmetry axis of the PDM, 2) the angular offset of the principal axes of inertia from the *B*-frame, and 3) the linear offset of the CoM from the nominal symmetry axis (Wertz, 1978). The first source can become insignificant relative to

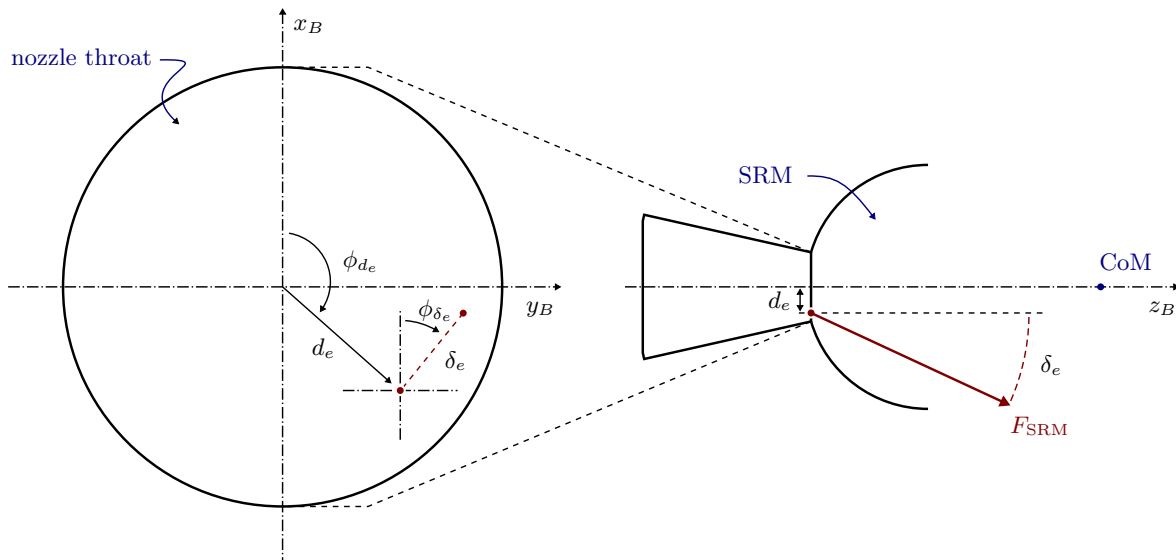


Figure 5-2: Linear and angular SRM thrust misalignments. The image on the left represents an enlarged rear view of the nozzle throat. The direction of the thrust vector in the right image does not correspond to the direction of the thrust vector in the left image. The misalignments are exaggerated for clarity. The location of the CoM in the figure is arbitrary.

the other sources if the SRM is carefully mounted onto the PDM, which may be assumed. The intensity of the second source depends on the degree of asymmetry of the PDM, of which the PoI are a quantitative measure. The PoI are nonzero if the actual CoM does not lie on one of the axes of the B -frame, which implies that the intensity of the second source is in part directly related to the linear offset between the actual CoM and the nominal CoM; the third source of misalignment. Hence, in calculating the disturbance torques due to misalignment of the thrust vector, only two offsets really need to be considered for the case of the PDM: the effective misalignment angle with respect to the SRM, denoted by $\delta_{e, \text{eff}}$, and the position vector of the actual CoM from the nominal CoM, denoted by $\mathbf{r}_{\text{cm, nom}}^{\text{cm, act}}$.

Knauber (1996) states a common *three-sigma value*¹ for $\delta_{e, \text{eff}}$ is 0.25° . The excursion of the CoM from the z_B -axis is the combined result of the off-nominal positions of the CoMs of the penetrator, the dry PDS, as well as the momentary solid and liquid propellant slugs, see also Section 2-3. The linear offsets of the CoMs of the penetrator and the dry PDS are assumed to remain within 5% of the maximum radius of the mass system concerned, *i.e.*, 0.48 cm for the penetrator and 0.88 cm for the PDS. The CoM of the solid propellant slug might diverge from the nominal symmetry axis due to an asymmetric burn. The misalignments that may occur because of this have already been accounted for in $\delta_{e, \text{eff}}$ (Knauber, 1996). Finally, since the liquid propellant slug makes up only a small fraction of the total mass of the PDM (see Section 2-2-1), and its shape remains well-conserved by a restraining diaphragm, any deviation of its CoM with respect to the nominal symmetry axis may be considered insignificant. Table 5-2 presents an overview of the significant offsets and their three-sigma

¹'Three-sigma' stands for three standard deviations from the mean in a normal distribution, which implies that 99.7% of the values are smaller than or equal to the given three-sigma value.

Table 5-2: Three-sigma values and probability distributions for offsets significantly contributing to the net misalignment of the thrust vector.

Parameter	3-sigma	Distribution	Unit
$\delta_{e, \text{eff}}$	0.25	$\mathcal{N}(0, 0.00694)$	deg
$\phi_{\delta_{e, \text{eff}}}$	n/a	$\mathcal{U}(0, 360)$	deg
$\delta r_{\text{cm, pen}}$	0.48	$\mathcal{N}(0, 0.0256)$	cm
$\alpha \delta r_{\text{cm, pen}}$	n/a	$\mathcal{U}(0, 360)$	deg
$\beta \delta r_{\text{cm, pen}}$	n/a	$\mathcal{U}(0, 360)$	deg
$\delta r_{\text{cm, PDS}}$	0.88	$\mathcal{N}(0, 0.0860)$	cm
$\alpha \delta r_{\text{cm, PDS}}$	n/a	$\mathcal{U}(0, 360)$	deg
$\beta \delta r_{\text{cm, PDS}}$	n/a	$\mathcal{U}(0, 360)$	deg

values and associated probability distributions; $\phi_{\delta_{e, \text{eff}}}$ is the phase angle associated with $\delta_{e, \text{eff}}$, measured from the x_B -axis; α and β are the angular distances from, respectively, the x -axis and z -axis of the local body frame; $\mathcal{N}(\mu, \sigma^2)$ denotes a *normal distribution* with mean μ and variance σ^2 ; $\mathcal{U}(a, b)$ denotes a *uniform distribution* with minimum value a and maximum value b .

In creating a worst-case scenario, the offsets are taken to be equal to their three-sigma values. Then simulating the DOM for four different spin rates yields the results depicted in Figures 5-3 and 5-4. From the top-left plot in Figure 5-3, it can be seen that the disturbance torques due to misalignment of the thrust vector are on the order of 10^1 N m. The shapes of the remaining plots in Figure 5-3 show agreement with those depicted in the SRM performance diagrams in Figure 2-6, confirming the correct functioning of the simulator. Additional verification is provided by the end values of the plots top-right and bottom-left in Figure 5-3, which match the actual values for the mass and the z -component of the CoM position vector for a dry PDM, respectively 45.7 kg and -0.225 m. Figure 5-4 shows the time histories of the x - and y -components of the angular velocity vector during and right after the DOM, for four different spin rates: 0, π , 2π and 4π rad s⁻¹. Note that the y -axis scaling in the top-left plot is different from the other plots. As can be observed from Figure 5-4, the transverse angular rates keep increasing until the DOM terminates at approximately 16 seconds, after which they settle into steady oscillation about their respective mean values. It is also seen that, as the spin rate increases, the responses show a more damped behaviour, which implies better stability. It is generally true that gyroscopic stability increases as the spin rate increases.

Nonzero angular rates transverse to the jet stream will induce a jet damping moment, which can be calculated by Equation (3.14). The jet damping moment counteracts the torques due to misalignment of the thrust vector to some extent, yet lacks the strength to fully prevent the nutation angle from growing. This can be seen in Figure 5-5, depicting the responses for the transverse angular rates, the jet damping moment, the nutation angle and the effective thrust force along the angular momentum vector \mathbf{h} (see Section 4-3-2), during and right after the DOM, for a 4π rad s⁻¹ spin rate. Observing the plot top-right, the x - and y -components of the jet damping moment increase in a direction opposite to the x - and y -components of the angular velocity vector, demonstrating the actual damping effect of the jet damping

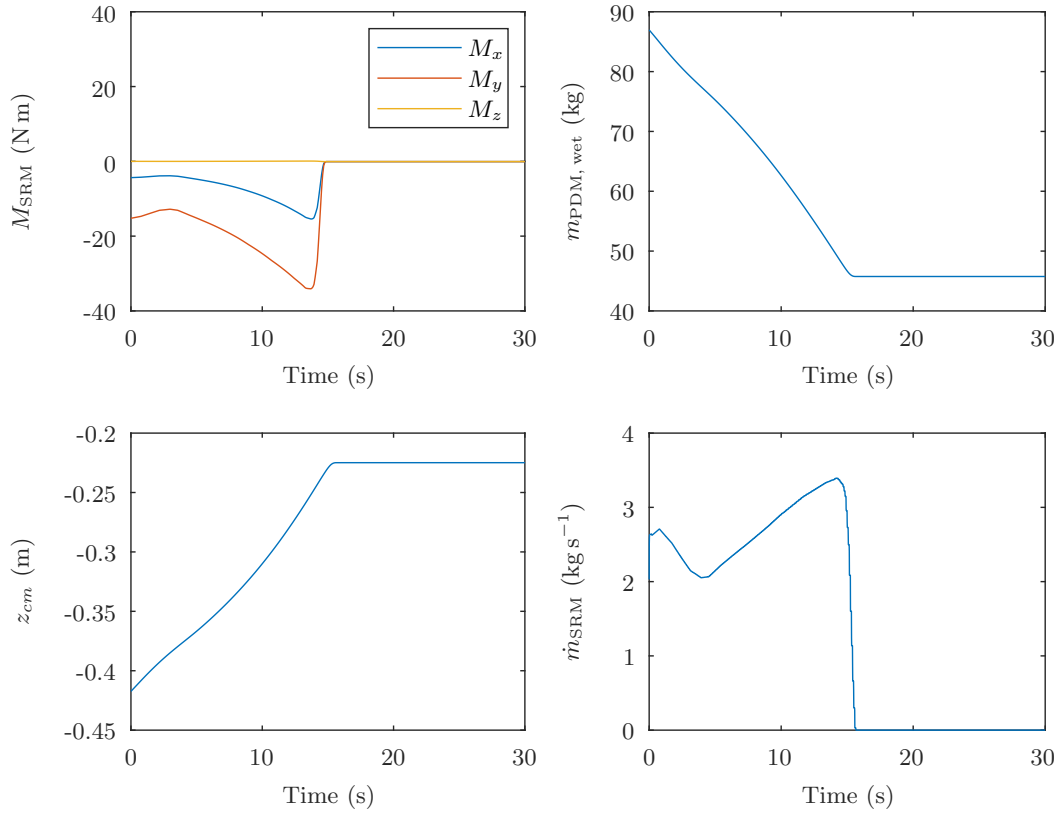


Figure 5-3: Time histories of the disturbance torques due to thrust misalignment (top left), the PDM wet mass (top right), the z -component of the CoM position vector (bottom left) and the propellant mass flow from the SRM (bottom right) during and right after the DOM. Misalignment settings: $\delta_{e, eff} = 0.25^\circ$, $\phi_{\delta_{e, eff}} = 100^\circ$, $\delta r_{cm, pen} = 0.48 \times 10^{-2}$ m, $\alpha_{\delta r_{cm, pen}} = 120^\circ$, $\beta_{\delta r_{cm, pen}} = 50^\circ$, $\delta r_{cm, PDS} = 0.88 \times 10^{-2}$ m, $\alpha_{\delta r_{cm, PDS}} = 150^\circ$ and $\beta_{\delta r_{cm, PDS}} = 60^\circ$.

moment. Notwithstanding, the nutation angle, which is calculated by Equation (4.20), is seen to increase during the DOM. The concept of nutational motion will be further explained in Section 4-3-2.

The bottom-right plot in Figure 5-5 depicts the response of the effective thrust force along the angular momentum vector, which is a function of the nutation angle θ_{nut} , as follows:

$$F_{z, SRM, eff} = F_{z, SRM} \cdot \cos(\theta_{nut}) \quad (5.1)$$

For comparison, the nominal thrust curve (as shown before in Figure 2-6) is plotted next to the effective thrust curve. The area in between both curves represents the loss of impulse due

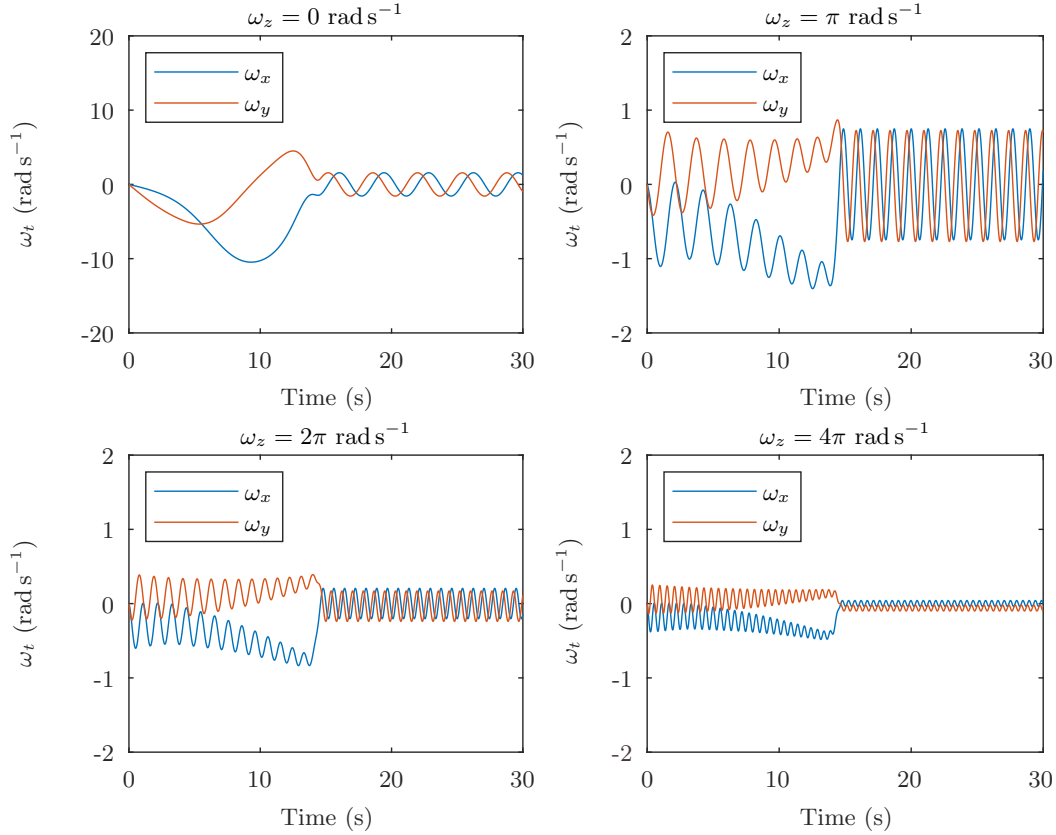


Figure 5-4: Time histories of the transverse angular rates during and right after the DOM, for four different spin rates. Misalignment settings are the same as for Figure 5-3.

to misalignment of the thrust vector, which is calculated by:

$$\Delta J_{\text{loss}} = J_{\text{nom}} - J_{\text{eff}} = \int_0^{t_{\text{DOM}}} (F_{z,\text{SRM}} - F_{z,\text{SRM,eff}}) dt \quad (5.2)$$

where t_{DOM} denotes the duration of the DOM, J_{nom} and J_{eff} respectively denote the nominal and effective total impulse delivered by the SRM, and $F_{z,\text{SRM}}$ and $F_{z,\text{SRM,eff}}$ represent the nominal and effective thrust force along the angular momentum vector, respectively. The impulse efficiency of the DOM is then determined by:

$$\eta_{\text{DOM}} = \frac{J_{\text{eff}}}{J_{\text{nom}}} \quad (5.3)$$

With regard to the bottom-right plot in Figure 5-5, the loss of impulse is about 3% of the nominal total impulse, meaning that in the worst-case scenario considered, the orbital velocity of approximately 1705 m s^{-1} (see Section 1-2-3) is reduced by only 97% and a horizontal

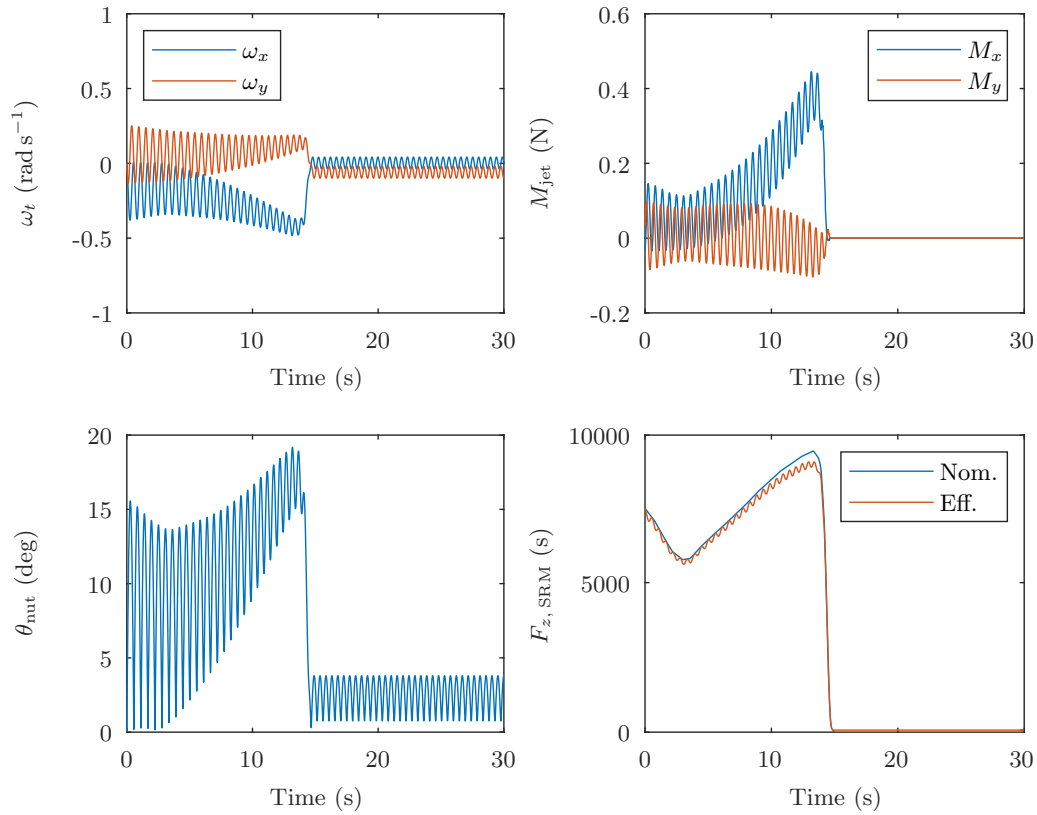


Figure 5-5: Time histories of the transverse angular rates (top left), the x - and y -components of the jet damping moment (top right), the nutation angle (bottom left) and the nominal and effective thrust force along the angular momentum vector (bottom right) during and right after the DOM, for a $4\pi \text{ rad s}^{-1}$ spin rate. Misalignment settings are the same as for Figure 5-3.

velocity of about 51 m s^{-1} remains (provided that the angular momentum vector was in fact aligned with the velocity vector). Given that the impact velocity will be about 300 m s^{-1} (see also Section 1-2-3), the *descent angle* δ , which is the angle between the local vertical and the velocity vector, will then be about 9.6° . This amply exceeds the 5° prescribed by mission requirement RQ-AOCS-PEN-04 (see Appendix B-2). As such, it can be concluded that a spin rate of $4\pi \text{ rad s}^{-1}$ is not sufficient to guarantee enough stability under worst-case expected misalignments, *i.e.*, $\delta_{e, \text{eff}} = 0.25^\circ$ and linear offsets of the CoMs of the penetrator and the dry PDS of 5% of their respective maximum radii. In such a situation, the RCS must be employed to reduce the horizontal velocity to acceptable limits before performing the post-DOM reorientation manoeuvre. This naturally requires the use of additional propellant and also leaves a narrower time window for subsequent control phases. A preventive measure would be to increase the spin rate of the PDM, however the SRM is only qualified for spin rates up to 120 rpm ($= 4\pi \text{ rad s}^{-1}$), see Table G-3.

In order to investigate the impact of the spin rate on the success rate of the DOM, a small

simulation study is conducted. In this regard, five different spin rates are considered: 2π , 3π , 4π , 5π and 6π rad s^{-1} . Additionally considered are three different three-sigma values for the linear offsets of the CoMs of the penetrator and the dry PDS, being 5%, 10% and 15% of their respective maximum radii. The three-sigma value for the effective thrust misalignment angle remains 0.25° . For each of the spin rates, three 1000-sample *Monte Carlo* simulations (explained in Section 6-3-3) are run, each one sampling from different normal distributions for the linear CoM offsets, defined based on one of the three associated three-sigma values. A successful sample is defined to have achieved a minimum impulse efficiency of 98.5%. This value was deduced from the prescribed maximum descent angle of 5° , assuming a 300 m s^{-1} impact velocity and a 1705 m s^{-1} orbital velocity. Using Equation (5.1), the average nutation angle corresponding to a 98.5% impulse efficiency is calculated to be 9.9° . The success rates associated with each of the Monte Carlo simulations are presented in Figure 5-6, from which it can be observed that for the maximum allowed spin rate of $4\pi \text{ rad s}^{-1}$, the success rate is 93% under currently assumed three-sigma values for the thrust misalignments considered. This rate increases to 99% for a $5\pi \text{ rad s}^{-1}$ spin rate. Furthermore it is seen that a spin rate of $6\pi \text{ rad s}^{-1}$ offers sufficient confidence to allow for increased uncertainty on the position of the CoM. Selecting a spin rate larger than $4\pi \text{ rad s}^{-1}$ would however require additional qualification testing for the currently proposed SRM. That said, it is concluded that, under the thrust profile of the current SRM, a $4\pi \text{ rad s}^{-1}$ spin rate manages to keep the risk of an insufficient DOM within acceptable limits, be it as long as the penetrator and the dry PDS are, qualitatively speaking, properly balanced.

5-2-1-2 Penetrator Release Spin Rate

Prior to releasing the penetrator, the PDM performs a spin-up about its symmetry axis to provide the uncontrolled penetrator with a stabilising spin upon release. Besides a linear tip-off velocity v_{tip} , the mechanism separating the penetrator from the PDS also imparts a perturbing transverse angular tip-off velocity ω_{tip} to the penetrator, causing a nutation in the spin-axis that, in the most pessimistic case, directly adds to any pre-existing nutation. Table 5-3 presents the anticipated nominal values for the relative linear and angular tip-off velocities, for which it holds that:

$$v_{\text{tip}} = v_{\text{tip,PDS}} + v_{\text{tip, Pen}} \quad (5.4)$$

$$\omega_{\text{tip}} = \omega_{\text{tip,PDS}} + \omega_{\text{tip, Pen}} \quad (5.5)$$

Table 5-3: Anticipated relative tip-off velocities at separation of the penetrator from the PDS.

Parameter	Mean	3-sigma	Distribution	Unit
v_{tip}	1.0	0.1	$\mathcal{N}(1.0, 0.00111)$	m s^{-1}
ω_{tip}	1.0	0.1	$\mathcal{N}(1.0, 0.00111)$	deg s^{-1}

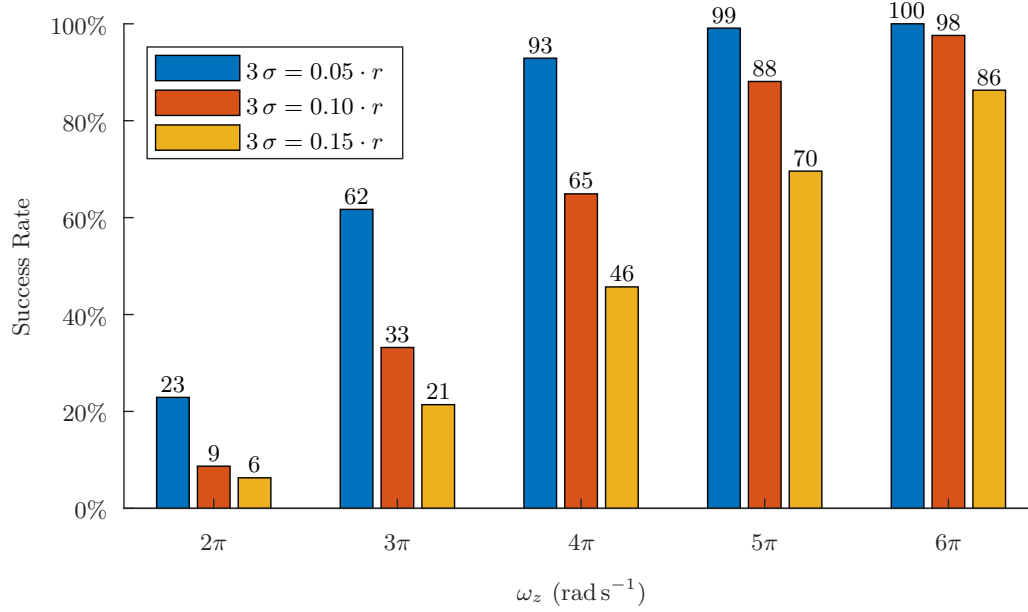


Figure 5-6: Success rates for the DOM for three different three-sigma values for the linear offsets of the CoMs of the penetrator and the dry PDS, against a range of different spin rates. Each bar represents the percentage of successes in a 1000-sample Monte Carlo simulation. The success criterion was 98.5% impulse efficiency.

The net tip-off velocities imparted to the penetrator and the PDS can be determined using the *law of conservation of momentum*:

$$m_{\text{PDS}} \cdot v_{\text{tip,PDS}} = m_{\text{Pen}} \cdot v_{\text{tip, Pen}} \quad (5.6)$$

$$I_{t, \text{PDS}} \cdot \omega_{\text{tip,PDS}} = I_{t, \text{Pen}} \cdot \omega_{\text{tip, Pen}} \quad (5.7)$$

where I_t denotes the MoI about the transverse axis. Combining Equations (5.4) and (5.6), the following equations for the net linear tip-off velocities can be derived:

$$v_{\text{tip,PDS}} = \frac{m_{\text{Pen}} \cdot v_{\text{tip}}}{m_{\text{PDS}} + m_{\text{Pen}}} \quad (5.8a)$$

$$v_{\text{tip, Pen}} = v_{\text{tip}} - v_{\text{tip,PDS}} \quad (5.8b)$$

Similarly, the net angular tip-off velocities can be calculated through:

$$\omega_{\text{tip,PDS}} = \frac{I_{t, \text{Pen}} \cdot \omega_{\text{tip}}}{I_{t, \text{PDS}} + I_{t, \text{Pen}}} \quad (5.9a)$$

$$\omega_{\text{tip, Pen}} = \omega_{\text{tip}} - \omega_{\text{tip, PDS}} \quad (5.9b)$$

The net linear tip-off velocity vectors with respect to the B -frames of the PDS and the penetrator are, respectively,

$$\mathbf{v}_{\text{tip, PDS, } B} = [0, 0, -v_{\text{tip, PDS}}]^T \text{ and } \mathbf{v}_{\text{tip, Pen, } B} = [0, 0, v_{\text{tip, Pen}}]^T.$$

These vectors can be transformed to the F -frame with Equation (E.1), using the inverse of the *direction cosine matrix* $\mathbf{C}^{B/F}$, which is obtained through Equation (E.2). The x - and y -components of the angular tip-off velocity are calculated by:

$$\omega_{x, \text{tip}} = \omega_{\text{tip}} \cdot \cos(\phi_{\omega_{\text{tip}}}) \quad (5.10a)$$

$$\omega_{y, \text{tip}} = \omega_{\text{tip}} \cdot \sin(\phi_{\omega_{\text{tip}}}) \quad (5.10b)$$

where $\phi_{\omega_{\text{tip}}} \sim \mathcal{U}(0^\circ, 360^\circ)$ is the phase angle associated with ω_{tip} , measured from the x_B -axis. The net angular tip-off velocity vectors for the PDS and the penetrator then become, respectively,

$$\boldsymbol{\omega}_{\text{tip, PDS}} = [-\omega_{x, \text{tip, PDS}}, -\omega_{y, \text{tip, PDS}}, 0]^T \text{ and } \boldsymbol{\omega}_{\text{tip, Pen}} = [\omega_{x, \text{tip, Pen}}, \omega_{y, \text{tip, Pen}}, 0]^T,$$

where the x - and y - components of both vectors can be calculated using Equation (5.9), filling out the appropriate MoIs and angular tip-off velocity values. In order to provide insight into the relation between the spin rate of the penetrator and the nutation angle resulting from the tip-off, the following equation is used (Wie, 2008):

$$\theta_{\text{nut, Pen}} = \arctan\left(\frac{I_{t, \text{Pen}} \cdot \omega_{t, \text{Pen}}}{I_{zz, \text{Pen}} \cdot \omega_{z, \text{Pen}}}\right) \quad (5.11)$$

where $\theta_{\text{nut, Pen}}$ is the nutation angle of the spinning penetrator, $\omega_{t, \text{Pen}}$ is the transverse angular velocity of the penetrator, $I_{s, \text{Pen}}$ is the MoI about the spin-axis of the penetrator and $\omega_{s, \text{Pen}}$ is the spin rate of the penetrator. The parameters in the numerator of the fraction in Equation (5.11) are defined by:

$$I_{t, \text{Pen}} = I_{xx, \text{Pen}} = I_{yy, \text{Pen}}; \quad \omega_{t, \text{Pen}} = \sqrt{\omega_{x, \text{Pen}}^2 + \omega_{y, \text{Pen}}^2} = \omega_{\text{tip, Pen}}$$

Using the inertial parameter values provided in Table 2-3, the worst-case expected value for $\omega_{\text{tip, Pen}}$ is calculated to be 1.039 deg s^{-1} . The relation between the spin rate of the penetrator and the nutation angle associated with this particular angular tip-off velocity is visualised in the top plot in Figure 5-7. From this plot, it is clear that the penetrator is more resilient against transverse disturbances when the spin rate is higher. There are, however, a few drawbacks to a higher spin rate. For one; more propellant is needed. Also; the vertical

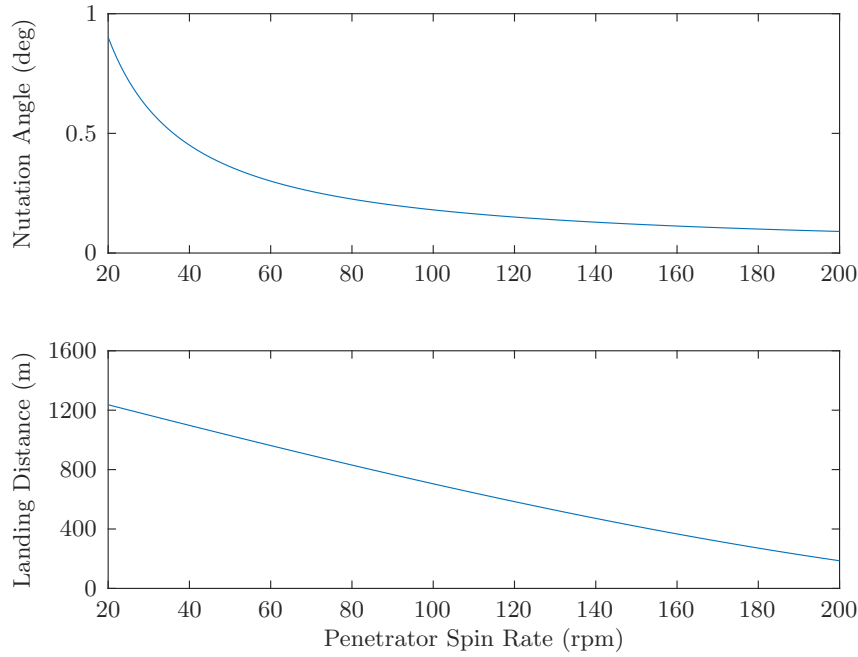


Figure 5-7: Nutation angle of the spinning penetrator and final landing distance between the PDS and the penetrator as a function of the spin rate of the penetrator. Settings: $\omega_{\text{tip, Pen}} = 1.039 \text{ deg s}^{-1}$ and $v_{\text{tip}} = 0.9 \text{ m s}^{-1}$.

velocity increment generated as a ‘by-product’ of the spin-up and spin-down manoeuvres (see Section 2-4) will be larger. The latter has two implications: 1) the free-fall time decreases, since the PDM gains more speed during the spin-up; 2) the drift time following the release of the penetrator increases, as the vertical distance between the PDS and the penetrator must grow larger to account for the larger linear impulse the PDS receives during the spin-down. Consequentially, the final horizontal distance that can be achieved between the PDS and the penetrator at landing will be smaller. Concluding, to select the appropriate spin rate for the penetrator, the impact on the landing distance must also be taken into account.

The first step in approximating the relation between the penetrator spin rate and the landing distance is to calculate the time available for the PDS to ‘fly away’ after it has spun down and slewed horizontally. To this end, the altitude at which the fly-away manoeuvre is set in must be determined. This can be done by evaluating the following equations:

$$s_5 = \frac{1}{2}g_m t_4^2 \quad (5.12)$$

$$s_6 = s_5 + (g_m t_4 + v_{\text{spin}, 5}) t_5 + \frac{1}{2}g_m t_5^2 \quad (5.13)$$

$$s_7 = s_6 + (g_m (t_4 + t_5) + v_{\text{spin}, 5}) t_6 + \frac{1}{2}g_m t_6^2 \quad (5.14)$$

$$s_8 = s_7 + (g_m (t_4 + t_5 + t_6) + v_{\text{spin}, 5} + v_{\text{spin}, 7}) t_7 + \frac{1}{2}g_m t_7^2 \quad (5.15)$$

with:

$$t_4 = t_{\text{spin},4} + t_{\text{reorient}} + T_s \quad (5.16)$$

$$t_5 = t_{\text{spin},5} + T_s \quad (5.17)$$

$$t_7 = t_{\text{spin},7} + t_{\text{reorient}} + T_s \quad (5.18)$$

and:

$$t_6 = \frac{v_{\text{spin},7} t_7}{v_{\text{tip}}} \quad (5.19)$$

$$t_{\text{spin}} = \frac{I_s \omega_s}{M} \quad (5.20)$$

$$v_{\text{spin}} = \frac{F t_{\text{spin}}}{m} \quad (5.21)$$

In Equations (5.12) to (5.21), s_i is the total vertical distance traversed at the start of control phase i (see Section 5-1), t_i is the duration of control phase i , t_{spin} is the time needed to perform a spin-up or spin-down manoeuvre, v_{spin} is the velocity change imparted during a spin-up or spin-down manoeuvre, v_{tip} is the linear tip-off velocity (Section 2-1), t_{reorient} is the time needed to perform a reorientation manoeuvre, T_s is the settling time following a manoeuvre and g_m is the Moon's gravitational acceleration, computed as:

$$g_m = \frac{\mu_m}{R_m^2} = \frac{4.905 \times 10^{12}}{(1.738 \times 10^6)^2} = 1.624 \text{ m s}^{-2}$$

In approximating s_8 , some restrictive assumptions are made. First of all, it is assumed that g_m is constant throughout the descent. Also, the inertial parameters and forces and torques remain constant during a control phase. Then, t_8 – the time available for the PDS to ‘fly away’ – is obtained by finding the positive root of the following quadratic equation:

$$\left(\frac{1}{2}g_m\right) t_8^2 + \left(g_m \sum_{i=4}^7 t_i + v_{\text{spin},5} + v_{\text{spin},7}\right) t_8 + (s_8 - h_{\text{freefall}}) = 0 \quad (5.22)$$

where h_{freefall} is the free-fall altitude. To determine the final horizontal landing distance that can be achieved, first the velocity increment resulting from the fly-away manoeuvre is calculated by:

$$v_{\text{fly}} = \frac{F_8 t_{\text{fly}}}{m_8} \quad (5.23)$$

where:

$$t_{\text{fly}} = \frac{m_{\text{hyd},8}}{\dot{m}_8} \quad (5.24)$$

Table 5-4: Parameter values used to visualise the relation between the spin rate of the penetrator and the achievable horizontal distance between the PDS and the penetrator at landing.

Parameter	Value	Unit
m_{solid}	0	kg
$m_{\text{hyd},5}$	0.2	kg
$m_{\text{hyd},\text{ini}}$	2.1	kg
F_{ave}	3.15	N
V_{tank}	0.006	m ³
p_{max}	24	bar
p_{min}	6	bar
θ_{thruster}	45	deg
ϕ_{thruster}	45	deg
h_{freefall}	28	km
g_{m}	1.624	m s ⁻²
t_{reorient}	2.5	s
$t_{\text{reorient, burn}}$	0.5	s
T_s	10	s

and:

$$m_{\text{hyd},8} = m_{\text{hyd},7} - \dot{m}_7 (t_{\text{spin},7} + t_{\text{reorient, burn}}) \quad (5.25)$$

$$m_{\text{hyd},7} = m_{\text{hyd},5} - \dot{m}_5 t_{\text{spin},5} \quad (5.26)$$

$$m_{\text{hyd},5} = m_{\text{hyd},4} - \dot{m}_4 t_{\text{spin},4} \quad (5.27)$$

The parameters on the right-hand sides of Equations (5.23) and (5.24) are assumed to be constant during the fly-away manoeuvre. The mass flow parameters showing up in Equations (5.24) to (5.26) can be calculated using Equation (2.7), remarking that for \dot{m}_5 and \dot{m}_7 , $n = 2$, and for \dot{m}_8 , $n = 4$. A conservative approximation of the landing distance between the PDS and the penetrator is then obtained by:

$$\Delta x_{\text{landing}} = \frac{1}{2} a_{\text{fly}} t_{\text{fly}}^2 + v_{\text{fly}} (t_8 - t_{\text{fly}}) = v_{\text{fly}} \left(t_8 - \frac{1}{2} t_{\text{fly}} \right) \quad (5.28)$$

Using the parameter values provided in Tables 2-3 and 5-4, the procedure as described at the end of Section 2-4 is followed to determine the force and torque capabilities of the PDM/PDS at the start of, and during each control phase. Then, the landing distance between the PDS and the penetrator is calculated as a function of the spin rate of the penetrator for the worst-case expected relative linear tip-off velocity; $v_{\text{tip}} = 0.9 \text{ m s}^{-1}$. The results of these calculations are plotted in the bottom plot of Figure 5-7. As can be seen, in regard to the landing distance, which preferably is as large as possible, a lower penetrator spin rate is desired. This contradicts the desire to minimise the nutation angle arising from the tip-off, for which a higher penetrator spin rate is in turn preferred.

Mission requirement RQ-AOCS-PDS-01 (see Appendix B-2) prescribes a minimum landing distance of 50 m. When observing the bottom plot in Figure 5-7, it is concluded that this requirement is met even for a spin rate of 200 rpm. However, when examining the top plot in Figure 5-7, it can be seen that a 200 rpm spin rate offers only little improvement over *e.g.*, a spin rate of 120 rpm: $\Delta\theta_{\text{nut, Pen}} = -0.060^\circ$ for the worst-case expected net angular tip-off velocity ($\omega_{\text{tip, Pen}} = 1.039 \text{ deg s}^{-1}$). As a lower spin rate inherently requires less propellant, it is hence decided to select a penetrator release spin rate of 120 rpm ($= 4\pi \text{ rad s}^{-1}$), for which the tip-off in a worst-case scenario will lead to a 0.15° increase in nutation angle. The corresponding achievable landing distance is approximated to be 580 m, yet this is only indicative, as the eventual landing distance will depend strongly on the time slots assigned to the various control phases, as well as the amount of liquid propellant left in the tank to perform the FAM.

5-2-2 Target Orientations

Control Phases 1, 4 and 7 involve a reorientation manoeuvre, which means that the controller requires the input of a target orientation. Obviously in such cases, the target angular velocity vector is zero. The target orientations for Control Phases 1, 4 and 7, respectively referred to as the *initial orientation*, the *free-fall orientation* and the *fly-away orientation*, are defined in Sections 5-2-2-1 to 5-2-2-3, respectively.

5-2-2-1 Initial Orientation

From Figure 3-1, it is clear that for Control Phase 1, the B -frame must be rotated by 90° in the negative direction about the y_B -axis, such that the nozzle of the SRM is directed forward (*i.e.*, in the direction of the orbital velocity vector). As such, the target orientation expressed in Euler angles with respect to the F -frame becomes:

$$[\phi \ \theta \ \psi]_1^T = [0 \ -90^\circ \ 0]^T$$

which, when converted to quaternions using Equation (D.1), transforms to:

$$\mathbf{q}_1 = [0 \ -0.7071 \ 0 \ 0.7071]^T$$

where the subscript 1 indicates that the vector is associated with Control Phase 1.

5-2-2-2 Free-Fall Orientation

The target orientation for Control Phase 4 depends on the expected direction of the velocity vector at impact, with respect to the F -frame. The objective for this control phase is to align the z_B -axis, the nominal symmetry axis of the PDM, with the velocity vector as expected at impact, so as to minimise the angle-of-attack (see Appendix B-1). In order to approximate the

components of the velocity vector at impact, it is assumed that the gravitational acceleration of the Moon is constant and the magnitudes of the velocity components in the x_F - and y_F -directions at the start of Control Phase 4 do not change. As such, the velocity vector at impact can be approximated by:

$$\mathbf{v}_{\text{impact}} \approx \mathbf{v}_4 + \begin{bmatrix} 0 \\ 0 \\ -g_m t_{\text{freefall}} \end{bmatrix} \text{ m s}^{-1} \quad (5.29)$$

where t_{freefall} is equal to the positive root of the quadratic equation

$$\frac{1}{2} g_m t_{\text{freefall}}^2 - (v_z)_4 t_{\text{freefall}} - h_4 = 0,$$

\mathbf{v}_4 is the 3×1 velocity vector and h_4 is the altitude of the PDM at the start of Control Phase 4, and $g_m = 1.624 \text{ m s}^{-2}$ (calculated in Section 5-2-1-2). Now the target orientation can be derived from $\mathbf{v}_{\text{impact}}$, knowing that the z_B -axis must point in the same direction. The angle between the z_F -axis and $\mathbf{v}_{\text{impact}}$ is the angle of rotation about a unit vector perpendicular to the plane of the z_F -axis and $\mathbf{v}_{\text{impact}}$. If this angle of rotation is called the *eigenangle*, then the unit vector in question represents the *eigenaxis*, see Section 3-2. Using this information, the target orientation can directly be computed in terms of quaternions. In order to obtain the eigenangle θ , as well as the components of the eigenaxis \mathbf{e} , one takes the cross product of the unit vector in the z_F -direction and the normalised $\mathbf{v}_{\text{impact}}$:

$$\mathbf{e}_4 \cdot \sin(\theta_4) = \begin{bmatrix} 0 \\ 0 \\ 1 \end{bmatrix} \times \frac{\mathbf{v}_{\text{impact}}}{\|\mathbf{v}_{\text{impact}}\|} \quad (5.30)$$

where $\sin(\theta_4)$ is equal to the magnitude of the resultant vector, \mathbf{e}_4 represents the normalised result of the resultant vector and subscript 4 indicates the parameters or vectors are associated with Control Phase 4. By definition, θ_4 is the angle between the two vectors and \mathbf{e}_4 is the unit vector perpendicular to the plane containing the two vectors. Then using Equations (3.2a) and (3.2b), the quaternion components can be calculated, constituting the target orientation for Control Phase 4:

$$\mathbf{q}_4 = \left[(e_1)_4 \sin(\theta_4/2) \quad (e_2)_4 \sin(\theta_4/2) \quad (e_3)_4 \sin(\theta_4/2) \quad \cos(\theta_4/2) \right]^T$$

5-2-2-3 Fly-Away Orientation

For Control Phase 7, the desired orientation is such that the z_B -axis of the PDS is aligned with the local horizontal. The shortest angular path towards the horizontal is achieved when the z_B -axis is pointing in the direction of the resultant of the x - and y -components of the

momentary velocity vector. The unit vector in this direction, with respect to the F -frame, is calculated by:

$$\mathbf{z}_B^F = \frac{\mathbf{z}_B'^F}{\|\mathbf{z}_B'^F\|} \quad (5.31)$$

where:

$$\mathbf{z}_B'^F = \begin{bmatrix} (v_x)_7 \\ (v_y)_7 \\ 0 \end{bmatrix} \text{ m s}^{-1} \quad (5.32)$$

Then, in a similar fashion as for Control Phase 4, the eigenangle between \mathbf{z}_B^F and the unit vector in the z_F -direction, as well as the associated eigenaxis are obtained through:

$$\mathbf{e}_7 \cdot \sin(\theta_7) = \begin{bmatrix} 0 \\ 0 \\ 1 \end{bmatrix} \times \mathbf{z}_B^F \quad (5.33)$$

Using the result of Equation (5.33), the target orientation for Control Phase 7 can be calculated in terms of quaternions:

$$\mathbf{q}_7 = \left[(e_1)_7 \sin(\theta_7/2) \quad (e_2)_7 \sin(\theta_7/2) \quad (e_3)_7 \sin(\theta_7/2) \quad \cos(\theta_7/2) \right]^T$$

where subscript 7 indicates the parameters or vectors are associated with Control Phase 7.

5-2-3 Overview of Target States

Table 5-5 presents an overview of the target rotational states for each control phase. In addition, the maximum duration per control phase is provided in seconds.

Table 5-5: Target rotational states and maximum duration per control phase.

Phase	Target Rotational State	Duration (s)
1	$\mathbf{x}_1 = [0 \quad -0.7071 \quad 0 \quad 0.7071 \quad 0 \quad 0 \quad 0]^T$	10
2	$\mathbf{x}_2 = [\text{n/a} \quad \text{n/a} \quad \text{n/a} \quad \text{n/a} \quad 0 \quad 0 \quad 4\pi]^T$	20
3	<i>No attitude control</i>	16
4*	$\mathbf{x}_4 = [(q_1)_4 \quad (q_2)_4 \quad (q_3)_4 \quad (q_4)_4 \quad 0 \quad 0 \quad 0]^T$	50
5	$\mathbf{x}_5 = [\text{n/a} \quad \text{n/a} \quad \text{n/a} \quad \text{n/a} \quad 0 \quad 0 \quad 4\pi]^T$	20
6	<i>No attitude control</i>	20
7*	$\mathbf{x}_7 = [(q_1)_7 \quad (q_2)_7 \quad (q_3)_7 \quad (q_4)_7 \quad 0 \quad 0 \quad 0]^T$	50
8	<i>No attitude control</i>	n/a

*Refer to Section 5-2-2 for specifics on how the quaternion components are determined.

Chapter 6

Simulation Study

In order to test the performance of the controller and determine the success rate of the mission from a descent-and-landing perspective, simulations will be performed. To this end, a simulator is built, incorporating the models created for the spacecraft and its environment, the controller and the mission manager logic. In addition, the simulator will include a thruster management function and a navigation system, which will both be covered in Section 6-1. Then, in Section 6-2, the architecture of the simulator will be explained. In Section 6-3, a detailed description of the set-up of the simulation study will be provided, for the purpose of reproducibility. Finally, the results of a nominal-case system test and the Monte Carlo simulation are presented and discussed in Section 6-4.

6-1 Simulator Elements

Besides the controller and the mission manager, there are other elements included in the simulator that need addressing before a full simulation can take place. First of all, the thruster management function, which is tasked with converting control commands received from the controller into operating commands comprehensible to the thrusters. The design of the thruster management function is discussed in Section 6-1-1. Secondly, the navigation system, which processes sensor measurements to provide an estimate of the state of the spacecraft. The implementation of a *surrogate* navigation system is discussed in Section 6-1-2.

6-1-1 Thruster Management Function

The Thruster Management Function (TMF) determines the firing duration Δt_i for each thruster $i = 1, \dots, n$, where n is the number of thrusters, based on the 3×1 control torque vec-

tor \mathbf{u} received from the controller. The sought-for $n \times 1$ firing duration vector $\Delta \mathbf{t}$, containing each Δt_i , must be defined in such a way that the following condition is satisfied:

$$\mathcal{M}_{\text{nom}} \Delta \mathbf{t} = \mathbf{u} \quad (6.1)$$

where \mathcal{M}_{nom} is the $3 \times n$ thruster torque response matrix, whose columns contain the components of nominal torque generated by each thruster. For the case of the PDM: $n = 4$, which implies that:

$$\mathcal{M}_{\text{nom}} = \begin{bmatrix} (M_x)_{\text{T1}} & (M_x)_{\text{T2}} & (M_x)_{\text{T3}} & (M_x)_{\text{T4}} \\ (M_y)_{\text{T1}} & (M_y)_{\text{T2}} & (M_y)_{\text{T3}} & (M_y)_{\text{T4}} \\ (M_z)_{\text{T1}} & (M_z)_{\text{T2}} & (M_z)_{\text{T3}} & (M_z)_{\text{T4}} \end{bmatrix}_{\text{nom}} \quad (6.2)$$

where ‘T1’ stands for ‘Thruster 1’, ‘T2’ for ‘Thruster 2’, *etc.* Since the number of thrusters exceeds the number of degrees-of-freedom, it generally holds that for any given control torque vector \mathbf{u} , there is a variety of firing duration vectors that satisfy Equation (6.1). In order to find the one solution for $\Delta \mathbf{t}$ that minimises the propellant consumption, the following optimisation problem is solved:

$$\begin{aligned} & \underset{\Delta \mathbf{t}}{\text{minimise}} && \sum_{i=1}^n \Delta t_i \\ & \text{subject to} && \mathcal{M}_{\text{nom}} \Delta \mathbf{t} = \mathbf{u}, \\ & && 0 \leq \Delta t_i, \quad i = 1, \dots, n. \end{aligned} \quad (6.3)$$

Problem (6.3) is also referred to as the *jet selection problem* and was first described by Crawford (1969). It should be noted that the *objective function* to be minimised here is the sum of the individual firing durations calculated for each thruster. Minimising the total firing duration of all thrusters combined in fact minimises the propellant consumption, as the PDM is equipped with *on/off*-type thrusters, see also Section 2-2-1. Problem (6.3) is subject to one *equality constraint*, defined by Equation (6.1), and one *inequality constraint*, that is, $0 \leq \Delta t_i$. The latter prohibits negative firing duration values. Notably, there is no upper bound defined for Δt_i in Problem (6.3). This reduces the complexity of the optimisation problem and actually guarantees convergence for a torque response matrix similar to the one associated with the thruster geometry of concern (see Figure 2-2). In reality, Δt_i is bounded by the minimum pulse width on the lower end, and by the controller’s sampling time T_{sampling} on the upper end, such that:

$$\Delta t_{\text{p, min}} \leq \Delta t_i \leq T_{\text{sampling}} \quad (6.4)$$

Rather than handling these lower and upper bounds in Problem (6.3) directly, they are imposed on $\Delta \mathbf{t}$ *after* the optimisation process. However, before imposing them, the firing duration vector must first be corrected for the force drop that occurs as a result of multiple thrusters firing simultaneously (see Section 2-2-1). The limitation of solving Problem (6.3)

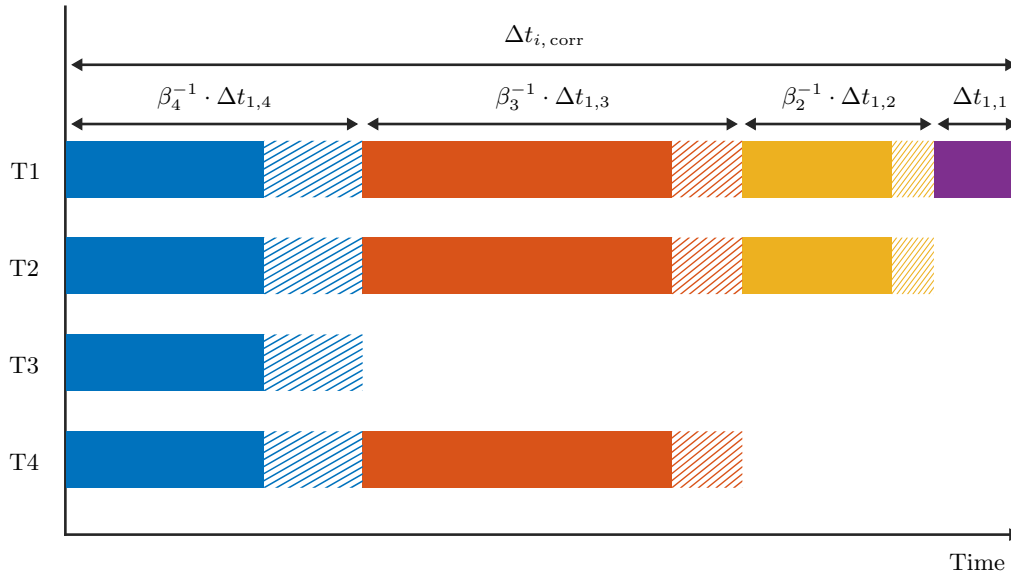


Figure 6-1: Graphical representation of the second step of the firing duration correction procedure, showing the obtained optimal firing durations (solid bars) and the applied corrections (hatched bars) to account for the force drop that occurs when multiple thrusters are fired at once. In this particular example, a configuration of four thrusters is considered. The bar length is arbitrary.

as is, is that it yields a solution that is calculated based only on the nominal torque response matrix and does not account for potential force drops. Hence, a correction must be applied, for which the following two-step procedure is devised:

1. At the start of each control cycle, the off-nominal torque response matrices are calculated based on the predetermined pressure drop factors (see Table 2-2). The ratio between an arbitrary element in the k -th off-nominal matrix and its corresponding element in the nominal matrix should be the same for all other element pairs and represents the momentary force drop factor β_k associated with off-nominal matrix \mathcal{M}_k , where $k = 2, \dots, n$, $\mathcal{M}_1 = \mathcal{M}_{\text{nom}}$ and $\beta_1 = 1$. Notably, the index of the torque response matrix corresponds to the number of thrusters that are firing at the same time (see also Section 2-2-1).
2. Using the obtained force drop factors, the individual firing durations in $\Delta \mathbf{t}$ are corrected for by increasing the parts that overlap with other firing durations proportional to the inverse of the relevant force drop factor. This process is graphically depicted in Figure 6-1. When each part $\Delta t_{i,k}$ of an individual firing duration Δt_i has been modified accordingly, the separate parts are glued together to form the corrected firing duration $\Delta t_{i,\text{corr}}$. The corrected individual firing durations are finally assembled in the corrected firing duration vector $\Delta \mathbf{t}_{\text{corr}}$, ready for further processing.

Now that $\Delta \mathbf{t}_{\text{corr}}$ has been obtained, the pulse constraints can be imposed. If the maximum element of $\Delta \mathbf{t}_{\text{corr}}$ exceeds T_{sampling} , the corrected firing duration vector is normalised by its

maximum value, and then multiplied by the sampling time:

$$\Delta t_{\text{corr}}^* = \begin{cases} \Delta t_{\text{corr}}, & \max(\Delta t_{\text{corr}}) \leq T_{\text{sampling}} \\ \frac{\Delta t_{\text{corr}}}{\max(\Delta t_{\text{corr}})} \cdot T_{\text{sampling}}, & \max(\Delta t_{\text{corr}}) > T_{\text{sampling}} \end{cases} \quad (6.5)$$

Equation (6.5) was slightly modified from Silva et al. (2005) to account for a non-unity sampling time. Notably, Jackson and Gonzalez (2007) use a similar method to impose the upper pulse constraint. Lastly, the lower bound is applied as follows:

$$\Delta t_{i,\text{corr}}^* = \begin{cases} \Delta t_{p,\text{min}}, & \frac{\Delta t_{p,\text{min}}}{2} \leq \Delta t_{i,\text{corr}}^* < \Delta t_{p,\text{min}} \\ 0, & \Delta t_{i,\text{corr}}^* < \frac{\Delta t_{p,\text{min}}}{2} \end{cases} \quad (6.6)$$

Returning to Problem (6.3), it is noted that the objective function as well as the constraints are linear, which renders Problem (6.3) a so-called *linear optimisation problem*. Two well-known classes of algorithms to solve a linear optimisation problem are the *simplex class* and the *interior-point class*. Since there is existing software in place that offers powerful solvers based on algorithms from both classes, it would be highly cumbersome to construct a solver from scratch. It is therefore chosen to employ an off-the-shelf solver to find an optimal solution to Problem (6.3). In selecting the most efficient solver, a performance comparison is drawn between a variety of solvers that can either be called directly from MATLAB or indirectly through *cvx*, which is described as a ‘‘MATLAB-based modelling system for convex optimisation’’¹. Since a linear programming problem is a special case of the general convex optimisation problem (Boyd & Vandenberghe, 2009), *cvx* is able to transform Problem (6.3) to a form compatible with any of its available solvers. Refer to Grant and Boyd (2008) for further details on *cvx*. For specifics on the simplex class of algorithms and the interior-point class of algorithms, refer to *e.g.*, Ficken (2015) and Boyd and Vandenberghe (2009), respectively. Table 6-1 presents a list of the different solvers considered along with their performance expressed in average time required to solve Problem (6.3) with similar precision. Clearly, the built-in MATLAB solvers outperform the *cvx* solvers by length in this respect. Among the algorithms that MATLAB’s Optimization Toolbox provides, the *interior-point-legacy*² algorithm proves to be fastest and is hence selected as the preferred algorithm to solve Problem (6.3).

In order to verify the correct implementation of the TMF as proposed, a reorientation manoeuvre is simulated. For such manoeuvres, the quaternion-error feedback controller described in Section 4-2-1 calculates the appropriate control torque vectors. Using the parameter values provided in Table 6-2, along with the inertial parameters for the dry PDM from Table 2-3, the RCS parameters from Table 2-5 and the pressure drop factors from Table 2-2, Figures 6-2 to 6-5 are generated, depicting the time histories of the quaternions, body rates, torque commands and actual torques, respectively. Notably, the natural frequency that is used to calculate the controller gains is computed using Equation (4.18), assuming a settling time

¹See: [CVX: MATLAB Software for Disciplined Convex Programming](#) (Visited: July 15, 2019)

²See: [Linear Programming Algorithms - MATLAB & Simulink](#) (Visited: July 15, 2019)

Table 6-1: Approximate time required for the solvers and algorithms considered to solve Problem (6.3) with similar precision.

System	Solver	Algorithm	Time (s)
MATLAB	linprog	dual-simplex	0.044
MATLAB	linprog	interior-point	0.030
MATLAB	linprog	interior-point-legacy	0.026
cvx	SDPT3 4.0	Interior-point method	0.22
cvx	SeDuMi 1.34	Interior-point method	0.19
cvx	Gurobi 7.52	Interior-point method	0.11
cvx	MOSEK 8.0.0.60	Interior-point method	0.55

of 20 seconds and an eigenangle-to-go of 90 degrees. In Figures 6-2 to 6-4, the actual responses are plotted next to their associated theoretical, or nominal responses to allow for comparison. It should be noted that in the nominal case, the commanded control torques are executed perfectly. For the actual case, this is by definition impossible, since 1) the torque capabilities of the PDM are finite, implicating that for control torques commanded outside the *controllability envelope*, the TMF will either refrain from taking action (when the torque command is too small) or saturate (when the torque command is too large), and 2) moreover, the PDM's minimally set up canted thruster configuration is inherently unable to *directly* replicate a commanded control torque vector containing more than one nonzero component, due to *cross-coupling* between the axes. The latter explains the somewhat erratic course of some of the plots representing the actual case in Figures 6-2 to 6-4.

Comparing the actual torques generated by the thrusters in Figure 6-5 with the actual torque commands in Figure 6-4, it is noted that, at first sight, there appears to be significant discrepancy. For example, at approximately one second into the simulation, the commanded torques about the x_B -axis are only mildly positive (on the order of 10^{-2}), whereas the corresponding actual torques reach values about 100 times as large. However, these torques are actually of very short duration (most of them of minimum duration, that is: 0.02 seconds), such that the impulses produced are, at maximum, 'only' one order of magnitude larger than the impulses otherwise generated by the commanded torques during corresponding control cycles. Still, the total angular impulse imparted by the thrusters (3.866 N m s) ends up being more than five times as large as commanded (0.736 N m s). It is not straightforward to pin down the immediate cause of this overshoot, yet a plausible explanation might come from the fact that, besides the inability of the thruster configuration as proposed to achieve direct replication of multidimensional commanded torques, the pulse constraints are applied outside of the optimisation problem. The latter in fact leads to suboptimal solutions. Nonetheless, the TMF is seen to translate the commanded control torques quite effectively, as the components of the rotational state of the PDM settle below their predefined thresholds (see Table 6-2) for the first time after about 22 seconds; very close to the predefined settling time of 20 seconds. As such, it can be concluded that the TMF as proposed is correctly implemented and, in addition, seems to be operating as desired.

However, further testing reveals a caveat. Figures 6-6 and 6-7 depict the results of three

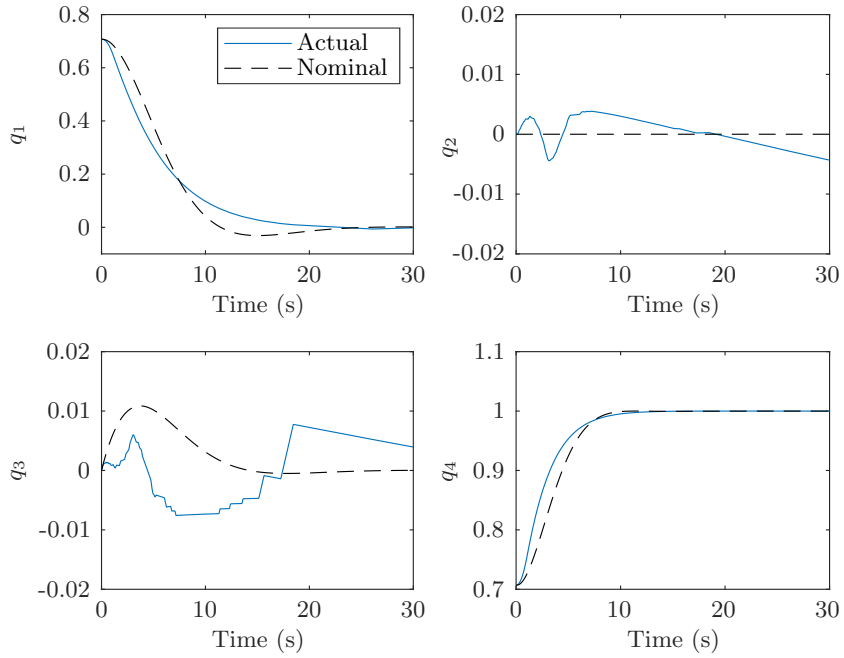


Figure 6-2: Time histories of the nominal and actual quaternions.

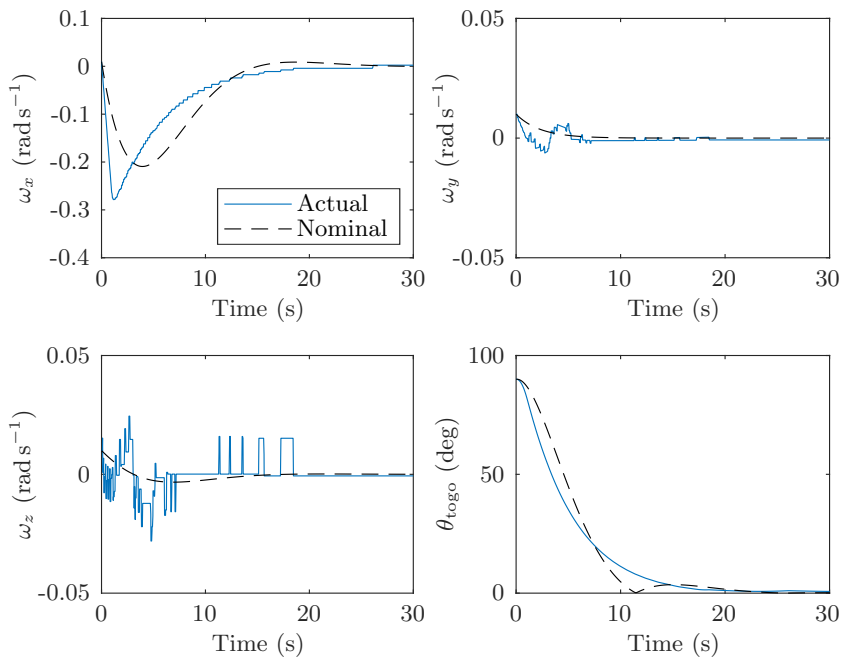


Figure 6-3: Time histories of the nominal and actual body rates and eigenangle-to-go.

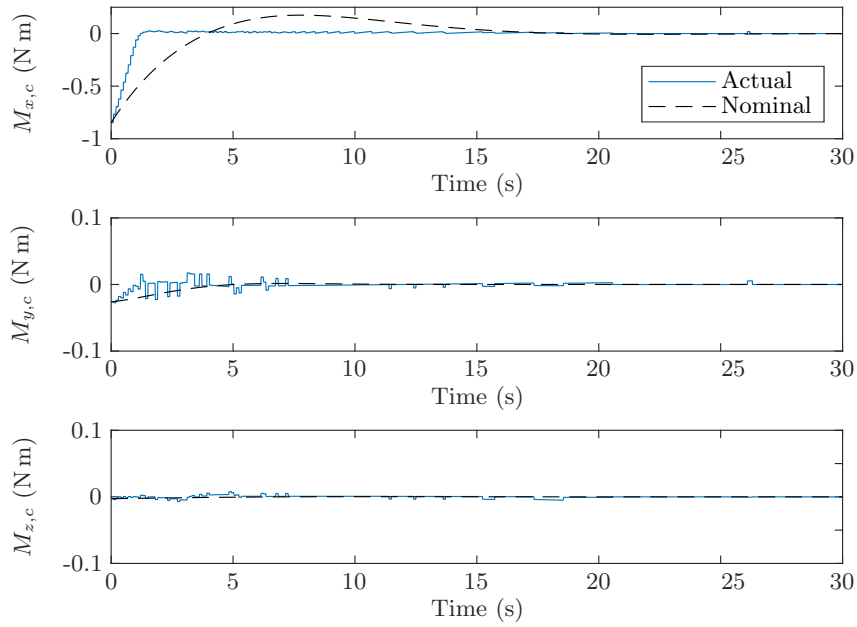


Figure 6-4: Time histories of the nominal and actual torque commands.

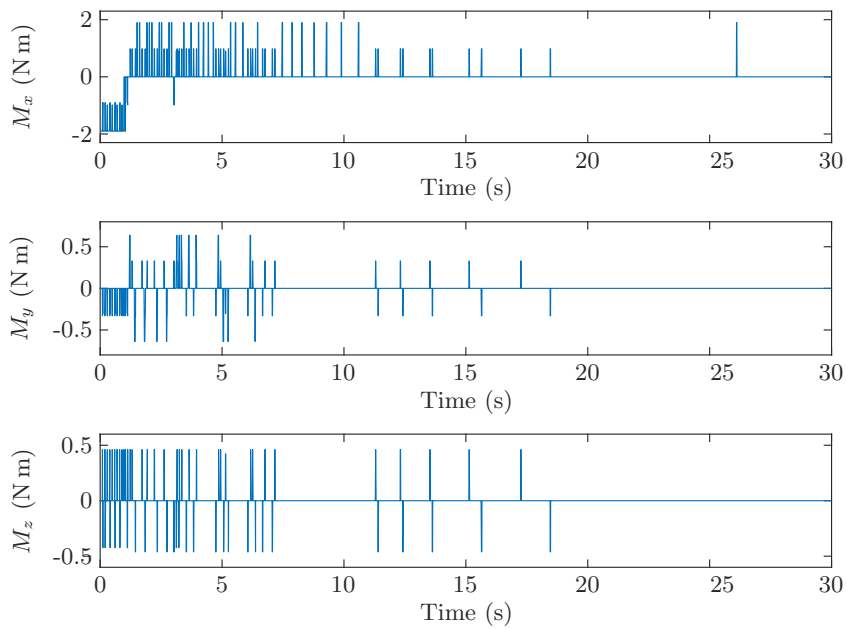


Figure 6-5: Time histories of the actual torques generated by the thrusters.

Table 6-2: Parameter values used to verify the correct implementation of the TMF as proposed.

Parameter	Value	Unit
m_{solid}	0	kg
m_{hyd}	1.0	kg
$m_{\text{hyd, ini}}$	2.1	kg
q_1, q_4	0.7071	-
q_2, q_3	0	-
$\omega_x, \omega_y, \omega_z$	0.01	rad s ⁻¹
ζ	0.707	-
μ	1	-
$q_{1,c}, q_{2,c}, q_{3,c}$	0	-
$q_{4,c}$	1	-
$\omega_{x,c}, \omega_{y,c}, \omega_{z,c}$	0	rad s ⁻¹
$\ \boldsymbol{\omega}\ _{\text{thres}}$	0.01	rad s ⁻¹
θ_{togo}	90	deg
θ_{thres}	1	deg
T_s	20	s
$\Delta t_{p, \text{min}}$	0.02	s
T_{sampling}	0.1	s

different reorientation manoeuvres executed by the PDM during Control Phase 4 (at which moment the SRM is depleted, yet the penetrator is still attached to the PDS), and the PDS during Control Phase 7 (at which moment the penetrator has been released and just the PDS remains), respectively. The results of concern are the time histories of the eigenangle-to-go and the angular velocity norm. Each reorientation manoeuvre starts from a different initial orientation, defined by a set of Euler angles (see Section 3-2); from left to right in Figures 6-6 and 6-7: $\{90^\circ, 0, 0\}$, $\{0, 90^\circ, 0\}$ and $\{0, 0, 90^\circ\}$. In generating these figures, the parameter values from Table 6-2 were used, with the exception of the initial quaternions, which are different for each manoeuvre, and $m_{\text{hydrazine}}$, which was assumed to be 0.5 kg for Control Phase 7 reorientation manoeuvres. From Figure 6-6, it is clear that the PDM proves successful in executing a Control Phase 4 reorientation manoeuvre about any of the body axes given a target settling time of 20 seconds. The PDS, on the other hand, is seen to experience difficulties performing a Control Phase 7 reorientation manoeuvre about the y_B -axis given that setting. The reason being that the torque capabilities of the PDS about the y_B -axis are significantly weaker than those of the PDM about the y_B -axis; compare the second rows of the nominal torque response matrices for Control Phase 4 and 7, respectively:

$$(\mathcal{M}_{\text{nom}})_4 = \begin{bmatrix} -0.993 & 0.993 & -0.993 & 0.993 \\ 0.334 & 0.334 & -0.334 & -0.334 \\ -0.466 & 0.466 & 0.466 & -0.466 \end{bmatrix} \text{ N m},$$

and

$$(\mathcal{M}_{\text{nom}})_7 = \begin{bmatrix} -0.619 & 0.619 & -0.619 & 0.619 \\ 0.008 & 0.008 & -0.008 & -0.008 \\ -0.432 & 0.432 & 0.432 & -0.432 \end{bmatrix} \text{ N m.}$$

Responsible for this strong decrease is the large backward shift of the CoM following the release of the penetrator. This shift (about -20 cm) causes the torques generated by thruster forces parallel to the x_B -axis to decrease, whereas those generated by thruster forces parallel to the z_B -axis – and thus going in the opposite direction – remain unchanged. The net result is that the torque capabilities about the y_B -axis diminish. This is a purely geometric issue, and hence the inability of the PDS to carry out a 90 degrees slew about the y_B -axis in 20-30 seconds has little to do with the performance of the TMF, which merely translates the control commands received into thruster commands. Rather, the *controller* should account for the different torque capabilities about each axis, and prevent control about ‘weaker’ axes as much as possible. The quaternion-error feedback controller as currently employed is unable to do as such. Clearly, in this respect, a different controller is recommended; namely one that solves an optimisation problem to generate the control commands. The development of such a controller would make an interesting topic for future work.

To improve the slew performance of the PDS about the y_B -axis, the target settling time is increased from 20 to 35 seconds. This value was determined by trial-and-error, and was found to yield acceptable responses, regardless the axis of rotation. This can be seen from Figure 6-8, depicting the results of three different reorientation manoeuvres executed by the PDS during Control Phase 7, given $T_s = 35$ s. Observing the responses, it is noted that the PDS needs about 40 seconds on average to reach an equilibrium. However, it is also seen that the target state is never reached. This is a direct result of raising the target settling time, which effectively reduces the controller gains (see Section 4-2-2) to such a degree that the torques commanded by the controller close to the target state are too small to be executed. Yet, as the Control Phase 7 reorientation manoeuvre is performed in anticipation of the FAM, for which it is only required that the front end of the PDS is pointing away from the penetrator (though preferably in a horizontal direction), a few degrees off the target state is acceptable.

6-1-2 Navigation System

The purpose of the navigation system is to process measurement data generated by the AOCS sensors in order to obtain a best estimate of the state of the spacecraft. The PDM is equipped with two sensing instruments: an inertial measurement unit (IMU) and a star tracker (see also Appendix A-2). Sensor measurements are inherently corrupted by systematic and random errors, which can be reduced by applying a filtering technique. Such techniques are generally also in place to fuse measurements from different sensors. A comprehensive design of the navigation system will not be covered in this thesis. Instead, realistic uncertainty (see Table 6-3) will be added to the propagated rotational state, such that the effects of noisy measurements and an imperfect navigation system are mimicked.

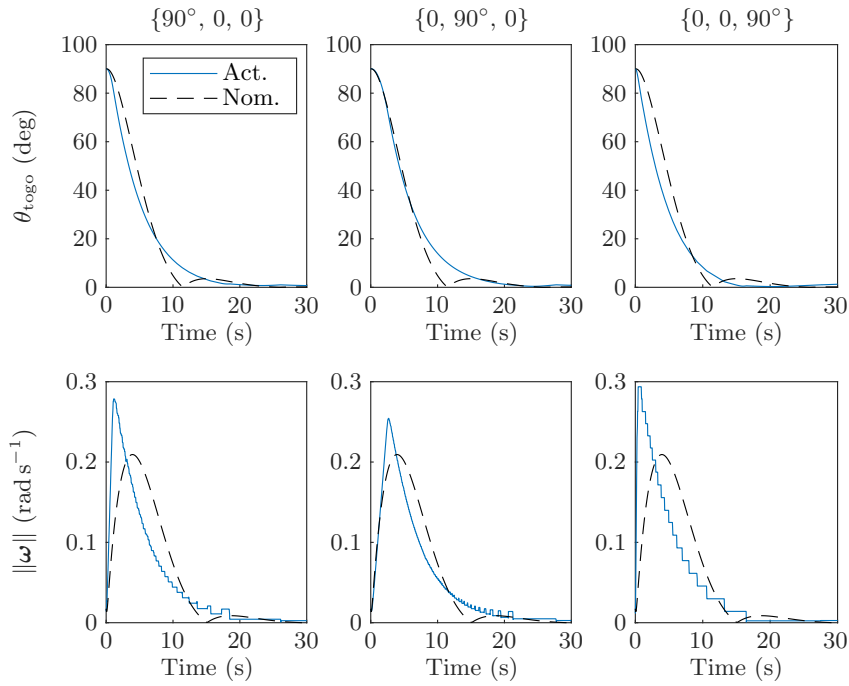


Figure 6-6: Nominal and actual time histories of the eigenangle-to-go and the angular velocity norm for three different Control Phase 4 reorientation manoeuvres; $m_{\text{hydrazine}} = 1.0$ kg.

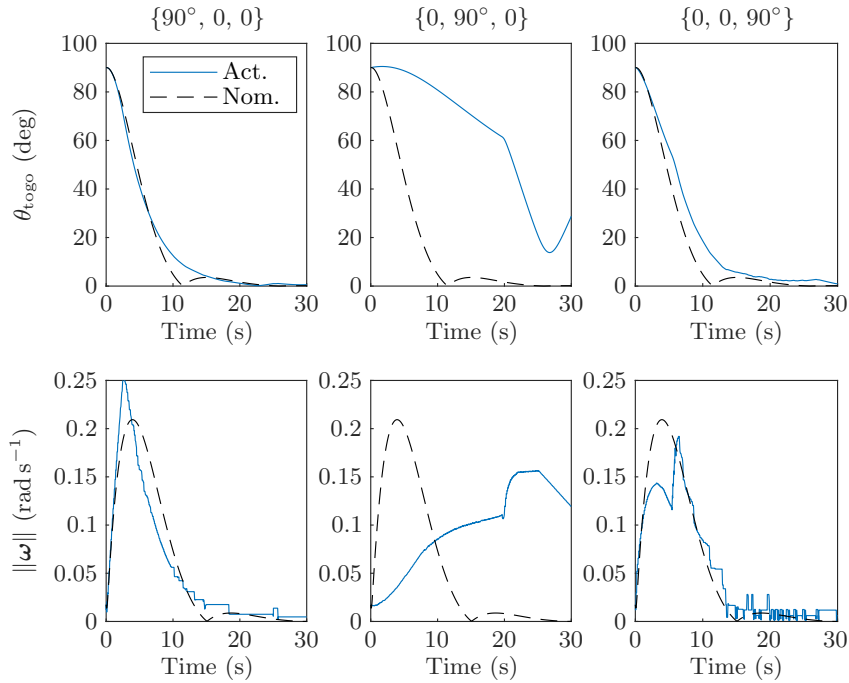


Figure 6-7: *Idem* to Figure 6-6, albeit for Control Phase 7; $m_{\text{hydrazine}} = 0.5$ kg.

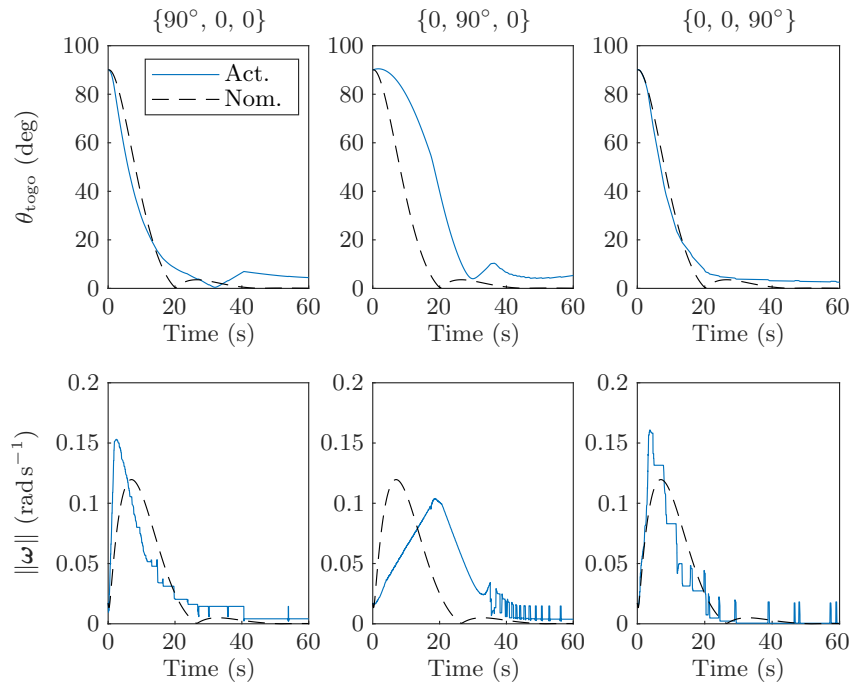


Figure 6-8: *Idem* to Figure 6-7, albeit given a target settling time of 35 seconds.

Table 6-3: Eigenangle and angular rate uncertainties caused by noisy sensor measurements.

Parameter	3-sigma	Distribution	Unit
$\delta\theta_{\text{nav}}$	0.5	$\mathcal{N}(0, 0.0278)$	deg
$\ \delta\omega_{\text{nav}}\ $	0.01	$\mathcal{N}(0, 1.11 \times 10^{-5})$	rad s^{-1}

6-2 Simulator Architecture

Figure 6-9 presents the architecture of the simulator, which was designed in Simulink. The simulator comprises the following interconnected blocks:

1. **Mission Manager.** Decides based on time-tagged Control Phases and the current ‘measured’ state of the spacecraft which Control Mode should be active. Its correct functioning was verified by inspection of the Control Phase and Control Mode histories, which matched expectations (see Figure 6-12).
2. **Controller.** Based on the Control Mode received from the Mission Manager block, the Controller block switches between Reorientation, Spin-Up/Down and Denutation algorithms, and generates a commanded control torque vector, based on the target rotational state received from the Mission Manager block. The algorithms were separately verified, in Sections 4-2-3, 4-3-1 and 4-3-2-3, respectively.

3. **Thruster Management Function.** The commanded control torque vector received from the Controller block is translated into appropriate firing durations for each thruster by the Thruster Management Function block. This is done once each control cycle of length T_{sampling} , based on the nominal thruster torque response matrix and the force drop factors received from the Force & Torque Capabilities block, see below. The Thruster Management Function block was verified in Section 6-1-1.
4. **Thrusters.** The firing duration vector generated by the Thruster Management Function block is converted into actual thruster torques by the Thrusters block, based on the momentary feed pressure calculated by the Force & Torque Capabilities block (see below), the actual position of the CoM of the spacecraft calculated by the Inertial Parameters block (see below), and the actual thruster geometry. The associated jet damping moment is also calculated, based on the actual rotational state received from the Rotational EoM PDM/PDS block (see below), the momentary moment arms and the momentary propellant mass flow. The Thrusters block was verified along with the Thruster Management Function block in Section 6-1-1.
5. **Rotational EoM PDM/PDS.** The torques produced by the Thrusters block are processed by the Rotational EoM PDM/PDS block, which propagates the rotational state of the PDM/PDS based on Equations (3.19) and (3.20). The integrator used is discussed in Section 6-3-2. The Rotational EoM PDM/PDS block was verified implicitly in Sections 4-2-3, 4-3-1, 4-3-2-3, 5-2-1-1 and 6-1-1.
6. **Navigation System Surrogate.** Adds uncertainty to the true rotational state received from the Rotational EoM PDM/PDS block, so as to simulate the presence of a navigation system. The correct functioning of this block was verified by inspection of its output.
7. **Inertial Parameters.** Based on the momentary propellant masses and the Control Phase, the Inertial Parameters block calculates the momentary total mass, nominal and actual CoM, and nominal and actual MoI of the spacecraft. This block was verified by comparing the output to values provided by CATIA.
8. **Force & Torque Capabilities.** Based on the momentary liquid propellant mass and the momentary nominal CoM of the spacecraft, the Force & Torque Capabilities block calculates the momentary thruster capabilities table (see Table 2-7), the nominal thruster torque response matrix, the feed pressure and the force drop factors. The correct functioning of this block was verified by inspection of its output.
9. **De-Orbit Manoeuvre.** Simulates the SRM burn by calculating the effective thrust in the z_B -direction and the resulting disturbance torques. The De-Orbit Manoeuvre block was verified in Section 5-2-1-1.
10. **Penetrator Release.** Simulates the release of the penetrator by adding the appropriate parts of the linear and angular tip-off velocities to the translational and rotational state vectors of the PDS and the penetrator. The correct functioning of this block was verified by close inspection of the responses for the linear and angular velocities.

11. **Fly-Away Manoeuvre.** Simulates the FAM by activating all four thrusters until the liquid propellant tank has been depleted.
12. **Translational EoM PDM/PDS.** The net forces produced by the SRM and the thrusters are processed by the Translational EoM PDM/PDS block, which propagates the translational state of the PDM/PDS based on Equation (F.4). The Translational EoM PDM/PDS block was verified in Section 5-2-1-1.
13. **Rotational & Translational EoM Penetrator.** Propagates the rotational and translational state of the released penetrator. The verified code of Blocks 5 and 12 was combined in this block. Verification was performed by inspection of the output.

It is interesting to note that Blocks 1 to 6 constitute a traditional feedback control loop. The correct functioning of the simulator architecture as a whole will be verified in Section 6-4-1.

6-3 Simulation Set-Up

For the purpose of reproducibility, this section provides a complete description of the simulation set-up. The input to the simulator is discussed in Section 6-3-1. The integrator chosen to solve the EoM is covered in Section 6-3-2. In Section 6-3-3, the general principle of a Monte Carlo simulation is briefly explained and the uncertain parameters are specified. Finally, the simulation output is discussed in Section 6-3-4.

6-3-1 Simulation Input

The input to the simulator can be divided into two groups: the *model parameters*, which represent the fixed nominal properties of the spacecraft, and the *decision variables*, which can be varied to attain the desired mission performance. In Table 6-4, an overview is provided of the nominal model parameters, which are subdivided into inertial parameters, geometric parameters and AOCs parameters. Notably, all positions are measured with respect to the G -frame. Table 6-5, in turn, presents an overview of the decision variables.

6-3-2 Integrator

Since the EoM defined in Section 3-4 and Appendix F cannot be solved analytically, a *numerical integrator* is employed to propagate the state of the spacecraft. The solutions obtained through numerical integration are approximate and discrete, and hence suffer from two types of errors: *truncation errors*, which originate from the inner workings of the integration scheme, and *rounding errors*, which arise as a result of the finite precision of the *floating-point* arithmetic used by computers to represent real numbers. The first type of error is typically on the order of $\mathcal{O}(h^n)$, where h denotes the integration step-size and n is the order of the integration scheme. The relevance of this error will thus depend on the size of these parameters. The second type of error is considered irrelevant in the context of integrating the EoM of

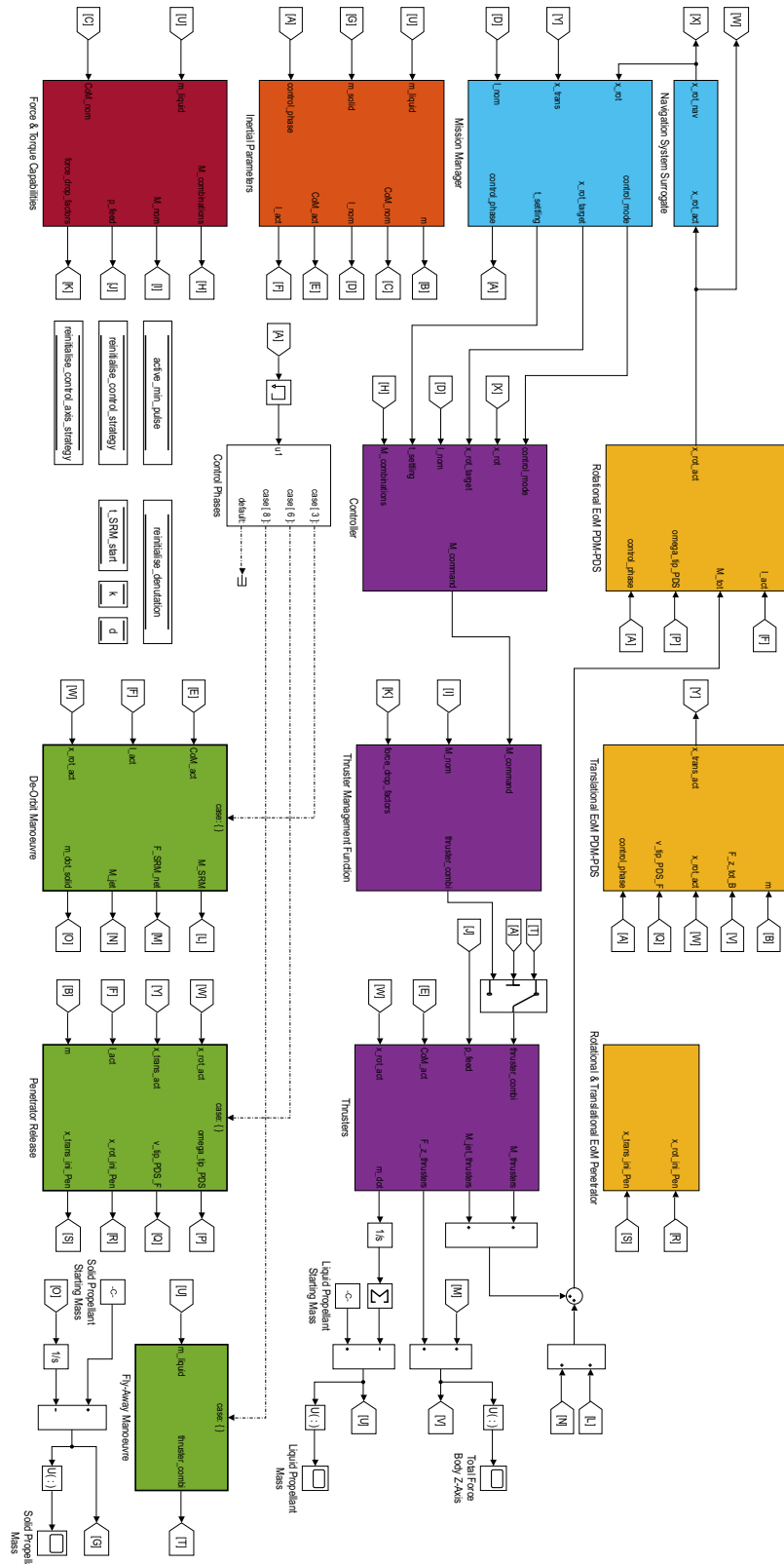


Figure 6-9: Architecture of the simulator.

Table 6-4: Overview of nominal model parameters.

Parameter	Value	Unit	Comment
Inertial Parameters			
m_{Pen}	17.6	kg	
$(z_{cm})_{\text{Pen}}^*$	0.119	m	
$(I_{xx})_{\text{Pen}}$	0.149	kg m ²	
$(I_{yy})_{\text{Pen}}$	0.149	kg m ²	
$(I_{zz})_{\text{Pen}}$	0.082	kg m ²	
m_{PDS}	28.1	kg	
$(z_{cm})_{\text{PDS}}^*$	-0.441	m	
$(I_{xx})_{\text{PDS}}$	2.553	kg m ²	
$(I_{yy})_{\text{PDS}}$	2.553	kg m ²	
$(I_{zz})_{\text{PDS}}$	0.526	kg m ²	
m_{solid}	39.0	kg	
$m_{\text{hyd, ini}}$	2.1	kg	Value at separation from Pathfinder
m_{hyd}	1.0	kg	Value at start simulation
Geometric Parameters			
r_{Pen}	0.096	m	Max. radius penetrator
r_{PDS}	0.176	m	Max. radius PDS
x_{thruster}^*	± 0.152	m	T1, T2: +; T3, T4: -
y_{thruster}^*	± 0.152	m	T2, T4: +; T1, T3: -
z_{thruster}^*	-0.660	m	
θ_{thruster}	45	deg	Thruster cant angle from z_G -axis
ϕ_{thruster}	45	deg	Thruster cant angle from x_G -axis
$z_{\text{SRM, front}}^*$	-0.433	m	
$z_{\text{SRM, throat}}^*$	-0.825	m	
$z_{\text{tank, rear}}^*$	-0.388	m	
AOCS Parameters			
V_{tank}	0.006	m ³	Tank volume
p_{max}	24	bar	Max. tank pressure
p_{min}	6	bar	Min. feed pressure
$\Delta t_{\text{p, min}}$	0.02	s	Min. pulse width

*Measured relative to the G -frame.

Table 6-5: Overview of decision variables.

Parameter	Value	Unit	Comment
Nominal Initial State			
$q_{1,0}, q_{3,0}$	0	-	
$q_{2,0}$	-0.707	-	
$q_{4,0}$	0.707	-	
$\omega_{x,0}, \omega_{y,0}, \omega_{z,0}$	0	rad s ⁻¹	
x_0, y_0	0	m	Values at start DOM
z_0	28	km	Value at start DOM
$v_{x,0}$	1704.827	m s ⁻¹	Value at start DOM
$v_{y,0}, v_{z,0}$	0	m s ⁻¹	Values at start DOM
Phase Durations			
Control Phase 1	10	s	
Control Phase 2	20	s	$\omega_{z,c} = 4\pi \text{ rad s}^{-1}$
Control Phase 3	16	s	
Control Phase 4	50	s	
Control Phase 5	20	s	$\omega_{z,c} = 4\pi \text{ rad s}^{-1}$
Control Phase 6	20	s	$v_{\text{tip}} = 1 \text{ m s}^{-1}, \omega_{\text{tip}} = 1 \text{ rad s}^{-1}$
Control Phase 7	50	s	
AOCS Parameters			
F_{ave}	3.15	N	
<i>Pressure drop factors</i>			
α_1	1	-	1 active thruster
α_2	0.96	-	2 active thrusters
α_3	0.90	-	3 active thrusters
α_4	0.83	-	4 active thrusters
Reorientation Controller			
ζ	0.707	-	Damping ratio
μ	1	-	Coupling torque damping factor
$T_{s,4}$	20	s	Control Phase 4
$T_{s,7}$	35	s	Control Phase 7
T_{sampling}	0.1	s	
Denutation Controller			
$T_{s,\text{denut}}$	10	s	For Control Phases 4 and 7
N	1	-	$\equiv 2$ pulses per nutation period
Optimal pulse width mode	ON	-	
Thresholds			
θ_{thres}	1	deg	Eigenangle threshold
$\ \boldsymbol{\omega}\ _{\text{thres}}$	0.01	rad s ⁻¹	Angular rate norm threshold
$\theta_{\text{nut, thres}}$	1	deg	Nutation angle threshold
$\omega_{z,\text{thres}}$	0.01	rad s ⁻¹	Spin-down spin rate threshold

the spacecraft, as MATLAB uses 16 digits by default to represent floating-point numbers (also referred to as the *double-precision* format). This is deemed sufficiently accurate for the type of application concerned. It should however be noted that rounding errors do cause the norm of the unit quaternion to drift away from unity, rendering the quaternion an invalid rotation. This problem is solved by re-normalising the quaternion after each integration step, through:

$$\mathbf{q} = \frac{\mathbf{q}}{\|\mathbf{q}\|} \quad (6.7)$$

There are two main types of integrators: *fixed-step* integrators, which keep h constant during the simulation, and *variable-step* integrators, which recompute h at each step based (indirectly) on the momentary rate of change of the state. Variable-step integrators can be substantially more efficient, yet fixed-step integrators are the preferred choice when simulating a model that contains algorithms designed to run on a real-time system. Therefore, the integrator used in the simulator is based on the fourth-order four-stage Runge-Kutta (RK4) scheme, which utilises an average slope to propagate state \mathbf{x}_n over one fixed integration step. The slope is obtained by taking a weighted average of four values of $f(t_n, \mathbf{x}_n)$, each calculated at different points on the interval $t_n \leq t \leq t_{n+1}$. The RK4 formula is given by (*e.g.*, Boyce & DiPrima, 2010):

$$\mathbf{x}_{n+1} = \mathbf{x}_n + h \left(\frac{k_{n,1} + 2k_{n,2} + 2k_{n,3} + k_{n,4}}{6} \right) \quad (6.8)$$

with:

$$\begin{aligned} k_{n,1} &= f(t_n, \mathbf{x}_n) \\ k_{n,2} &= f(t_n + 0.5h, \mathbf{x}_n + 0.5hk_{n,1}) \\ k_{n,3} &= f(t_n + 0.5h, \mathbf{x}_n + 0.5hk_{n,2}) \\ k_{n,4} &= f(t_n + h, \mathbf{x}_n + hk_{n,3}) \end{aligned} \quad (6.9)$$

where \mathbf{x} is the time-dependent state vector, $f(t_n, \mathbf{x}_n)$ is the time-derivative of vector \mathbf{x} at time-step n and h is the fixed step-size, which was chosen to be equal to 0.001 s for the simulator. As such, truncation errors will be on the order of 10^{-12} , and can hence be safely neglected.

6-3-3 Monte Carlo Simulations

The nominal model parameters in Table 6-4, as well as several of the decision variables in Table 6-5, are each subject to some degree of uncertainty. In order to study the effects of uncertainty on the performance of the modelled system, a so-called Monte Carlo simulation is carried out. Monte Carlo simulations provide a means to gain insight into the probability distribution of the outcome of models dealing with uncertain input. To this end, typically a large number of simulations is run. Each simulation starts with different values for the

Table 6-6: Overview of model parameter and decision variable uncertainties.

Parameter	3-sigma	Distribution	Unit
State Uncertainty			
$\delta\theta_{\text{ini}}$	3	$\mathcal{N}(0, 1)$	deg
$\ \delta\omega_{\text{ini}}\ $	0.03	$\mathcal{N}(0, 1 \times 10^{-4})$	rad s ⁻¹
$\delta\theta_{\text{nav}}$	0.5	$\mathcal{N}(0, 2.78 \times 10^{-2})$	deg
$\ \delta\omega_{\text{nav}}\ $	0.01	$\mathcal{N}(0, 1.11 \times 10^{-5})$	rad s ⁻¹
$\delta h_{\text{freefall}}$	300	$\mathcal{N}(0, 1 \times 10^4)$	m
Inertial Uncertainty			
$\delta r_{\text{cm, pen}}$	0.48	$\mathcal{N}(0, 2.56 \times 10^{-2})$	cm
$\alpha_{\delta r_{\text{cm, pen}}}$	n/a	$\mathcal{U}(0, 360)$	deg
$\beta_{\delta r_{\text{cm, pen}}}$	n/a	$\mathcal{U}(0, 360)$	deg
$\delta r_{\text{cm, PDS}}$	0.88	$\mathcal{N}(0, 8.60 \times 10^{-2})$	cm
$\alpha_{\delta r_{\text{cm, PDS}}}$	n/a	$\mathcal{U}(0, 360)$	deg
$\beta_{\delta r_{\text{cm, PDS}}}$	n/a	$\mathcal{U}(0, 360)$	deg
Thrust Uncertainty			
$\delta_{e, \text{eff}}$	0.25	$\mathcal{N}(0, 6.94 \times 10^{-3})$	deg
$\phi_{\delta_{e, \text{eff}}}$	n/a	$\mathcal{U}(0, 360)$	deg
$\delta F_{\text{thruster}}$	0.03	$\mathcal{N}(0, 1 \times 10^{-4})$	%
$\delta\theta_{\text{thruster}}$	0.25	$\mathcal{N}(0, 6.94 \times 10^{-3})$	deg
$\delta\phi_{\text{thruster}}$	0.25	$\mathcal{N}(0, 6.94 \times 10^{-3})$	deg
Tip-Off Uncertainty			
δv_{tip}	0.1	$\mathcal{N}(0, 1.11 \times 10^{-3})$	m s ⁻¹
$\delta\omega_{\text{tip}}$	0.1	$\mathcal{N}(0, 1.11 \times 10^{-3})$	deg s ⁻¹
$\phi_{\delta\omega_{\text{tip}}}$	n/a	$\mathcal{U}(0, 360)$	deg

uncertain input parameters, which are (pseudo)randomly drawn from associated probability distributions. The latter can be achieved through a *pseudorandom number generator*.

The pseudorandom number generator used for the Monte Carlo simulation in this thesis is the *Mersenne Twister*, with seed 0. Table 6-6 provides an overview of the uncertainties considered, along with their three-sigma values (where applicable) and probability distributions. For each simulation run, pseudorandom offsets are generated, which are then added to their associated nominal value. The output of each simulation, as well as the input, is stored for post-processing.

6-3-4 Simulation Output

Since the Monte Carlo simulation is carried out in the MATLAB/Simulink environment, the output of the individual simulations will be stored in .mat-format. In order to avoid memory allocation errors, all but the recurring parameters are cleared from the workspace after a run

Table 6-7: Overview of simulation output parameters.

Output Parameter	Parameter Name	Simulator Block
Commanded Torques	M_command	Controller
Transverse Angular Rate Threshold	omega_thres	Denutation Algorithm
SRM Net Force Body Z-Axis	F_z_SRM_net_B	De-Orbit Manoeuvre
SRM Mass Flow	m_dot_solid	De-Orbit Manoeuvre
SRM Jet Damping Moment	M_jet_SRM	De-Orbit Manoeuvre
SRM Disturbance Torque	M_SRM	De-Orbit Manoeuvre
Nutation Angle DOM	theta_nut_DOM	De-Orbit Manoeuvre
Force Drop Factors	force_drop_factors	Force & Torque Capabilities
Feed Pressure	p_feed	Force & Torque Capabilities
Actual CoM PDM/PDS	CoM_act	Inertial Parameters
Nominal CoM PDM/PDS	CoM_nom	Inertial Parameters
Actual Inertia Tensor PDM/PDS	I_act	Inertial Parameters
Nominal Inertia Tensor PDM/PDS	I_nom	Inertial Parameters
Total Mass PDM/PDS	m_tot	Inertial Parameters
Total Force Body Z-Axis	F_z_tot_B	Main
Liquid Propellant Mass	m_liquid_history	Main
Solid Propellant Mass	m_solid_history	Main
Control Mode	control_mode_vs_time	Mission Manager
Control Phase	control_phase_vs_time	Mission Manager
Target Rotational State	x_rot_target	Mission Manager
Measured Rotational State PDM/PDS	x_rot_measured	Navigation System Surrogate
Rotational State Penetrator	x_rot_Pen	Rot. & Trans. EoM Penetrator
Translational State Penetrator	x_trans_Pen	Rot. & Trans. EoM Penetrator
Total Torque	M_tot	Rotational EoM PDM/PDS
Actual Rotational State PDM/PDS	x_rot_actual	Rotational EoM PDM/PDS
Thruster Combinations	thruster_combi	Thruster Management Function
Thruster Force Body Z-axis	F_z_thrusters_B	Thrusters
Thrusters Mass Flow	m_dot_thrusters	Thrusters
Thrusters Jet Damping Moment	M_jet_thrusters	Thrusters
Thruster Torque	M_thrusters	Thrusters
Total Force Inertial Frame	F_tot_F	Translational EoM PDM/PDS
Actual Translational State PDM/PDS	x_trans_actual	Translational EoM PDM/PDS

has been concluded. Table 6-7 presents a complete overview of the simulation output. The collected raw data contains the information needed to answer the research question, which is extracted during two post-processing steps, further elaborated in Section 6-4.

6-4 Simulation Results

In this section, the simulation results are presented. Section 6-4-1 covers the results of a nominal-case system test, verifying the correct functioning of the simulator. Then, in Section 6-4-2, the results of the Monte Carlo simulation are discussed. Also, the performance of the controller under off-nominal conditions is evaluated.

6-4-1 Nominal Case

In order to verify the correct functioning of the simulator as a whole, a nominal-case system test is performed, using the parameters from Tables 6-4 and 6-5. In the nominal case, the simulation input is assumed to be free from uncertainty.

A three-dimensional representation of the descent trajectory, resulting from the nominal-case simulation, is depicted in Figure 6-10. It should be noted that the trajectory shown starts at ignition of the SRM. The first three plots in Figure 6-11 represent side views of Figure 6-10. The fourth plot (bottom right) is a zoom in on the first plot (top left), showing the absolute distance between the landing sites of the PDS and the penetrator. In the top-right plot of Figure 6-11, it can be seen that the landing occurs slightly ahead of the along-track position reached at the end of the DOM, implying that the PDM had a velocity in the negative along-track direction during its free-fall descent to the surface. This velocity surplus is caused by parasitic velocity increments in the z_B -direction, generated as a by-product of the spin-up and spin-down manoeuvres. These velocity increments were not accounted for when determining the amount of solid propellant required to cancel the orbital velocity. This, in itself, is not considered to be really problematic, as in the off-nominal case, the efficiency of the DOM will be less than 100%, rendering such velocity increments a form of compensation.

In Figure 6-12, the nominal time histories of the rotational state variables of the PDM/PDS are shown. For reference, the time histories of active control phases and control modes are also depicted. Contrary to Figures 6-10 and 6-11, the plots in Figure 6-12 cover the entire second phase of the descent scenario. It is noted that the penetrator lands after 217.66 seconds from the start of the simulation; only slightly before the PDS, which lands after 217.72 seconds. This very subtle difference of less than one-tenth of a second is traced back to the release of the penetrator, where the penetrator is pushed away from the PDS, gaining some velocity, and the PDS endures a recoil, losing some. Although this loss is amply made up for during the spin-down, it is still the penetrator that reaches the surface earlier, in the nominal case.

Observing the first plot in Figure 6-12, it is easy to distinguish between the reorientation manoeuvres, which are characterised by relatively slowly changing quaternion elements, and the minor-axis spin manoeuvres, which are associated with rapidly oscillating quaternion elements. The minor-axis spin manoeuvres can also be recognised from the second plot, where it is seen that the angular velocity about the z_B -axis increases towards the target spin rate during the spin-up, remains constant during the actively controlled subsequent spin, and finally decreases to nearly zero during the spin-down. The third and fourth plot in Figure 6-12 confirm the correct functioning of the mission manager logic, seeing the control phases and control modes switch as intended.

The first plot in Figure 6-13 shows the time history of the thruster-generated torques. Clearly noticeable are two periods of increased control activity about all three axes. Chronologically, these periods designate the reorientation manoeuvres performed during Control Phase 4 and Control Phase 7. The ‘rectangular’ responses seen spread across the plot represent the spin-up manoeuvres (when positive) and spin-down manoeuvres (when negative). Notably, said responses coincide with the ‘spikes’ observed from the second plot in Figure 6-13, representing the time history of the Coriolis moments induced by thruster firings. During the spin-up

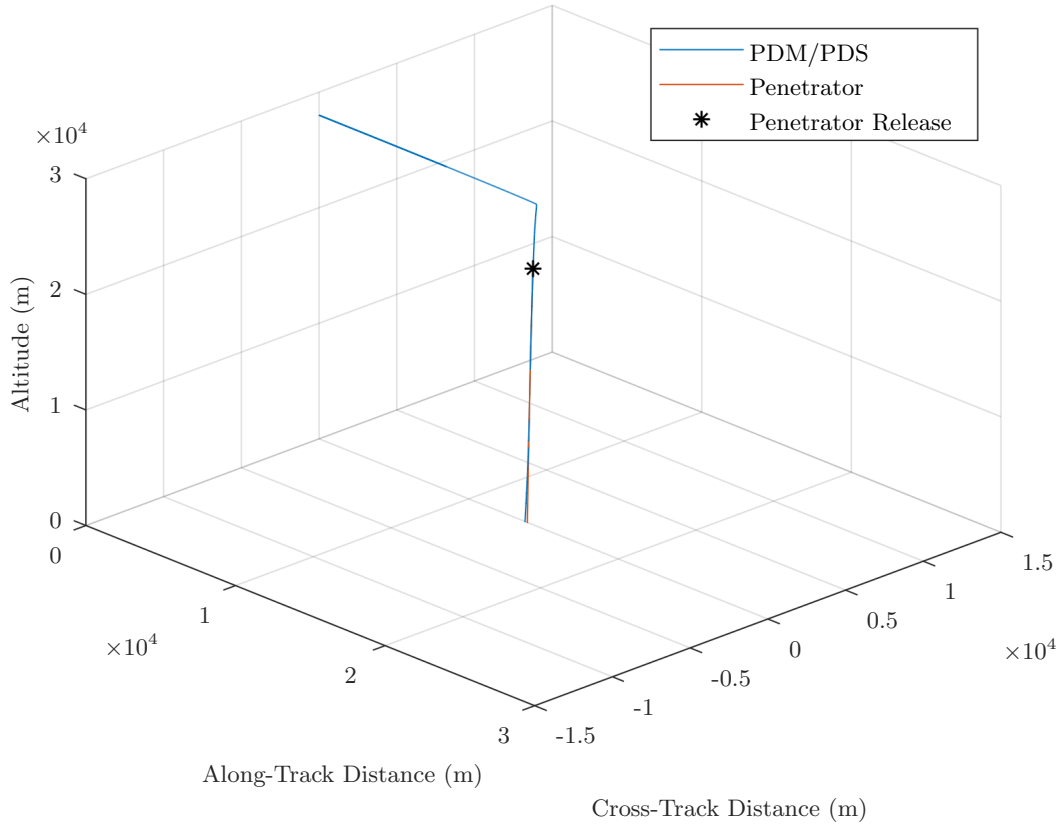


Figure 6-10: Nominal descent trajectory of the PDM/PDS and the penetrator. The point at which the penetrator separates from the PDS is denoted by an asterisk.

manoeuvres, a Coriolis moment solely about the z_B -axis arises, which – although negligibly small – is seen to increase in the negative direction. This is expected. First of all, Equation (3.14) dictates that when the mass flow and angular velocity are both nonzero, and the position vector of the centre of mass flow and the angular velocity vector are not collinear, the Coriolis moment will be nonzero. The Coriolis moments emerging about the x_B - and y_B -axes cancel out in this case, because a spin-up (or spin-down, for that matter) is achieved using a diagonal pair of thrusters, whose x_B and y_B position coordinates are mutually mirrored, nominally. Secondly, Equation (3.14) shows that the Coriolis moment (which is assumed to be only caused by the jet damping effect, see Section 3-4-1) is proportional to the angular rate, which increases during a spin-up. As such, the Coriolis moment also increases, albeit, in the opposite direction – hence its damping effect. Conversely, during a spin-down, the magnitude of the Coriolis moment is seen to decrease, as a result of a decreasing angular rate.

In the third plot of Figure 6-13, which represents the time history of thruster forces in the z_B -direction, positive responses can be observed during the spin-up and spin-down manoeuvres. It is these forces that underlie the aforementioned parasitic velocity increments. It is also interesting to note that activating all four thrusters during the FAM, which starts at

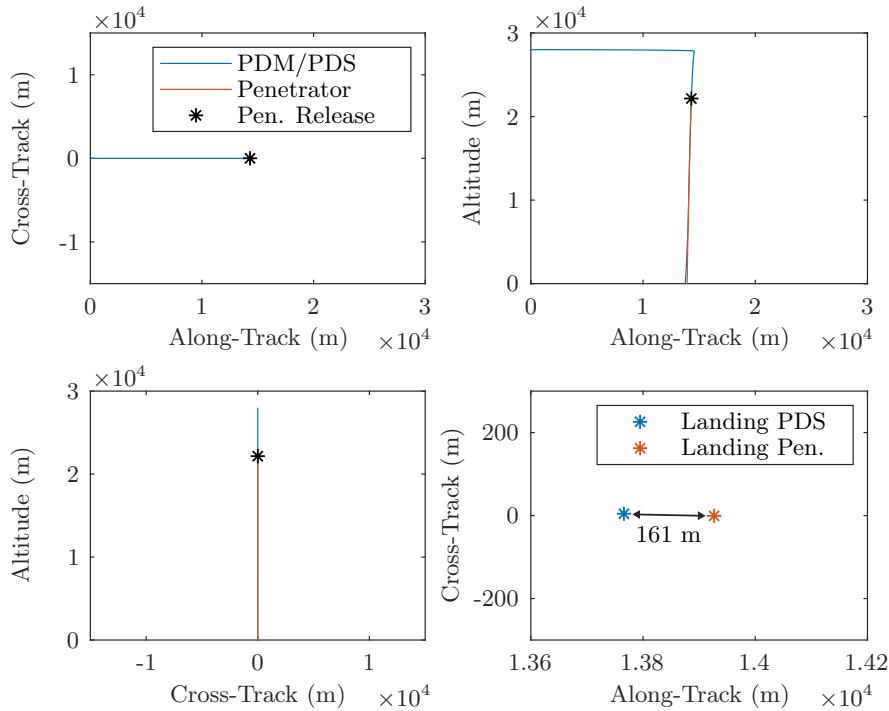


Figure 6-11: Side views of Figure 6-10, and a close-up of the landing area of the PDS and the penetrator (bottom right).

approximately 185 seconds into the simulation, does not produce twice as much thrust as two thrusters do. This illustrates the effect of the pressure drop that occurs when multiple thrusters are simultaneously active. Also, the thrust level is seen to gradually decrease during the FAM, which is a direct consequence of the RCS operating in a blow-down mode. Lastly, in the fourth and fifth plot of Figure 6-13, the time histories of the hydrazine mass and the tank pressure are depicted, respectively. As expected, they show a similar downward course, where the steepness of the different slopes observed depends on the number of thrusters active at that time.

In Figure 6-14, the time histories of the inertial parameters are plotted, along with the time history of active control phases, for reference. The first plot of Figure 6-14 concerns the total mass of the spacecraft, which starts at 85.7 kg. This is 1.1 kg less than the actual starting mass (see Table A-1) – a reduction equivalent to the amount of liquid propellant consumed during the first phase of the descent scenario, which is not simulated. During the DOM (Control Phase 3), 39.0 kg of solid propellant is burned in less than 16 seconds. This event can be recognised as a steep decrease in the total mass of the spacecraft, which indeed ends up at 46.7 kg after the SRM burns out. Lastly, 116 seconds into the simulation, there is a sudden drop in the total mass of the spacecraft, which is caused by the release of the penetrator (Control Phase 6). From the second and third plot in Figure 6-14, representing the time histories of the CoM and MoI of the spacecraft, respectively, similar phenomena can be observed at

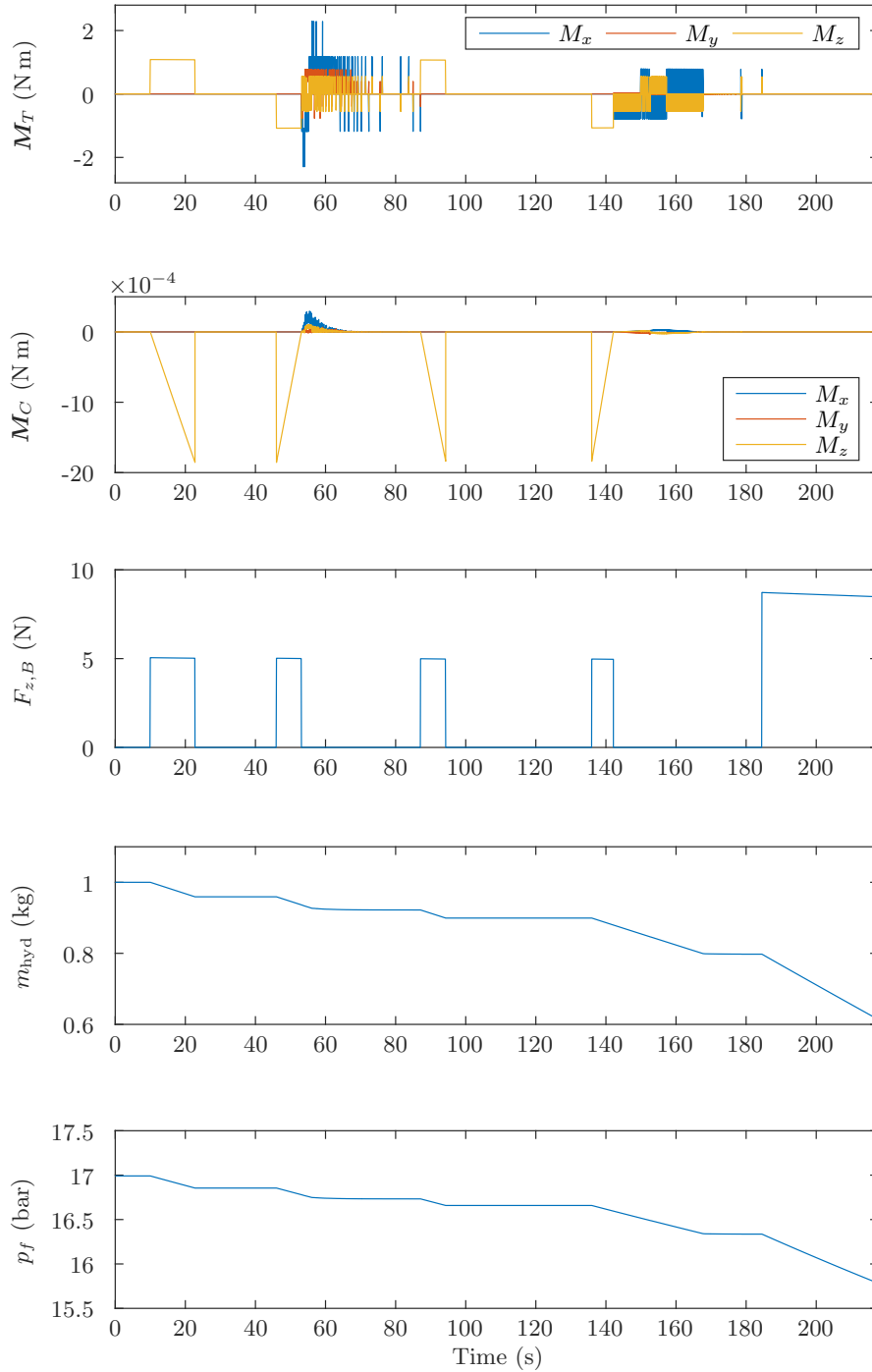


Figure 6-13: Nominal time histories of the thruster-generated torques, the jet damping moment, the force along the z_B -axis, the hydrazine mass and the tank pressure.

Table 6-8: Descent parameters for the nominal case.

Descent Parameter	Symbol	Value	Unit
Eigenangle Offset			
<i>Control Phase 1</i>	$\epsilon_{\theta,1}$	0	deg
<i>Control Phase 4</i>	$\epsilon_{\theta,4}$	0.797	deg
<i>Control Phase 7</i>	$\epsilon_{\theta,7}$	0.204	deg
Angular Rate Offset			
<i>Control Phase 1</i>	$\epsilon_{\omega,1}$	0	rad s ⁻¹
<i>Control Phase 4</i>	$\epsilon_{\omega,4}$	0.010	rad s ⁻¹
<i>Control Phase 7</i>	$\epsilon_{\omega,7}$	0.011	rad s ⁻¹
DOM Efficiency	η_{DOM}	100	%
Propellant Consumption	Δm_{hyd}	0.383	kg

the epochs mentioned. Note that the CoM gradually moves forward during the DOM, which improves control capabilities about the y_B -axis (see Section 6-1-1), and then falls backward when the penetrator is released, significantly diminishing said control capabilities. On a final note: the inertial parameters prove to vary only very mildly during rotational manoeuvres.

To assess the performance of the controller in the nominal case, a first post-processing step is applied to obtain the results for the *descent parameters*. Table 6-8 presents these descent parameters, which consist of the eigenangle offsets and angular rate offsets at the end of each reorientation manoeuvre, as well as the impulse efficiency rate of the DOM and the amount of liquid propellant consumed during the second phase of the descent scenario. The eigenangle offsets are obtained through Equation (3.2b), using the scalar part of the error quaternion, which is calculated by Equation (4.3). The angular rate offsets are calculated by simply taking the norm of the momentary angular velocity vector (as the target angular rate is zero). The DOM efficiency is determined by Equation (5.3). Lastly, the difference between the starting mass and end mass of the liquid propellant yields the propellant mass consumed.

Inspecting the results presented in Table 6-8, the first thing to note is that the offsets at the end of Control Phase 1 are zero. This is because the nominal initial state already matches the target state. Secondly, it is seen that the eigenangle offsets at the end of Control Phase 4 and Control Phase 7 are both below 1°, the threshold value for the eigenangle (see Table 6-5). In addition, the angular rate offsets are observed to be on or very close to the threshold value of 0.01 rad s⁻¹. As such, it is concluded that the controller performs the reorientation manoeuvres as desired. No conclusion can be drawn as to the performance of the controller in regard to denutation, as it turns out that in the nominal case, no significant nutational motion arises. Denutation manoeuvres will be further investigated in Section 6-4-2. Lastly, it can be seen from Table 6-8 that the efficiency of the DOM is 100%, which is expected for the nominal case, and the propellant mass consumed amounts to 0.383 kg, which is much lower than the 1.0 kg of liquid propellant allotted to the second phase of the descent scenario. As a result, the amount of liquid propellant could be slightly reduced.

To assess whether the penetrator has in fact landed successfully, success criteria have elabo-

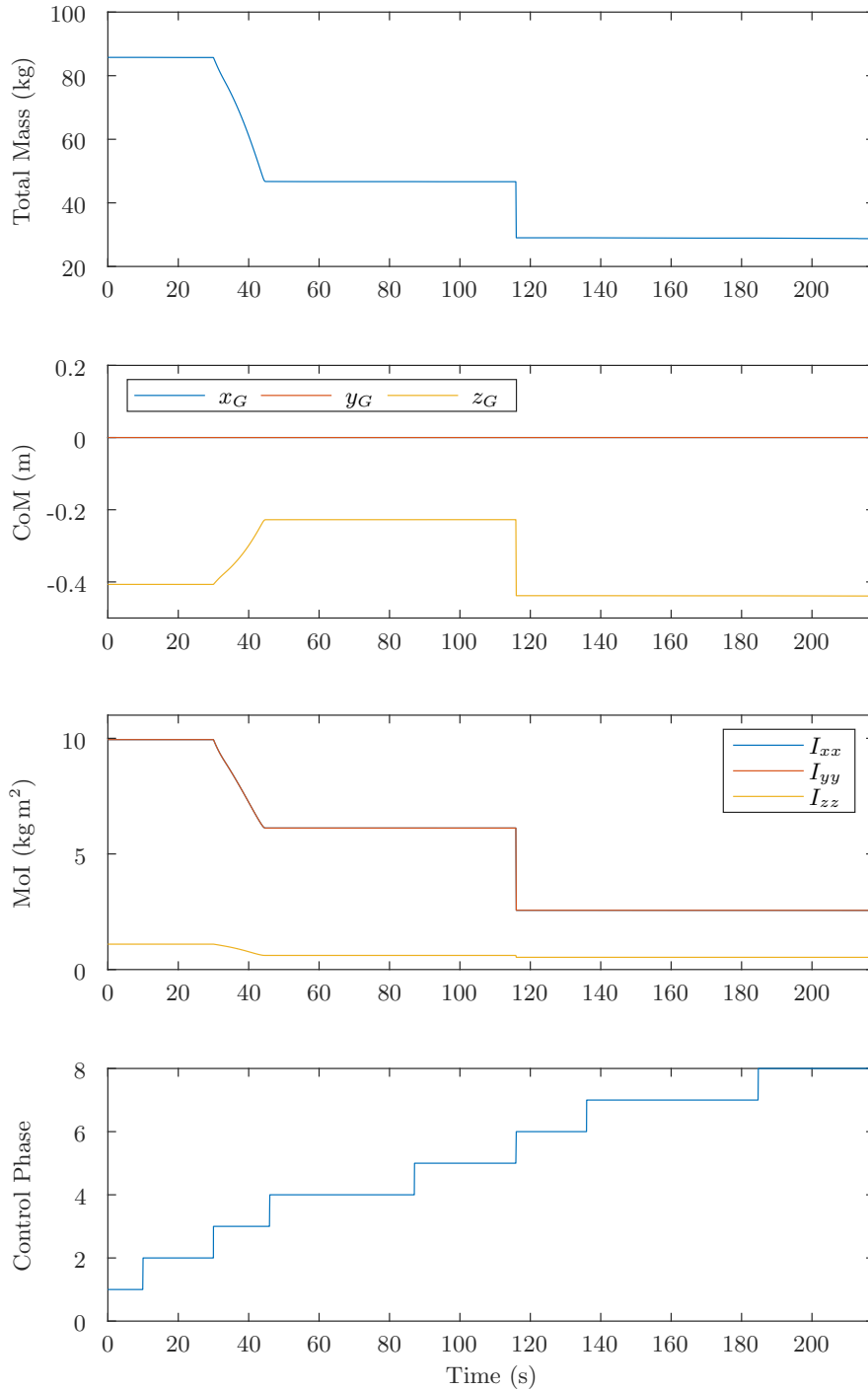


Figure 6-14: Nominal time histories of the total mass, the CoM with respect to the G -frame and the Mol with respect to the B -frame, along with the time history of active control phases.

Table 6-9: Criteria for a successful penetrator landing.

Landing Parameter	Symbol	Value	Unit
Nadir Angle	η	< 10	deg
Attack Angle	α	< 5	deg
Distance from PDS	$\Delta x_{\text{landing}}$	> 50	m
Impact Velocity	v_{landing}	< 315	m s^{-1}

rately been defined in Appendix B. For convenience, they are summarised in Table 6-9. The *landing parameters* of concern are presented in Table 6-10, and consist of four key angles, which are defined in Figure B-1, as well as two parameters of translational nature, *i.e.*, the landing distance achieved between the PDS and the penetrator and the impact velocity.

In order to find the results for the landing parameters, a second post-processing step is applied. The key angles related to penetration can be deduced from their associated vector pair, see Figure B-1. For example, the nadir angle is defined as the angle between the z_B -axis, whose unit vector is given by $[0, 0, 1]^T$ with respect to the B -frame, and the local vertical \mathbf{Z}_F , which is given by $[0, 0, -1]^T$ and expressed relative to the F -frame. Transforming the unit vector in the direction of the z_B -axis to the F -frame using Equations (E.1) and (E.2), along with the quaternion elements just prior to impact, gives \mathbf{Z}_B . The nadir angle η between the two vectors \mathbf{Z}_B and \mathbf{Z}_F can then best be obtained by (*e.g.*, Acampora et al., 2020, p. 78):

$$\eta = \text{atan2}(\|\mathbf{Z}_B \times \mathbf{Z}_F\|, \mathbf{Z}_B \cdot \mathbf{Z}_F) \quad (6.10)$$

where `atan2` is the *four-quadrant inverse tangent*, a built-in MATLAB function used to avoid the ambiguities encountered with regular `atan`. In a similar fashion, the remaining key angles can be calculated. The landing distance between the PDS and the penetrator can be obtained by taking the norm of the vector difference between the mutual x_F - and y_F -coordinates of both position vectors. Lastly, taking the norm of the velocity vector just prior to impact yields the impact velocity.

The results for the nominal landing parameters are presented in Table 6-10, from which it can be concluded that the penetrator landed successfully: the resulting nadir angle and attack angle are both well below their maximum allowed value, the landing distance achieved between the PDS and the penetrator amply exceeds the minimum value defined, and the impact velocity is, as planned, 300 m s^{-1} . In Figure 6-15, the time histories of the rotational state variables of the penetrator, the key angles and the relative distance and velocity between the PDS and the penetrator are plotted. In the first plot, quaternion elements q_1 and q_2 are seen to oscillate about the zero line, which is the result of a positive spin about the z_B -axis, see the second plot. More difficult to notice is that quaternion elements q_3 and q_4 also oscillate, due to the angular rates about the x_B - and y_B -axes being slightly nonzero. Better visible proof of this can be found in the third plot of Figure 6-15, where it is seen that the nutation angle is slightly larger than zero. This also explains the oscillating behaviour of the nadir angle and attack angle, which both vary as a function of \mathbf{Z}_B on the nutation cone. The decreasing

Table 6-10: Penetrator landing parameters for the nominal case.

Landing Parameter	Symbol	Value	Unit
Nadir Angle	η	0.724	deg
Attack Angle	α	0.469	deg
Descent Angle	δ	0.712	deg
Nutation Angle	θ_{nut}	0.137	deg
Distance from PDS	$\Delta x_{\text{landing}}$	161	m
Impact Velocity	v_{landing}	300	m s^{-1}

trend observed for the attack angle and the descent angle during the penetrator's passively stable free-fall descent to the surface is attributed to an increasing velocity in the negative z_F -direction, which changes the direction of the velocity vector. This was already anticipated for in formulating the target state for the reorientation manoeuvre of Control Phase 4 (see Section 5-2-2-2), which predominantly determines the final attitude of the penetrator. Finally, in the fifth plot of Figure 6-15, which represents the relative velocity between the PDS and the penetrator, it is seen that immediately after separation, there is a positive relative velocity along the z_B -axis of 1 m s^{-1} , which is equal to the linear tip-off velocity defined in Table 6-5. After 20 seconds of drift, which indeed creates a relative distance of 20 m between the PDS and the penetrator (see the fourth plot in Figure 6-15), the relative velocity decreases to zero as the PDS performs a spin-down in anticipation of the reorientation manoeuvre of Control Phase 7. As was mentioned multiple times throughout this report, spin-up/down manoeuvres also impart a velocity change in the positive z_B -direction. Lastly, when Control Phase 8 sets in at around 185 seconds into the simulation, the relative distance and velocity between the PDS and the penetrator are seen to increase due to the FAM. Hence, considering all of the above, it can be concluded that the nominal-case system test was successful.

6-4-2 Off-Nominal Cases

In order to investigate the sensitivity of the system to off-nominal conditions, a 1000-sample Monte Carlo simulation is carried out. This particular number of samples was chosen so as to maintain a proper balance between representative statistical results and computation time. Using the parameters from Tables 6-4 and 6-5, along with their associated uncertainties listed in Table 6-6, the Monte Carlo simulation is executed. The observations made from the results of the Monte Carlo simulation are discussed in Section 6-4-2-1. Then, in Section 6-4-2-2, a statistical analysis is conducted, in an attempt to identify those factors that affect the performance of the system the most.

6-4-2-1 Observations

In Figure 6-16, the penetrator landing sites resulting from the Monte Carlo simulation are plotted. In the figure, successful landings are represented by blue dots, whereas orange dots designate failed landings. For reference, the nominal landing site (see also Figure 6-10) is

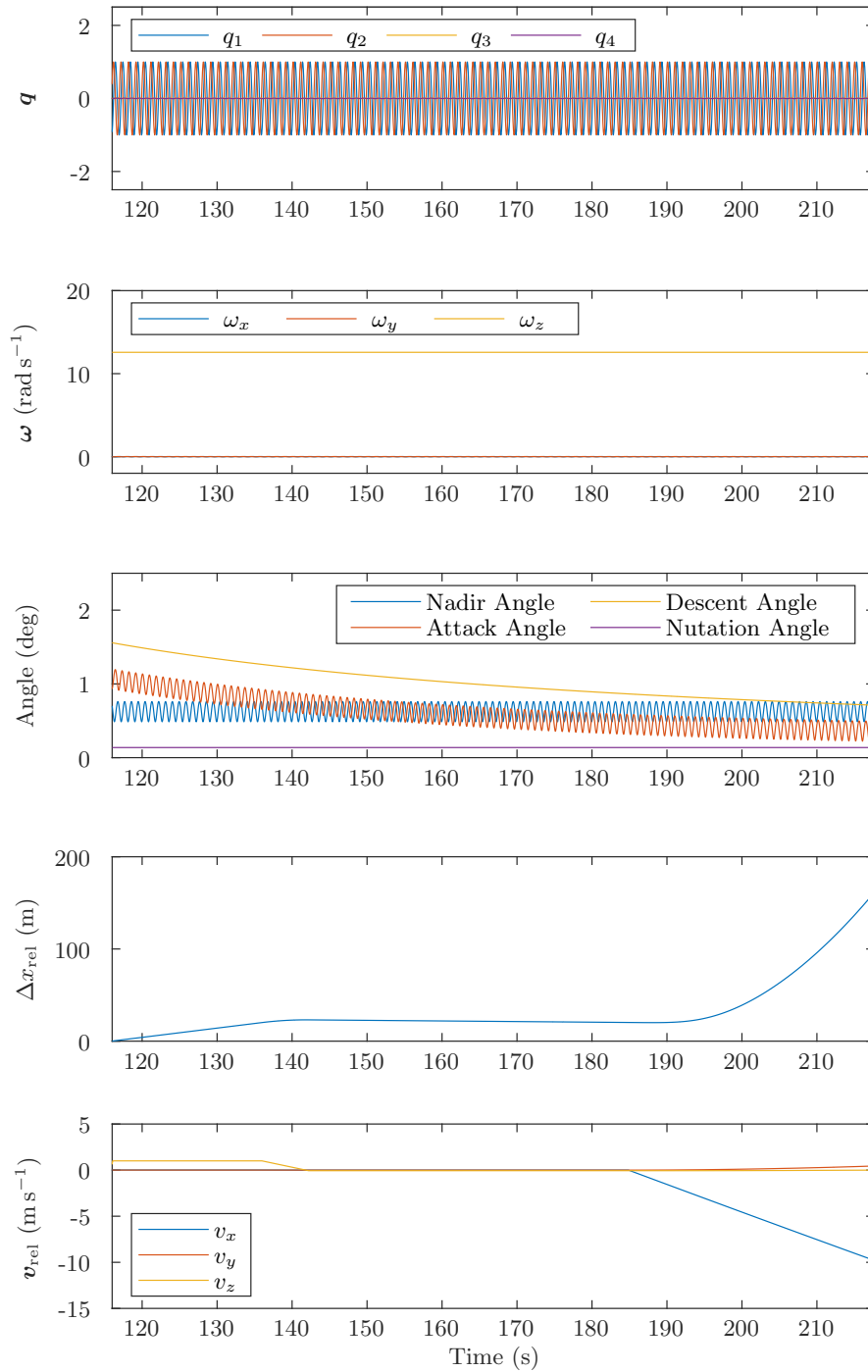


Figure 6-15: Nominal time histories of the rotational state variables of the penetrator, the key angles and the relative distance and velocity between the PDS and the penetrator.

Table 6-11: Penetrator landing success and failure rates related to the local surface slope, based on numerical data from a 1000-sample Monte Carlo simulation. Note that the success rate does not increase further below 10 degrees.

Local Slope	Max. Nadir Angle	Success Rate	Failure Rate
20°	10°	58.5%	41.5%
10°	20°	74.2%	25.8%
0°	30°	74.2%	25.8%

marked by an asterisk. The landing parameters for each individual sample were obtained by applying the relevant post-processing step described in Section 6-4-1. Evaluating the obtained results against the success criteria listed in Table 6-9, it can be concluded that, from a descent-and-landing perspective, the success rate of the mission is 58.5%. Considering that in spaceflight, it is conventional to design to a ‘three-sigma’, *i.e.*, 99.7% success rate (Lorenz, 2011), this value is rather low. The success rate can be artificially boosted to 74.2%, when assuming a local slope of 10°, instead of 20°. This allows for an increased tolerance on the nadir angle, which, so it appears, has a significant positive influence on the success rate. Notwithstanding, from Table 6-11, it can be seen that increasing the tolerance even further does not deliver additional improvements. Through a statistical analysis, an attempt will be made at revealing the key factors ultimately driving the success rate of the mission.

That said, first some remarks in regard to Figure 6-16 are made. What immediately stands out when observing Figure 6-16, is the imaginary parabolic line beyond which the overwhelming majority of the landings take place. This rather non-conventional footprint can be attributed to a non-conventional descent trajectory, involving a de-orbit manoeuvre which reduces the orbital velocity to zero, 28 km above the surface. Given that the SRM performing this manoeuvre is loaded accordingly, there are only two ways in which the PDM could eventually gain speed in the *negative* along-track direction: firstly, through parasitic velocity increments imparted during the spin-up manoeuvre in anticipation of the DOM, as well as during the spin-down manoeuvre afterwards (as was seen in Section 6-4-1); secondly, when the DOM is performed at a higher altitude than expected, implying a lower orbital velocity, which will lead to an overcompensating SRM burn. Regarding the latter, it is noted that the three-sigma value for the altitude offset is assumed to be 300 m, see Table 6-6. At a worst-case 28.3 km altitude, the orbital velocity is only 0.2 ms^{-1} less than at 28 km. Concluding, the PDM cannot gain substantial velocity in the negative along-track direction, which explains why there are no landings observed substantially ahead of the nominal landing site.

The parabolic shape of the landing footprint can be explained as follows. When the orientation of the PDM is slightly off during the DOM, both radial and cross-track velocities can occur. In such cases, the orbital velocity will not be fully cancelled and a residual velocity in the positive along-track direction remains. Generally, the larger the radial and/or cross-track velocities, the larger the residual along-track velocity. Larger velocities will in turn lead to larger distances, which is what can be observed from Figure 6-16. Inspection of some of the outliers revealed that those beyond the imaginary parabolic line had an upward radial velocity, giving them more ‘airtime’ to traverse a larger distance, whereas those ahead of this line were

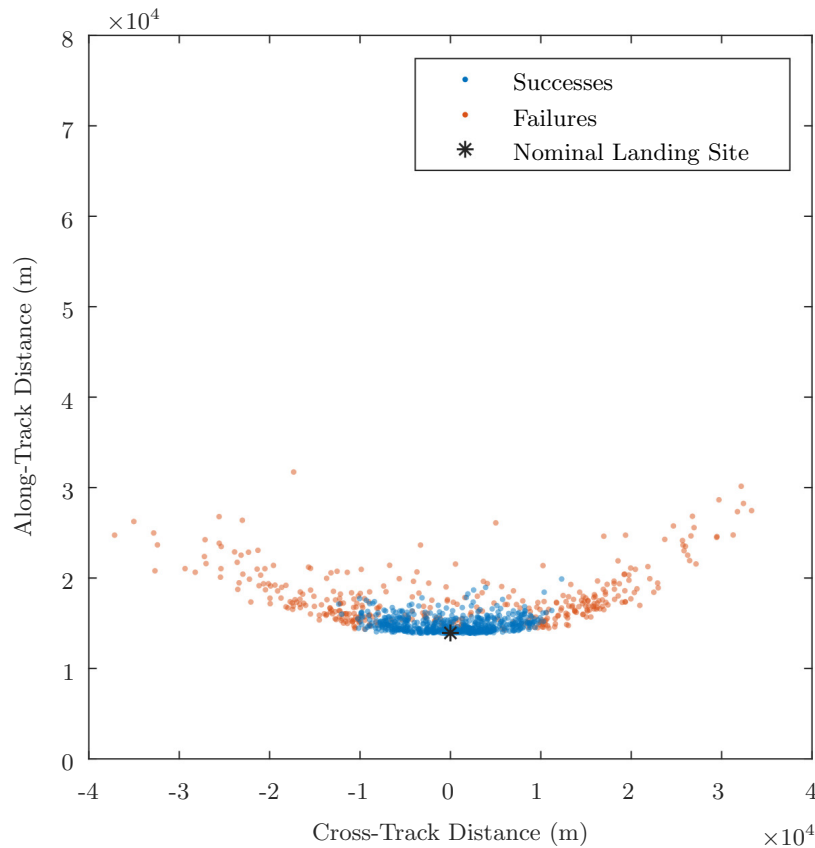


Figure 6-16: Penetrator landing sites resulting from a 1000-sample Monte Carlo simulation. Based on the success criteria defined in Table 6-9, the success rate is 58.5%. Relevant statistics are presented in Table 6-12.

affected by the DOM in the downward radial direction, resulting in a premature landing.

Further inspection of the output of the Monte Carlo simulation revealed some noteworthy off-nominal phenomena. First of all, it was seen with many of the samples that, during the DOM, the spin rate would either increase or decrease. Figure 6-17, for example, shows a decreasing spin rate for sample 93 in its first plot. Responsible for this decrease is a negative torque about the z_B -axis, which, as can be seen from the second plot in Figure 6-17, has a shape consistent with the thrust curve of the SRM (see Figure 2-6). The disturbance torque about the z_B -axis was able to arise due to misalignment of the principal axes, meaning that the principal axes do not coincide with the axes of the B -frame. Equivalently it can be stated that the products of inertia were nonzero, leading to an unbalanced condition. Such unbalance can directly be attributed to an offset CoM position. The stronger the offset, the stronger the change in spin rate.

On a final note regarding Figure 6-17, in the second plot, some erratic behaviour can be observed in the period between 50 and 56 seconds. This is caused by irregularity in thruster

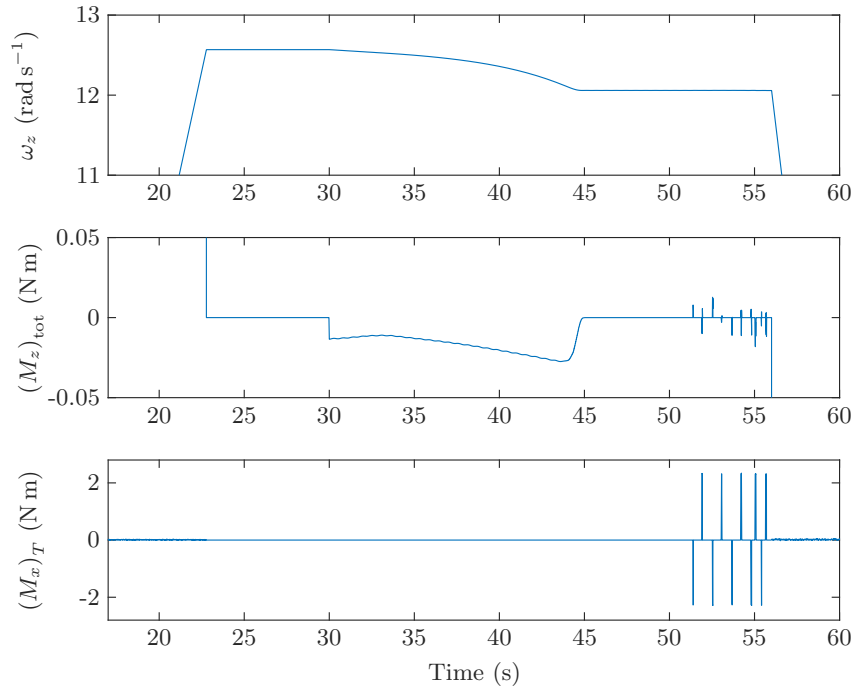


Figure 6-17: Time histories of the angular rate about the z_B -axis, total torque about the z_B -axis and thruster torques about the x_B -axis, around the period of the DOM. The output is associated with Monte Carlo sample 93.

performance, which was assumed to be as high as 3% of the nominal performance (see Table 6-6). During this period, the PDM executes a denutation manoeuvre, which can be recognised from the spikes in the third plot of Figure 6-17, representing the time history of the thruster torques about the x_B -axis. As thrust levels vary irregularly per thruster, firing them in pairs with the intention to generate a torque solely about the x_B -axis unintentionally induces torques about the z_B -axis (and y_B -axis). This is reflected in the second plot of Figure 6-17. Although more difficult to see, the third plot also shows traces of thruster roughness. That is, at the start of the curve, when a spin-up manoeuvre is carried out, and at the end, during a spin-down manoeuvre.

Another noteworthy off-nominal issue often encountered in the sample set, is the unfortunate ineffectiveness of the denutation algorithm in the presence of (larger) inertia uncertainty. To illustrate this, the first plot in Figure 6-18 depicts the time histories of the transverse angular rates around the period of release of the penetrator, associated with sample 93. From this plot, it can be clearly seen that, while the penetrator is still attached to the PDS, the velocities transverse to the spin-axis oscillate about separate nonzero means. Following the spin-up at 104 seconds into the simulation, the response for the angular rate about the x_B -axis is seen to initially cross the zero line periodically. As can be observed from the second plot in Figure 6-18, which represents the time history of the thruster torques about the x_B -axis, these zero crossings (in conjunction with the threshold crossings) trigger the denutation algorithm four

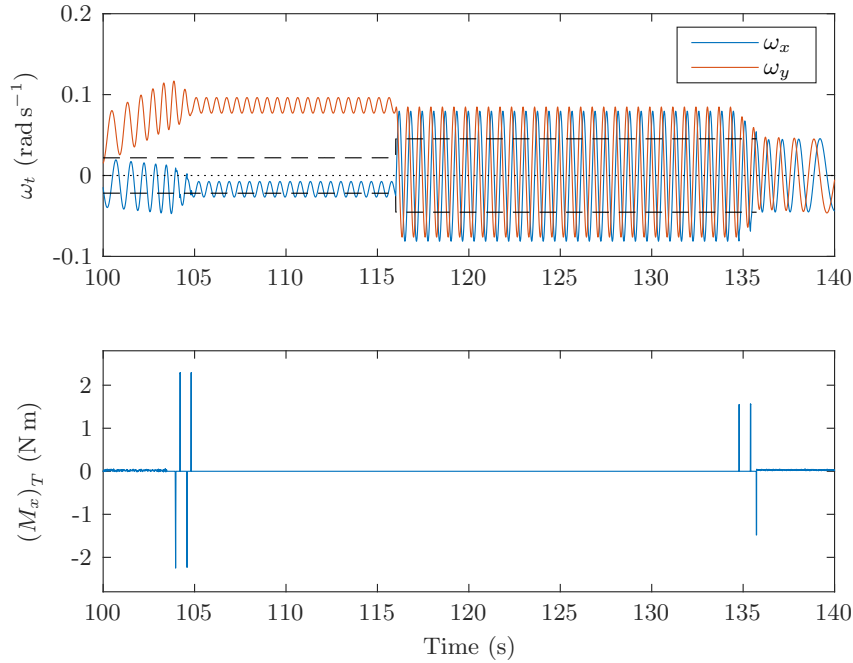


Figure 6-18: Time histories of the transverse angular rates and corresponding thruster torques about the x_B -axis, around the period of release of the penetrator. The dashed lines in the top plot represent a deadband. The output is associated with Monte Carlo sample 93.

consecutive times, until the response settles below the zero line. Both transverse angular rates, however – and in particular ω_y – have not settled within the deadband. Since neither response crosses the zero line, the controller remains idle, which represents a major shortcoming of the denutation algorithm as currently implemented. To address this issue, it is recommended to develop a more intelligent controller, incorporating a routine that is able to deduce the actual CoM and products of inertia in real-time, based on which appropriate control commands can be generated. An example controller in this sense was proposed by [Elias and Vega-Nevarez \(2008\)](#), in the context of unbalanced ballistic missiles. This controller leveraged the routine developed by [Wilson et al. \(2002\)](#) to identify the inertia properties.

To conclude the discussion on the first plot of [Figure 6-18](#), it is lastly noted that, following the release of the penetrator at 116 seconds into the simulation, the transverse angular rates of the spinning PDS are seen to immediately start oscillating about their associated close-to-zero mean values. As the threshold, calculated by [Equation \(4.25\)](#), is also crossed, the controller is triggered and is subsequently seen to command three short torques about the x_B -axis, reducing the transverse angular rates to within the deadband. This, in fact, confirms the proper functioning of the denutation algorithm on a system level.

Table 6-12: Penetrator landing site statistical descriptors, based on numerical data from a 1000-sample Monte Carlo simulation.

Case	μ_x (km)	μ_y (km)	$3\sigma_x$ (km)	$3\sigma_y$ (km)
Nominal	13.9	0	n/a	n/a
Off-Nominal				
<i>All</i>	16.0	0.2	7.5*	31.0
<i>Successes</i>	14.8	0.1	2.6*	15.2

*The distribution for the along-track distance is *positively skewed*.

6-4-2-2 Statistical Analysis

Table 6-12 presents the statistical descriptors of the penetrator landing site distribution. These characterise the landing footprint, which, though out of the scope of this thesis, can be used in selecting an appropriate landing site. Nominally, the penetrator lands at an along-track distance of 13.9 km, measured from the start of the DOM. The mean along-track distance for the off-nominal cases is 16.0 km with a three-sigma value of 7.5 km. Considering only successful landings, these values reduce to 14.8 km and 2.6 km, respectively. Notably, the along-track distance distribution is positively skewed. Furthermore, it can be seen that the mean cross-track distance is close to the centre line, both for the entire group of landings as for the success group. The associated three-sigma values, on the other hand, do vary, and come down to 31.0 km and 15.2 km, respectively.

Histograms representing the distributions of the landing parameters are depicted in Figure 6-19. In addition, associated statistical descriptors, *i.e.*, the *measures of central tendency*; the mean, median and mode, are presented. The distributions are, each to a varying extent, observed to be positively skewed, which implies that the mean and median are both greater than the mode. Evaluating the statistics of the landing parameters by which success is measured (see Table 6-9), it can be concluded that their measures of central tendency all pass their associated success criterion. As such, it can be stated that, on average, the system performs well. This is also reflected in the success rate, which is higher than 50%. The landing parameters indicative of the performance of the controller are the attack angle and the nutation angle. Close evaluation of their distributions reveals that in 98.7% of all cases, the success criterion for the attack angle is met, while in 99.8% of all cases, the controller manages to reduce the nutation angle to below the maximum prescribed value of 1° (see Appendix B).

The descent parameters of relevance in assessing the performance of the controller are the eigenangle offsets and angular rate offsets at the end of each reorientation manoeuvre. Figure 6-20 depicts the histograms of the descent parameters. As can be seen from the upper two histograms, the distributions of the eigenangle offset and angular rate offset at the end of Control Phase 4 centre around 1° and 0.01 rad s^{-1} , respectively. These values correspond, not quite accidentally, to the thresholds defined in Table 6-5. Furthermore, the mean values of the distributions of said offsets at the end of Control Phase 1 are observed to be lower than the thresholds defined. This is not surprising, since the initial state uncertainty distributions

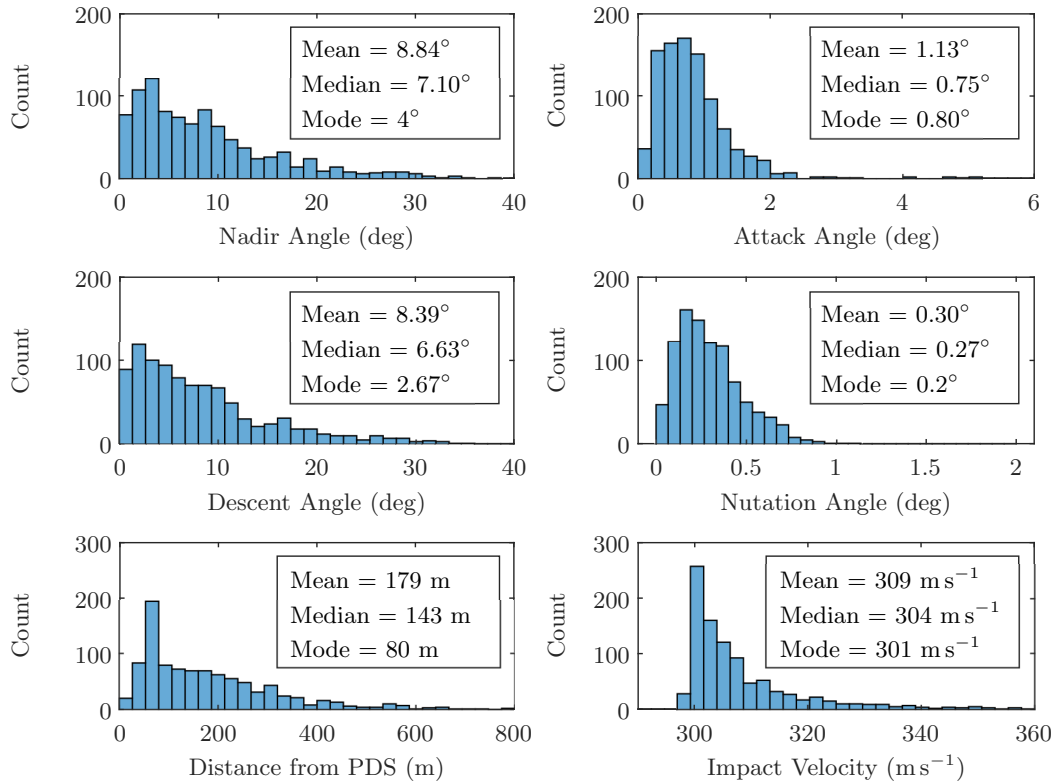


Figure 6-19: Histograms of the penetrator landing parameters and associated statistical descriptors, based on numerical data from a 1000-sample Monte Carlo simulation.

have standard deviations equal to these thresholds (see Table 6-6). As such, in roughly 68%³ of the cases, the initial eigenangle and angular velocity will already be within their respective deadbands. Another factor probably contributing to these lower-than-anticipated mean values, is the fact that initial state offsets, when larger than their thresholds, will still be small. In combination with a commanded settling time of 10 seconds (see Table 6-5), which is relatively large in this respect, this leads to low gains for the quaternion-error feedback controller. As a result, more delicate control commands are generated, which, when executed, may be more likely to reduce the offsets to below their thresholds. This would also explain why the mean angular rate offset at the end of Control Phase 7 is lower than 0.01 rad s^{-1} . In regard to this latter distribution, it is noted that it is positively skewed, with a rather long tail. This illustrates the erratic performance of the controller during Control Phase 7 (see Section 6-1-1). Another testimony of this, is the rather flat distribution of the eigenangle offset at the end of Control Phase 7, the mean of which lies between 1° and 2° . Nevertheless, it can be concluded that, given the successful results obtained for both the landing parameters and the descent

³Representing a bandwidth of two standard deviations centred on the mean in a normal distribution.

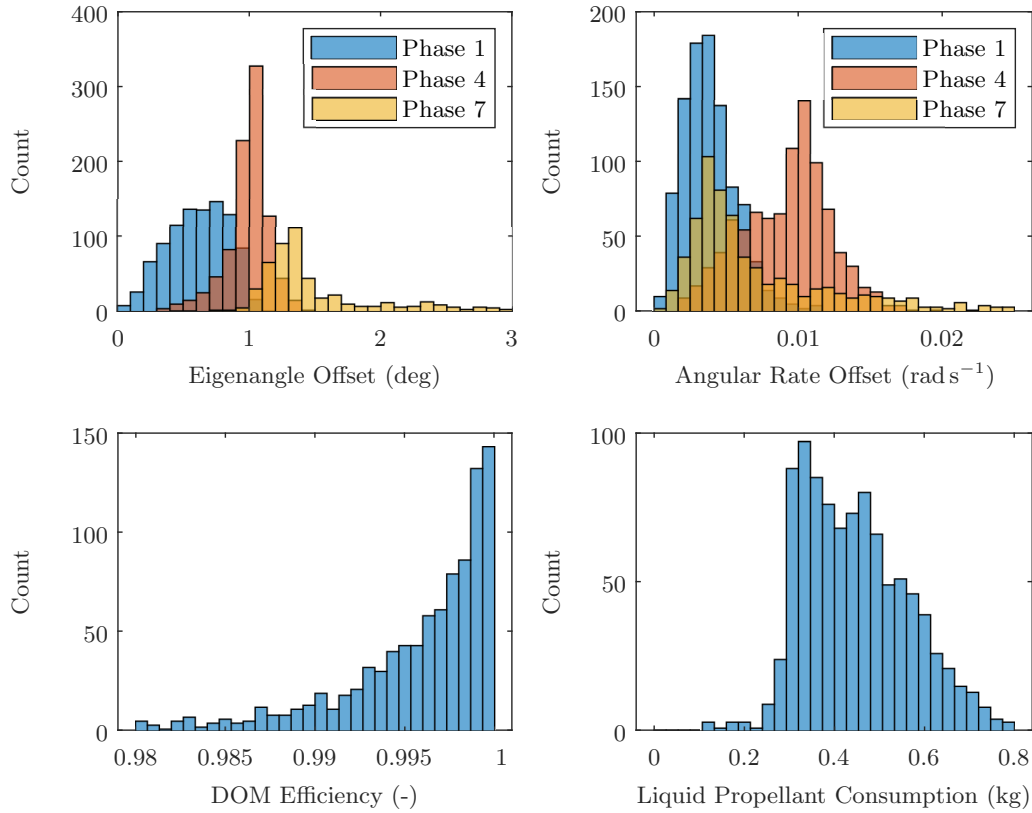


Figure 6-20: Histograms of the descent parameters, based on numerical data from a 1000-sample Monte Carlo simulation. The mean DOM efficiency is 0.995 and the mean liquid propellant consumption is 0.45 kg.

parameters, the controller generally performs very well.

As was shown in Section 6-4-2-1, the success rate of the mission from a descent-and-landing perspective turned out to be merely 58.5%. To identify the underlying cause(s) behind this relatively low success rate, the group of failed landings is analysed. In Table 6-13, the landing parameters are ranked, based on the percentage of failures that did not achieve their success criterion. It turns out that in 83% of the failed cases, the nadir angle was larger than 10°, which explains why increasing the tolerance on the nadir angle had such a beneficial effect on the success rate, see Table 6-11. The runner-up to the nadir angle is the impact velocity, whose prescribed maximum value was violated in 47% of the failed cases. To investigate the correlation between the nadir angle and the impact velocity, their correlation coefficient ρ was calculated. This was done using the built-in MATLAB function `corrcoef`, which also returns the p -value for testing the *null hypothesis* that there is no relationship between the two parameters. When the p -value is smaller than the 0.05 significance level, the correlation is qualified to be statistically significant. As can be seen from Table 6-13, the correlation coefficient between the nadir angle and the impact velocity, $\rho_{\eta, v_{\text{landing}}}$, was found to be 0.362,

Table 6-13: For each key landing parameter, 1) the percentage of failures attributed to not achieving its success criterion, and 2) its correlation coefficient $\rho_{i,j}$ with respect to other key landing parameters.

#	Landing Parameter i	Rate	$\rho_{i,\eta}$	$\rho_{i,v_{\text{landing}}}$	$\rho_{i,\Delta x_{\text{landing}}}$	$\rho_{i,\alpha}$
1	Nadir Angle	83%	1	0.362	0.111	0.712
2	Impact Velocity	47%	0.362	1	-0.246	-0.092*
3	Distance from PDS	22%	0.111	-0.246	1	0.064*
4	Attack Angle	3%	0.712	-0.092*	0.064*	1

* p -value is larger than 0.05 significance level, so correlation is statistically insignificant.

implying there is some correlation between them. This is expected, considering the nadir angle varies as a function of the velocity vector. Next in ranking is the landing distance between the PDS and the penetrator, which turned out to be insufficient in 22% of the failed cases. Notably, there is a statistically significant negative correlation of -0.246 between the landing distance and the impact velocity. This makes sense, as the PDS has less time to perform the FAM when it has an increased velocity in the downward radial direction (due to the DOM). The fourth and last landing parameter in ranking is the attack angle, whose success criterion was not met in 3% of the failed cases. This, in fact, reaffirms the proper performance of the controller. Finally, the fact that the nadir angle varies as a function of the attack angle explains the relatively strong positive correlation found between the two parameters, see Table 6-13.

It is clear from the foregoing that the vast majority of failed landings can be traced back to insufficient translational control, given that violations of the maximum nadir angle and the maximum impact velocity were listed as the main causes of failure. It is highly likely that an unsuccessful DOM leads to such violations. Table 6-14 indeed statistically confirms a moderately negative and a strong negative correlation between the efficiency of the DOM, and the nadir angle and the impact velocity – their respective coefficients being -0.39 and -0.91 . Previous analysis in Section 5-2-1-1 already revealed that the efficiency of the DOM is affected by CoM offsets and the effective SRM thrust misalignment angle. Generally, the larger these parameters, the less efficient is the DOM. Observing the correlation coefficients between said parameters and the efficiency of the DOM from Table 6-15, statistically significant negative correlations can indeed be confirmed: respectively, -0.54 , -0.19 and -0.23 , for the CoM offset of the PDS, the CoM offset of the penetrator and the thrust misalignment angle.

However, it should be noted that the mean efficiency of the DOM was found to be 0.995 (see Figure 6-20). Also, the *success rate* for the DOM was previously shown to be 93% (see Figure 5-6), under currently assumed uncertainties (see Table 6-6). Hence, the low success rate of the mission cannot be solely attributed to the DOM efficiency, that is, the way the parameter is currently defined. Evaluating its definition, which is given by Equation (5.3), it is noted that the effective impulse efficiency in the numerator is calculated by integrating the effective thrust force – given by Equation (5.1) – over time. As the effective thrust force directly depends on the nutation angle, so does implicitly the efficiency of the DOM. The above mentioned statistics were obtained based on this very definition. However, it should

Table 6-14: Correlation coefficients ρ between the descent parameters and penetrator landing parameters of the failure group, along with their associated p -values. Statistically significant correlations ($p < 0.05$) are printed in bold.

	Nadir Angle		Impact Velocity		Distance from PDS		Attack Angle	
	ρ	p	ρ	p	ρ	p	ρ	p
Eigenangle Offset								
<i>Control Phase 1</i>	0.12	0.03	0.06	0.26	0.00	0.99	0.09	0.08
<i>Control Phase 4</i>	0.10	0.06	-0.16	0.00	0.08	0.11	0.43	0.00
<i>Control Phase 7</i>	0.00	0.98	0.35	0.00	-0.24	0.00	-0.04	0.47
Angular Rate Offset								
<i>Control Phase 1</i>	0.04	0.43	0.01	0.80	0.09	0.09	-0.01	0.84
<i>Control Phase 4</i>	0.12	0.02	-0.15	0.00	0.10	0.06	0.45	0.00
<i>Control Phase 7</i>	-0.02	0.67	0.28	0.00	-0.16	0.00	0.00	0.97
DOM Efficiency	-0.39	0.00	-0.91	0.00	0.16	0.00	0.07	0.18

in fact also be taken into account that the effective thrust force, which is defined in the B -frame and directed along the z_B -axis, is transformed to the F -frame, as propagation of the translational state is done with respect to the latter. In the presence of nutational motion, the attitude of the PDM varies continuously, meaning that the direction of the effective thrust force, expressed in the F -frame, does so as well. This imparts velocity changes not only in the intended negative along-track direction, but also in the cross-track and radial directions, the result of which is seen in Figure 6-16. These effects are moreover exacerbated by a growing nutation angle as a result of increasing disturbance torques during the DOM (see the plot top-left in Figure 5-3). All of the above affects the efficiency of the DOM as well. Concluding, the underlying cause behind the low success rate is indeed the DOM efficiency, albeit more broadly defined than before in this report.

Table 6-15: Correlation coefficients ρ between the descent parameters mutually, and between the uncertain model parameters of the failure group, along with their associated p -values. Statistically significant correlations ($p < 0.05$) are printed in bold.

	Eigenangle Offset						Angular Rate Offset						DOM Eff.	
	Phase 1		Phase 4		Phase 7		Phase 1		Phase 4		Phase 7		ρ	p
	ρ	p	ρ	p	ρ	p	ρ	p	ρ	p	ρ	p		
Eigenangle Offset														
<i>Control Phase 1</i>	1.00	0.00	0.08	0.14	0.04	0.45	0.18	0.00	0.09	0.09	0.05	0.32	-0.06	0.22
<i>Control Phase 4</i>	0.08	0.14	1.00	0.00	-0.02	0.73	-0.04	0.49	0.97	0.00	0.08	0.14	0.12	0.03
<i>Control Phase 7</i>	0.04	0.45	-0.02	0.73	1.00	0.00	-0.06	0.22	-0.03	0.56	0.70	0.00	-0.29	0.00
Angular Rate Offset														
<i>Control Phase 1</i>	0.18	0.00	-0.04	0.49	-0.06	0.22	1.00	0.00	-0.02	0.69	0.05	0.33	-0.02	0.76
<i>Control Phase 4</i>	0.09	0.09	0.97	0.00	-0.03	0.56	-0.02	0.69	1.00	0.00	0.07	0.16	0.11	0.04
<i>Control Phase 7</i>	0.05	0.32	0.08	0.14	0.70	0.00	0.05	0.33	0.07	0.16	1.00	0.00	-0.28	0.00
DOM Efficiency	-0.06	0.22	0.12	0.03	-0.29	0.00	-0.02	0.76	0.11	0.04	-0.28	0.00	1.00	0.00
Altitude Offset	0.06	0.22	0.08	0.14	-0.06	0.26	0.09	0.10	0.08	0.12	0.02	0.77	0.03	0.59
CoM PDS Offset	0.11	0.04	-0.12	0.02	0.46	0.00	-0.04	0.50	-0.12	0.02	0.44	0.00	-0.54	0.00
CoM Pen. Offset	-0.01	0.79	0.09	0.10	0.00	0.94	-0.05	0.33	0.09	0.09	-0.01	0.89	-0.19	0.00
SRM Misalignment	-0.02	0.76	-0.03	0.51	-0.03	0.60	0.14	0.01	-0.01	0.80	-0.04	0.48	-0.23	0.00
Linear Tip-Off Offset	-0.06	0.25	-0.04	0.48	-0.06	0.27	-0.02	0.73	-0.02	0.74	0.05	0.38	-0.07	0.16
Angular Tip-Off Offset	0.06	0.28	0.01	0.88	-0.02	0.64	0.08	0.11	0.04	0.47	0.02	0.77	-0.01	0.90

Conclusions and Recommendations

This thesis was concerned with the design, verification and testing of a suitable attitude controller for the thruster-controlled descent module of a current-technology penetrator mission targeted for an airless body – specifically: ELUPE. In designing the controller, two different types of rotational manoeuvres needed to be addressed: 1) large-angle slew manoeuvres, which entail a 90 degree, highly nonlinear reorientation, and 2) minor-axis spin manoeuvres, which involve a spin-up, an actively controlled subsequent spin and a spin-down about the *minor axis*. Furthermore, varying system parameters had to be accounted for, *i.e.*, the inertial parameters and the torque capabilities of the descent module. The latter not only due to shifts in the centre-of-mass, but also because the descent module incorporates a reaction control system operating in a *blow-down mode*.

It was decided to design a controller based on classical control techniques. First of all, because such techniques are still the norm in the aerospace industry and, hence, the design of a classical controller would be of good practical value. Secondly, the test results obtained for a classical controller would establish a benchmark for potential future research.

For the large-angle slew manoeuvres, a legacy quaternion-error feedback controller was implemented, which is theoretically able to generate control commands for a rotation about the eigenaxis. The original method to determine the gains of the controller was slightly modified to address the nonlinear effects introduced by one of its underlying assumptions. For the minor-axis spin manoeuvres, a legacy algorithm for spin-axis denutation was implemented. The algorithm was extended by the development of an adaptive logic to obtain the optimal thruster pulse duration, as well as a strategy to enable dual-axis control for enhanced nutation damping. In order to translate the control commands into appropriate thruster actions, a thruster management function was developed, which solves the classical jet selection problem at each control cycle by means of an interior-point method. A two-step procedure was devised to correct the resulting firing duration vector for the force drop that occurs when multiple thrusters operating in a blow-down setting fire simultaneously. The correct implementation of the aforementioned control algorithms was verified by reproducing the results presented in

their associated papers. The correct functioning of the thruster management function was demonstrated by simulating a large-angle slew manoeuvre, for which the control commands were generated by the quaternion-error feedback controller.

In order to test the performance of the verified controller in the context of the ELUPE mission, a simulator was developed. To this end, models were created for the descent module and its environment. The reaction control system elements and the de-orbit motor were modelled using actual specifications and performance diagrams. The pressure drop factors associated with multiple thrusters firing simultaneously were obtained from the literature. The inertial parameters of the dry descent module were provided by CATIA. To attain the inertial parameters of the wet descent module, assumptions were made in regard to the geometries of the propellant slugs, which were in part composed of a (hemi)spherical cap and a hemispherical frustum. Analytic equations for the mass moments of inertia of both geometrical objects and for the centroid of a hemispherical frustum, in terms of their mass, height and spherical radius, were derived and verified. These equations were not found in the open literature. In modelling the dynamics, the disturbance torques caused by the gravity gradient, solar radiation and viscous friction between the liquid propellant slug and the propellant tank were considered. None were found to be significant enough to be included in the dynamics model. However, investigating the effects of viscous friction involved making some questionable assumptions. As such, some restraint is appropriate. Finally, as part of the simulator, a mission manager logic was developed, centrally coordinating which target state is transmitted to the controller and which control mode is active.

The controller was tested in a simulation of the second phase of ELUPE's descent scenario, which involves both types of rotational manoeuvres mentioned. A nominal system test showed the simulator functioning as intended. To assess the performance of the controller under off-nominal conditions, a 1000-sample Monte Carlo simulation was run, involving variations on the initial state vectors (both translational and rotational), the centre-of-mass (and implicitly the inertia tensor) of the dry descent module, the effective SRM thrust misalignment angle, the penetrator tip-off velocities, the thruster cant angles, the thruster performance, and the actual state (to simulate the output of a navigation system). Based on the results of this Monte Carlo simulation, it was found that the success rate of the ELUPE mission, from a descent-and-landing perspective, is 58.5% for a local surface slope of 20° , and 74.2% for a slope of 10° or lower. Analysis of the *attack angle* and the *nutation angle* – two key penetrator landing parameters – revealed their success criteria were met in 98.7% and 99.8% of all cases, respectively. These successful results can be fully attributed to the controller. In addition, further inspection of the failure group revealed that only 3% of the failures was caused by violation of the maximum attack angle. As such, an answer can be formulated to the first part of the research question:

Is it possible to satisfactorily solve the attitude control problem of a current-technology penetrator mission targeted for an airless body through the use of classical control techniques, ...

In short: yes, it is possible, yet not completely satisfactory. Although the thruster management function showed to operate as desired, early simulation results revealed that for a large

backward shift of the centre-of-mass, the gain determination method for the quaternion-error feedback controller proved to be no longer applicable. The reason being that, due to the strong centre-of-mass shift, the torque capabilities about one of the body axes of the descent module were greatly diminished. This turned out to be a thruster geometry issue, which the quaternion-error feedback controller was not able to address in a proper way. The problem was unsatisfactorily solved by reducing the controller gains, for which a great deal of performance was traded. It is clear that, in this respect, a different controller is desired, preventing control about ‘weaker’ axes as much as possible. Seeing the nature of this objective, it is likely that such a controller solves an optimisation problem to generate the control commands. The development of a controller of this kind is a recommended topic for future work.

In addition to the restricted quaternion-error feedback controller, the denutation algorithm also demonstrated a significant flaw, as it proved to be ineffective in the presence of (larger) inertia uncertainty. For the denutation algorithm to be activated, the responses for the transverse angular rates need to consecutively cross the zero line and a threshold. Misalignment of the principal axes causes the responses to oscillate about nonzero means, which can lead to a situation where the responses do not even cross the zero line. In such cases, the controller remains idle, which represents a major shortcoming. To address this issue, it is recommended to implement a different controller, incorporating a routine that is able to deduce the actual inertial parameters from sensor measurements. Based on this, it would be possible to reevaluate the torque capabilities and generate correct control commands. Perhaps, such an identification routine could be combined with the controller outlined above.

With regard to the efforts made in this thesis to improve the general performance of the legacy control algorithms considered, it can be stated that, given the revealed limitations, and the recommendation to implement a different controller, these contributions are solely of theoretical value.

On to answering the second part of the research question:

...and if so, what are, from a descent-and-landing perspective, the key factors affecting the success rate of such a mission?

A success rate of 58.5% is not particularly high, especially when compared against the ‘three-sigma’, *i.e.*, 99.7% success rates to which spacecraft are typically designed. Analysis of the failure group revealed that in 83% of the failed cases, the maximum nadir angle was violated. The runner-up cause was a violation of the maximum impact angle, in 47% of the failed cases. Notably, the nadir angle and impact velocity distributions were found to be partially correlated, with a correlation coefficient of 0.36. As the nadir angle varies as a function of the impact velocity, this correlation entails that part of the cases that violated the maximum impact angle, also violated the maximum nadir angle. Failing to meet the success criteria of said parameters can be traced back to insufficient translational control. It was shown that the nadir angle and the impact velocity had a moderately negative and a strong negative correlation with the DOM efficiency; -0.39 and -0.91 , respectively. Early simulation results already revealed that the efficiency of the DOM was strongly affected by the centre-of-mass offset and the effective SRM misalignment angle. Indeed, statistical analysis confirmed a

negative, and statistically significant correlation between these parameters and the efficiency of the DOM. As such, the centre-of-mass offset and the effective SRM misalignment angle can be identified as the key factors affecting the success rate. As further constraining these parameters is not preferred, it is hence recommended to modify the thrust curve of the SRM or incorporate a different SRM.

To conclude this thesis, some noteworthy limitations, as well as some recommendations for future work, are summarised below.

LIMITATIONS

- The simulator lacked a comprehensive model of the navigation system. Sensor performance and placement were not considered, and the *observability* of the system was not assessed.
- Assumptions were made in regard to:
 - the shape and sloshing characteristics of the liquid propellant slug inside the PEPT-230 tank, as test data could not be obtained.
 - the shape of the solid propellant slug and the centre-of-mass shift during the SRM burn, as test data was not available.
 - the feed pressure drop when multiple thrusters are operated simultaneously, as these have to be obtained through dedicated experimentation.

Besides that it is recommended to address the above mentioned limitations in future work, the following additional recommendations are made.

RECOMMENDATIONS

- Design a different controller, which solves an optimisation problem at each control cycle to generate the control commands, and incorporates a routine to identify the actual inertial parameters.
- Find the ideal thrust curve for the SRM, so that disturbances emerging during the DOM are minimised, and the success rate of the mission is improved.
- Simulate the first phase of the descent scenario, for which it is necessary to develop a guidance routine for the periapsis lowering manoeuvre.

Appendix A

Penetrator Descent Module

This appendix is intended for the interested reader and serves to provide complementary information about the design of the instrumented penetrator and the PDS, which together form the PDM. These systems are discussed in Appendices [A-1](#) and [A-2](#), respectively. Appendix [A-3](#) presents a mass budget of the PDM and briefly addresses potential mass savings.

A-1 Penetrator

Based on European heritage ([Smith et al., 2010](#); [Vijendran et al., 2014](#)), the instrumented penetrator is baselined to be comprised of a 5 mm steel outer shell with a reinforced spherically blunted ogive nose, and a 4 mm aluminium internal compartment containing the penetrator science payload and subsystems. See Figures [A-1](#) and [A-2](#) for a CATIA render and a schematic representation of the penetrator body, respectively. Out of thermal considerations, the internal compartment is decoupled from the outer shell by leaf springs fabricated of a low-conductive material (such as Torlon). The resulting void between the outer wall of the internal compartment and the inner wall of the outer shell is evacuated of any medium (analogous to the concept of a vacuum flask), thereby minimising heat exchange through thermal conduction and convection.

The suite of science instruments incorporated in the penetrator has been adopted from the L-DART penetrator mission proposal ([Barber et al., 2017](#)) and includes a mass spectrometer, a set of accelerometers and a thermal sensor package. It should be noted that there is no drill mechanism included in the science payload to acquire regolith samples, as mechanisms are inherently susceptible to high-g deceleration. Rather than by mechanical means, sampling is proposed to be performed passively by allowing ingress of gaseous volatiles, released as a direct and indirect result of the penetration event, through one or more apertures in the penetrator shell. The working of a similar ‘sniffing’ method was successfully demonstrated on-board of the Philae lander during surface operations on Comet 67P ([Wright et al., 2015](#)). The

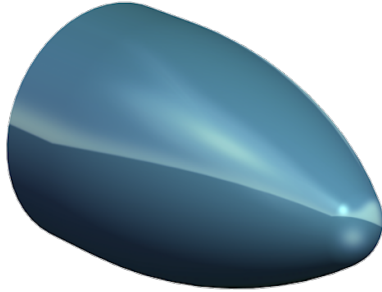


Figure A-1: Render of the instrumented penetrator body with a spherically blunted ogive nose.

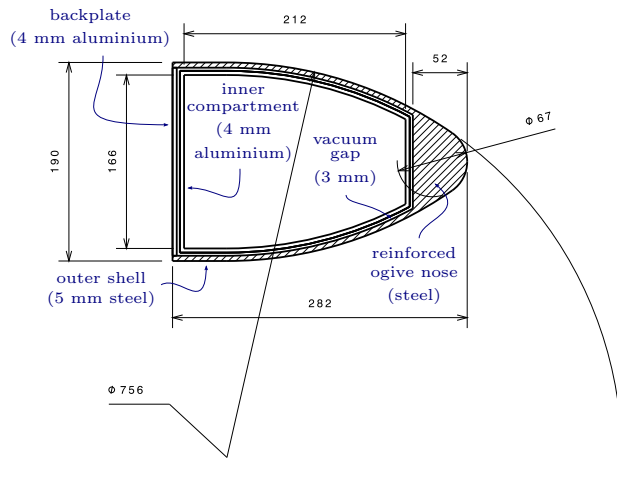


Figure A-2: Schematic representation of the penetrator body. The dimensions shown are in millimetres.

implementation of apertures in the shell does however have implications on the penetrator's structural and thermal integrity. The extent of these implications should be topic of further investigation.

Inspired by the JEO Penetrator concept proposed at the end of its Phase 2 study (Waugh & Perkinson, 2013), the penetrator science payload is supported by an Integrated Avionics System (incorporating the penetrator on-board computer (OBC), UHF transceiver and Power Conditioning and Distribution Unit (PCDU)), a battery of lithium carbon monofluoride pouch cells and a patch antenna mounted on the rear plate of the penetrator. To protect the antenna from a backfill of regolith after penetration, it is enclosed by a dedicated radome. Data transmission will occur through the lunar regolith – the extent to which the signal is attenuated during its propagation through the overlying layer of material is currently under research at The Open University¹. Given the vacuum gap between the penetrator rear plate and the internal compartment, a wireless connection between antenna and transceiver is established by means of capacitive coupling. The antenna beamwidth is reasonably assumed to be ± 30 degrees centred on a vertical boresight. This assumption has a direct impact on the design of the descent trajectory, as the penetrator must be 'visible' to the Pathfinder at impact.

The penetrator system design strategy aimed at implementation of ruggedised solutions, implying that resilience to high-g deceleration is either proven or almost certainly expected. As such, the instruments and subsystems included in the design comply with this criterion. It is though emphasised that still a substantial lot of development would be required before the system could be flight-ready. In this respect, the instruments and subsystems would generally 'only' need to be tailored to the mission needs, as they were either already successfully impact tested during previous penetrator studies, or are otherwise inherently shock tolerant. The penetrator structure would however require more work, as its shape and size must be

¹Barber, S.J., personal communication, 2017

optimised to maximise structural integrity, maximise stability and minimise mass, while also fitting the (spatial) needs of the payload and subsystems.

A-2 Penetrator Delivery System

As is schematically depicted in Figure 2-1, the PDS consists of an avionics compartment and a structure providing support to the SRM and the hydrazine RCS with four thrusters. The avionics compartment houses the electronic equipment (OBC, battery, PCDU and ancillaries) and the AOCS sensors (IMU and star tracker), and is made of a 4 mm thick aluminium alloy to sufficiently shield its contents from incoming radiation. Attached to the small circular end of the avionics compartment is a yet to be designed release mechanism that separates the passive penetrator from the PDS before impact. Notably, the design of this mechanism is not within the scope of this thesis. Therefore, assumptions are made regarding tip-off velocities during simulations of the descent trajectory.

The PDS supporting structure is fabricated of 4 mm carbon fiber reinforced polymer (CFRP) and has the shape of a truncated hollow cone. Within, a compartment is created for the hydrazine tank, separated from the SRM by a bulkhead. The rear end of the cone transitions into a tubular section to which a 4 mm thick CFRP ring is attached, providing structural support to the thrusters. The outside of the PDS offers a platform for a descent camera to be mounted on, as well as an array of omni-directional patch antennas that are coupled to the penetrator transceiver, removing the need for an extra transceiver in the PDS. It is proposed for the descent camera to employ a *push broom* imaging technique sampling a >90 degrees wide swath parallel to the PDM spin-axis, covering the region between nadir and the local horizon. As the rotation of the PDM will provide the scanning of the sampling swath across the surface, the camera is effectively passive. In front of the camera, multiple fixed filters are mounted covering different spectral ranges, so that multispectral imaging can be achieved.

It is noted that no mechanism has yet been specified or designed to separate the PDM from the Pathfinder, however it is contemplated that it could be similar to a bomb ejector mechanism seen with military aircraft. As such, the mechanism would stay attached to the Pathfinder rather than to the PDM after separation, which would hence preserve the latter's symmetry. The PDM could in this respect be clamped at its tubular sections.

A-3 Mass Budget

The instrumented penetrator is currently estimated to weigh 17.6 kg, including maturity margins and a 20% system margin. The PDS has an estimated mass of 28.1 kg, also including these margins. The total PDM wet mass amounts to 86.8 kg (39.0 kg of which is attributed to solid propellant and 2.1 kg to liquid propellant). In Table A-1, a detailed breakdown of the total mass – the mass budget – is provided. It is noted that potential mass savings are identified in *e.g.*, the adoption of a penetrator outer shell made of titanium (instead of steel), and an efficient cutaway format for the PDS structure.

Table A-1: Mass budget of the PDM.

System	Basic mass (kg)	Margin (%)	System mass (kg)
Payload			
Mass spectrometer ^a	0.750	20%	0.900
Accelerometer (+ datalogger) ^a	0.218	20%	0.262
Thermal sensor package ^a	0.010	50%	0.015
Descent imager ^b	0.160	20%	0.192
Penetrator			
Avionics	0.970	20%	1.164
Communications	0.340	20%	0.408
Battery	0.066	20%	0.079
Interfacing	0.200	20%	0.240
Packing materials	1.569	20%	1.883
Structure	8.120	20%	9.744
PDS			
Propulsion			
Solid rocket motor	5.800	5%	6.090
Mono-propellant blowdown system			
Thrusters	2.362	5%	2.480
Tank	1.300	5%	1.365
Ancillaries	1.390	5-20%	1.500
Avionics	0.850	20%	1.020
Sensors	0.590	20%	0.708
Communications	0.400	20%	0.480
Interfacing	0.800	20%	0.960
Mechanisms	0.540	20%	0.648
Structure	6.658	20%	7.989
PDM dry mass (incl. maturity margins)			38.1
System margin		20%	
PDM dry mass (incl. system margin)			45.7
Propellant			
Solid propellant			39.0
Liquid propellant			2.1
PDM wet mass			86.8

^aIncorporated in the penetrator.

^bMounted on the PDS.

Appendix B

Mission Requirements

Key to a successful mission from a descent-and-landing perspective is successful penetration, that is, the instrumented penetrator penetrates the surface under desired impact conditions. In addition, the PDS, after releasing the penetrator, must land at a sufficient distance away from the impact site of the penetrator. To help constrain the design of the controller and eventually assess its performance, a set of top-level mission requirements is formulated, related to penetration (Appendix B-1) and the fly-away manoeuvre (Appendix B-2).

B-1 Penetration

The moment just prior to impact, it is of vital importance that the penetrator has achieved the right orientation (and velocity) with respect to the surface, so that penetration may occur successfully. Figure B-1 provides a schematic to define the key angles related to the penetration event. They are described as follows:

\mathbf{Z}_F	=	normal to local horizontal	(-)
$\mathbf{n}_{\text{actual}}$	=	normal to actual horizontal	(-)
\mathbf{V}_B	=	velocity vector	(m s ⁻¹)
\mathbf{Z}_B	=	symmetry axis of the body	(-)
\mathbf{h}	=	angular momentum vector	(kg m ² s ⁻¹)
θ_{nut}	=	nutation angle	(deg)
α	=	angle-of-attack	(deg)
ψ	=	heading angle	(deg)
i	=	impact angle	(deg)
σ_{local}	=	local slope	(deg)
δ	=	descent angle	(deg)
η	=	nadir angle	(deg)

RQ-AOCS-PEN-02. The nadir angle η shall be $0 \pm 10^\circ$.

Comment: The nadir angle is defined as the angle between \mathbf{Z}_B and \mathbf{Z}_F . The tolerance is directly derived from RQ-AOCS-PEN-01. The nadir angle may not exceed 10° .

RQ-AOCS-PEN-03. The angle-of-attack α shall be $0 \pm 5^\circ$.

Comment: The angle-of-attack is defined as the angle between \mathbf{Z}_B and \mathbf{V}_B and varies as a function of the position of \mathbf{Z}_B on the nutation cone; see Figure B-1. When the nutation angle is zero, the angle-of-attack is also defined as the angle between \mathbf{h} and \mathbf{V}_B . Previous studies for LUNAR-A (Shiraishi et al., 2008) and MoonLITE (Smith et al., 2009) defined a maximum tolerable angle-of-attack of 8° . For ELUPE, this error margin is brought down to 5° , so that the margin for the descent angle can be raised from a narrow 2° to a better achievable 5° , while still complying with RQ-AOCS-PEN-02.

RQ-AOCS-PEN-04. The descent angle δ shall be $0 \pm 5^\circ$.

Comment: The descent angle is defined as the angle between \mathbf{Z}_F and \mathbf{V}_B . It varies as a function of the residual horizontal velocity, thus is solely influenced by translational factors. The error margin is derived from equal repartition of the 10° nadir angle margin into an the attack angle margin and a descent angle margin.

RQ-AOCS-PEN-05. The nutation angle θ_{nut} shall be $0 \pm 1^\circ$.

Comment: The nutation angle is defined as the angle between \mathbf{Z}_B and \mathbf{h} . Nutation arises as a result of a perturbing angular rate transverse to the spin-axis, and is for example caused by the angular tip-off velocity imparted to the penetrator during its separation from the PDS. The 1° tolerance covers the nutation originating from the release event as well as any pre-existing nutation.

RQ-AOCS-PEN-06. The impact velocity magnitude $|\mathbf{V}|$ shall be $300 \pm 15 \text{ m s}^{-1}$.

Comment: The error margin is based on the results of impact tests conducted in the context of previous penetrator studies, which demonstrated the survivability of the technologies tested at impact velocities of 315 m s^{-1} (Smith et al., 2010; Vijendran et al., 2014).

B-2 Fly-Away Manoeuvre

Following release of the spin-stabilised penetrator, the PDS autonomously completes a sequence of operations to prevent itself from landing on top of or in close vicinity to the penetrator. This sequence of operations is referred to as the *fly-away manoeuvre* (see Section 1-2-3). As part of a successful mission, the PDS must achieve landing at a certain safe distance away from the penetrator impact site, formalised in the requirement below.

FLY-AWAY MANOEUVRE - TOP-LEVEL REQUIREMENT:

RQ-AOCS-PDS-01. The horizontal distance between the impact sites of the penetrator and the PDS shall be at least 50 m.

Comment: The distance specified is adopted from Vijendran et al. (2010), however should actually result from analysis of the ballistics of the debris plume that is expected to emerge from the impact of the PDS, which is out of the scope of this thesis.

Appendix C

Propellant Slugs

During translational and rotational manoeuvres, the inertia tensor of the wet PDM/PDS can be calculated by adding the momentary inertia tensors of the solid and liquid propellant slugs to the inertia tensor of the *dry* PDM/PDS, provided that each inertia tensor is expressed with respect to a coordinate system located at the momentary CoM of the *wet* PDM/PDS. While the inertia tensor of the dry PDM/PDS is known and assumed to be constant, the inertia tensors of the solid and liquid propellant slugs change as the slugs are consumed. In Appendix C-1, relations between the mass of the solid propellant slug and its CoM and MoI are derived. In Appendix C-2, the same is done for the liquid propellant slug.

C-1 Solid Propellant Slug

For the derivation of the relations between the mass of the solid propellant slug and its CoM and MoI, it is to a good approximation assumed that the slug follows the shape of the SRM case and burns uniformly across the surface. As such, the slug can be represented by a composition of simple geometries, whose individual inertia tensors are easily calculated. From Figure C-1, which shows a schematic of a partial slug inside the SRM case, it can be seen that when the SRM is fully loaded, the slug is comprised of two hemispheres and a cylindrical section. As the slug is consumed, its composition changes, and throughout the SRM burn, four consecutive compositions (abbreviated **Comp.**) can be distinguished:

- **Solid Comp. 0:** Hemisphere + cylinder + hemisphere (fully loaded SRM)
- **Solid Comp. 1:** Hemisphere + cylinder + hemispherical frustum
- **Solid Comp. 2:** Hemisphere + cylinder
- **Solid Comp. 3:** Hemispherical cap

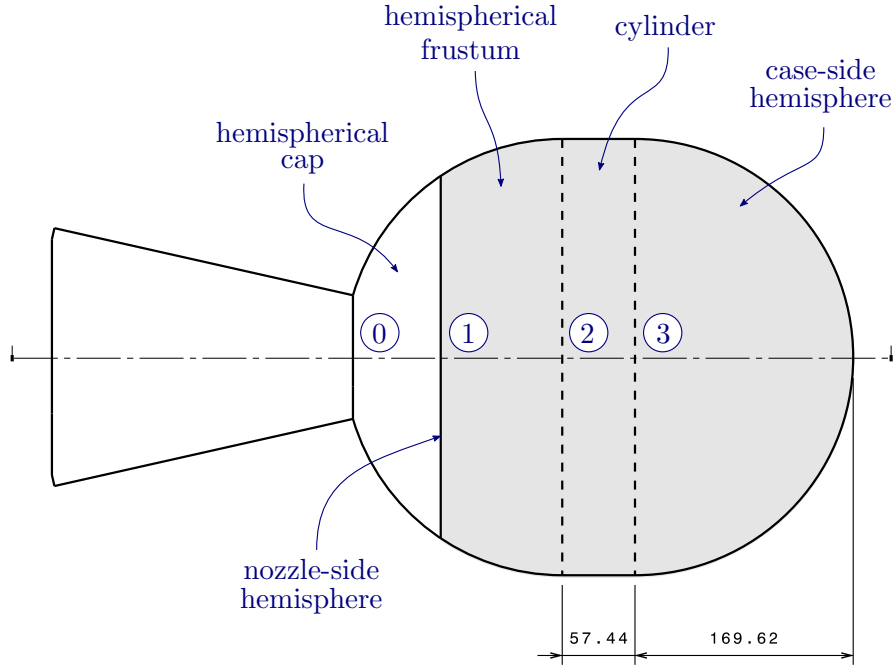


Figure C-1: Schematic representation of a partial solid propellant slug (light grey area) inside Northrop Grumman's STAR 13B motor. The definitions of the geometries are given. The numbered circles indicate the consecutive geometric compositions of the slug. The dimensions shown are in millimetres.

Figure C-1 shows the geometries associated with the aforementioned compositions. Given that the slug has a symmetry axis and is furthermore assumed to have uniform density ρ , the CoM travels along the symmetry axis and the nondiagonal elements of the inertia tensor are zero. As such, the inertia tensor of the solid propellant slug can be written as:

$$\mathbf{I}_{\text{solid}} = \begin{bmatrix} I_{xx} & 0 & 0 \\ 0 & I_{yy} & 0 \\ 0 & 0 & I_{zz} \end{bmatrix}_{\text{solid}} \quad (\text{C.1})$$

where I_{xx} , I_{yy} and I_{zz} are the MoI of the slug about the centroidal x -, y - and z -axis, respectively. These parameters can be found by summing the corresponding elements of the inertia tensors of the individual geometries that constitute the slug, after each of these elements has been recalculated about an axis that 1) passes through the centroid (CoM) of the slug and 2) is parallel to the reference axis that passes through the centroid of the geometry concerned. This can be achieved with the *parallel axis theorem* (Jakob Steiner, 1796-1863), which in scalar form is written as:

$$I = I_0 + md^2 \quad (\text{C.2})$$

or in tensor form as (Balafoutis & Patel, 1991, p. 100):

$$\mathbf{I} = \mathbf{I}_0 + m [(\mathbf{R} \cdot \mathbf{R})\mathbf{E}_3 - \mathbf{R}\mathbf{R}^T] \quad (\text{C.3})$$

where I is the mass moment of inertia to be calculated, I_0 is the reference mass moment of inertia, m is the mass of the rigid body, d is the perpendicular distance between the parallel axes, \mathbf{I} is the inertia tensor to be calculated, \mathbf{I}_0 is the reference inertia tensor, \mathbf{R} is the displacement vector from the reference point to the new point and \mathbf{E}_3 is the 3×3 identity matrix. The CoM of a system of masses is calculated by:

$$\mathbf{r}_{cm} = \frac{1}{m_{tot}} \sum_{i=1}^n m_i \mathbf{r}_i \quad (\text{C.4})$$

where \mathbf{r}_{cm} are the coordinates of the CoM with respect to the origin of the coordinate system concerned, m_{tot} is the sum of masses, m_i is the mass of mass i and \mathbf{r}_i are the coordinates of mass i . In the following, expressions to calculate the volume, centroid and MoI of each of the geometries depicted in Figure C-1 are presented.

Cylinder. The volume of a uniform cylinder is calculated by:

$$V_{cyl} = \pi r_{cyl}^2 h_{cyl} \quad (\text{C.5})$$

where r_{cyl} is the radius and h_{cyl} is the length of the cylinder. The centroid of a uniform cylinder is calculated by:

$$\bar{z}_{cyl} = \frac{h_{cyl}}{2} \quad (\text{C.6})$$

where \bar{z}_{cyl} is measured with respect to the base of the cylinder. The MoI of a uniform cylinder about the centroidal axes are calculated by (Kane & Levinson, 1985, p. 368):

$$I_{xx, cyl} = I_{yy, cyl} = \frac{1}{12} m_{cyl} (3r_{cyl}^2 + h_{cyl}^2) \quad (\text{C.7a})$$

$$I_{zz, cyl} = \frac{1}{2} m_{cyl} r_{cyl}^2 \quad (\text{C.7b})$$

where m_{cyl} is the mass of the cylinder.

Hemisphere. The volume of a uniform hemisphere is calculated by:

$$V_{hemi} = \frac{2}{3} \pi r_{hemi}^3 \quad (\text{C.8})$$

where r_{hemi} is the radius of the hemisphere. The centroid of a uniform hemisphere is calculated by (Kane & Levinson, 1985, p. 369):

$$\bar{z}_{hemi} = \frac{3}{8} r_{hemi} \quad (\text{C.9})$$

where \bar{z}_{hemi} is measured with respect to the base of the hemisphere. The MoI of a uniform hemisphere about the centroidal axes are calculated by (Kane & Levinson,

1985, p. 369):

$$I_{xx, \text{hemi}} = I_{yy, \text{hemi}} = \frac{83}{320} m_{\text{hemi}} r_{\text{hemi}}^2 \quad (\text{C.10a})$$

$$I_{zz, \text{hemi}} = \frac{2}{5} m_{\text{hemi}} r_{\text{hemi}}^2 \quad (\text{C.10b})$$

where m_{hemi} is the mass of the hemisphere.

Hemispherical Cap. The volume of a uniform hemispherical cap is calculated by (Harris & Stocker, 1998, p. 107):

$$V_{\text{cap}} = \frac{1}{3} \pi h_{\text{cap}}^2 (3r_{\text{hemi}} - h_{\text{cap}}) \quad (\text{C.11})$$

where h_{cap} is the height of the cap. The centroid of a uniform hemispherical cap is calculated by (Harris & Stocker, 1998, p. 107):

$$\bar{z}_{\text{cap}} = \frac{3(2r_{\text{hemi}} - h_{\text{cap}})^2}{4(3r_{\text{hemi}} - h_{\text{cap}})} \quad (\text{C.12})$$

where \bar{z}_{cap} is measured with respect to the centre of the associated sphere. Equations for the MoI of a uniform hemispherical cap about the centroidal x -, y - and z -axes were not found in the literature and will therefore be derived. Starting with the general *Cartesian* definitions of the MoI of a solid object occupying region E about the three coordinate axes (Stewart, 2008, p. 996):

$$I_{xx} = \iiint_E (y^2 + z^2) \rho(x, y, z) dV \quad (\text{C.13a})$$

$$I_{yy} = \iiint_E (x^2 + z^2) \rho(x, y, z) dV \quad (\text{C.13b})$$

$$I_{zz} = \iiint_E (x^2 + y^2) \rho(x, y, z) dV \quad (\text{C.13c})$$

where dV is a volume element. For the case of a uniform axisymmetric hemispherical cap, it holds that $\rho(x, y, z) = \text{constant}$ and $I_{xx} = I_{yy}$. Figure C-2 depicts the geometry of a hemispherical cap with respect to its associated sphere. Given the rotational symmetry about the z -axis, the *triple integrals* in Equations (C.13a) to (C.13c) can be simplified using *cylindrical coordinates*.

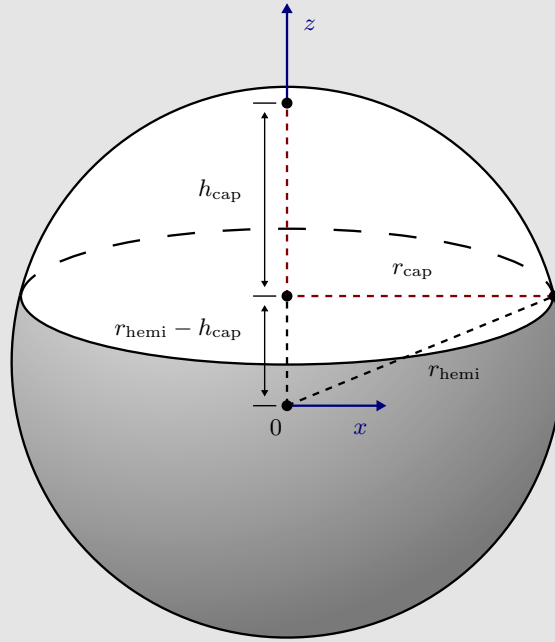


Figure C-2: Geometry of a hemispherical cap with respect to its associated sphere.

To express Cartesian coordinates in cylindrical coordinates, the following relations are used (Stewart, 2008, p. 1001):

$$x = r \cos \theta \quad y = r \sin \theta \quad z = z \quad (\text{C.14})$$

where r and θ are the polar coordinates of point Q , which is the projection of point P onto the xy -plane, and z is the distance between Q and P . Other useful relations to convert Equations (C.13a) to (C.13c) from Cartesian to cylindrical coordinates are (Stewart, 2008, pp. 1001-1002):

$$x^2 + y^2 = r^2 \quad (\text{C.15})$$

$$dV = r dr dz d\theta \quad (\text{C.16})$$

Considering the geometry of a hemispherical cap as depicted in Figure C-2, it is convenient to define the limits of integration for r , z and θ with respect to the centre of the associated sphere^a, so that:

$$E = \left\{ (r, \theta, z) \mid 0 \leq \theta \leq 2\pi, r_{\text{hemi}} - h_{\text{cap}} \leq z \leq r_{\text{hemi}}, 0 \leq r \leq \sqrt{r_{\text{hemi}}^2 - z^2} \right\}$$

Filling out Equations (C.14) and (C.16) in Equation (C.13a) and applying the limits defined for region E gives:

$$\begin{aligned} (I_{xx, \text{cap}})_{\text{sphere}} &= (I_{yy, \text{cap}})_{\text{sphere}} \\ &= \frac{m_{\text{cap}}}{V_{\text{cap}}} \int_0^{2\pi} \int_{r_{\text{hemi}} - h_{\text{cap}}}^{r_{\text{hemi}}} \int_0^{\sqrt{r_{\text{hemi}}^2 - z^2}} (r^2 \sin^2 \theta + z^2) r \, dr \, dz \, d\theta \end{aligned} \quad (\text{C.17a})$$

where m_{cap} is the mass of the cap. Equation (C.17a) calculates the MoI of the hemispherical cap about the x - and y -axes passing through the centre of the associated sphere. Given that the centroid of a hemispherical cap \bar{z}_{cap} is measured with respect to the centre of the associated sphere, the MoI about the *centroidal* x - and y -axes can be derived using the *parallel axis theorem*^b. Using Equation (C.11), Equation (C.17a) solves as:

$$\begin{aligned} (I_{xx, \text{cap}})_{\text{sphere}} &= (I_{yy, \text{cap}})_{\text{sphere}} = \frac{m_{\text{cap}}}{20(3r_{\text{hemi}} - h_{\text{cap}})} (-9h_{\text{cap}}^3 + 45h_{\text{cap}}^2 r_{\text{hemi}} \\ &\quad - 80h_{\text{cap}} r_{\text{hemi}}^2 + 60r_{\text{hemi}}^3) \end{aligned} \quad (\text{C.17b})$$

The MoI about the *centroidal* x - and y -axes can now be derived using Equation (C.2), for which $I = (I_{xx, \text{cap}})_{\text{sphere}}$, $d = \bar{z}_{\text{cap}}$ and $I_0 = (I_{xx})_{\text{cap}}$. Solving for $(I_{xx})_{\text{cap}}$ then yields:

$$\begin{aligned} I_{xx, \text{cap}} &= I_{yy, \text{cap}} = \frac{m_{\text{cap}} h_{\text{cap}}}{80(h_{\text{cap}} - 3r_{\text{hemi}})^3} (-9h_{\text{cap}}^3 + 72h_{\text{cap}}^2 r_{\text{hemi}} \\ &\quad - 220h_{\text{cap}} r_{\text{hemi}}^2 + 240r_{\text{hemi}}^3) \end{aligned} \quad (\text{C.18})$$

As the z -axis passing through the centre of the associated sphere coincides with the *centroidal* z -axis of the hemispherical cap, the mass moment of inertia about the *centroidal* z -axis is obtained by filling out Equations (C.15) and (C.16) in Equation (C.13c) and applying the limits defined for region E , which gives:

$$I_{zz, \text{cap}} = \frac{m_{\text{cap}}}{V_{\text{cap}}} \int_0^{2\pi} \int_{r_{\text{hemi}} - h_{\text{cap}}}^{r_{\text{hemi}}} \int_0^{\sqrt{r_{\text{hemi}}^2 - z^2}} r^3 \, dr \, dz \, d\theta \quad (\text{C.19a})$$

Using Equation (C.11), Equation (C.19a) then solves as:

$$I_{zz, \text{cap}} = \frac{m_{\text{cap}} h_{\text{cap}}}{10(3r_{\text{hemi}} - h_{\text{cap}})} (3h_{\text{cap}}^2 - 15h_{\text{cap}} r_{\text{hemi}} + 20r_{\text{hemi}}^2) \quad (\text{C.19b})$$

Equations (C.18) and (C.19b) have been implemented as MATLAB functions and were verified by comparing their output to the values CATIA provides for a hemispherical cap, see also Table C-2.

^aSee also: <https://physics.stackexchange.com/q/123556> (Visited: February 7, 2019)

^bSee also: <https://physics.stackexchange.com/q/459054> (Visited: February 7, 2019)

Hemispherical Frustum. A hemispherical frustum can be described as a hemisphere with the top truncated by a plane parallel to its base. The volume of a uniform hemispherical frustum is calculated by (Harris & Stocker, 1998, p. 107):

$$V_{\text{frus}} = \frac{1}{6}\pi h_{\text{frus}}(3r_{\text{hemi}}^2 + 3r_{\text{frus}}^2 + h_{\text{frus}}^2) \quad (\text{C.20})$$

where h_{frus} is the height and r_{frus} is the radius of the upper base of the hemispherical frustum, calculated by:

$$r_{\text{frus}} = \sqrt{(r_{\text{hemi}}^2 + h_{\text{frus}}^2)} \quad (\text{C.21})$$

which when substituted in Equation (C.20) gives:

$$V_{\text{frus}} = \frac{1}{3}\pi h_{\text{frus}}(3r_{\text{hemi}}^2 - h_{\text{frus}}^2) \quad (\text{C.22})$$

The centroid of a uniform hemispherical frustum was not found in the literature, yet can be derived using Equation (C.4), along with $m = \rho V$, $V_{\text{hemi}} = V_{\text{frus}} + V_{\text{cap}}$ and $r_{\text{hemi}} = h_{\text{frus}} + h_{\text{cap}}$, as well as Equations (C.8), (C.9), (C.11) and (C.12). After some algebraic manipulation, the centroid is found to be:

$$\bar{z}_{\text{frus}} = \frac{3h_{\text{frus}}(2r_{\text{hemi}}^2 - h_{\text{frus}}^2)}{4(3r_{\text{hemi}}^2 - h_{\text{frus}}^2)} \quad (\text{C.23})$$

where \bar{z}_{frus} is measured with respect to the centre of the associated sphere, or equivalently, the centre of the base of the hemispherical frustum. In an analogous fashion, the MoI of a uniform hemispherical frustum, which were also not found in the literature, can be derived using Equation (C.2). Realising that $\mathbf{I}_{\text{hemi}} = (\mathbf{I}_{\text{frus}})_{\text{hemi}} + (\mathbf{I}_{\text{cap}})_{\text{hemi}}$ and $m_{\text{cap}} = V_{\text{cap}}m_{\text{frus}}V_{\text{frus}}^{-1}$, the following equation can be set up for the MoI about the centroidal x - and y -axes:

$$I_{xx, \text{frus}} = I_{yy, \text{frus}} = I_{xx, \text{hemi}} - I_{xx, \text{cap}} - (V_{\text{cap}}m_{\text{frus}}V_{\text{frus}}^{-1})(\bar{z}_{\text{cap}} - \bar{z}_{\text{hemi}})^2 - m_{\text{frus}}(\bar{z}_{\text{frus}} - \bar{z}_{\text{hemi}})^2 \quad (\text{C.24a})$$

With the knowledge that $h_{\text{cap}} = r_{\text{hemi}} - h_{\text{frus}}$, Equation (C.24a) solves as:

$$I_{xx, \text{frus}} = I_{yy, \text{frus}} = \frac{m_{\text{frus}}}{80(3r_{\text{hemi}}^2 - h_{\text{frus}}^2)^2} (180r_{\text{hemi}}^6 - 120r_{\text{hemi}}^4h_{\text{frus}}^2 + 32r_{\text{hemi}}^2h_{\text{frus}}^4 - 9h_{\text{frus}}^6) \quad (\text{C.24b})$$

For the mass moment of inertia about the centroidal z -axis, the following equation can be set up:

$$I_{zz, \text{frus}} = I_{zz, \text{hemi}} - I_{zz, \text{cap}} \quad (\text{C.25a})$$

which solves as:

$$I_{zz, \text{frus}} = \frac{m_{\text{frus}}}{30r_{\text{hemi}}^2 - 10h_{\text{frus}}^2} (15r_{\text{hemi}}^4 - 10r_{\text{hemi}}^2h_{\text{frus}}^2 + 3h_{\text{frus}}^4) \quad (\text{C.25b})$$

Equations (C.24b) and (C.25b) have been implemented as MATLAB functions and were verified by comparing their output to the values CATIA provides for a hemispherical frustum, see also Table C-2.

In order to calculate the inertia tensor of the solid propellant slug, its composition must first be determined. This can be done by calculating the propellant mass fraction:

$$n_{\text{solid}} = \frac{m_{\text{solid}}}{m_{\text{solid, max}}} \quad (\text{C.26})$$

where m_{solid} is the current mass of the slug and $m_{\text{solid, max}}$ is the maximum mass of the slug. The latter and other characteristics of the slug are listed in Table C-1.

Table C-1: Characteristics of the solid propellant slug.

Characteristic	Value	Comment
$h_{\text{cyl, solid}}$	0.0574 m	Derived from CATIA
$r_{\text{hemi, solid}}$	0.170 m	Derived from CATIA
$m_{\text{solid, max}}$	41.2 kg	Source: STAR 13B specifications ^a
$V_{\text{solid, max}}$	0.0256 m ³	Calculated
ρ_{solid}	$1.61 \times 10^3 \text{ kg m}^{-3}$	Calculated

^aNorthrop Grumman Innovation Systems - Propulsion Products Catalog (2018)

The composition of the slug can be derived from n_{solid} , as follows:

$$V_{\text{solid}} = \begin{cases} V_{\text{solid, max}}, & n_{\text{solid}} = 1 & (\text{C.27a}) \\ V_{\text{hemi, solid}} + V_{\text{cyl, solid}} + V_{\text{frus}}(r_{\text{hemi, solid}}, h_{\text{frus}}), & c_2 < n_{\text{solid}} < 1 & (\text{C.27b}) \\ V_{\text{hemi, solid}} + V_{\text{cyl}}(r_{\text{hemi, solid}}, h_{\text{cyl}}), & c_3 < n_{\text{solid}} \leq c_2 & (\text{C.27c}) \\ V_{\text{cap}}(r_{\text{hemi, solid}}, h_{\text{cap}}), & 0 \leq n_{\text{solid}} \leq c_3 & (\text{C.27d}) \end{cases}$$

where

$$c_2 = \frac{V_{\text{hemi, solid}} + V_{\text{cyl, solid}}}{V_{\text{solid, max}}} \quad (\text{C.28})$$

$$c_3 = \frac{V_{\text{hemi, solid}}}{V_{\text{solid, max}}} \quad (\text{C.29})$$

with $V_{\text{hemi, solid}} = V_{\text{hemi}}(r_{\text{hemi, solid}})$ and $V_{\text{cyl, solid}} = V_{\text{cyl}}(r_{\text{hemi, solid}}, h_{\text{cyl, solid}})$. The current volume of the slug is calculated by:

$$V_{\text{solid}} = \frac{m_{\text{solid}}}{\rho_{\text{solid}}} \quad (\text{C.30})$$

For **Solid Comp. 1**, the height of the hemispherical frustum can be calculated by:

$$h_{\text{frus}} = \text{Re} \left[\frac{-(1 + i\sqrt{3}) \sqrt[3]{\sqrt{9V_{\text{frus}}^2 - 4\pi^2 r_{\text{hemi}}^6} - 3V_{\text{frus}}}}{2\sqrt[3]{2\pi}} - \frac{(1 - i\sqrt{3}) \sqrt[3]{\pi r_{\text{hemi}}^2}}{2^{\frac{2}{3}} \sqrt[3]{\sqrt{9V_{\text{frus}}^2 - 4\pi^2 r_{\text{hemi}}^6} - 3V_{\text{frus}}}} \right] \quad (\text{C.31})$$

where i is the unit imaginary number, $r_{\text{hemi}} = r_{\text{hemi, solid}}$ and $\text{Re}[\dots]$ is the real part of a complex number. From Equation (C.27b) it can be derived that $V_{\text{frus}} = V_{\text{solid}} - V_{\text{hemi, solid}} - V_{\text{cyl, solid}}$. The inertia tensor of **Solid Comp. 1** can be obtained by carrying out the following three steps:

1. Calculate the individual MoI of the hemisphere, cylinder and hemispherical frustum using Equations (C.10a) and (C.10b), Equations (C.7a) and (C.7b), and Equations (C.24b) and (C.25b), respectively, as well as their masses, and centroids, using Equation (C.9), Equation (C.6) and Equation (C.23), respectively.
2. Express the found centroids in vector form with respect to the centre of the outer edge of the case-side hemisphere (see Figure C-1), and use Equation (C.4) to find the CoM of the composition.
3. Use Equation (C.3) to express the inertia tensors of the individual geometries with respect to the parallel coordinate system located at the CoM of the composition, and add them together to find the inertia tensor of the composition.

For **Solid Comp. 2**, the height of the cylinder can be calculated by:

$$h_{\text{cyl}} = \frac{V_{\text{cyl}}}{\pi r_{\text{hemi}}^2} \quad (\text{C.32})$$

where from Equation (C.27c) it can be derived that $V_{\text{cyl}} = V_{\text{solid}} - V_{\text{hemi, solid}}$. The inertia tensor of **Solid Comp. 2** can be obtained by first calculating the individual MoI of the hemisphere and cylinder using Equations (C.10a) and (C.10b), and Equations (C.7a) and (C.7b), respectively, as well as their masses and centroids, using Equation (C.9) and Equation (C.6), respectively. Then steps 2 and 3 as described above must be completed.

For **Solid Comp. 3**, the height of the hemispherical cap can be calculated by:

$$h_{\text{cap}} = \text{Re} \left[\frac{-(1 + i\sqrt{3}) \sqrt[3]{\sqrt{3}\sqrt{3V_{\text{cap}}^2 - 4\pi r_{\text{hemi}}^3 V_{\text{cap}} + 2\pi r_{\text{hemi}}^3} - 3V_{\text{cap}}}}{2\sqrt[3]{2\pi}} - \frac{(1 - i\sqrt{3}) \sqrt[3]{\pi r_{\text{hemi}}^2}}{2^{\frac{2}{3}} \sqrt[3]{\sqrt{3}\sqrt{3V_{\text{cap}}^2 - 4\pi r_{\text{hemi}}^3 V_{\text{cap}} + 2\pi r_{\text{hemi}}^3} - 3V_{\text{cap}}}} + r_{\text{hemi}} \right] \quad (\text{C.33})$$

Table C-2: Overview of the equations in this section that are implemented as MATLAB functions and their means of verification.

Equation(s)	Function	Verification
(C.4)	centre_of_mass.m	b
(C.5), (C.6)	cylinder.m	a
(C.32)	cylinder_height.m	a
(C.7a), (C.7b)	cylinder_inertia.m	b
(C.8), (C.9)	hemisphere.m	b
(C.10a), (C.10b)	hemisphere_inertia.m	b
(C.11), (C.12)	hemispherical_cap.m	b
(C.33)	hemispherical_cap_height.m	c
(C.18), (C.19b)	hemispherical_cap_inertia.m	b
(C.22), (C.23)	hemispherical_frustum.m	b
(C.31)	hemispherical_frustum_height.m	c
(C.24b), (C.25b)	hemispherical_frustum_inertia.m	b
(C.3)	parallel_axis.m	d
(C.27)	solid_propellant_slug.m	b

^a Analytically.

^b Comparing output to values CATIA provides.

^c Plugging in volume of hemisphere and comparing output to radius of hemisphere.

^d Combining inertias hemispherical frustum and cap to find inertia hemisphere.

where from Equation (C.27d) it can be derived that $V_{\text{cap}} = V_{\text{solid}}$. The inertia tensor of the hemispherical cap that is **Solid Comp. 3** can be calculated using Equations (C.18) and (C.19b). Its centroid can be calculated using Equation (C.12), which is then expressed with respect to the centre of the outer edge of the case-side hemisphere.

Table C-2 shows which of the expressions discussed in this section are implemented as MATLAB functions and how they were verified. Using `solid_propellant_slug.m` and the constants listed in Table C-1, the relations between the mass of the solid propellant slug and its CoM and MoI are visualised, see Figures C-3 and C-4. To reduce computational loads during the simulation study, each relation is stored as a MATLAB callable *piecewise linear interpolant*, which can be evaluated at each m_{solid} .

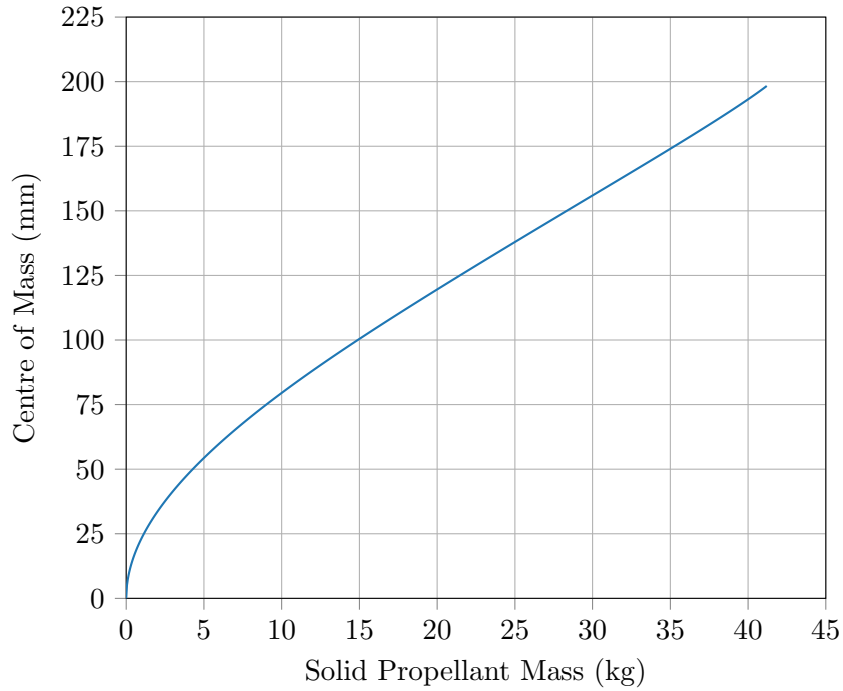


Figure C-3: CoM of the solid propellant slug (with respect to the centre of the outer edge of the case-side hemisphere) as a function of the mass of the slug.

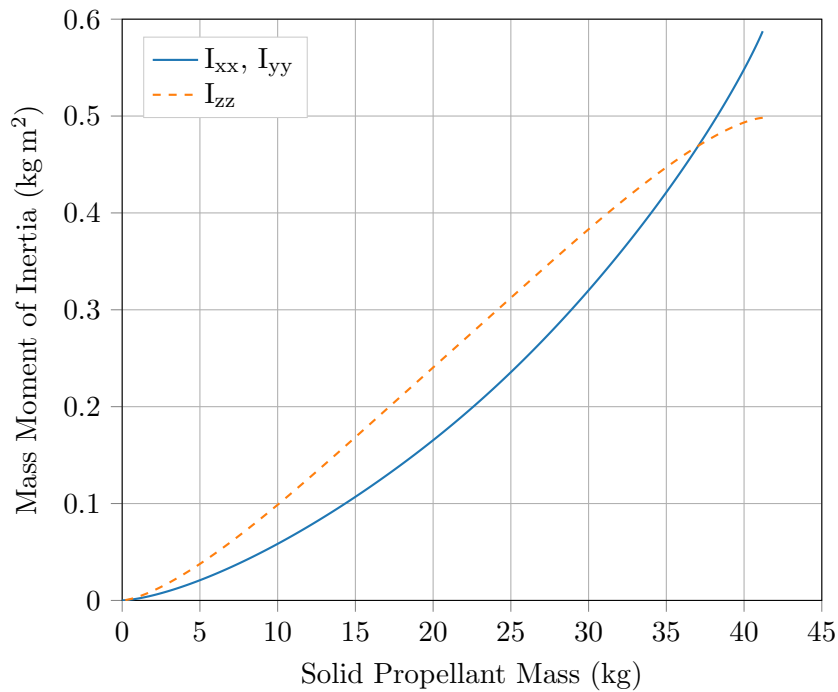


Figure C-4: Mol of the solid propellant slug about its centroidal axes as a function of the mass of the slug.

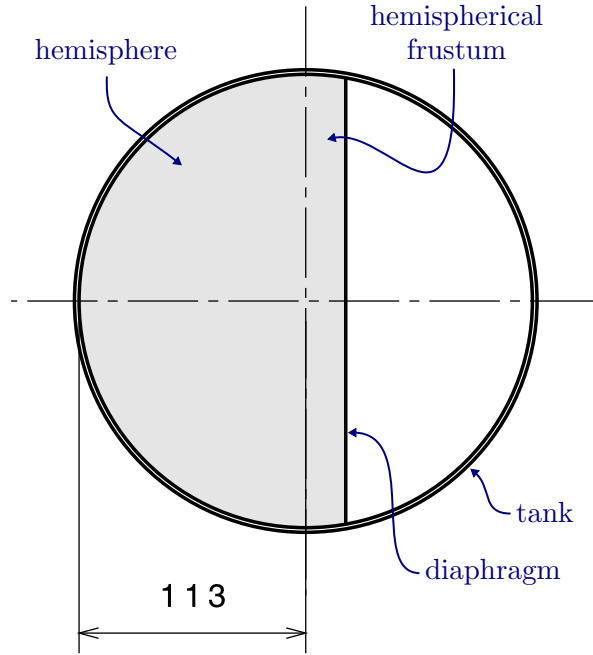


Figure C-5: Schematic representation of an arbitrary partial liquid propellant slug (light grey area) inside RAFAEL's PEPT-230 propellant tank. The definitions of the geometries are given. The radius shown is in millimetres.

C-2 Liquid Propellant Slug

For the derivation of the relations between the mass of the liquid propellant slug and its CoM and MoI, it is assumed that the slug is bounded by a spherical propellant tank on the one side, and a flat surface representing a *diaphragm* (see Section 2-2-1) on the other side. The shape of the slug is thus composed of simple geometries, see Figure C-5. While the slug is consumed, two consecutive slug compositions are distinguished:

- **Liquid Comp. 1:** Hemisphere + hemispherical frustum
- **Liquid Comp. 2:** Hemispherical cap

The liquid propellant slug has a symmetry axis and is assumed to be uniformly hydrazine, hence the CoM of the slug lies on the symmetry axis and the inertia tensor is diagonal:

$$\mathbf{I}_{\text{liquid}} = \begin{bmatrix} I_{xx} & 0 & 0 \\ 0 & I_{yy} & 0 \\ 0 & 0 & I_{zz} \end{bmatrix}_{\text{liquid}} \quad (\text{C.34})$$

The inertia tensor of the liquid propellant slug can be calculated once its composition is established. The first step in deriving the composition is to calculate the following mass

fraction:

$$n_{\text{liquid}} = \frac{m_{\text{liquid}}}{m_{\text{liquid, max}}} \quad (\text{C.35})$$

where m_{liquid} is the current mass and $m_{\text{liquid, max}}$ is the maximum mass of the liquid propellant slug. Table C-3 provides values for the latter as well as for other relevant characteristics.

Table C-3: Characteristics of the liquid propellant slug.

Characteristic	Value	Comment
$r_{\text{hemi, liquid}}$	0.113 m	Derived from CATIA
$m_{\text{liquid, max}}$	4.3 kg	Calculated in Section 2-2-1
ρ_{hyd}	$1.008 \times 10^3 \text{ kg m}^{-3}$	Source: Ley et al. (2009)
$V_{\text{liquid, max}}$	$4.266 \times 10^{-3} \text{ m}^3$	Calculated

The mass fraction n_{liquid} is then used to determine how the momentary volume of the liquid propellant slug is obtained:

$$V_{\text{liquid}} = \begin{cases} V_{\text{hemi, liquid}} + V_{\text{frus}}(r_{\text{hemi, liquid}}, h_{\text{frus}}), & d_1 < n_{\text{liquid}} \leq 1 \\ V_{\text{cap}}(r_{\text{hemi, liquid}}, h_{\text{cap}}), & 0 \leq n_{\text{liquid}} \leq d_1 \end{cases} \quad (\text{C.36a})$$

$$0 \leq n_{\text{liquid}} \leq d_1 \quad (\text{C.36b})$$

where

$$d_1 = \frac{V_{\text{hemi, liquid}}}{V_{\text{liquid, max}}} \quad (\text{C.37})$$

with $V_{\text{hemi, liquid}} = V_{\text{hemi}}(r_{\text{hemi, liquid}})$. The momentary volume of the liquid propellant slug is calculated by dividing its momentary mass by its density:

$$V_{\text{liquid}} = \frac{m_{\text{liquid}}}{\rho_{\text{hyd}}} \quad (\text{C.38})$$

For **Liquid Comp. 1**, the height of the hemispherical frustum can be calculated using Equation (C.31). From Equation (C.36a) it can be derived that $V_{\text{frus}} = V_{\text{liquid}} - V_{\text{hemi, liquid}}$. The inertia tensor can be obtained by carrying out the following three steps:

1. Calculate the individual MoI of the hemisphere and the hemispherical frustum using Equations (C.10a) and (C.10b), and Equations (C.24b) and (C.25b), respectively, as well as their masses, and centroids, using Equation (C.9) and Equation (C.23), respectively.
2. Express the found centroids in vector form with respect to the centre of the edge of the tank-side hemisphere (see Figure C-5), and use Equation (C.4) to find the CoM of the composition.

3. Use Equation (C.3) to express the inertia tensors of the individual geometries with respect to the parallel coordinate system located at the CoM of the composition, and add them together to find the inertia tensor of the composition.

For **Liquid Comp. 2**, the height of the hemispherical cap can be calculated with Equation (C.33), where from Equation (C.36b) it can be derived that $V_{\text{cap}} = V_{\text{liquid}}$. The inertia tensor of the hemispherical cap that solely constitutes the composition can be calculated using Equations (C.18) and (C.19b). Its centroid can be calculated using Equation (C.12), which is then expressed with respect to the centre of the edge of the tank-side hemisphere.

Equation (C.36) is implemented as the MATLAB function `liquid_propellant_slug.m` with calls to the relevant functions listed in Table C-2, and is verified by comparing its output to the values CATIA provides for a render of the liquid propellant slug.

Using `liquid_propellant_slug.m` in conjunction with the constants provided in Table C-3, the relations between the mass of the liquid propellant slug and its CoM and MoI are obtained, see Figures C-6 and C-7. Similar to what was done for the solid propellant slug (see Appendix C-1, each relation is stored as a MATLAB callable *piecewise linear interpolant* to be evaluated at each m_{liquid} , so as to save computational power during the simulations.

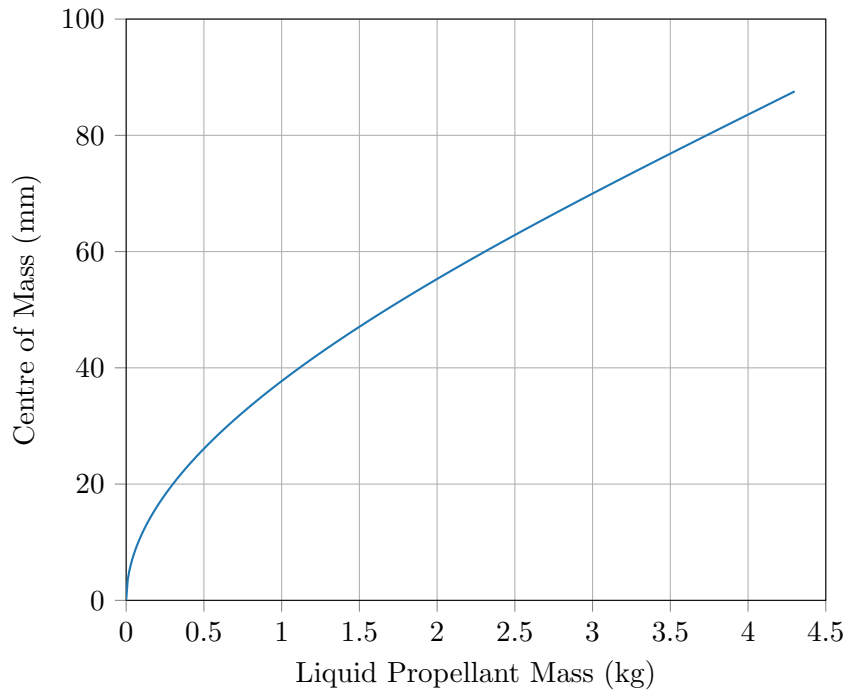


Figure C-6: CoM of the liquid propellant slug (with respect to the centre of the edge of the tank-side hemisphere) as a function of the mass of the slug.

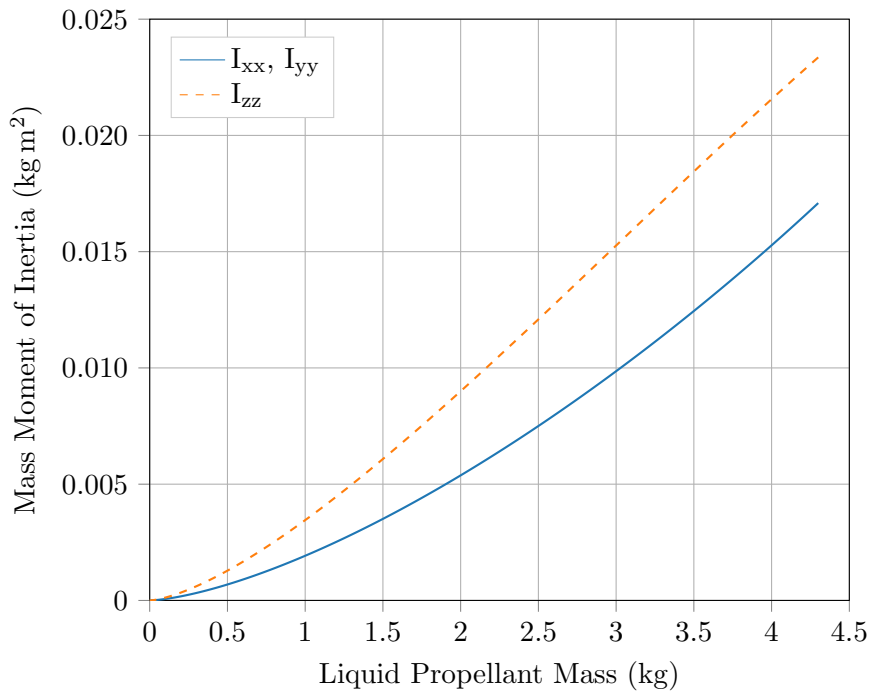


Figure C-7: Mol of the liquid propellant slug about its centroidal axes as a function of the mass of the slug.

Appendix D

State Variable Transformations

This appendix is dedicated to providing the necessary mathematics for converting one state variable set into another.

D-1 Euler Angles to Unit Quaternions

Given an orientation expressed in Euler angles $\{\phi, \theta, \psi\}$ and a $(\phi \leftarrow \theta \leftarrow \psi)$ rotation sequence (most commonly used in aerospace applications, see Section 3-2), the corresponding unit quaternion $\{q_1, q_2, q_3, q_4\}$, where q_4 is the scalar part, can be calculated by (Diebel, 2006):

$$\mathbf{q}_{123}(\phi, \theta, \psi) = \begin{bmatrix} q_1 \\ q_2 \\ q_3 \\ q_4 \end{bmatrix} = \begin{bmatrix} \sin \frac{\phi}{2} \cos \frac{\theta}{2} \cos \frac{\psi}{2} - \cos \frac{\phi}{2} \sin \frac{\theta}{2} \sin \frac{\psi}{2} \\ \cos \frac{\phi}{2} \sin \frac{\theta}{2} \cos \frac{\psi}{2} + \sin \frac{\phi}{2} \cos \frac{\theta}{2} \sin \frac{\psi}{2} \\ \cos \frac{\phi}{2} \cos \frac{\theta}{2} \sin \frac{\psi}{2} - \sin \frac{\phi}{2} \sin \frac{\theta}{2} \cos \frac{\psi}{2} \\ \cos \frac{\phi}{2} \cos \frac{\theta}{2} \cos \frac{\psi}{2} + \sin \frac{\phi}{2} \sin \frac{\theta}{2} \sin \frac{\psi}{2} \end{bmatrix} \quad (\text{D.1})$$

Equation (D.1) has been implemented as the MATLAB function `euler2quat.m`, which was verified by performing back-and-forth conversions with `quat2euler.m` (see Appendix D-2).

D-2 Unit Quaternions to Euler Angles

Given an orientation expressed in quaternions $\{q_1, q_2, q_3, q_4\}$, where q_4 is the scalar part, and the rotation sequence is $(\phi \leftarrow \theta \leftarrow \psi)$, then the quaternion set can be converted to Euler angles $\{\phi, \theta, \psi\}$ by (Diebel, 2006):

$$\mathbf{u}_{123}(q_1, q_2, q_3, q_4) = \begin{bmatrix} \phi \\ \theta \\ \psi \end{bmatrix} = \begin{bmatrix} \text{atan2}(2q_2q_3 + 2q_1q_4, q_3^2 + q_4^2 - q_1^2 - q_2^2) \\ -\arcsin(2q_1q_3 - 2q_2q_4) \\ \text{atan2}(2q_1q_2 + 2q_3q_4, q_1^2 + q_4^2 - q_2^2 - q_3^2) \end{bmatrix} \quad (\text{D.2})$$

where `atan2` is a built-in MATLAB function. However, when $\theta \approx \pm 90^\circ$, or equivalently, $(1 - |2q_1q_3 - 2q_2q_4|) \approx 0$, a singularity occurs. To programmatically account for this singularity, the quaternion set is converted by Equation (D.3)¹ in case the aforementioned term goes below 1×10^{-5} .

$$\mathbf{u}_{123}(q_1, q_2, q_3, q_4) = \begin{bmatrix} \phi \\ \theta \\ \psi \end{bmatrix} = \begin{bmatrix} 0 \\ -\arcsin(2q_1q_3 - 2q_2q_4) \\ \text{atan2}(-2q_1q_2 - 2q_3q_4, q_2^2 + q_4^2 - q_1^2 - q_3^2) \end{bmatrix} \quad (\text{D.3})$$

It should be noted that in order for a quaternion to be a valid rotation, its Euclidean norm must be equal to one. Equations (D.2) and (D.3) have been implemented as the MATLAB function `quat2euler.m`, which was verified by performing back-and-forth conversions with `euler2quat.m` (see Appendix D-1).

¹Extracted from the source code of Three.js, see <https://github.com/mrdoob/three.js/blob/dev/src/math/Euler.js> (Visited: March 10, 2019)

Appendix E

Frame Transformations

Vectors given with respect to one right-handed Cartesian frame of reference can be expressed with respect to another by applying the following transformation (Diebel, 2006):

$$\mathbf{x}_Q = \mathbf{C}^{Q/P} \mathbf{x}_P \quad (\text{E.1})$$

where \mathbf{x}_Q is the vector expressed in an arbitrary Q -frame, \mathbf{x}_P is the vector expressed in an arbitrary P -frame and $\mathbf{C}^{Q/P}$ is the so-called *Direction Cosine Matrix* (DCM). The DCM rotates the vector concerned without changing its magnitude, and is defined depending on the attitude parameterisation. The DCM in terms of quaternions is given by (*e.g.*, Diebel, 2006):

$$\mathbf{C}^{Q/P} = \mathbf{C}(\mathbf{q}^{Q/P}) = \begin{bmatrix} 1 - 2(q_2^2 + q_3^2) & 2(q_1q_2 + q_3q_4) & 2(q_1q_3 - q_2q_4) \\ 2(q_2q_1 - q_3q_4) & 1 - 2(q_1^2 + q_3^2) & 2(q_2q_3 + q_1q_4) \\ 2(q_3q_1 + q_2q_4) & 2(q_3q_2 - q_1q_4) & 1 - 2(q_1^2 + q_2^2) \end{bmatrix}_{Q/P} \quad (\text{E.2})$$

where $\mathbf{q}^{Q/P}$ is the quaternion associated with the transformation from the P -frame to the Q -frame. In case this transformation involves two successive rotations, such that:

$$\mathbf{q}^{P'/P} : P' \leftarrow P \quad (\text{E.3a})$$

$$\mathbf{q}^{Q/P'} : Q \leftarrow P' \quad (\text{E.3b})$$

then:

$$\mathbf{C}(\mathbf{q}^{Q/P}) = \mathbf{C}(\mathbf{q}^{Q/P'}) \mathbf{C}(\mathbf{q}^{P'/P}) = \mathbf{C}(\mathbf{q}^{Q/P'} \otimes \mathbf{q}^{P'/P}) \quad (\text{E.4})$$

where the notation \otimes for *quaternion multiplication*, which is *noncommutative*, is adopted from Shuster (1993) and

$$\mathbf{q}^{Q/P} = \mathbf{q}^{Q/P'} \otimes \mathbf{q}^{P'/P} = \begin{bmatrix} q_4^{Q/P'} \mathbf{q}^{P'/P} + q_4^{P'/P} \mathbf{q}^{Q/P'} + \mathbf{q}^{P'/P} \times \mathbf{q}^{Q/P'} \\ q_4^{P'/P} q_4^{Q/P'} - (\mathbf{q}^{P'/P})^T \mathbf{q}^{Q/P'} \end{bmatrix} \quad (\text{E.5})$$

which can also be written as (Shuster, 1993):

$$\mathbf{q}^{Q/P} = \begin{bmatrix} q_1 \\ q_2 \\ q_3 \\ q_4 \end{bmatrix}_{Q/P} = \begin{bmatrix} q_4 & q_3 & -q_2 & q_1 \\ -q_3 & q_4 & q_1 & q_2 \\ q_2 & -q_1 & q_4 & q_3 \\ -q_1 & -q_2 & -q_3 & q_4 \end{bmatrix}_{Q/P'} \begin{bmatrix} q_1 \\ q_2 \\ q_3 \\ q_4 \end{bmatrix}_{P'/P} \quad (\text{E.6})$$

Equation (E.6) is known as the *composition rule* and its 4×4 orthonormal matrix is referred to as the *quaternion matrix* (Wie, 2008).

Appendix F

Translational Equations of Motion

Analogous to Equation (3.8), the translational EoM of a non-elastic mass-varying body, relative to an inertial reference frame, can be written as (Cornelisse et al., 1979):

$$\mathbf{F}_{\text{ext}} + \mathbf{F}_C + \mathbf{F}_{\text{rel}} = m \frac{d^2 \mathbf{r}_I}{dt^2} = m \ddot{\mathbf{r}}_I \quad (\text{F.1})$$

with:

$$\mathbf{F}_C = -2 \dot{m} \boldsymbol{\omega} \times \mathbf{r}_e \quad (\text{F.2})$$

$$\mathbf{F}_{\text{rel}} = -\dot{m} \mathbf{v}_e \quad (\text{F.3})$$

where \mathbf{F}_C and \mathbf{F}_{rel} are the Coriolis force and relative force arising as a result of a variable mass distribution, respectively. Furthermore, \mathbf{F}_{ext} is the sum of external forces acting on the body, expressed in the inertial frame and \mathbf{r}_I is the position of the CoM of the body with respect to the inertial frame. Notably, \mathbf{F}_C and \mathbf{F}_{rel} are apparent forces that, when examining Equations (F.2) and (F.3), emerge only when propellant is being consumed. When this happens, it is noted that the following holds for the DOM as well as during thruster firings:

$$|\boldsymbol{\omega} \times \mathbf{r}_e| \ll |\mathbf{v}_e|$$

meaning that, in effect, \mathbf{F}_C can be neglected. Redefining \mathbf{F}_{rel} as \mathbf{F}_T – the thrust force – neglecting any environmental disturbance forces, and rewriting Equation (F.1) then yields:

$$m \ddot{\mathbf{r}}_I = \mathbf{F}_T \quad (\text{F.4})$$

Appendix G

Hardware Specifications

Table G-1: Specifications of Aerojet's MR-111C hydrazine thruster.

Characteristic	Value ^a
Manufacturer	Aerojet
Model	MR-111C
Propellant	Hydrazine (N ₂ H ₄)
Minimum Pulse Width	0.020 s
Inlet Pressure Range	27.6 - 5.5 bar
Thrust Range	5.3 - 1.3 N
Specific Impulse Range	229 - 215 s

^aAerojet - Monopropellant Rockets Catalog

Table G-2: Specifications of RAFAEL's PEPT-230 mono-propellant tank.

Characteristic	Value ^a
Manufacturer	RAFAEL
Model	PEPT-230
Material	Titanium
Propellant	Hydrazine (N ₂ H ₄)
Propellant Storage	Rubber Diaphragm
Nominal Volume	6 l
Operating Pressure Range	24 - 5.5 bar

^aRAFAEL - Space Propulsion Catalog (2014)

Table G-3: Specifications of Northrop Grumman's STAR 13B rocket motor.

Characteristic	Value ^a
Manufacturer	Northrop Grumman Innovation Systems
Model	STAR 13B
Maximum Propellant Loading	41.2 kg
Minimum Propellant Loading	33.0 kg ^b
Average Thrust	7598 N
Maximum Thrust	9608 N
Burn Time	14.8 s
Action Time	16.1 s
Spin Experience	120 rpm

^aNorthrop Grumman Innovation Systems - Propulsion Products Catalog (2018)

^bCorresponds to a 20% off-loading – maximum off-loading before any motor modifications are necessary. Source: Lara, M. (Northrop Grumman), personal communication, 2018.

Bibliography

- Acampora, G., Pedrycz, W., Vasilakos, A., & Vitiello, A. (2020). *Computational Intelligence for Semantic Knowledge Management* (1st ed.). Cham, Switzerland: Springer. Retrieved from <https://www.springer.com/gp/book/9783030237585> doi: 10.1007/978-3-030-23760-8
- Armstrong, R. S. (1965, feb). *Errors Associated With Spinning-Up and Thrusting Symmetric Rigid Bodies* (Tech. Rep.). Pasadena, California: NASA Jet Propulsion Laboratory. Retrieved from <http://hdl.handle.net/2060/19650008264>
- Balafoutis, C. A., & Patel, R. V. (1991). *Dynamic Analysis of Robot Manipulators: A Cartesian Tensor Approach* (1st ed.). New York: Springer.
- Barber, S., Sheridan, S., Wright, I., Sargeant, H., Church, P., Perkinson, M.-C., . . . Griffiths, A. (2017). *L-DART: Lunar Direct Analysis of Resource Traps* (Tech. Rep.). Milton Keynes, United Kingdom: The Open University. (Unpublished)
- Barraclough, S., Perkinson, M.-C., Peacocke, L., & Vijendran, S. (2015, jun). Penetrator for the Exploration of Europa. In *Proceedings of the 12th International Planetary Probe Workshop*. Cologne, Germany.
- Blanc-Paques, P. (2005, jun). *Thruster Calibration for the SPHERES Spacecraft Formation Flight Testbed* (Tech. Rep.). Cambridge, Massachusetts: Massachusetts Institute of Technology. Retrieved from http://ssl.mit.edu/spheres/library/Thruster_calibration1.pdf
- Bouma, W. J. (2017, oct). *Concept Study: ESA Lunar Penetrator Mission for In-Situ Volatile Detection* (Tech. Rep.). Noordwijk, The Netherlands: ESA/ESTEC. (Unpublished)
- Boyce, W. E., & DiPrima, R. C. (2010). *Elementary Differential Equations and Boundary Value Problems* (9th ed.). Hoboken, New Jersey: John Wiley & Sons, Inc.
- Boyd, S., & Vandenberghe, L. (2009). *Convex Optimization* (7th ed.). Cambridge, United Kingdom: Cambridge University Press.
- Braun, R. D., Mitcheltree, R. A., & Cheatwood, F. M. (1999, may). Mars Microprobe Entry-to-Impact Analysis. *Journal of Spacecraft and Rockets*, 36(3), 412–420. Retrieved from <http://arc.aiaa.org/doi/10.2514/2.3461> doi: 10.2514/2.3461

- Carpenter, J., Fisackerly, R., & Houdou, B. (2016, aug). Establishing lunar resource viability. *Space Policy*, 37, 52–57. Retrieved from <http://dx.doi.org/10.1016/j.spacepol.2016.07.002> doi: 10.1016/j.spacepol.2016.07.002
- Colaprete, A., Schultz, P., Heldmann, J., Wooden, D., Shirley, M., Ennico, K., ... Sollitt, L. (2010, oct). Detection of Water in the LCROSS Ejecta Plume. *Science*, 330(6003), 463–468. Retrieved from <http://www.sciencemag.org/cgi/doi/10.1126/science.1186986> doi: 10.1126/science.1186986
- Cornelisse, J. W., Schöyer, H. F. R., & Wakker, K. F. (1979). *Rocket Propulsion and Spaceflight Dynamics* (1st ed.). London: Pitman Publishing Ltd.
- Crawford, B. (1969, aug). Configuration design and efficient operation of redundant multi-jet systems. In *Astrodynamics Conference*. Reston, Virginia: American Institute of Aeronautics and Astronautics. Retrieved from <http://arc.aiaa.org/doi/10.2514/6.1969-845> doi: 10.2514/6.1969-845
- Curtis, H. D. (2014). *Orbital Mechanics for Engineering Students* (3rd ed.). Boston: Butterworth-Heinemann.
- Dalmo, M., & Egeland, O. (1997). State feedback H_∞ control of a rigid spacecraft. *IEEE Transactions on Automatic Control*, 42(8), 1186–1191. Retrieved from <http://ieeexplore.ieee.org/document/618253/> doi: 10.1109/9.618253
- Devey, W., Field, C., & Flook, L. (1977, mar). An Active Nutation Control System for Spin Stabilised Satellites. *Automatica*, 13(2), 161–172. Retrieved from <http://linkinghub.elsevier.com/retrieve/pii/0005109877900401> doi: 10.1016/0005-1098(77)90040-1
- Diebel, J. (2006, oct). *Representing attitude: Euler angles, unit quaternions, and rotation vectors* (Tech. Rep.). Stanford, California: Stanford University. Retrieved from <https://www.astro.rug.nl/software/kapteyn/downloads/attitude.pdf>
- Dodge, F. T. (2000). *The New Dynamic Behaviour of Liquids in Moving Containers* (Tech. Rep.). San Antonio, Texas: Southwest Research Institute.
- Dwyer, T. A. W., & Sira-Ramirez, H. (1988, may). Variable-structure control of spacecraft attitude maneuvers. *Journal of Guidance, Control, and Dynamics*, 11(3), 262–270. Retrieved from <http://arc.aiaa.org/doi/10.2514/3.20303> doi: 10.2514/3.20303
- Elias, R., & Vega-Navarez, J. (2008, aug). Active Nutation and Precession Control for Exoatmospheric Spinning Ballistic Missiles. In *AIAA Guidance, Navigation and Control Conference and Exhibit* (Vol. 32816). Reston, Virginia: American Institute of Aeronautics and Astronautics. Retrieved from <http://arc.aiaa.org/doi/10.2514/6.2008-6998> doi: 10.2514/6.2008-6998
- Feldman, W. C., Maurice, S., Binder, A. B., Barraclough, B. L., Elphic, R. C., & Lawrence, D. J. (1998, sep). Fluxes of Fast and Epithermal Neutrons from Lunar Prospector: Evidence for Water Ice at the Lunar Poles. *Science*, 281(5382), 1496–1500. Retrieved from <http://www.sciencemag.org/cgi/doi/10.1126/science.281.5382.1496> doi: 10.1126/science.281.5382.1496
- Feldman, W. C., Maurice, S., Lawrence, D. J., Little, R. C., Lawson, S. L., Gasnault, O., ... Binder, A. B. (2001, oct). Evidence for water ice near the lunar poles. *Journal of Geophysical Research*, 106(E10), 23231–23251. Retrieved from <https://agupubs.onlinelibrary.wiley.com/doi/abs/10.1029/2000JE001444> doi: https://doi.org/

- 10.1029/2000JE001444
- Ficken, F. (2015). *The Simplex Method of Linear Programming* (1st ed.). Mineola, New York: Dover Publications.
- Gao, Y., Phipps, A., Taylor, M., Crawford, I. A., Ball, A. J., Wilson, L., ... Gowen, R. (2008, mar). Lunar science with affordable small spacecraft technologies: Moon-LITE and Moonraker. *Planetary and Space Science*, *56*(3-4), 368–377. Retrieved from <http://linkinghub.elsevier.com/retrieve/pii/S0032063307003364> doi: 10.1016/j.pss.2007.11.005
- Grant, M. C., & Boyd, S. P. (2008). Graph Implementations for Nonsmooth Convex Programs. In *Recent Advances in Learning and Control* (pp. 95–110). London: Springer London.
- Grasshoff, L. H. (1968, may). An Onboard, Closed-Loop, Nutation Control System for a Spin-Stabilized Spacecraft. *Journal of Spacecraft and Rockets*, *5*(5), 530–535. Retrieved from <https://arc.aiaa.org/doi/10.2514/3.29300> doi: 10.2514/3.29300
- Gui, H., & Vukovich, G. (2015, dec). Robust adaptive spin-axis stabilization of a symmetric spacecraft using two bounded torques. *Advances in Space Research*, *56*(11), 2495–2507. Retrieved from <https://linkinghub.elsevier.com/retrieve/pii/S0273117715006997> doi: 10.1016/j.asr.2015.09.038
- Harris, J. W., & Stocker, H. (1998). *Handbook of Mathematics and Computational Science* (1st ed.). New York: Springer-Verlag.
- Hayne, P. O., Hendrix, A., Sefton-Nash, E., Siegler, M. A., Lucey, P. G., Retherford, K. D., ... Paige, D. A. (2015, jul). Evidence for exposed water ice in the Moon's south polar regions from Lunar Reconnaissance Orbiter ultraviolet albedo and temperature measurements. *Icarus*, *255*, 58–69. Retrieved from <http://dx.doi.org/10.1016/j.icarus.2015.03.032> doi: 10.1016/j.icarus.2015.03.032
- Hibbeler, R. (2010). *Engineering Mechanics: Statics* (12th ed.). Singapore: Pearson Education.
- Hrastar, J. A. (1974, may). *Testing a Satellite Automatic Nutation Control System* (Tech. Rep.). Greenbelt, MD: NASA Goddard Space Flight Center. Retrieved from <http://hdl.handle.net/2060/19740013787>
- Ibrahim, R. A. (2005). *Liquid Sloshing Dynamics: Theory and Applications* (1st ed.). Cambridge, United Kingdom: Cambridge University Press.
- Jackson, M., & Gonzalez, R. (2007, aug). Orion Orbit Reaction Control Assessment. In *Aiaa guidance, navigation and control conference and exhibit* (pp. 1–16). Reston, Virginia: American Institute of Aeronautics and Astronautics. Retrieved from <http://arc.aiaa.org/doi/10.2514/6.2007-6684> doi: 10.2514/6.2007-6684
- Joshi, S., Kelkar, A., & Wen, J.-Y. (1995). Robust attitude stabilization of spacecraft using nonlinear quaternion feedback. *IEEE Transactions on Automatic Control*, *40*(10), 1800–1803. Retrieved from <http://ieeexplore.ieee.org/document/467669/> doi: 10.1109/9.467669
- Kane, T. R., & Levinson, D. A. (1985). *Dynamics: Theory and Applications* (1st ed.). New York: McGraw-Hill.
- Kang, W. (1995, jul). Nonlinear H_∞ control and its application to rigid spacecraft. *IEEE Transactions on Automatic Control*, *40*(7), 1281–1285. Retrieved from <http://ieeexplore.ieee.org/document/400476/> doi: 10.1109/9.400476

- Knauber, R. N. (1996, nov). Thrust Misalignments of Fixed-Nozzle Solid Rocket Motors. *Journal of Spacecraft and Rockets*, 33(6), 794–799. Retrieved from <https://arc.aiaa.org/doi/10.2514/3.26840> doi: 10.2514/3.26840
- Kozák, Š. (2014, may). State-of-the-art in control engineering. *Journal of Electrical Systems and Information Technology*, 1(1), 1–9. Retrieved from <https://linkinghub.elsevier.com/retrieve/pii/S2314717214000038> doi: 10.1016/j.jesit.2014.03.002
- Lawrence, D. A., & Holden, T. E. (2007, nov). Essentially Globally Asymptotically Stable Nutation Control Using a Single Reaction Wheel. *Journal of Guidance, Control, and Dynamics*, 30(6), 1783–1793. Retrieved from <http://arc.aiaa.org/doi/10.2514/1.27790> doi: 10.2514/1.27790
- Ley, W., Wittmann, K., & Hallmann, W. (2009). *Handbook of Space Technology* (1st ed.). Chichester, United Kingdom: John Wiley & Sons, Ltd.
- Li, S., Lucey, P. G., Milliken, R. E., Hayne, P. O., Fisher, E., Williams, J.-P., ... Elphic, R. C. (2018, sep). Direct evidence of surface exposed water ice in the lunar polar regions. *Proceedings of the National Academy of Sciences*, 115(36), 8907–8912. Retrieved from <http://www.pnas.org/lookup/doi/10.1073/pnas.1802345115> doi: 10.1073/pnas.1802345115
- Lissauer, J. J., & De Pater, I. (2013). *Fundamental Planetary Science: Physics, Chemistry and Habitability* (1st ed.). Cambridge, United Kingdom: Cambridge University Press.
- Lo, S.-C., & Chen, Y.-P. (1995, nov). Smooth Sliding-Mode Control for Spacecraft Attitude Tracking Maneuvers. *Journal of Guidance, Control, and Dynamics*, 18(6), 1345–1349. Retrieved from <http://arc.aiaa.org/doi/10.2514/3.21551> doi: 10.2514/3.21551
- Lorenz, R. (2011, aug). Planetary penetrators: Their origins, history and future. *Advances in Space Research*, 48(3), 403–431. Retrieved from <http://dx.doi.org/10.1016/j.asr.2011.03.033> doi: 10.1016/j.asr.2011.03.033
- Lumpkin, C. K. (1974, aug). *Mars Penetrator: Subsurface Science Mission* (Tech. Rep.). Albuquerque, New Mexico: Sandia National Labs. Retrieved from <http://hdl.handle.net/2060/19750004806>
- Manning, L. A. (1977, jun). *Mars Surface Penetrator - System Description* (Tech. Rep.). Moffett Field, California: NASA Ames Research Center. Retrieved from <http://hdl.handle.net/2060/19770025116>
- Markley, F. L., & Crassidis, J. L. (2014). *Fundamentals of Spacecraft Attitude Determination and Control* (1st ed.). New York: Springer.
- Meyer, R. X. (1999). *Elements of Space Technology* (1st ed.). London, United Kingdom: Academic Press.
- Mooij, E. (1994). *The motion of a vehicle in a planetary atmosphere* (Tech. Rep.). Delft. Retrieved from <http://resolver.tudelft.nl/uuid:e5fce5a0-7bce-4d8e-8249-e23293edbb55> (Delft University of Technology, Faculty of Aerospace Engineering, Report LR-768)
- Morita, Y., Kawaguchi, J., Nakajima, T., Hinada, M., & Naide, T. (1992, aug). Attitude dynamics of the LUNAR-A penetrator. In *Guidance, Navigation and Control Conference*. Reston, Virginia: American Institute of Aeronautics and Astronautics. Retrieved from <http://arc.aiaa.org/doi/10.2514/6.1992-4370> doi: 10.2514/6.1992-4370
- Mosher, T. J., & Lucey, P. (2006, oct). Polar Night: A lunar volatiles expedition. *Acta*

- Astronautica*, 59(8-11), 585–592. Retrieved from <http://linkinghub.elsevier.com/retrieve/pii/S0094576505002080> doi: 10.1016/j.actaastro.2005.07.033
- Nakajima, T., Hinada, M., Mizutani, H., Saitoh, H., Kawaguchi, J., & Akio, F. (1996, jul). Lunar penetrator program: LUNAR-A. *Acta Astronautica*, 39(1-4), 111–119. Retrieved from <http://linkinghub.elsevier.com/retrieve/pii/S0094576596001282> doi: 10.1016/S0094-5765(96)00128-2
- Nise, N. S. (2011). *Control Systems Engineering* (1st ed.). Chichester, United Kingdom: John Wiley & Sons, Ltd.
- Nozette, S., Lichtenberg, C. L., Spudis, P., Bonner, R., Ort, W., Malaret, E., ... Shoemaker, E. M. (1996, nov). The Clementine Bistatic Radar Experiment. *Science*, 274, 1495–1498. Retrieved from <http://science.sciencemag.org/content/274/5292/1495> doi: 10.1126/science.274.5292.1495
- Pisacane, V. L. (2005). *Fundamentals of Space Systems* (2nd ed.). Oxford: Oxford University Press.
- Rahn, C. D., & Barba, P. M. (1991, jul). Reorientation Maneuver for Spinning Spacecraft. *Journal of Guidance, Control, and Dynamics*, 14(4), 724–728. Retrieved from <http://arc.aiaa.org/doi/10.2514/3.20705> doi: 10.2514/3.20705
- Raus, R., Gao, Y., Wu, Y., & Watt, M. (2012, jul). Analysis of state-of-the-art single-thruster attitude control techniques for spinning penetrator. *Acta Astronautica*, 76, 60–78. Retrieved from <http://linkinghub.elsevier.com/retrieve/pii/S0094576512000495> doi: 10.1016/j.actaastro.2012.02.014
- Saunders, C., Jason, S., Friend, J., & Cosby, M. (2016, September 23). *Lunar Mission Flight Opportunity for Small Missions and Payloads*. (Document Ref: XRNG 0272376, Issue 2)
- Shiraishi, H., Tanaka, S., Fujimura, A., & Hayakawa, H. (2008, jul). The present status of the Japanese Penetrator Mission: LUNAR-A. *Advances in Space Research*, 42(2), 386–393. Retrieved from <http://linkinghub.elsevier.com/retrieve/pii/S0273117707009052> doi: 10.1016/j.asr.2007.08.022
- Shuster, M. D. (1993, oct). A Survey of Attitude Representations. *The Journal of the Astronautical Sciences*, 41(4), 439–517.
- Si, J., Gao, Y., & Chanik, A. (2018, mar). Feedback slew algorithms for prolate spinners using Single-Thruster. *Acta Astronautica*, 144(November 2017), 39–51. Retrieved from <https://linkinghub.elsevier.com/retrieve/pii/S0094576516312358> doi: 10.1016/j.actaastro.2017.11.044
- Sidi, M. (1997). *Spacecraft Dynamics and Control: A Practical Engineering Approach*. Cambridge, United Kingdom: Cambridge University Press.
- Silva, N., Martel, F., & Delpy, P. (2005, oct). Automated Transfer Vehicle Thrusters Selection and Management Function. In *6th international esa conference on guidance, navigation and control systems*. Loutraki, Greece.
- Singh, S. (1987, may). Nonlinear Adaptive Attitude Control of Spacecraft. *IEEE Transactions on Aerospace and Electronic Systems*, AES-23(3), 371–379. Retrieved from <http://ieeexplore.ieee.org/document/4104351/> doi: 10.1109/TAES.1987.310835
- Smith, A., Crawford, I. A., Gowen, R. A., Ambrosi, R., Anand, M., Banerdt, B., ... Wright, I. (2012, apr). Lunar Net—a proposal in response to an ESA M3 call in 2010 for a medium

- sized mission. *Experimental Astronomy*, 33(2-3), 587–644. Retrieved from <http://link.springer.com/10.1007/s10686-011-9250-5> doi: 10.1007/s10686-011-9250-5
- Smith, A., Crawford, I. A., Gowen, R. A., Ball, A. J., Barber, S. J., Church, P., . . . Sims, M. (2009, mar). LunarEX—a proposal to cosmic vision. *Experimental Astronomy*, 23(3), 711–740. Retrieved from <http://link.springer.com/10.1007/s10686-008-9109-6> doi: 10.1007/s10686-008-9109-6
- Smith, A., Gowen, R., Rees, K., Theobald, C., Brown, P., Pike, W., . . . Wells, N. (2010, jun). Application of penetrators within the solar system, technology challenges and status. *Advances in Geosciences*, 19, 307–320. Retrieved from https://doi.org/10.1142/9789812838162_0024 doi: 10.1142/9789812838162_0024
- Smrekar, S., Catling, D., Lorenz, R., Magalhães, J., Moersch, J., Morgan, P., . . . Blaney, D. (1999, nov). Deep Space 2: The Mars Microprobe Mission. *Journal of Geophysical Research: Planets*, 104(E11), 27013–27030. Retrieved from <http://doi.wiley.com/10.1029/1999JE001073> doi: 10.1029/1999JE001073
- Speyerer, E. J., & Robinson, M. S. (2013, jan). Persistently illuminated regions at the lunar poles: Ideal sites for future exploration. *Icarus*, 222(1), 122–136. Retrieved from <http://dx.doi.org/10.1016/j.icarus.2012.10.010> doi: 10.1016/j.icarus.2012.10.010
- SSSERVI. (2015, December 03). *Workshop Without Walls: Polar Regolith*. <https://sservi.nasa.gov/polar-regolith-workshop/>. (Accessed: 2019-05-24)
- Stewart, J. (2008). *Calculus: Early Transcendentals* (6th ed.). Belmont, California: Brooks/Cole - Cengage Learning.
- Surkov, Y., & Kremnev, R. (1998, nov). Mars-96 mission: Mars exploration with the use of penetrators. *Planetary and Space Science*, 46(11-12), 1689–1696. Retrieved from <http://linkinghub.elsevier.com/retrieve/pii/S0032063398000713> doi: 10.1016/S0032-0633(98)00071-3
- Surkov, Y., Moskaleva, L., Shcheglov, O., Sheretov, E., Kremnev, R., Pichkhadze, K., . . . Dolgopolov, V. (1999, aug). Lander and scientific equipment for exploring of volatiles on the Moon. *Planetary and Space Science*, 47(8-9), 1051–1060. Retrieved from <http://linkinghub.elsevier.com/retrieve/pii/S0032063399000288> doi: 10.1016/S0032-0633(99)00028-8
- Swink, D., Morgan, O., & Robinson, J. (1999, jun). Design and Analysis of a Low-Cost Reaction Control System for GPS IIF. In *35th Joint Propulsion Conference and Exhibit*. Reston, Virginia: American Institute of Aeronautics and Astronautics. Retrieved from <http://arc.aiaa.org/doi/10.2514/6.1999-2469> doi: 10.2514/6.1999-2469
- Tsiotras, P., & Longuski, J. M. (1994, dec). Spin-axis stabilization of symmetric spacecraft with two control torques. *Systems & Control Letters*, 23(6), 395–402. Retrieved from <http://linkinghub.elsevier.com/retrieve/pii/0167691194900930> doi: 10.1016/0167-6911(94)90093-0
- Urey, H. C. (1952). *The Planets: Their Origin and Development*. New Haven, Connecticut: Yale University Press.
- Vadali, S. (1986, mar). Variable-Structure Control of Spacecraft Large-Angle Maneuvers. *Journal of Guidance, Control, and Dynamics*, 9(2), 235–239. Retrieved from <http://arc.aiaa.org/doi/10.2514/3.20095> doi: 10.2514/3.20095

- Van Der Ha, J. C., & Janssens, F. L. (2005, may). Jet-Damping and Misalignment Effects During Solid-Rocket-Motor Burn. *Journal of Guidance, Control, and Dynamics*, 28(3), 412–420. Retrieved from <http://arc.aiaa.org/doi/10.2514/1.3852> doi: 10.2514/1.3852
- Van Den Bosch, P., Jongkind, W., & Van Swieten, A. (1986, mar). Adaptive attitude control for large-angle slew manoeuvres. *Automatica*, 22(2), 209–215. Retrieved from <http://linkinghub.elsevier.com/retrieve/pii/0005109886900828> doi: 10.1016/0005-1098(86)90082-8
- Vasavada, A. R., Paige, D. A., & Wood, S. E. (1999, oct). Near-surface temperatures on Mercury and the Moon and the stability of polar ice deposits. *Icarus*, 141(2), 179–193. Retrieved from <http://linkinghub.elsevier.com/retrieve/pii/S0019103599961754> doi: 10.1006/icar.1999.6175
- Vijendran, S., Fielding, J., Köhler, J., Gowen, R., Church, P., & Falkner, P. (2010, jan). A penetrator for the Jupiter Ganymede Orbiter Mission. In *Proceedings of the 7th International Planetary Probe Workshop*. Barcelona, Spain.
- Vijendran, S., Perkinson, M.-C., Waugh, L., Ratcliffe, A., Kennedy, T., Church, P., ... Taylor, N. (2014, apr). Development and testing of a Europa Penetrator for Astrobiology. In *European Planetary Science Congress 2014, EPSC Abstracts, id. EPSC2014-586* (Vol. 9). Retrieved from <http://adsabs.harvard.edu/abs/2014EPSC...9..642V>
- Watson, K., Murray, B., & Brown, H. (1961a, may). On the possible presence of ice on the Moon. *Journal of Geophysical Research*, 66(5), 1598–1600. Retrieved from <http://doi.wiley.com/10.1029/JZ066i005p01598> doi: 10.1029/JZ066i005p01598
- Watson, K., Murray, B. C., & Brown, H. (1961b, sep). The behavior of volatiles on the lunar surface. *Journal of Geophysical Research*, 66(9), 3033–3045. Retrieved from <http://doi.wiley.com/10.1029/JZ066i009p03033> doi: 10.1029/JZ066i009p03033
- Waugh, L., & Perkinson, M.-C. (2013). *Penetrator Phase 2: Final Report* (Tech. Rep.). Stevenage, United Kingdom: Astrium. (Doc. Ref.: PP2.TN.0017.AEU, Unpublished)
- Webster, E. (1985, jul). Active nutation control for spinning solid motor upper stages. In *21st Joint Propulsion Conference*. Reston, Virginia: American Institute of Aeronautics and Astronautics. Retrieved from <http://arc.aiaa.org/doi/10.2514/6.1985-1382> doi: 10.2514/6.1985-1382
- Wen, J., & Kreutz-Delgado, K. (1991). The attitude control problem. *IEEE Transactions on Automatic Control*, 36(10), 1148–1162. Retrieved from <http://ieeexplore.ieee.org/document/90228/> doi: 10.1109/9.90228
- Wertz, J. R. (1978). *Spacecraft Attitude Determination and Control* (1st ed.). Dordrecht, The Netherlands: Springer.
- Wertz, J. R. (2005). *Space Mission Analysis and Design* (3rd ed.). El Segundo, California: Microcosm.
- Wie, B. (2008). *Space Vehicle Dynamics and Control* (2nd ed.). Reston, Virginia: American Institute of Aeronautics and Astronautics, Inc.
- Wie, B., & Barba, P. M. (1985, may). Quaternion feedback for spacecraft large angle maneuvers. *Journal of Guidance, Control, and Dynamics*, 8(3), 360–365. Retrieved from <http://arc.aiaa.org/doi/10.2514/3.19988> doi: 10.2514/3.19988
- Wie, B., Weiss, H., & Arapostathis, A. (1989, may). Quaternion Feedback Regulator for

- Spacecraft Eigenaxis Rotations. *Journal of Guidance, Control, and Dynamics*, 12(3), 375–380. Retrieved from <http://arc.aiaa.org/doi/10.2514/3.20418> doi: 10.2514/3.20418
- Wiener, T. (1962). *Theoretical analysis of gimballess inertial reference equipment using delta-modulated instruments* (Dissertation, Massachusetts Institute of Technology). Retrieved from <https://dspace.mit.edu/handle/1721.1/14454>
- Wilson, E., Lages, C., & Mah, R. (2002). On-Line Gyro-Based, Mass-Property Identification for Thruster-Controlled Spacecraft using Recursive Least Squares. In *The 2002 45th Midwest Symposium on Circuits and Systems*. Tulsa, Oklahoma: IEEE. Retrieved from <https://ieeexplore.ieee.org/document/1186866/> doi: 10.1109/MWSCAS.2002.1186866
- Wörner, J. (2016, November 23). *Moon Village: A vision for global cooperation and Space 4.0*. <http://blogs.esa.int/janwoerner/2016/11/23/moon-village/>. (Visited: March 5, 2019)
- Wright, I. P., Sheridan, S., Barber, S. J., Morgan, G. H., Andrews, D. J., & Morse, A. D. (2015, jul). CHO-bearing organic compounds at the surface of 67P/Churyumov-Gerasimenko revealed by Ptolemy. *Science*, 349(6247). Retrieved from <http://www.sciencemag.org/cgi/doi/10.1126/science.aab0673> doi: 10.1126/science.aab0673
- Yang, C.-D., & Kung, C.-C. (2000, mar). Nonlinear H_∞ Flight Control of General Six-Degree-of-Freedom Motions. *Journal of Guidance, Control, and Dynamics*, 23(2), 278–288. Retrieved from <http://arc.aiaa.org/doi/10.2514/2.4520> doi: 10.2514/2.4520
- Zhang, H.-H., Wang, F., & Trivailo, P. M. (2008, dec). Spin-axis stabilisation of underactuated rigid spacecraft under sinusoidal disturbance. *International Journal of Control*, 81(12), 1901–1909. Retrieved from <http://www.tandfonline.com/doi/abs/10.1080/00207170801930217> doi: 10.1080/00207170801930217